Summer 9-1-2014

Studies of Structural and Chemical Ordering in Metallic Liquids and Glasses Using Electrostatic Levitation

Adam Vogt
Washington University in St. Louis

WASHINGTON UNIVERSITY IN ST. LOUIS

Department of Physics

Dissertation Examination Committee:
Kenneth F. Kelton, Chair
Katharine Flores
Patrick Gibbons
Erik Henriksen
Zohar Nussinov
Li Yang

Studies of Structural and Chemical Ordering in Metallic Liquids and Glasses Using Electrostatic Levitation

by

Adam Joseph Vogt

A dissertation presented to the
Graduate School of Arts and Sciences
of Washington University in
partial fulfillment of the
requirements for the degree
of Doctor of Philosophy

August 2014

St. Louis, Missouri

Contents

List of Figures

List of Tables

List of Abbreviations and Common Terms

APS	Advanced Photon Source
APS 2011	Series of XRD experiments of amorphous ribbons carried out in October 2011 at the APS
APS 2012	Series of XRD experiments of amorphous ribbons carried out in August 2012 at the APS
ARCS	Wide Angular-Range Chopper Spectrometer
BESL	Beamline Electrostatic Levitation (Levitator)
BESL 2010	Series of BESL experiments carried out in August 2010 at the APS
BESL 2013	Series of BESL experiments carried out in June 2013 at the APS
BMG	Bulk Metallic Glass
CCR	Critical Cooling Rate
CCT	Critical Casting Thickness
CNCS	Cold Neutron Chopper Spectrometer
CRMC	Constrained Reverse Monte Carlo
CSRO	Chemical Short-Range Order
DLR	German Aerospace Institute
DRPHS	Dense Random Packing of Hard Spheres
DSC	Differential Scanning Calorimetry
DTA	Differential Thermal Analysis
EAM	Embedded Atom Model
ECP	Efficient Cluster Packing
EML	Electromagnetic Levitation
ESL	Electostaic Levitation (Levitator)
EXAFS	Extended X-ray Absorption Fine Structure
fcc	Face-Centered Cubic
FCS	First Coordination Shell
FZ	Faber-Ziman
GFA	Glass-Forming Ability
HA	Honeycutt-Anderson common neighbor analysis
hcp	Hexagonal close-packed
HV	High Voltage
ISRO	Icosahedral Short-Range Order
ISU	Iowa State University
LED	Light Emitting Diode
LRO	Long-Range Order
MD	Molecular Dynamics
MG	Metallic Glass
MMC	Metropolis Monte Carlo
MRO	Medium-Range Order
MUCAT	Midwestern Universities Collaborative Access Team
NASDA	National Space Agency of Japan

NESL	Neutron Electrostatic Levitator
NIST	National Institute of Standards and Technology
NOMAD	Nanoscale-Ordered Materials Diffractometer
ORNL	Oak Ridge National Laboratory
PDF	Pair Distribution Function
PPCF	Partial Pair Correlation Function
PSD	Position Sensitive Detector
PSF	Partial Structure Factor
RMC	Reverse Monte Carlo
SNS	Spallation Neutron Source
SRO	Short-Range Order
TEM	Transmission Electron Microscopy
T_g	Glass Transition Temperature
T_L	Liquidus Temperature
TM	Transition Metal
T_r	Reduced Undercooling Temperature
T_{rg}	Reduced Glass Transition Temperature
T_S	Solidus Temperature
TTL	Transistor-Transistor Logic
T_X	Crystallization (Devitrification) Temperature
UV	Ultra Violet
VULCAN	Engineering Materials Diffractometer
WU-BESL	Washington University Beamline Electrostatic Levitator
WUSTL	Washington University in St. Louis
XAS	X-ray Absorption Spectroscopy
XRD	X-ray Diffraction

Acknowledgements

First and foremost, I would like to thank my advisor Prof. Ken Kelton. His dedication to his craft, his colleagues, his team, and, in particular, to his students is outstanding. Without his knowledge, enthusiasm, support, and advice, this work would not have been possible. Your devotion to our scientific pursuits has been an inspiration.

I would like to thank Prof. Zohar Nussinov and Prof. Pat Gibbons for their mentoring throughout the years. Your support and commitment is greatly appreciated. I would also like to thank Dr. Anup Gangopadhyay for his guidance, support, and useful discussions through which much of this work was made possible. I would specifically like to thank Dr. Nicholas Mauro for his mentorship, experience, friendship, and collaboration throughout my graduate career. Your commitment and enthusiasm has been an inspiration. I would also like to thank past and current members of the Kelton research team: Vic Wessels, James Bendert, Kevin Derendorf, Matt Blodgett, Mark Johnson, Chris Pueblo, and Jen Gewin. Vic and James, your experience and guidance on both on both technical and non-technical matters were indispensible. To Kevin, Matt, Mark, and Chris, I am extremely grateful for your camaraderie, dedication, and support through these years. A special thanks to Matt, Mark, and Chris for their aid in developing this work and proofing this dissertation. Finally, I would like to thank the many undergraduates who helped support the work of the group, and in particular, I would like to thank Zachary Markow for his help, work, and useful discussions.

I would like to thank the Washington University Physics Department Faculty and Staff. Much of the work and construction would not have been possible without the help and guidance of the R & D shop team: Todd Hardt, Denny Huelsman, and Tony Biondo. I am also grateful for

the work and useful discussion from our collaborators, Ryan Soklaski and Li Yang. I would also like to thank our collaborators. Evan Ma and Jun Ding of Johns Hopkins University, I thank you for your work and collaboration. Alan Goldman, Andreas Kreyssig of Iowa State University, Matt Kramer and Matt Besser of Ames Laboratory, and Doug Robinson of Argonne National Laboratory, I thank you for your support, guidance, expertise, and valuable discussions on the topics of X-ray scattering for our work at the Advanced Photon Source. Takeshi Egami and Konstantin Lokshin of the University of Tennessee, I thank you for your help and expertise provided for work on the NESL and neutron scattering experiments at the Spallation Neutron Source. I would also like to thank the engineers, scientists, and support staff at Oak Ridge National Laboratory for making the NESL work possible, and, in particular, Cory Fletcher for all of his help. Finally, I would like to thank fellow students Gustav Rustan and Dante Quirinale of Iowa State University for their advice, support, camaraderie, and useful discussions in our electrostatic levitation development and experiments.

I acknowledge the agencies that funded this work: Washington University in St. Louis under the Summer Hughes Fellowship, the National Science Foundation under grants DMR-08-56199, DMR-12-06707, and DMR-09-59465, and the National Aeronautics and Space Agency under grants NNX07AK27G and NNX10AU19G. The synchrotron measurements were made on the Sector 6 (formerly MUCAT) 6-ID-D beamline at the Advanced Photon Source. Use of the Advanced Photon Source, an Office of Science User Facility operated for the U.S. Department of Energy (DOE) Office of Science by Argonne National Laboratory, was supported by the U.S. DOE under Contract No. DE-AC02-06CH11357.

I would like to thank former educators and mentors at Truman State University, St. Pius X High School, and Our Lady School in Festus. I would also like to thank my friends and family who have always been there for me. I thank my parents, Phil and Sue, and my brother, Bob, for the unending support, encouragement, and love. Finally, I thank my beautiful wife, Mickey, for always supporting me from both near and far. You make it all worthwhile. I love you, alwayses and forevers.

ABSTRACT OF THE DISSERTATION

Studies of Structural and Chemical Ordering in Metallic Liquids and Glasses Using Electrostatic Levitation

by

Adam Joseph Vogt

Doctor of Philosophy in Physics

Washington University in St. Louis, 2014

Professor Kenneth F. Kelton, Chair

Since the discovery of the first metallic glass in 1960, there has been a large research effort dedicated to understanding the glass transition and the formation of metallic glass from the supercooled liquid state. Knowledge of the relationship between the liquid's structure and its thermophysical and kinetic properties provide insight into why some metallic alloy liquids form glasses more easily than others. Such structure and property measurements of high temperature, highly reactive metallic liquids in both their equilibrium and metastable, supercooled states are made possible through the use of the electrostatic levitation (ESL) technique. Presented here are the results of *in situ* high-energy X-ray scattering studies of metallic liquids and glasses utilizing the Washington University Beamline Electrostatic Levitation (WU-BESL) facility. Structural studies of binary Cu-Zr and Cu-Hf bulk glass-forming liquids and glasses reveal signatures of chemical ordering in the liquid with decreasing temperature and evidence for accelerated ordering in the deeply supercooled state. Novel experimental measurements and Reverse Monte Carlo simulations of the structure of bulk glass-forming $Pd_{82}Si_{18}$ liquid show a lack of acceleration in ordering, in contrast with the behavior of the widely studied Cu-Zr binary

alloy liquids. Measurements of the liquid structures of Si-containing alloys ($Au_{81}Si_{19}$, $Pd_{82}Si_{18}$, $Ni_{75}Si_{25}$, and $Pd_{77}Cu_6Si_{17}$) reveal a variety of chemical and topological signatures that may provide insight into differences in their glass-forming ability. More specifically, a signature of kinetic strength in structures of the $Pd_{77}Cu_6Si_{17}$ liquid and glass support previous results while leading to a prediction of the structural behavior of the deeply supercooled $Pd_{82}Si_{18}$ liquid. In addition, the development of and first results from of a new ESL facility for complimentary neutron diffraction studies for use at the Spallation Neutron Source are also described.

Chapter 1

Introduction

The study of viscous liquids, glasses, and the glass transition remains "one of the most significant unsolved problems in condensed matter physics" [1] and is important for the future development of better materials for a wide variety of applications [2, 3]. The unique properties of glasses and other amorphous solids make for interesting and useful materials. While they have been fashioned and used throughout human history, the true nature of the transition from the liquid state to the amorphous solid remains poorly understood. The study of the atomic structure of liquids and glasses, necessary for any materials application, poses an interesting problem given the lack of long-range order (LRO) that is found in crystalline solids. Even though they lack LRO, liquids and glasses do contain a significant amount of short-range order (SRO) as well as some medium-range order (MRO). The ability for a liquid to bypass crystallization and form a glass by radically slowing the rate of atomic structural rearrangements is fundamental to the glass transition, and understanding the evolving structures of supercooled liquids (i.e. liquids below their liquidus temperature, T_L) with temperature and the relation of those structures to those of glasses are necessary to probe the nature of this process.

Recent developments in the discovery and preparation of metallic glasses (MG) have led to intense research activity over the last 60 years that has improved our understanding of the nature of liquids and glasses [4-6]. Because of the high cooling rates typically required to form glasses from metallic liquids, however, their applications and usefulness have only been recently

realized. The ability to supercool a liquid without crystallizing is necessary for glass formation and depends on the ability to cool the liquid sufficiently fast. The glass-forming ability (GFA), or ease with which a metallic liquid can be formed in to a glass varies significantly with the number and type of constituent elements, as well as the precise composition within a given alloy system. The research presented here is focused on developing an understanding of why particular alloys and compositions vary in their GFA and how this variation is related to the structures of the supercooled liquids and glasses. This chapter begins with a general overview of liquids, glasses, and the glass transition (Sect. 1.1), and follows with a summary of research relating to bulk metallic glasses (BMG) (Sect. 1.2). The current understanding of the supercooled liquid and metallic glass atomic structures and their relationship to the system's kinetics/thermodynamics will be briefly discussed (Sect. 1.3). Finally, the use of containerless processing techniques for the study of supercooled liquids will be described (Sect 1.4).

1.1 Liquids, Glasses, and the Glass Transition

As previously discussed, liquids and glasses (amorphous solids) do not contain the LRO that describes crystalline solids. However, this lack of LRO does not mean that the atomic positions are random. Unlike diffuse gasses, where there is a complete lack of correlation in the position of the atoms, dense liquids have defined arrangements of atoms within their nearest and even second-nearest neighbor coordination shells. Glasses exhibit similar local structure, but unlike liquids, glasses are rigid solids, due to the greatly reduced atomic mobility. An example of defined local order without LRO is given in figure 1.1, where the number of bonds around a particular atom is fixed, resulting in significant SRO and some MRO. The bond lengths and angles are allowed to vary slightly, resulting in a non-crystalline structure.

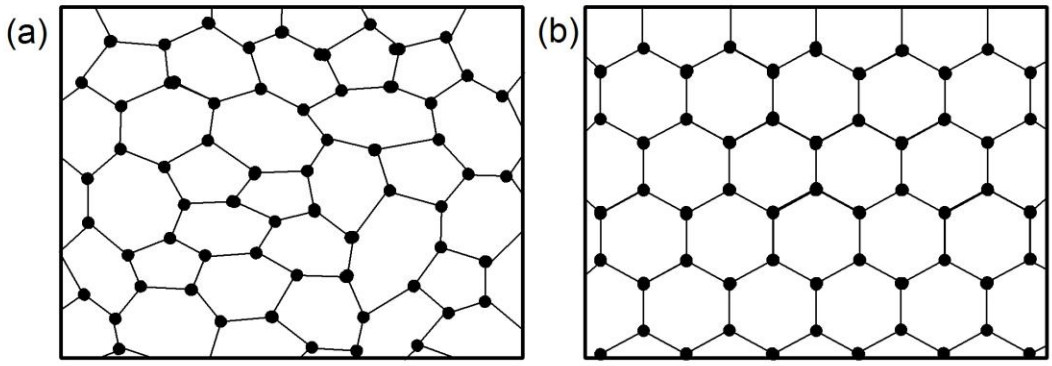

Figure 1.1: A two-dimensional representation of order in (a) an amorphous structure and (b) a crystalline structure. While the SRO is well defined in both examples, only (b) exhibits LRO.

Glasses are formed when a liquid is cooled sufficiently fast to essentially bypass crystallization. Thermodynamically, glasses and supercooled liquids are metastable, since below a material's T_L (the temperature at which the equilibrium system transitions from partially crystalline to fully liquid) the crystalline phase is energetically favored. The kinetic properties of the system influence its ability to reach thermodynamic equilibrium. As a liquid is cooled, the atomic mobility is lowered preventing the rearrangement of the atomic structure to the energetically preferred crystalline form.

The glass transition temperature, T_g, is the point at which the atomic mobility becomes small enough that the atoms are "frozen" in their positions. At the glass transition, the system abruptly changes character. Some thermodynamic properties continuously change in their temperature dependence, such as volume, enthalpy, and entropy, with slopes becoming similar to those of the crystalline solid (Fig. 1.2). Other thermodynamic properties change abruptly, nearly discontinuously, such as specific heat [7] and thermal expansion, characterizing the glass transition as an "apparent, diffuse, second-order [phase] transition" [8].

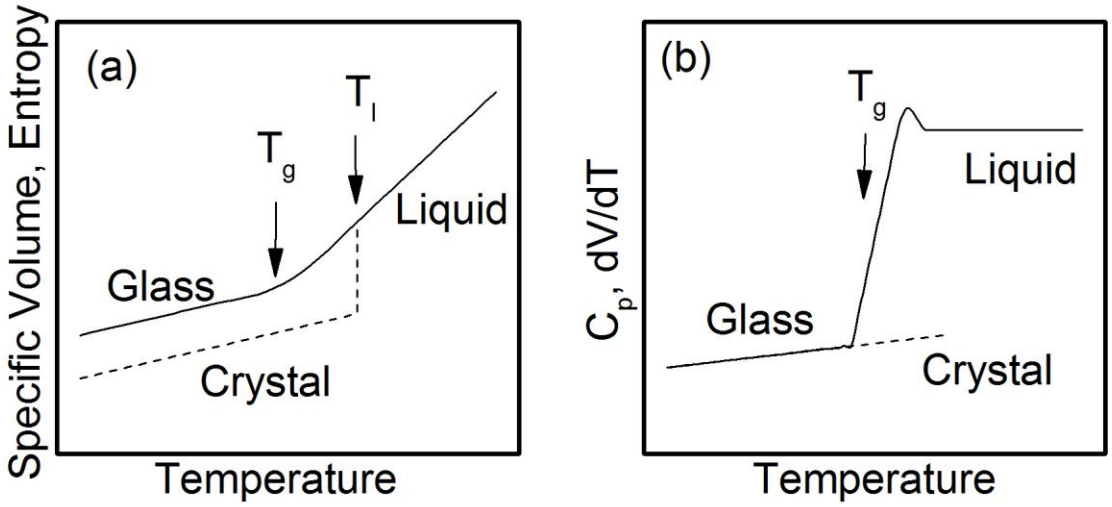

Figure 1.2: Schematic diagrams of the temperature dependence of thermophysical properties through the glass transition. (a) During glass formation, crystallization is bypassed as the liquid is cooled below T_L while the glassy properties approach those of the crystalline state below T_g. (b) An example of an abrupt property change near T_g.

A key characteristic of the glass transition from the supercooled liquid is the rapid increase in the viscosity in the liquid with decreasing temperature. The viscosity increases by orders of magnitude over a very small temperature range near the glass transition. In terms of the system's viscosity, the glass transition temperature, T_g, is empirically defined as the temperature at which the viscosity reaches 10^{12} Pa·s. The temperature dependence of the viscosity varies among different liquids, and this variation is related to the inherent structure of the liquid.

The relationship between the structure and the dynamical properties of the supercooled liquid and glass can be understood via the framework of the energy landscape [9]. The energy landscape model defines a multidimensional hypersurface in 3N+1 space corresponding to the potential energy for each possible configuration of the N atoms in the system (Fig. 1.3). Sampling the potential energy surface, or movement along the landscape, is related to the dynamic behavior of the system [10], where local movements are related to rearrangements of

atoms within clusters and larger movements relate to larger scale atomic rearrangements. Saddle points, or local maxima, correspond to high energy states and serve as energy barriers to atomic rearrangement. Minima in the landscape correspond to low energy states, and the global minimum corresponds to the lowest energy, or crystalline, configuration. Local minima, on the other hand, are metastable states and may be part of larger megabasins, such as the ideal glass basin, where the potential energy of the local minima is close to, but not as small as the global minimum.

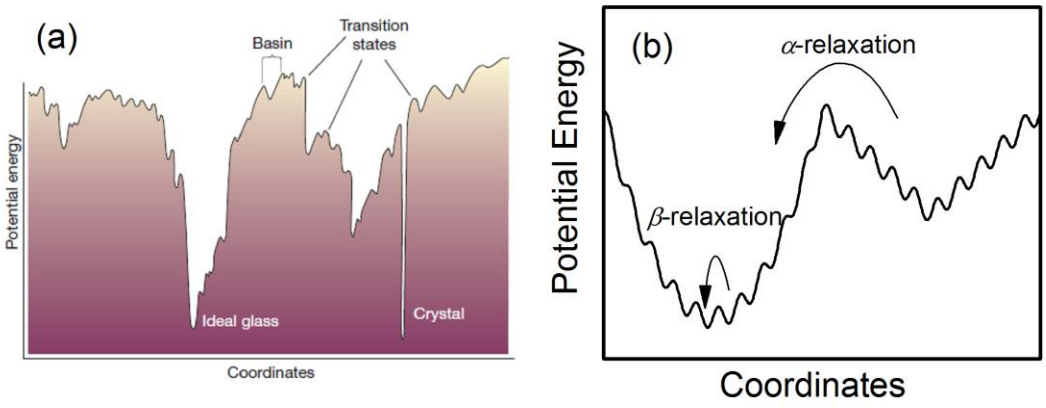

Figure 1.3: (a) Schematic illustration of an energy landscape. The x-axis represents all configurational coordinates [Adapted by permission from Macmillan Publishers Ltd: NATURE [9] copyright (2001)]. (b) Enlarged view of the landscape with respective representations of α- and β-relaxation between and within potential energy basins.

At high temperatures, the system has enough kinetic energy to sample the entire energy landscape and is therefore ergodic. The rates, or relaxation times, at which the system makes movements along the hypersurface are similar. These relaxation times begin to diverge as the system is cooled; β-relaxation relates to local atomic or cluster rearrangements (movements to local minima within a larger energy basin), and α-relaxation refers to larger, more cooperative atomic rearrangements (movements between megabasins) (Fig. 1.3) [11]. Once the kinetic

energy is low enough, α-relaxation disappears and the system can no longer sample the entire configuration space. The system becomes non-ergodic, marking the glass transition.

Systems with a few, large megabasins exhibit only local atomic or cluster rearrangements with β-relaxation dominating. The movement of atoms in such a system resembles an activated process, giving an Arrhenius temperature dependence for the viscosity,

$$\eta = \eta_0 \exp(E_A/RT) \tag{1.1}$$

where η is the viscosity, T is the temperature, E_A is the activation energy, R is the gas constant (related to the Boltzmann constant), and η_0 is a constant related to the viscosity at infinite temperature. Alternatively, systems with a large number of basins would exhibit α-relaxation dominated atomic rearrangements, and as the system approaches T_g, movement across the energy landscape would decrease dramatically. This non-Arrhenius behavior is marked with an apparent increase in the activation energy with decreasing temperature. The classification of glass-forming liquids by the temperature dependence of the viscosity near T_g as either strong (more Arrhenius) or fragile (less Arrhenius) (Fig 1.4) was proposed by Angell [1, 12].

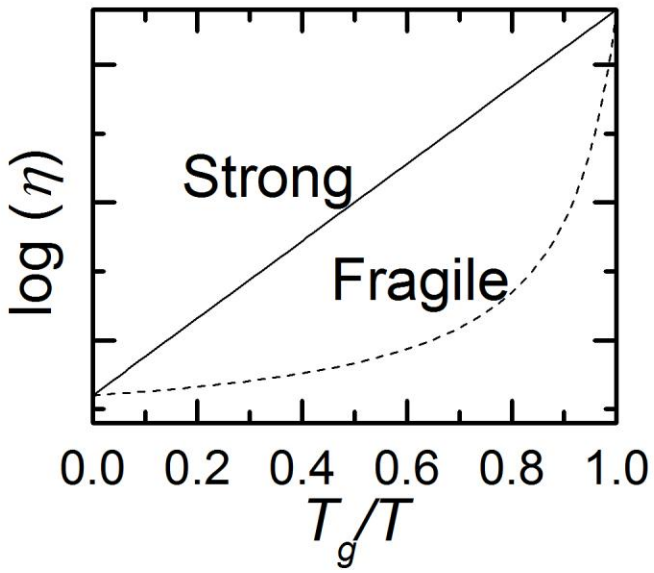

Figure 1.4: Schematic diagram of the temperature dependence of the viscosity. Strong liquids approaching the glass transition exhibit Arrhenius temperature dependence, as described in Eq. 1.1, while fragile liquids exhibit non-Arrhenius temperature dependence.

The relaxation dynamics of the supercooled liquid is also connected with thermodynamic properties via the Adam-Gibbs equation [13],

$$\eta = \eta_0 \exp[B/T\, S_C(T)], \tag{1.2}$$

Where B is a constant and $S_C(T)$ is the configurational entropy of the liquid. The configurational entropy term again relates the structure to the dynamics of the liquid, and its temperature dependence will influence the temperature dependence of the viscosity. If S_C is T-independent, the liquid viscosity should follow an Arrhenius behavior. However, in most liquids S_C does have a temperature dependence leading to a more fragile, non-Arrhenius behavior of the viscosity. The temperature dependence of S_C is also related to the "excess specific heat", ΔC_p, or the difference in the constant-pressure specific heat between the supercooled liquid and the crystal or frozen glass, as given by $\left(\frac{\partial S_C}{\partial T}\right)_p = \frac{\Delta C_p}{T}$. Experimental [14] and theoretical [15] evidence has

been found relating the temperature dependence of ΔC_p to the liquid fragility, ultimately relating the structure of the supercooled liquid to its dynamics [15]. Recent experimental measurements of the liquid structure have also shown evidence for a structural signature of the liquid dynamics [16-19].

1.2 Bulk Metallic Glasses

As mentioned before, glasses can be found in many places in everyday life and are most typically associated with silicate glasses (window glass, drinkware, Pyrex cooking glass). Other amorphous solids are common in other everyday materials, such as polymers like PVC or polystyrene, and can also be found naturally, such as obsidian formed from volcanic lava flows. Because of their high GFA, or ease with which they form glasses, traditional glasses are typically materials associated with complex network structures, though "nearly all liquids can, if cooled fast enough and far enough, be prepared as amorphous solids" [8]. GFA is typically defined in terms of a liquid's critical cooling rate (CCR; minimum rate of cooling in order to effectively bypass crystallization) or critical casting thickness (CCT; the size of the smallest dimension of the glass quenched from the liquid).

The relatively recent study and production of metallic glasses began with the first reported MG, $Au_{75}Si_{25}$, by Klement et al. [20]. Because metallic alloys easily crystallize upon solidification, their GFA is much lower than for more common network glasses. Metallic alloys require very high cooling rates (10^5-10^6 K/s) in order to form a glass. Since the first MG, many glass-forming alloys have been discovered involving nearly all of the metallic elements in the periodic table [21]. Metallic glasses with improved critical cooling rates (~10^3 K/s) were discovered beginning with Chen [22] by casting of Pd-Cu-Si alloys into millimeter diameter

rods. Turnbull et al. [23, 24] were able to produce ~1 cm BMGs of Pd-Ni-P at even lower cooling rates (10^2 K/s). With the development of Zr-based glass formers with improved critical cooling rates, Peker et al. [25] reported that the alloy $Zr_{41.2}Ti_{13.8}Cu_{12.5}Ni_{10.0}Be_{22.5}$ (Vitreloy 1) could be cast in to rods several centimeters in diameter at a critical cooling rate of ~1 K/s, making the first commercially viable MG.

High GFA materials with low critical cooling rates and large critical casting thicknesses form by avoiding crystallization through a particularly effective suppression of nucleation and growth of the crystalline phase. As the temperature of a liquid falls below the equilibrium melting temperature, the free energy of the equilibrium crystal phase becomes lower than that of the liquid phase, driving the rearrangement of the atomic structure towards the thermodynamically preferred crystalline phase. The process of creating clusters of atoms that resemble the new thermodynamically favored ordered phase is known as nucleation. In classical nucleation theory, a barrier to nucleation arises from an energy penalty for the formation of an interface between the parent (supercooled liquid) and daughter (crystalline) phases. The work of cluster formation, $W(n)$, is given by the equation

$$W(n) = n\Delta\mu + A\sigma, \tag{1.3}$$

where n is the size of a cluster, $\Delta\mu$ is the free energy difference between the parent and daughter phases, σ is the interfacial free energy, and A is the surface area of the cluster. Since $\Delta\mu$ is negative and σ is positive, a critical cluster size, n^*, is then defined when the energy cost of cluster formation equals the driving free energy for forming a cluster of the new phase. Clusters larger than n^* are energetically favored to grow. The kinetic model for nucleation, formulated by

Volmer and Weber [26], describes the rate of nucleation as the rate at which single atoms (or molecules) attach or detach from a cluster of size n. On average, clusters larger than n^* will grow while clusters smaller than n^* will shrink or dissolve. Therefore, avoidance of crystallization, and ultimately GFA, is affected by the free energy difference between the supercooled liquid and crystalline phase, the interfacial energy arising from the structural and chemical differences between the two phases, and the kinetic ability for the new phase to grow from the parent phase.

In order to find the metallic alloy compositions with the best GFA, empirical rules for BMG formation have been formulated by Inoue [27, 28]. The rules include: (i) multicomponent alloys with more than three elements, (ii) an atomic size mismatch greater than 12%, and (iii) a large negative heat mixing between the components. These rules account for the factors mentioned above that help avoid crystallization. Well mixed multicomponent alloys in the liquid phase can have a large compositional difference between that phase and the often more complicated equilibrium intermetallic phases, increasing the interfacial free energy. Atomic size mismatches and large negative heats of mixing between constituent elements affect clustering and local arrangements of atoms, often creating large interfacial barriers to crystallization as well as limiting atomic mobility and crystal nucleation kinetics.

Empirically, GFA is also found to improve for near-eutectic compositions. Because of the competition between the increasing driving free energy for crystallization (thermodynamics) and the increasing viscosity (kinetics) in the supercooled liquid as it cools, a narrow supercooled region improves glass formation [7]. The liquid at the eutectic composition is thermodynamically stable down to temperatures much lower than the melting temperatures of the constituent elements, and the reduced glass transition temperature ($T_{rg} = T_g/T_L$) tends to be

higher, much like in common nonmetallic glasses [29], especially since T_g typically has a smaller dependence on the alloy composition than does T_L in this region (as shown in Figure 1.4). A composition with a narrow supercooled region, or high reduced glass transition temperature, has a smaller driving free energy to crystallization and higher viscosity in the supercooled liquid regime because it remains as an equilibrium liquid down to much lower temperatures.

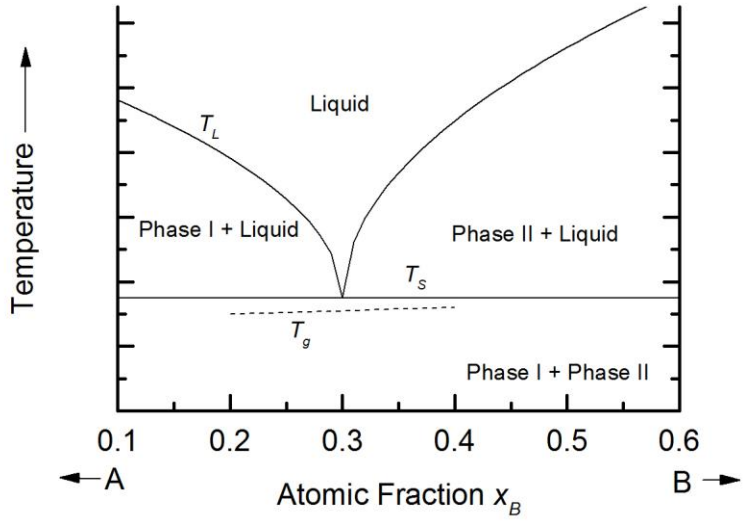

Figure 1.5: Schematic phase diagram representing a eutectic composition region. The dashed line indicates the glass transition temperature with respect to composition of element *B* in the alloy.

GFA has also been correlated to several dynamical and thermophysical properties of the liquid, including density [30], expansivity [31], specific heat (C_p) evolution with temperature [14], and kinetic fragility [14, 32-35]. The high viscosity of strong liquids at temperatures much higher than the glass transition temperature dramatically slows crystal nucleation and growth kinetics, making it important to GFA [36, 37]. Multicomponent alloys, suggested to have higher GFA, are reported to be stronger than those with fewer components [36]. Others have also shown that stronger liquids have higher GFA [32, 33].

Important exceptions to these empirical rules for BMG formation include binary metallic liquids. BMGs with critical casting thicknesses of 2 mm or greater have been found for systems

including Cu-Zr [30, 38-41], Cu-Hf [40, 42-44], Ni-Nb [45], Ni-Ta [46], and Pd-Si [47, 48]. Some of these systems show BMG formation over a wide composition range, not just at eutectics, allowing for studies of the compositional dependence of GFA. Because of their relative simplicity compared to multicomponent alloys, binary liquids and glasses are also ideal for studies of topological and chemical ordering and the relationship to kinetic and thermophysical properties of the system. The properties of some of these systems will be discussed in more detail in Chapters 3-5.

1.3 Structures in Liquids and Glasses

Before the first metallic glass was discovered in 1960 [20], Turnbull [49] successfully supercooled Hg droplets, showing that metallic liquids can have significant supercooling if heterogeneous nucleation is minimized. Because of the similar coordination numbers of metallic liquids and close-packed crystal phases, and the small change in density upon melting from the crystalline state, large undercooling of metallic liquids and ultimately glass formation was thought impossible, especially given the ease at which the liquids could rearrange their atomic structures to form the close-packed fcc and hcp crystalline structures. In order to explain the supercooling of pure metallic liquids, Frank [50] hypothesized that the local structures in metallic liquids must be different from those in the crystalline solid, resulting in the suppression of nucleation. However, the liquids still had to have a structure that was consistent with their high coordination number and density. Frank suggested that the icosahedron, a 12-coordinated nearest neighbor cluster like fcc and hcp structures, would be the preferred local arrangement in metallic liquids. The fivefold rotational symmetry of the icosahedrons would be incompatible

with LRO, therefore maintaining the metastable, undercooled liquid by suppressing nucleation of the preferred crystalline structure.

The concept of icosahedral short-range order (ISRO) has since inspired a large body of work in the description of the structures of metallic glasses and liquids [6]. Recently, the existence of ISRO in pure metallic liquids was reported in liquid Pb at the solid-liquid (Si-Pb) interface [51] as well as in pure bulk liquids, including Fe, Zr, Ni, Co, Ti, and Cu [52-57]. The connection between ISRO and the nucleation barrier, confirming Frank's hypothesis, was reported in several recent experiments [58, 59]. Additionally, liquid structures determined by *ab initio* molecular dynamics (MD) simulations also confirm icosahedral-like SRO (with various levels of distortion from the perfect icosahedrons) in pure Ni, Cu, Fe , Zr, Ta, and Ti [60-65]. Similar iscosahedral and icosahedral-like SRO has been reported in experimental and MD simulation data for many multicomponent metallic liquids and glasses as well [6].

Given the apparent importance of the local structure of liquids and glasses to the stability of these metastable states, a variety of models have been developed to describe the general structure of metallic systems. The most basic is the dense random packing of hard spheres (DRPHS) model, established by Bernal, Scott, and Finney [66-70] in which the densest packing of identical hard spheres form local tetrahedral clusters. Three-dimensional space tiling cannot be fulfilled by equilateral tetrahedron only and therefore tetrahedra and octahedra are involved in the close-packed face-centered cubic (fcc) and hexagonal close-packed (hcp) structures. Bernal suggested five canonical holes, clusters of identical spheres (including the tetrahedron and octahedron) that contain a hole not large enough to accommodate another sphere, which might be the basic structural units of a monatomic liquid. The holes other than the tetrahedron and octahedraon, believed to be present in liquids, are incompatible with LRO and therefore frustrate

the system. The DRPHS structures generated by experiments and simulations, confirming the significant presence of these structures, show many five-edged faces. The major shortcoming of the model is that it predicts a maximum packing fraction of 0.64, much lower than the packing fraction of hcp or fcc crystals, even though the density difference between the liquid and crystalline solid is small. The model in particular does not capture the correct chemistry because the packing of metal atoms is not random and metal atoms are not hard spheres. Rather, realistic metallic bonding exhibits some sort of interaction potential between atoms which serves to increase the system's packing density. In particular, the affinity, or lack-thereof, between chemical species, as measured by the elemental heat of mixing, can significantly change their average bond distance and, therefore, can dramatically influence the short to medium-range order in the liquid.

Strong chemical order in transition metal/metalloid (TM-metalloid) alloy MGs could not be explained by DRPHS, and the stereochemical model was proposed by Gaskell [71, 72]. In the stereochemical model, the SRO of the liquid or glass is the same as in the crystal, and differences occur in the MRO and how the clusters are related to each other. The stereochemical model was partially successful in describing covalently bonded systems, but struggled in describing the structure of other metallic systems.

The polytetrahedral packing model describes coordination shells by equally spacing nearest neighbor atoms around a central one. DRPHS is frustrated polytetrahedral packing [6]. Introducing disclinations in to polytetrahedral packing, with early work by Nelson and Spaepen [73], is found to increase the packing fraction and relieve frustration, particularly for multicomponent systems. Frank and Kasper [74, 75] introduced Z clusters that maximize tetrahedrality for different coordination numbers, describing a system in which local structure

dominates the system without accounting for the possibility of medium- or long-range order. More recently, Miracle [76, 77] proposed the efficient cluster packing (ECP) model to account for the importance of atomic size differences between constituent elements to SRO. While ECP provides a useful to look at the structure from the viewpoint of solute centered clusters, it cannot fully account for the MRO in the system.

Studies of the correlation between local atomic structure and the dynamics of the system represent the next logical step towards understanding GFA in liquid systems. As the liquid is cooled below T_L, the atomic mobility can become spatially heterogeneous, with some liquid-like regions where the atomic mobility is high, and some solid-like regions where the atoms can become caged or immobile [6]. This dynamical heterogeneity can be correlated with the atomic structure and the structural heterogeneities that form in the supercooled liquid. Configurational potential energy and configurational entropy in liquids is determined by the topological order, and some simulation studies indicate that slower particles may have lower configurational potential energy [78-81]. Connections between the low configurational entropy of the icosahedral cluster [82, 83], diffusivity, and non-Arrhenius dynamical slowdown in the supercooled liquid have been reported [84-87]. In MD simulations of Cu-Zr supercooled liquids, the fraction of Cu-centered icosahedra increases dramatically with decreasing temperature, and is correlated with decreased atomic mobility and deviation from Arrhenius behavior [88]. Similar results were found in other MD simulation studies of the Cu-Zr [15, 89-92] and Cu-Zr-Al [93] liquids. Experimentally determined links between icosahedral order and the kinetics/thermodynamics of the supercooled liquid [58, 59, 94, 95] provide credibility to conclusions drawn from MD simulations.

1.4 Containerless Processing

Supercooling in liquids has been studied since Fahrenheit's demonstration of the possibility of supercooling liquid water [96]. The key to achieving supercooling in liquids is the elimination of heterogeneous nucleation. Early techniques to minimize heterogeneous nucleation involved the use of clean crucibles and a reduction of atmosphere around the sample. Emulsion and substrate techniques were used to study small droplets of the liquid of interest in an appropriate, non-reactive medium or on a surface. A significant number of droplets contain no heterogeneous sites if the dispersion of droplets is sufficiently fine [97]. The original dilotometric studies of supercooled Hg by Turnbull [49] were performed in a dispersion medium.

In order to study larger samples of high-temperature, highly-reactive liquids, containerless processing techniques become necessary. Early techniques involved the use of drop tubes, when a sample is melted and allowed to crystallize while falling in an evacuated or inert gas-filled tube. It is difficult to measure the precise undercooling and impossible to measure thermophysical processes with this technique, limiting its usefulness. Precision measurements of liquids, however, can be made using levitation techniques. Aerodynamic levitation [98] utilizes controlled gas flow to counteract the force of gravity, but the use of flowing gas increases the difficulty of temperature and position control. Acoustic levitation [99] combined with aerodynamic levitation, while still suffering from some of the problems of pure aerodynamic levitation, has been successfully used to process nonvolatile materials, particularly nonconducting oxides and ceramics.

For the study of metallic liquids, the best techniques are electromagnetic (EML) [100] and electrostatic (ESL) levitation [101]. EML utilizes RF current in a coil to induce eddy currents in metallic samples from a changing magnetic flux. EML is useful for thermophysical

property and electrical resistivity measurements [97], particularly when performed in micro gravity [102], but suffers from several disadvantages when used terrestrially. In EML, the resistive heating of the sample is coupled to the levitation process, limiting the temperature range over which samples can be studied. Also, levitation coils can reduce the line-of-sight to the sample, limiting x-ray and neutron scattering studies as well as the number of simultaneous thermophysical property measurements. ESL, on the other hand, utilizes high-voltage electric fields in vacuum to counteract the force of gravity with coulomb attraction. The position of the sample is controlled by the voltage applied to orthogonal sets of electrodes. Samples are heated using high-intensity lasers instead of from eddy currents induced as a process of levitation, completely decoupling heating from levitation. The sample can be viewed from a wider range of angles, allowing for optimization of non-contact thermophysical property as well as X-ray [103, 104] and neutron diffraction studies [105-107]. The ESL technique will be discussed further in Chapters 2 and 6.

1.5 Summary

The overview in this chapter covers the background for the work that will be discussed in the following chapters. Understanding the kinetic and thermophysical properties and structures of liquids and glasses, as well as their relationship to the glass transition and glass formation, is essential to the work of this thesis. The relationship between the structural evolution and the kinetic and thermophysical properties of metallic liquids is investigated through experimental diffraction measurements of the liquid structure. Chapter 2 outlines the experimental and analysis techniques used to obtain the results presented in the subsequent chapters, including the use of the Beamline Electrostatic Levitation (BESL) [104] technique for liquid structure and

property determination. Studies of Cu-Zr and Cu-Hf binary liquids and glasses are presented in Chapter 3, relating structural and chemical ordering in these systems to possible structural signatures of their liquid kinetic strength. In Chapter 4, the results of novel containerless structural studies of $Pd_{82}Si_{18}$ are discussed and compared to previous results from MD simulations. Further studies of chemical structure, structural ordering, and structural signatures of dynamical behavior are presented from the analysis of structural measurements of Au-Si, Pd-Si, Pd-Cu-Si, and Ni-Si liquids and glasses. Finally, Chapter 6 describes the development of a new ESL optimized for neutron scattering studies at the Spallation Neutron Source (SNS) at Oak Ridge National Laboratory in Oak Ridge, TN.

1.6 References

[1] C. A. Angell, Proceedings of the National Academy of Sciences **92** (15), 6675 (1995).
[2] A. Inoue and N. Nishiyama, MRS Bulletin **32** (08), 651 (2007).
[3] W. H. Wang, Advanced Materials **21** (45), 4524 (2009).
[4] A. L. Greer and E. Ma, MRS Bulletin **32** (08), 611 (2007).
[5] C. A. Angell, MRS Bulletin **33** (05), 544 (2008).
[6] Y. Q. Cheng and E. Ma, Progress in Materials Science **56** (4), 379 (2011).
[7] D. Turnbull, Contemporary Physics **10** (5), 473 (1969).
[8] R. Zallen, in *The Physics of Amorphous Solids* (Wiley-VCH Verlag GmbH, 2007), pp. 1.
[9] P. G. Debenedetti and F. H. Stillinger, Nature **410** (6825), 259 (2001).
[10] S. Sastry, P. G. Debenedetti and F. H. Stillinger, Nature **393** (6685), 554 (1998).
[11] F. H. Stillinger, Science **267** (5206), 1935 (1995).
[12] C. A. Angell, Journal of Physics and Chemistry of Solids **49** (8), 863 (1988).
[13] G. Adam and J. H. Gibbs, Journal of Chemical Physics **43** (1), 139 (1965).
[14] R. Busch, J. Schroers and W. H. Wang, MRS Bulletin **32** (08), 620 (2007).
[15] J. Ding, Y.-Q. Cheng, H. Sheng and E. Ma, Physical Review B **85** (6), 060201 (2012).
[16] N. A. Mauro, M. L. Johnson, J. C. Bendert and K. F. Kelton, Journal of Non-Crystalline Solids **362** (0), 237 (2013).
[17] N. A. Mauro, A. J. Vogt, M. L. Johnson, J. C. Bendert and K. F. Kelton, Applied Physics Letters **103** (2) (2013).
[18] N. A. Mauro, A. J. Vogt, M. L. Johnson, J. C. Bendert, R. Soklaski, L. Yang and K. F. Kelton, Acta Materialia **61** (19), 7411 (2013).
[19] N. A. Mauro, M. Blodgett, M. L. Johnson, A. J. Vogt and K. F. Kelton, Nature Materials, (In Review) (2014).
[20] W. Klement, R. H. Willens and P. O. L. Duwez, Nature **187** (4740), 869 (1960).

[21] Y. Li, S. J. Poon, G. J. Shiflet, J. Xu, D. H. Kim and J. F. Löffler, MRS Bulletin **32** (08), 624 (2007).
[22] H. S. Chen, Acta Metallurgica **22** (12), 1505 (1974).
[23] A. J. Drehman, A. L. Greer and D. Turnbull, Applied Physics Letters **41** (8), 716 (1982).
[24] H. W. Kui, A. L. Greer and D. Turnbull, Applied Physics Letters **45** (6), 615 (1984).
[25] A. Peker and W. L. Johnson, Applied Physics Letters **63** (17), 2342 (1993).
[26] M. Volmer and A. Weber, Zeitschrift für Physikalische Chemie **119**, 277 (1926).
[27] A. Inoue, Acta Materialia **48** (1), 279 (2000).
[28] A. Inoue, Materials Transactions **36** (7), 866 (1995).
[29] D. Turnbull, Metallurgical Transactions B **12** (2), 217 (1981).
[30] Y. Li, Q. Guo, J. A. Kalb and C. V. Thompson, Science **322** (5909), 1816 (2008).
[31] J. C. Bendert, A. K. Gangopadhyay, N. A. Mauro and K. F. Kelton, Physical Review Letters **109** (18), 185901 (2012).
[32] E. S. Park, J. H. Na and D. H. Kim, Applied Physics Letters **91** (3) (2007).
[33] H. Tanaka, Journal of Non-Crystalline Solids **351** (8–9), 678 (2005).
[34] A. Meyer, R. Busch and H. Schober, Physical Review Letters **83** (24), 5027 (1999).
[35] J. C. Bendert and K. F. Kelton, Journal of Non-Crystalline Solids **376** (0), 205 (2013).
[36] L. Shadowspeaker and R. Busch, Applied Physics Letters **85** (13), 2508 (2004).
[37] R. Busch, JOM **52** (7), 39 (2000).
[38] D. Wang, Y. Li, B. B. Sun, M. L. Sui, K. Lu and E. Ma, Applied Physics Letters **84** (20), 4029 (2004).
[39] D. Xu, G. Duan and W. L. Johnson, Physical Review Letters **92** (24), 245504 (2004).
[40] A. Inoue and W. Zhang, Materials Transactions **45** (2), 584 (2004).
[41] G. Duan, D. Xu, Q. Zhang, G. Zhang, T. Cagin, W. L. Johnson and W. A. Goddard, Physical Review B **71** (22), 224208 (2005).
[42] G. Duan, D. Xu and W. L. Johnson, Metallurgical and Materials Transactions A **36 A** (2), 455 (2005).
[43] L. Xia, D. Ding, S. T. Shan and Y. D. Dong, Journal of Physics: Condensed Matter **18** (15), 3543 (2006).
[44] P. Jia and J. Xu, Journal of Materials Research **24** (1), 96 (2009).
[45] L. Xia, W. H. Li, S. S. Fang, B. C. Wei and Y. D. Dong, Journal of Applied Physics **99** (2) (2006).
[46] Y. Wang, Q. Wang, J. Zhao and C. Dong, Scripta Materialia **63** (2), 178 (2010).
[47] Y. Ke-Fu and R. Fang, Chinese Physics Letters **22** (6), 1481 (2005).
[48] K. Yao and N. Chen, Science in China Series G **51** (4), 414 (2008).
[49] D. Turnbull, The Journal of Chemical Physics **20** (3), 411 (1952).
[50] F. C. Frank, Proceedings of the Royal Society of London A **215**, 43 (1952).
[51] H. Reichert, O. Klein, H. Dosch, M. Denk, V. Honkimäki, T. Lippmann and G. Reiter, Nature **408** (6814), 839 (2000).
[52] T. Schenk, D. Holland-Moritz, V. Simonet, R. Bellissent and D. M. Herlach, Physical Review Letters **89** (7), 075507 (2002).
[53] D. Holland-Moritz, T. Schenk, R. Bellissent, V. Simonet, K. Funakoshi, J. M. Merino, T. Buslaps and S. Reutzel, Journal of Non-Crystalline Solids **312-314**, 47 (2002).
[54] G. W. Lee, A. K. Gangopadhyay, K. F. Kelton, R. W. Hyers, T. J. Rathz, J. R. Rogers and D. S. Robinson, Physical Review Letters **93** (3), 037802 (2004).

[55] D. Holland-Moritz, O. Heinen, R. Bellissent and T. Schenk, Materials Science and Engineering A **448-451**, 42 (2007).
[56] T. H. Kim and K. F. Kelton, The Journal of Chemical Physics **126** (5) (2007).
[57] A. Di Cicco, A. Trapananti, S. Faggioni and A. Filipponi, Physical Review Letters **91** (13), 135505 (2003).
[58] K. F. Kelton, G. W. Lee, A. K. Gangopadhyay, R. W. Hyers, T. J. Rathz, J. R. Rogers, M. B. Robinson and D. S. Robinson, Physical Review Letters **90** (19), 195504 (2003).
[59] Y. T. Shen, T. H. Kim, A. K. Gangopadhyay and K. F. Kelton, Physical Review Letters **102** (5), 057801 (2009).
[60] N. Jakse and A. Pasturel, The Journal of Chemical Physics **120** (13), 6124 (2004).
[61] P. Ganesh and M. Widom, Physical Review B **74** (13), 134205 (2006).
[62] P. Ganesh and M. Widom, Physical Review B **77** (1), 014205 (2008).
[63] N. Jakse and A. Pasturel, Physical Review Letters **91** (19), 195501 (2003).
[64] N. Jakse, O. Le Bacq and A. Pasturel, Physical Review B **70** (17), 1 (2004).
[65] B. Lee and G. W. Lee, The Journal of Chemical Physics **129** (2) (2008).
[66] J. D. Bernal, Nature **185** (4706), 68 (1960).
[67] G. D. Scott, Nature **188** (4754), 908 (1960).
[68] J. D. Bernal, Proceedings of the Royal Society of London A **280** (1382), 299 (1964).
[69] J. Finney, Proceedings of the Royal Society of London A **319** (1539), 479 (1970).
[70] J. Finney, Proceedings of the Royal Society of London A **319** (1539), 495 (1970).
[71] P. H. Gaskell, Nature **276** (5687), 484 (1978).
[72] P. H. Gaskell, Journal of Non-Crystalline Solids **32** (1-3), 207 (1979).
[73] D. R. Nelson and F. Spaepen, (1989), Vol. 42, pp. 1.
[74] F. C. Frank and J. S. Kasper, Acta Crystallographica **11** (3), 184 (1958).
[75] F. C. Frank and J. S. Kasper, Acta Crystallographica **12** (7), 483 (1959).
[76] D. B. Miracle, Nature Materials **3** (10), 697 (2004).
[77] D. B. Miracle, Acta Materialia **54** (16), 4317 (2006).
[78] A. Widmer-Cooper, P. Harrowell and H. Fynewever, Physical Review Letters **93** (13), 135701 (2004).
[79] A. Widmer-Cooper and P. Harrowell, Journal of Physics: Condensed Matter **17** (49), S4025 (2005).
[80] G. S. Matharoo, M. S. G. Razul and P. H. Poole, Physical Review E **74** (5), 050502 (2006).
[81] E. La Nave, S. Sastry and F. Sciortino, Physical Review E **74** (5), 050501 (2006).
[82] J. P. K. Doye and D. J. Wales, Science **271** (5248), 484 (1996).
[83] J. P. K. Doye, D. J. Wales, F. H. M. Zetterling and M. Dzugutov, Journal of Chemical Physics **118** (6), 2792 (2003).
[84] F. H. M. Zetterling, M. Dzugutov and S. I. Simdyankin, Journal of Non-Crystalline Solids **293-295** (1), 39 (2001).
[85] M. Dzugutov, Physical Review E **65** (3), 032501 (2002).
[86] M. Dzugutov, S. I. Simdyankin and F. H. M. Zetterling, Physical Review Letters **89** (19), 195701 (2002).
[87] M. Li, C.-Z. Wang, M. I. Mendelev and K.-M. Ho, Physical Review B **77** (18), 184202 (2008).
[88] Y. Q. Cheng, H. W. Sheng and E. Ma, Physical Review B **78** (1), 014207 (2008).
[89] N. Jakse and A. Pasturel, Physical Review B **78** (21), 214204 (2008).

[90] M. I. Mendelev, M. J. Kramer, R. T. Ott and D. J. Sordelet, Philosophical Magazine **89** (2), 109 (2009).
[91] H. L. Peng, M. Z. Li, W. H. Wang, C.-Z. Wang and K. M. Ho, Applied Physics Letters **96** (2) (2010).
[92] S. G. Hao, C. Z. Wang, M. J. Kramer and K. M. Ho, Journal of Applied Physics **107** (5) (2010).
[93] Y. Q. Cheng, E. Ma and H. W. Sheng, Applied Physics Letters **93** (11) (2008).
[94] G. W. Lee, A. K. Gangopadhyay, T. K. Croat, T. J. Rathz, R. W. Hyers, J. R. Rogers and K. F. Kelton, Physical Review B **72** (17), 174107 (2005).
[95] V. Wessels, A. K. Gangopadhyay, K. K. Sahu, R. W. Hyers, S. M. Canepari, J. R. Rogers, M. J. Kramer, A. I. Goldman, D. Robinson, J. W. Lee, J. R. Morris and K. F. Kelton, Physical Review B **83** (9), 094116 (2011).
[96] D. G. Fahrenheit, Philosophical Transactions **33** (381-391), 78 (1724).
[97] K. Kelton and A. L. Greer, *Nucleation in condensed matter: applications in materials and biology*. (Access Online via Elsevier, 2010).
[98] L. Hennet, S. Krishnan, I. Pozdnyakova, V. Cristiglio, G. J. Cuello, H. E. Fischer, A. Bytchkov, F. Albergamo, D. Zanghi and J.-F. Brun, Pure and Applied Chemistry **79** (10), 1643 (2007).
[99] J. K. R. Weber, D. S. Hampton, D. R. Merkley, C. A. Rey, M. M. Zatarski and P. C. Nordine, Review of Scientific Instruments **65** (2), 456 (1994).
[100] D. Holland-Moritz, T. Schenk, P. Convert, T. Hansen and D. M. Herlach, Measurement Science and Technology **16** (2), 372 (2005).
[101] W. K. Rhim, M. Collender, M. T. Hyson, W. T. Simms and D. D. Elleman, Review of Scientific Instruments **56** (2), 307 (1985).
[102] R. W. Hyers, Measurement Science and Technology **16** (2), 394 (2005).
[103] A. K. Gangopadhyay, G. W. Lee, K. F. Kelton, J. R. Rogers, A. I. Goldman, D. S. Robinson, T. J. Rathz and R. W. Hyers, Review of Scientific Instruments **76** (7) (2005).
[104] N. A. Mauro and K. F. Kelton, Review of Scientific Instruments **82** (3) (2011).
[105] P.-F. Paradis, T. Ishikawa and S. Yoda, Journal of Non-Crystalline Solids **312–314** (0), 309 (2002).
[106] H. Aoki, P.-F. Paradis, T. Ishikawa, T. Aoyama, T. Masaki, S. Yoda, Y. Ishii and T. Itami, Review of Scientific Instruments **74** (2), 1147 (2003).
[107] T. Kordel, D. Holland-Moritz, F. Yang, J. Peters, T. Unruh, T. Hansen and A. Meyer, Physical Review B **83** (10), 104205 (2011).

Chapter 2

Experimental Methods and Analysis

2.1 Overview

In this chapter, sample preparation details (Sect. 2.2) and characterization techniques, as well as experimental measurement methods, will be discussed. Most samples, particularly those for major experimental runs, were prepared by the majority of members in Kelton's research group [including A. K. Gangopadhyay, V. Wessels, N. A. Mauro, J. C. Bendert, M. E. Blodgett, J. M. Gewin (J. McKnight), M. L. Johnson, C. Pueblo, Mike Nadeau, Austin Hope, Corie Miller, and Sirish Veligati]. Characterization of those samples, including thermal analysis, low-energy X-ray diffraction (XRD) measurements, and thermophysical property measurements (Sect. 2.3 and 2.4), were performed by a majority of the members of the group before, during, and after the experimental runs. While the responsibilities of data collection, both during high-energy XRD experiments (Sect. 2.5) and otherwise, were typically divided among Kelton's research group, data analysis (Sect. 2.6 and 2.7) was accomplished through individual effort, often in collaboration for larger bodies of work. The development of experimental procedures and techniques are credited throughout the chapter, and collaboration on data analysis is credited with the presentation of experimental results in subsequent chapters.

2.2 Sample Preparation

All samples for diffraction and electrostatic levitation (ESL) studies reported in this thesis were prepared in Compton Labs Room 50/52. Before alloying, the source material was chosen carefully for its purity, particularly in reference to its O_2 content. Because many of the alloy elements in this study are highly reactive in normal atmosphere, due to their large oxygen affinity, purity and reduction of O_2 was a major concern. Purity of the sample influences melting and undercooling, particularly since some of the oxides present in our alloys require high temperatures for dissolution and they, therefore, can act as heterogeneous nucleation sites in the undercooled liquid sample. Other elemental impurities may also produce similar effects, but to a smaller extent than oxygen. Table 2.1 lists the information for the source materials used to prepare the samples studied in this thesis.

Table 2.1: Elemental materials used for sample preparation (from Alfa Aesar)

Element	Form	Purity (%)	Lot	Stock
Au	Wire	99.9	10197	H08940
Cu	Slug	99.995+	44258	J19R029
Cu	Slug	99.9999	42958	K02W004
Hf	Slug	99.97	39711	A19K06
Ni	Slug	99.995	42333	L02X015
Pd	Wire	99.99+	10961	H18X018
Si	Lump	99.9999	43006	61001037
Si	Lump	99.9999	43006	I17N40
Zr	Slug	99.95	42556	D21K11
Zr	Slug	99.9+	42559	B11X056

2.2.1 Master Ingot Preparation

Approximately 1 g of the source material for a master ingot was first cut from the source material and the mass measured using a Mettler Toledo AB54-S/FACT analytical balance with a precision of ±0.05 mg. To be used, the maximum error in mass that was allowed was such as to

produce less than one half of an atomic percent in the final sample composition. An in-house-built arc-melting facility, using a Miller Synchrowave 250 DX arc welding power source connected to a tungsten tip, was used to resistively heat and alloy the source material. Both the tungsten tip and the water-cooled copper hearth, on which the source material was placed, are housed inside a vacuum chamber. The chamber was evacuated to a pressure of ~5 mTorr (~10^{-4} to 10^{-5} Torr using a new setup as of November 2011) and backfilled to nearly one atmosphere of pressure using high purity (99.999%) Ar gas. Pumping and backfilling of the chamber was repeated 3-4 times to reduce to the amount of remaining atmosphere. To ensure well mixed alloys and to limit evaporation, elemental materials were carefully arranged in the hemispherical bowl on the copper hearth by the value of their melting temperatures. High melting temperature materials were placed toward the center of the arc-melter (closer to the tungsten tip) with lower melting temperature materials surrounding.

Before melting the sample material, a $Ti_{50}Zr_{50}$ getter was first melted with the arc for ~30 s. Because of the getter's large oxygen solubility, this allowed the O_2 content from the atmosphere in the chamber to be further reduced before alloying the sample material. Master ingots were then subsequently melted for ~30-45 s. The ingot was subsequently flipped and the process was repeated 2-3 more times to ensure mixing of the sample. After melting, the mass of the ingot was again determined in order to measure any mass loss due to evaporation. Mass loss was typically less than 1%, and ingots were rejected based on high mass loss from an assumed alloy compositional shift. If the copper hearth showed signs of "blackening" due to high O_2 content during melting, the ingot was also rejected, due to assumed contamination. Further details on arc-melting and master ingot preparation can be found elsewhere [1, 2].

2.2.2. Melt-spun Ribbon Preparation

Because many of the alloys studied have marginal bulk-glass formability at best, they require high cooling rates in order to bypass crystallization. To achieve this, samples were melted and the liquid ejected on to a large, rotating copper wheel. The result of this process is thin, continuous ribbons of amorphous material. A rapidly spinning copper wheel with a large thermal mass provides a continuously cool surface on to which the liquid can be quenched in to a glass. A faster wheel speed results in higher cooling rates, allowing the quench rates to be controlled for glass preparation. The production of a thin material is also useful for studying the glass via transmission techniques, such as transmission electron microscopy (TEM) and transmission geometry X-ray and neutron diffraction.

Glass ribbons produced for studies in this thesis were made in the quench box located in room 50/52 of the Compton Lab. The quench box is a vacuum chamber housing an 8" copper wheel that is connected to a motor to provide a maximum tangential speed of 100 m/s. A quartz tube containing the sample is inserted through a vacuum sealed port in the top of the box, and a solenoid valve is connected to the top of the quartz tube. Inside of the quartz tube, the master ingot is placed in a graphite crucible with a ~1 mm diameter hole in the bottom. A Lepel T-10-3-KC-HW radio frequency (RF) generator is connected to a water-cooled copper coil surrounding the end of the quartz tube just above the copper wheel. The RF field couples to the graphite crucible, resistively heating it and melting the ingot. Once the ingot is melted, the solenoid switch is thrown, allowing pressurized Ar gas to force the liquid out of the crucible, through the bottom hole, and onto the copper wheel. Ribbons are spun off and collected inside the box and the connected collection tube. Further details of the quench box design and operation can be found elsewhere [2].

For the X-ray diffraction studies in this thesis, glassy ribbons were prepared by melting samples to 100-150 K above their liquidus temperature, T_L, in a high purity (99.998%) Ar atmosphere. Before melting, the quench box was evacuated and back filled with Ar 3-4 times. Copper wheel speeds ranged from ~60-70 m/s, producing continuous 3-10 cm ribbons with an average cross-section of 1-2 mm x 20-30 μm. More specific quench details can be found in Table 2.2.

Table 2.2: Quench speed and density measurements for glass ribbon samples studied in this thesis. Room temperature density measurements were made in-house using the procedure outlined in Sect. 2.3.3.

Sample	ID	Quench Speed (RPM)	Density (gcm^{-3})
$Cu_{46}Zr_{54}$	02_run2	6000	7.3
$Cu_{54}Zr_{46}$	03	6000	7.43
$Cu_{55}Hf_{45}$	02_run2	6000	11.54
$Cu_{60.8}Hf_{39.2}$	01	5800	10.86

2.2.3 ESL Sample Preparation

Spherical samples for experiments utilizing both the Beamline Electrostatic Levitation (BESL) and the Neutron Electrostatic Levitation (NESL) techniques were prepared by arc-melting the elemental source material in the hemispherical bowls of the copper hearth, allowing the surface tension of the liquid to form the sample into a sphere. BESL samples specifically were made by first crushing master ingots into fine pieces and weighing the necessary material to create a 2-3 mm diameter sample. Sample masses for this size range were initially calculated assuming ideal mixing among constituent elements. The masses were chosen for this size range for optimization of both measurement (diffraction and thermophysical property) and levitation. Arc-melting of the samples followed the procedure mentioned above, with the exception of just a single, quick melt at a lower current for the BESL samples. This was sufficient to make the

samples spherical while minimizing evaporation, especially since the sample material should already have been well mixed during ingot preparation. Samples were weighed again in order to calculate mass loss, and rejected if mass loss is sufficiently high. Specific sample details can be found in Table 2.3.

Table 2.3: Sample ID and thermophysical property data measured for BESL samples in this thesis. Measurements were made in-house unless otherwise specified.

Sample	Sample ID	Mass (mg)	X-ray ID	T_L (°C)	Density ρ at T_L (gcm^{-3})	$d\rho/dT$ ($gcm^{-3}K^{-1}$)
$Cu_{60.8}Hf_{39.2}$	-	72.32	STL11030	985 [3]	10.77	-8.72E-04
$Cu_{54}Zr_{46}$	132B-02	60.51	STL11049	930	7.14	-4.83E-04
$Cu_{46}Zr_{54}$	131B-05	58.97	STL11057	927	6.99	-4.48E-04
$Cu_{55}Hf_{45}$	95A-03	58.97	STL11071	1030	11.18	-8.38E-04
$Au_{81}Si_{19}$	AG21-02	83.39	STL11099	359 [4]	15.58	-1.17E-03
$Pd_{77}Cu_6Si_{17}$	03	80.06	STL13037	855 [5]	10.004	-7.24E-04
$Ni_{75}Si_{25}$	09	77.89	STL13066	1200	7.002	-7.15E-04
$Pd_{82}Si_{18}$	02	83.97	STL13104	808	10.14	-7.52E-04

Typical samples that were studied in NESL ranged from 5 to 6 mm in diameter and from 200 to 450 mg in mass. While some samples were prepared from master ingots, similar to the procedure for the the BESL samples, others were prepared by measuring out amounts of elemental source material for just a single sample. In the latter case, samples were prepared following a similar procedure to that used to prepare the master ingots, with 2-3 melts in order to ensure alloy mixing. A lower current was used to limit evaporation and mass loss of the sample.

2.3 Sample Characterization

Before the acquistion of high-energy X-ray or neutron scattering data, the basic structural and thermophysical properties of the samples must first be determined. Both metastable and equilibrium thermodynamic properties of the alloy material must be measured in order to

calibrate temperature measurements during diffraction experiments. Proper sample preparation, particularly ensuring that the quenched samples were amorphous, must also first be verified by lower-energy X-ray diffraction (XRD) experiments. In-house differential scanning calorimetry (DSC), low-energy XRD, and density measurements were performed, before and after the high-energy X-ray and neutron scattering experiments, for these purposes, particularly when lacking published data on the measurements of interest. Further details on these techniques can be found elsewhere [2, 6].

2.3.1 Differential Scanning Calorimetry (DSC)

The DSC technique measures the difference in power, as function of temperature, required to maintain a sample and reference at the same temperature while heating at a set rate. The direct measure of power during heating can be used to determine transition temperatures as well as the specific heat and enthalpies of transition of the sample. For measurements of the solidus and liquidus temperatures, T_S, and T_L, a SETARAM Labsys DTA/DSC was used. (For DTA, or differential thermal analysis, the difference in temperature between the sample and a reference is measured as a common furnace heats and cools the two). Samples of 30-50 mg were measured with a heating rate of ~5 K/min under an Ar gas atmosphere (99.999% purity). For both the sample and the reference, good thermal contact with the Al_2O_3 crucible in the DTA was obtained by filling the crucibles with Al_2O_3 powder. Typical standards, including Au, Ag, and Cu, were used to calibrate the DTA. The measured T_S was used to calibrate the pyrometer measurements made during ESL experiments.

A Perkin Elmer DSC 7 was used to measure the glass transition temperature, T_g, and the crystallization (devitrification) temperature, T_X, for amorphous samples. Samples were placed in

Al pans (Cu pans for scans above 600 °C) and a reference of pure Ni was typically used to calibrate instrumental shifts during scanning. The values obtained for T_g and T_X were used to calibrate the temperature during X-ray diffraction studies of amorphous ribbons. Because of the limited maximum temperature range of the experimental apparatus (~ 700 °C), most measurements of T_S and T_L were made using the SETARAM Labsys DTA/DSC.

2.3.2 Low-energy X-ray Diffraction (XRD)

Initial structural characterization of samples was accomplished by performing low-energy XRD measurements using a Rigaku Geigerflex diffractometer with a stationary Cu K_α source (λ = 1.54 Å). Ribbon samples were cut in to 1 mm strips and attached to a glass or open aluminum slide, and XRD studies were made in a reflection geometry. Quenched ribbons were examined for the absence of sharp diffraction peaks, ensuring that the samples were amorphous, before they were studied further with high-energy XRD.

2.3.3 Density Measurements of Glass Ribbons

Density measurements of glass ribbons were made using the Archimedean technique. A Cahn C-29 precision electrobalance, with precision ± 5 μg, was used to weigh small sections of the ribbon at room temperature (20 °C) both in air, which has a density of 0.0012 gcm^{-3} [7], and in toluene, which has a density of 0.8674 gcm^{-3} [8]. The density of the ribbon samples was then calculated by $\rho = (\rho_{\text{Air}} m_{\text{Toluene}} - \rho_{\text{Toluene}} m_{\text{Air}})/(m_{\text{Air}} - m_{\text{Toluene}})$, where ρ and m represent the densities and the weighed masses respectively.

2.4 Beamline Electrostatic Levitation (BESL)

Most liquid studies for this thesis were made using the BESL technique [9]. This containerless processing technique allows for *in situ* X-ray diffraction measurements of bulk liquids in a high-vacuum environment, alongside simultaneous temperature and thermophysical property measurements. Liquid diffraction data presented in this thesis were collected at Station 6-ID-D of the Advanced Photon Source (APS) using the Washington University BESL (WU-BESL) [2, 10] sample environment (discussed in Sect. 2.5). Thermophysical property measurements (transition temperature, density and viscosity) were made from May 2010 to the time of writing this thesis, noting that some modifications to the WU-BESL facility [6] were made in the intervening years.

2.4.1 WU-BESL Description

WU-BESL features a high-vacuum chamber that is capable of reaching pressures of 10^{-7} Torr, with several ports designated for optical control and measurement of the samples (Fig. 2.1). Charged samples with masses ranging from 10-150 mg (2-4 mm diameter) are levitated in an electric field of 0 to 2.5 MV/m. Sample position is maintained by the electrostatic forces resulting from three sets of orthogonal electrodes (see Fig. 2.1). A 0 to -20 kV high-voltage amplifier, connected via a high-voltage vacuum feedthrough to the top electrode, maintains a negative potential across the vertical electrodes, counteracting the force of gravity with an electrostatic force applied to a positively charged sample. Similarly, ±3 kV high-voltage amplifiers produce electrostatic potentials between lateral electrodes in the horizontal x-y directions for additional positioning. Two ultraviolet sources maintain the charge on the sample via the photoelectric effect.

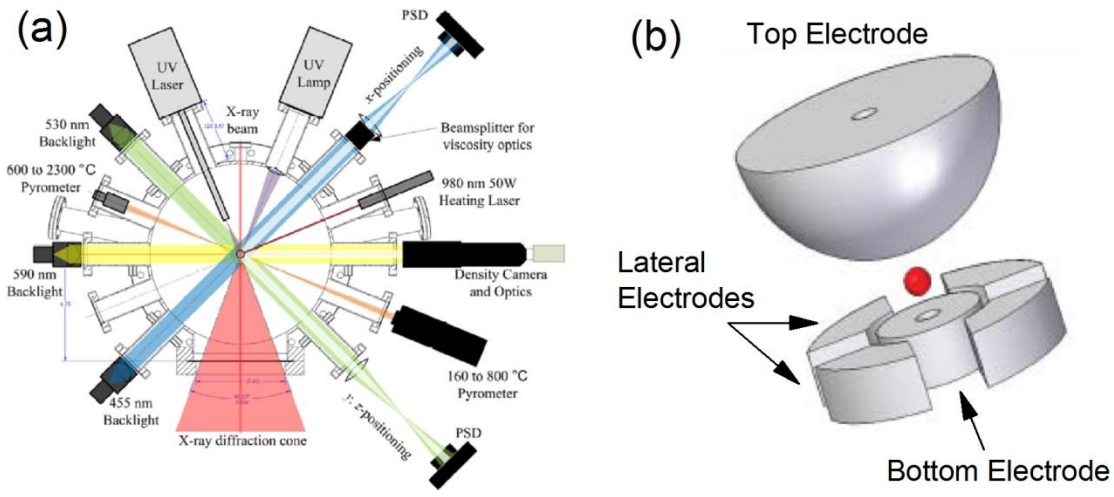

Figure 2.1: (a) Diagram of optical sources and detectors for the WU-BESL (reprinted from [6] with permission). (b) Electrode configuration used in WU-BESL. The curved upper electrode (radius of curvature, *r*, is 15 mm) creates an additional lateral potential barrier, improving sample stability. A hole is bored axially through the center to allow sample changing, preprocessing on a raised post, or additional sample line-of sight [Reprinted with permission from [10]. Copyright (2011), AIP Publishing LLC.].

The position of the sample is measured by shadows cast onto orthogonal position sensitive detectors (PSDs). The PSDs send positional information to a computer, which adjusts the voltages on the electrodes via the amplifiers based on a feedback algorithm [11]. The shadow of the sample that is cast on the PSDs was originally produced by light from two orthogonal red laser diodes. In 2010, the diodes were replaced by Helium-Neon lasers, with the light passing through optical beam expanders that were coupled to fiber optic cables. In June of 2012, the lasers were replaced by high-intensity color LEDs combined with focusing optics. The new configuration improved detector sensitivity and ultimately sample positioning [6].

Samples are heated and melted using a fiber-coupled diode laser (980 nm, 50 W continuous maximum power) and allowed to radiatively free cool. A steady-state sample temperature can be maintained by using a constant laser power, while cooling can be controlled by the rate of reduction in laser power. During heating and processing, the charge on the surface

of the sample can be lost, requiring regeneration with the UV source(s). At sufficiently high temperatures, thermionic emission recharges the samples, allowing the UV sources to be shuttered off.

2.4.2 Thermophysical Property Measurement

Sample temperature is measured from 160 °C to 2300 °C using two infrared pyrometers with overlapping temperature ranges. Lower temperatures (160-800 °C) are measured using a single color Process Sensors Metis MI18 MB8, operating at a wavelength of 1.89 μm, while a Process Sensors Metis MQ22 two color ratio pyrometer, operating at wavelengths of 1.40 and 1.64 μm, is used at high temperatures (600-2300 °C). Emissivity changes with temperature are accounted for by using ratio pyrometers, producing more accurate measurements [12]. The emissivity ratios are calibrated by matching the observed melt plateau of the sample in the ESL with the measured T_S obtained from DSC (Sect. 2.3.1). Further details of optical pyrometry can be found elsewhere [6].

Temperature measurements are correlated with non-contact volume measurements made using the shadow method [13, 14]. A Pixelink PL-B741G CMOS camera is used to measure the shadow of the sample that is backlit with a third high-intensity LED. The pixel dimensions are calibrated using levitated brass (radius r = 0.046875 ± 0.0005 in.) and tungsten carbide (r = 0.046875 ± 0.00015 in.) standards. By integrating the area of the measured shadow around the vertical axis, the volume of the sample is determined. Details for the machine vision volume measurement algorithm are provided elsewhere [6, 14]. By dividing the measured volume by the mass (described in Sect. 2.2.1 and 2.3.3), which is measured both before and after the experiment to account for any loss, the density of the sample is obtained. Viscosity and surface tension

measurements are made by modulating the levitation field near the resonance mode of the spherical liquid sample and measuring the decay of the volume oscillation amplitude when the driving force is removed. Further details of the viscosity and surface tension measurements can be found elsewhere [6].

2.4.3 Beamline Integration

The compact design of the WU-BESL facility allows it to be transported and integrated into the beamline at the APS for X-ray diffraction studies. The WU-BESL also features two designated ports for X-ray diffraction measurements (Fig. 2.1). Both entrance and exit ports contain 0.015" thick Beryllium windows for X-ray transparency. The exit port allows for a wide scattering angle, 2θ, of ~20° allowing high momentum transfer measurements (of high-energy X-ray scattering) for PDF determination. All of the optical equipment is mounted to a 30" x 30" table, while ancillary pieces of equipment (amplifiers, control boxes, etc.) are modular and connected separately. While the sample position can be measured and adjusted to within a limited range between the electrodes by manipulating parameters of the feedback algorithm, sample alignment with the beam is initially performed by adjusting a custom alignment stage [2, 10] on which the optical table sits. All control and measurement equipment is remotely controlled from outside of the beamline hutch, with several components (alignment stage motors, etc.) integrated in to the beamline system. Though currently optimized for use at Sector 6, Station 6-ID-D of the APS, WU-BESL can be easily modified for integration in to other high-energy beamlines. Further details about the beamline integration of the WU-BESL can be found elsewhere [2, 10].

2.5 High-energy X-ray Diffraction measurements

The results of high-energy synchrotron X-ray diffraction studies were obtained over the course of four experimental runs at the Advanced Photon Source (APS), located at Argonne National Laboratory. All experimental runs were performed at Sector 6 (formerly the MUCAT Sector) in station 6-ID-D. Section 2.4.1 describes the first experimental run, hereafter referred to as "BESL 2010", which took place over 23 days in August of 2010 using the WU-BESL (Sect. 2.3) to study a wide range of liquid metallic alloys. Section 2.5.2 describes the second run, "APS 2011", which took place over 4 days in October of 2011, during which high-energy XRD measurements of as-quenched amorphous ribbon samples were made at room temperature. Section 2.5.3 describes the third run, "APS 2012", which took place over 4 days in August of 2012 and during which a wide range of glass ribbon samples were studied, including some of those from APS 2011, at room temperature as well as at elevated temperatures using a custom furnace (described in Sect. 2.5.3). Finally, Section 2.5.4 refers to "BESL 2013", the most recent experimental run, which took place over 22 days in June of 2013 and again utilized the WU-BESL to study a wide variety of metallic liquids and glasses.

2.5.1 BESL 2010

In August of 2010, the WU-BESL was installed at Station 6-ID-D for metallic liquid studies. Diffraction studies were made in a transmission geometry using high-energy X-rays (E = 129 keV, λ = 0.0961 Å, beam profile = 0.7 x 0.7 mm^2), and data were obtained over a scattering range of 1 to 14 $Å^{-1}$. Scattering data were measured at sampling rates of 1-2 Hz using a GE Revolution 41-RT amorphous Si flat panel X-ray detector [15], located approximately 910 mm beyond the sample and operating in Angio mode (400 μm by 400 μm pixel size, 1k x 1k

total pixels). Data were collected continuously during radiative free cooling cycles as well as during long exposures (~10s), while holding the sample at a single temperature. "Dark frames" were obtained while the X-ray shutter was closed before and after exposures, and "empty chamber frames" were collected between sample runs either without a sample between the electrodes or with a sample sitting on the bottom electrode and outside of the X-ray beam. Detector distance calibration data were collected periodically for levitated polycrystalline Si samples. NIST SRM 640c Si standard powder in a capillary was placed in the position of a levitated sample to confirm the detector calibration values obtained from the levitated polycrystalline Si.

2.5.2 APS 2011

Diffraction data for glass ribbons were collected in October of 2011 at the same station (6-ID-D) used during BESL 2010. Samples, consisting of 10 – 20 mm long ribbon segments stacked 10 – 15 ribbons thick, were attached to plastic holders (Fig. 2.2) and inserted in to a mount on the station's goniometer. All high-energy X-ray (E = 100 keV, λ = 0.124 Å) measurements were taken in a transmission geometry in atmosphere at room temperature; 1 Hz data were collected over a scattering range of 1 $Å^{-1}$ to 20 $Å^{-1}$. A beam size of 0.7 x 0.7 mm^2 was used in combination with the same GE Revolution 41-RT detector; this time located approximately 200 mm beyond the sample and operating in RAD mode (200 μm by 200 μm pixel size, 2 k x 2 k total pixels). Typical exposures were of duration 20 - 60 s, with 5 s dark exposures taken before and after. Empty chamber exposures of 20 s were acquired between samples. Periodic diffraction data for detector calibration were taken using NIST SRM 640c Si standard powder layered on Kapton tape that was attached to a metal holder (see Fig. 2.2) and

placed in the same geometry as the samples. Measurements of the X-ray absorption by the samples were made by measuring photocurrents in a biased photodiode located on the X-ray incident and exit sides of the sample (details can be found elsewhere [16]).

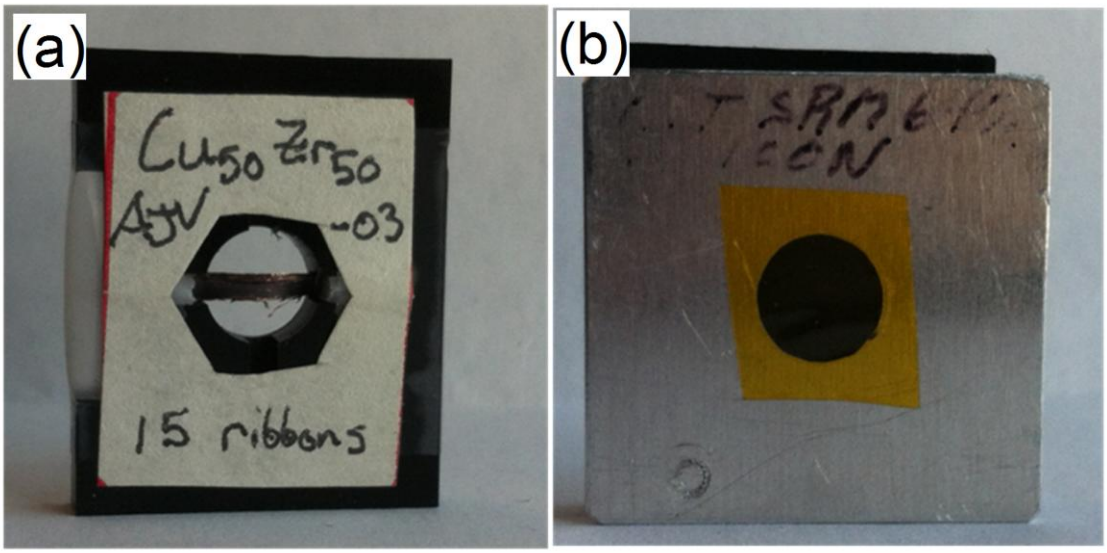

Figure 2.2: (a) Stacked ribbon samples secured to a plastic holder for transmission geometry diffraction measurements, and (b) Si standard powder secured to metal holder between sheets of Kapton tape.

2.5.3 APS 2012

Glass ribbon data were collected again in August, 2012 at the same beamline station (6-ID-D) using a new sample environment. Glass ribbons were cut and 10-20 centimeter-long strands placed in 2.0 mm diameter quartz capillaries with 0.01 mm thick walls. The capillaries were then inserted into a 2" diameter, copper coil furnace (Fig. 2.3) mounted to the station's goniometer. The capillaries were evacuated, reaching pressures on the order of 10^{-3} Torr. A thermocouple located inside the furnace measured the air and capillary surface temperature. Diffraction patterns were obtained for a series of isothermal holds by setting the furnace temperature, waiting approximately 30 - 60 s for thermal stabilization of the ribbons, and then

acquiring scattering data for 10 s. The same GE Revolution 41-RT detector was again used, located approximately 210 mm from the sample and operated in RAD mode. High-energy X-ray (E = 100 keV, λ = 0.124 Å) data were collected at a frequency of 1 Hz in transmission geometry over a q-range of 1 to 14 $Å^{-1}$. Capillaries containing NIST SRM 640c Si standard powder were used for detector calibration, and both 5 s dark (taken before and after data acquisition) and 60 s empty chamber exposures (taken between samples) were acquired for background correction.

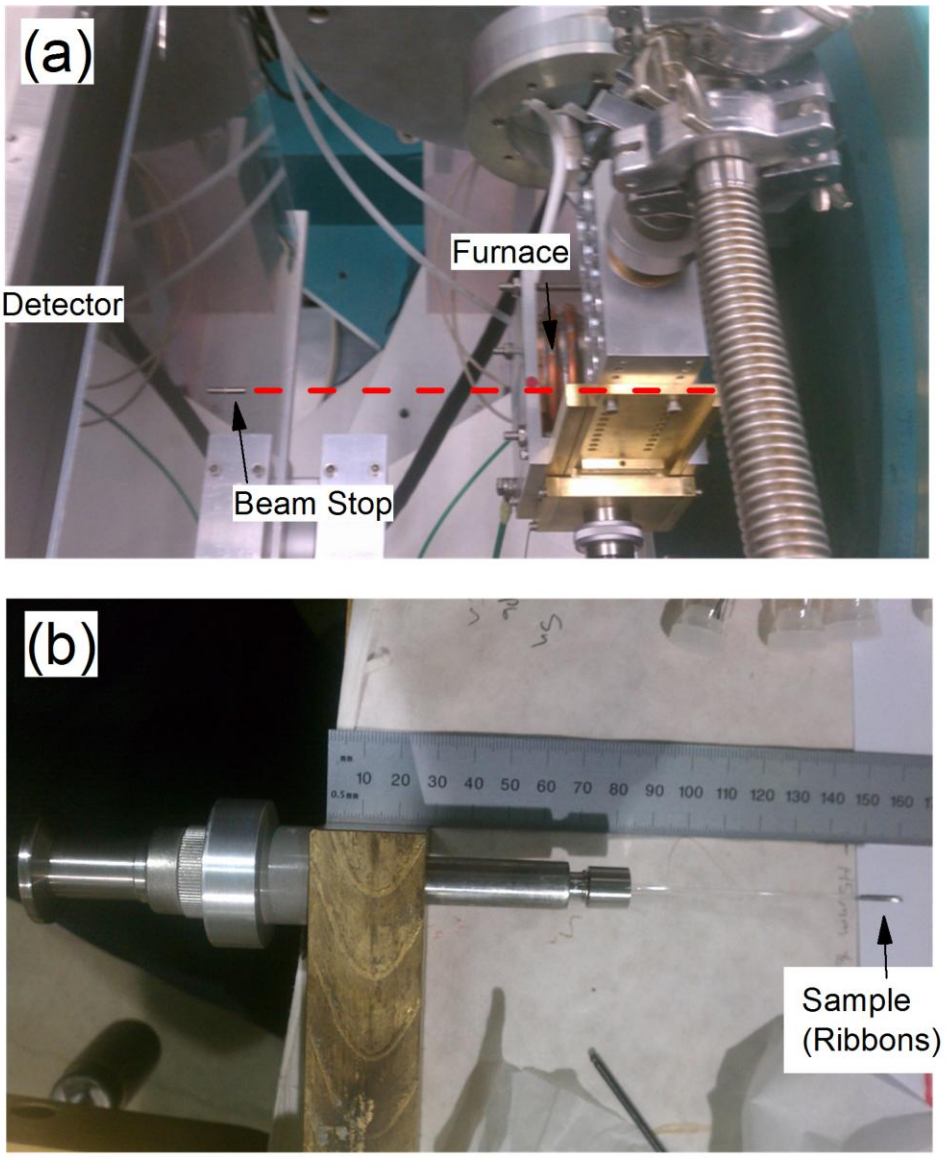

Figure 2.3: (a) Top-down view of the furnace, detector, and beam stop in relation to the incident beam path (red dotted line), and (b) sample in the glass capillary held by the furnace insert with KF flange (left).

2.5.4 BESL 2013

In June of 2013 the WU-BESL was again installed in Station 6-ID-D at the APS, and liquid data were collected in a similar mode as that followed for BESL 2010. High-energy X-ray data (E = 132 keV, λ = 0.094 Å, beam profile = 0.7 x 0.7 mm^2) were collected continuously at varying rates (1, 2, 3, 4, 5, and 8 Hz) in a transmission geometry during radiative free cools and

for 10-20 s isothermal holds. The same GE Revolution 41-RT detector, operated in RAD mode, was located approximately 560 mm from the sample, and data were obtained over a q-range of 1 to 15 $Å^{-1}$. For background correction, dark frames were collected ~5 s immediately before and after exposures, while 20 s empty chamber frames were obtained between samples. Periodically diffraction data were obtained from levitated polycrystalline Si samples again used for detector calibration, while levitated spheres of NIST SRM 640d Si standard powder suspended in high-vacuum epoxy were used to confirm the detector calibration from the polycrystalline Si samples.

Scattering data from glass ribbons were also obtained using a new experimental setup (designed by N. Mauro) that was integrated in to the WU-BESL sample environment. In this setup, the ribbon sample holder (Fig. 2.4) was attached to the electrode assembly, allowing a single ribbon sample to be placed in a position similar to that of the levitated sample. After the chamber was evacuated the ribbon was resistively heated using a Matsusada RK45-9 regulated DC power supply that was connected to the leads of the sample holder via high-vacuum electrical feed-through connections that were previously used for the grounded lateral electrodes. The temperature of the sample was measured using the single color Process Sensors Metis MI18 MB8 pyrometer mentioned in Section 2.4.2, and the emissivity was corrected by matching the crystallization temperature in the X-ray diffraction pattern to T_X as measured in the DSC (see Sect. 2.3.1).

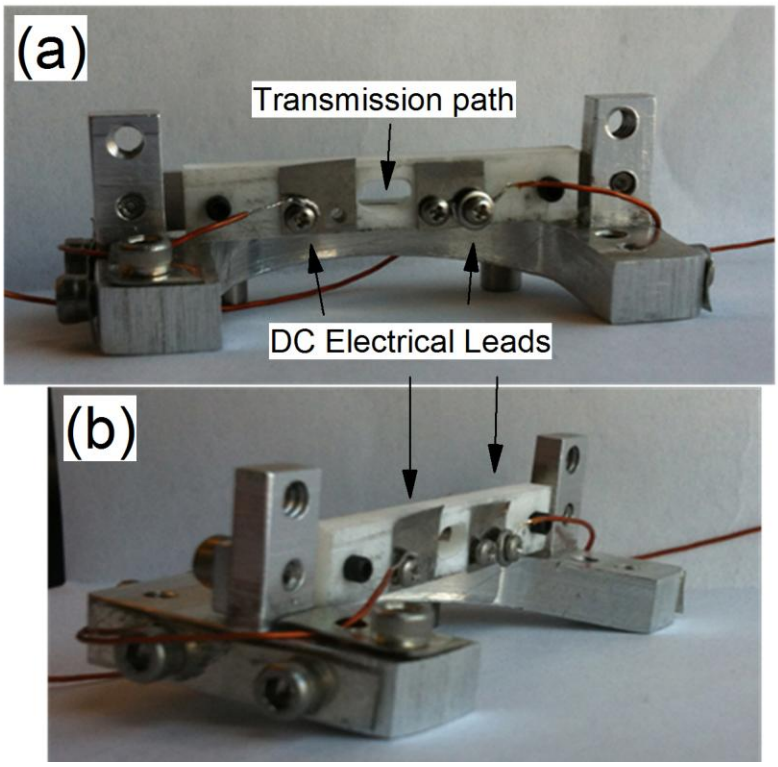

Figure 2.4: Ribbon sample holder, viewed from (a) the front and (b) at an angle, featuring DC electrical leads connected to the ribbon pins with a Macor (white) base for thermal and electrical isolation.

Using a beam size of 1.0 x 1.0 mm^2, 1 Hz diffraction data were obtained during 20 – 60 s exposures for isothermal holds and continuously during non-isothermal heating cycles over a scattering range similar to that for the liquid diffraction data. For initial room temperature exposures, beam profiles were adjusted between 0.7 x 0.7 and 1.0 x 1.0 mm^2 to account for possible beam size differences between the liquid and glass scattering data. Background corrections were made using 5 s dark frames, taken before and after sample exposures, and 120 s empty chamber exposures were taken between glass acquisition runs with the empty ribbon holder in place inside the chamber. NIST SRM 640c Si standard powder held in Kapton tape was periodically placed in the ribbon holder and used for detector calibration.

2.6 X-ray Diffraction Analysis

In order to generate the static structure factor, $S(q)$, from the measured intensity in the detector images, a series of corrections are required. The data were analyzed using an in-house LabVIEW^{TM}-based software package developed by J. C. Bendert [16]. The same package was used to obtain the pair-distribution function, PDF or $g(r)$, from $S(q)$, with estimates of uncertainty in both measures included. A TTL signal, generated by the detector when it was acquiring frames, was used for temporal synchronization between the image acquisition and the temperature data, using in-house data acquisition programs written in LabVIEW^{TM} [10]. Finally, a peak analysis of $S(q)$ and $g(r)$ data was made using in-house LabVIEW^{TM} packages developed by J. C. Bendert and M. L. Johnson [17]. A complete description of the in-house X-ray analysis software can be found elsewhere [6].

2.6.1 X-ray Corrections

In this section, a brief overview of the standard corrections applied to X-ray data will be discussed. Scattering data for this thesis were collected in a transmission geometry with a flat plate detector (GE Revolution 41-RT amorphous Si flat panel X-ray detector, see Sect. 2.5) (Fig 2.5). More comprehensive reviews of the specific corrections made can be found elsewhere [6, 16, 18].

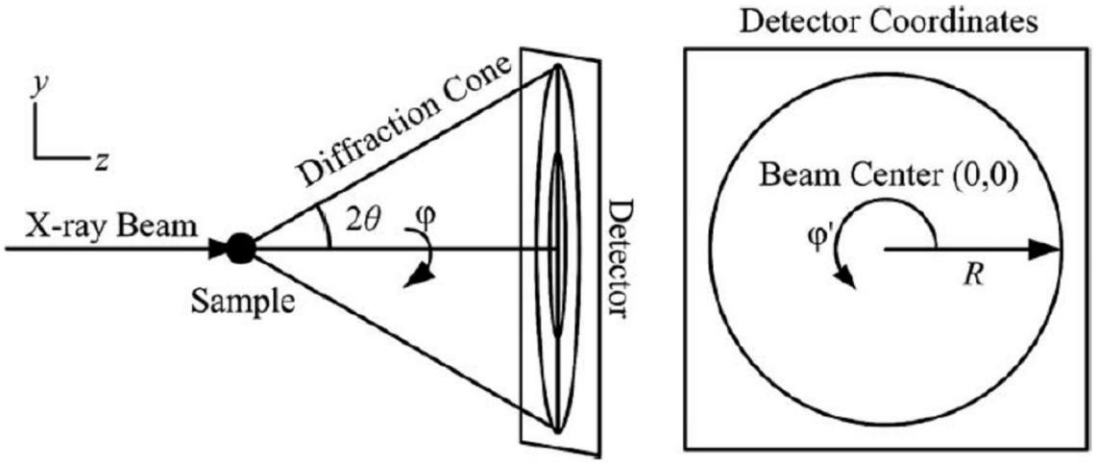

Figure 2.5: Schematic diagram of diffraction in a transmission geometry on to a flat plate detector [reprinted from [16] (http://dx.doi.org/10.1107/S0021889813013162) with permission from IUCr].

As mentioned in Section 2.5, dark and empty chamber frames were acquired alongside scattering data in order to account for signal contributions other than those from sample scattering. Empty chamber frames, or X-ray exposures without a sample, were taken to account for scatter from other sources, such as air, the Be entrance and exit windows, and other potential scattering sources from the experimental setup. Dark frames, taken without X-ray exposure to the detector, account for the dark current in the detector. Together, these frames were used to account for the background intensity, which was subtracted from the scattered intensity of the sample to generate a corrected scattered intensity,

$$I_{Corrected} = \Gamma\left(I_{Sample} - I_{Background}\right), \tag{2.1}$$

where Γ is a scaling factor for each pixel determined from the applied gain map for the specific detector at the specific incident X-ray energy. Gain maps were produced by empirically measuring the detector efficiency at a given incident energy for each detector pixel. For the

analysis in this thesis, background subtraction was performed in a 1:1 ratio after scaling the intensities of background and the raw images to their respective number of frames.

As mentioned in Section 2.5, scattering data from Si standards were collected periodically to account for corrections related to the position and tilt of the flat plate detector relative to the sample, the incident beam, and diffracted beam. Because the diamond structure and lattice constants of Si are well known, the diffraction pattern, particularly the first diffraction ring, can be used for detector calibration. A tilt correction maps the polar detector coordinates, R and φ', to the solid angle coordinates of the diffracted beam, 2θ and φ, by

$$I_{Sample}(R, \varphi') \rightarrow I_{Sample}(2\theta, \varphi) \tag{2.2}$$

Given the calculated tilt of the detector, subsequent geometric, $d\Omega/dA$, and oblique incidence, O, corrections could be made to each pixel of the detector. For the oblique incidence corrections used in this thesis, the transmission of X-rays through the detector (at normal incidence) was set to 0.75 [19].

The background corrected intensity was also scaled by other X-ray and sample-dependent corrections. To account for the polarization of scattered X-rays by the sample, a polarization correction, P, as a function of scattering angle was applied to the measured intensity. The polarization correction contains both an angle of the polarization plane of the incident beam and a fraction of polarization at that angle. The self-absorption correction, or correction due to attenuation by the sample (denoted by V/V'), is a function of the scattering angle. Self-absorption was also related to the radius of the incident beam as well as the sample's attenuation coefficient, size, shape and transmission geometry. Similarly, the self-scattering, or secondary scattering,

correction was calculated from the ratio of the secondary scattering to the primary scattering, I_2/I_1. It is related to the properties of the incident beam and sample parameters as well as the atomic numbers of the individual elements of the composition. The absorption and secondary scattering corrections were recently derived for elastic scattering of spherical samples located at positions offset from the incident beam [20]. For the liquid samples studied in this thesis, sample parameters, such as density and mass, were obtained from the synchronized, emissivity corrected temperature data obtained from WU-BESL pyrometry, while attenuation coefficients were estimated from tabulated data [19]. For glass ribbon samples, attenuation coefficients were calculated from experimental measurements (during APS 2011, see Sect. 2.5.2) or drawn from tabulated data.

Liquids and glasses are isotropic and homogeneous, and therefore produce diffraction patterns that are azimuthally symmetric. Intensities for pixels located at a given 2θ from the incident beam could then be averaged about the polar angle, φ, to produce a one-dimensional diffraction pattern [21], giving

$$I(2\theta) = \oint \mathrm{d}\,\varphi \frac{I_{sample}(2\theta, \varphi)}{[(V/V')^{-1} OP(1 + I_2/I_1)(\mathrm{d}\Omega/\mathrm{d}A)]}. \tag{2.3}$$

Averaging azimuthally improves the signal-to-noise ratio for the data. A transformation of the intensity as a function of angle to the coordinates of the momentum transfer, q, $I(2\theta) \rightarrow I(q)$, is given by

$$q = \frac{4\pi \sin(2\theta/2)}{\lambda}, \tag{2.4}$$

where λ is the wavelength of the incident and diffracted X-ray beam.

Contributions to the measured intensity due to inelastic Compton scattering, $n^{\mathrm{Inc}}(q)$ were accounted for by subtracting the measured intensity per atom, given by $(E_C/E)^{\alpha} i(M)$. $(E_C/E)^{\alpha}$ is the Breit-Dirac recoil factor, related to the incident photon energy and the electron mass, which accounts for the radiation pressure on a scattering element. The exponent α, to which the energy dependence is scaled, is set to a value of 3 for the intensity-measuring detector used in this thesis [18]. The intensity of modified scattering, $i(M)$, is related to the atomic numbers of the constituent elements as well as their electron form factors, which are analytically fit to published tabulated data [22].

Finally, the structure factor, $S(q)$, is a scaled form of the coherent scattering intensity, $I(q)$, minus the incoherent scattering intensity, $n^{\mathrm{Inc}}(q)$. The scaling removes the monotonic cross section, or Laue diffuse scattering $[(\sum c_i f_i^2) - (\sum c_i f_i)^2]$, and normalizes to the square average of the atomic form factor, giving

$$S(q) = \frac{NI(q) - F - n^{\mathrm{Inc}}(q) - [(\sum c_i f_i^2) - (\sum c_i f_i)^2]}{(\sum c_i f_i)^2}, \qquad (2.5)$$

where f_i and c_i are the form factor and atomic fraction of the i^{th} element, respectively. The atomic form factors are calculated from analytic fits to tabulated X-ray from factor data [23]. N and F refer to the intensity normalization and fluorescence correction, respectively. The intensity normalization scales the intensity from arbitrary detector units to electron units. The fluorescence correction accounts for uniform fluorescence background when atoms absorb incident photons and reemit at a longer wavelength. Because fluorescence and intensity normalization are difficult to estimate, the corrections were determined by fitting (to be

discussed in Sect. 2.6.2). The fluorescence correction is small for some systems in this thesis, but can become problematic for high-fluorescing elements studied with high-energy X-rays.

2.6.2 PDF Generation

The pair-distribution function is related to $S(q)$ by a simple Fourier transform. A direct Fourier transformation of the reduced structure function, $F(q) = q[S(q) - 1]$, results in the reduced pair-distribution function, $G(r)$, given by

$$G(r) = \frac{2}{\pi}\int_0^\infty q[S(q) - 1]\sin(qr)\,dq. \tag{2.6}$$

In practice, $S(q)$ is experimentally measured at discrete intervals over a finite range of q_{min} to q_{max}. Since numerical integration over this finite range can result in truncation error, fitting approximations were made to produce a $G(r)$ that better represents physical reality. The "low-r" correction, applied in the X-ray analysis of this thesis, determines the intensity normalization, N, and fluorescence correction, F, by minimizing the Peterson metric [24]. The Peterson metric quantifies unphysical ripples in the low-r region of $G(r)$, the region within the hard-sphere limit. Using the $S(q)$ determined by corrections from the "low-r" minimization, the PDF is given by

$$g(r) = 1 + \frac{G(r)}{4\pi r\rho_0} = 1 + \frac{1}{2\pi^2 r\rho_0}\int_0^\infty q[S(q) - 1]\sin(qr)\,dq, \tag{2.7}$$

where ρ_0 is the number density, determined in this thesis from the experimental measurements described in Section 2.3.3 for glass ribbons and Section 2.4.2 for liquids.

2.6.3 Peak Analysis

Positions and heights of the peaks in the $S(q)$ and PDF were determined using an automated fitting program written in LabVIEW^{TM}. Using search inputs for a specified data range and an initial estimate of the peak position, the program fits the peak either with a specified function (i.e. a Gaussian function) or by interpolation of the data using a cubic spline fit. Peak heights and positions were then determined from the fits. Error estimates for the peak heights and positions were generated using statistical errors associated with the input data (which were estimated following the method described by Hammersley [21]), variations in the fluorescence and normalization corrections, and measurement errors from density determination (for fits to the PDF).

The peak information determined in this thesis utilized the spline fitting technique, with crude position estimates determined from the original $S(q)$ and $g(r)$ outputs. Peak search ranges were estimated from the positions of half-maximum positions. One-sigma error bars were generated for the peak data by the program.

2.7 RMC Analysis and Structure Characterization

Local atomic structures were further analyzed by the generation of three-dimensional atomic configurations from reverse Monte Carlo (RMC) simulation fits to the experimentally determined total structure factors, $S(q)$. The local order in the simulated configurations was then characterized by Honeycutt-Anderson (HA) [25] common neighbor and Voronoi polytetrahedral [26-29] analyses. Structural analysis was correlated with temperature and thermophysical

property data. Results were then used for direction comparison with data from theoretical models and molecular dynamics (MD) simulations.

2.7.1 Reverse Monte Carlo

The reverse Monte Carlo method [30] attempts to create an atomic arrangement that reproduces experimentally determined structural data. The atomic configurations generated by RMC are, therefore, candidates for representing the true structure. Configurations were generated utilizing a variation of the Metropolis Monte Carlo (MMC) method [30], by which random movements of atoms in the configuration are accepted or rejected on the basis of improving the simulated fit to the input experimental data.

The MMC method drives the model by establishing a "potential energy" for each configuration, related by a Boltzmann distribution with a "temperature" term, and finds a potential energy minimum by sampling the configuration space. The procedure begins by (i) calculating the initial structure parameter (i.e. $S(q)$, $g(r)$, etc.) from a randomly generated starting configuration and comparing it to the input experimental data by calculating the fit residue

$$\chi_0^2 = \sum_i \frac{[S_0(q_i) - S_E(q_i)]^2}{\sigma^2(q_i)}, \tag{2.8}$$

where $S_0(q)$ is the total structure factor calculated from the initial atomic configuration, $S_E(q)$ is the experimental data, and σ is the temperature term that nominally represents the experimental error in the data. The initial fit residue, χ_0^2, represents a "potential energy" for the atomic configuration. (ii) Atoms are then randomly moved to sample the configuration space. (iii) The

new structure parameter, $S_n(q)$, is calculated from the new configuration and the new fit is measured by

$$\chi_n^2 = \sum_i \frac{[S_n(q_i) - S_E(q_i)]^2}{\sigma^2(q_i)}. \quad (2.9)$$

(iv) χ_n, is then compared to that from the previous fit, χ_0, and the atomic moves are accepted if $\chi_n^2 < \chi_0^2$. If $\chi_n^2 > \chi_0^2$, the moves are accepted with probability $\exp[-(\chi_n^2 - \chi_0^2)/2]$.

The RMC technique provides an alternative to molecular dynamics (MD) simulations in reconstructing the atomic positions from a liquid diffraction experiment. The RMC technique has many advantages over MD: (i) in this thesis, no interaction potential is used, eliminating reliance on assumptions about the atomic interactions and questions raised from those assumptions, (ii) RMC simulations are less computationally intensive allowing for larger sampling sizes and decreased computation time, and (iii) RMC simulation results, as designed, are generally more consistent with experimental data. Even considering the advantages of RMC, it is not without problems or criticisms. Configurations produced by the technique are not unique and typically reflect the most disordered structure that is consistent with the input data. Further, nonphysical structures can appear when the simulation lacks proper constraints (i.e. proper details about the distance of closest-approach or chemical correlation information from partial PDFs), and information regarding the chemical specific topology is typically unreliable. Finally, because no interaction potential is used, kinetic and thermodynamic information about the configuration cannot be inferred, nor can "inherent structures" [31, 32] (the structure independent of vibrational noise) be extracted. Even with the problems, overall topological structures from average structural information consistent with experimental data can still be

obtained, especially with the input of and constraint from other experimental results. Further discussion of the RMC technique and its merits can be found elsewhere [30].

RMC simulations for this work were performed using the RMC++ [33] and RMC_POT [34] programs. Both programs employ the MMC method with additional constraints. Typical simulations were run for 10 - 60 hours (generating on the order of $10^7 – 10^8$ atomic moves) and performed on 10,000 atom ensembles. Simulations were constrained to experimental $S(q)$ data, and q-dependent atomic from factors (see Sect. 2.6.1) were assumed when calculating total $S(q)$ from the atomic configuration. Cubic box-sizes were calculated from experimentally determined densities (see Sect. 2.3.2 and 2.4.2). Hard-sphere cut-off constraints, rejecting moves of atoms to within a specified distance of a neighboring atom, were determined for each chemically-specific pair of elements and calculated based on the total or partial $g(r)$ information available. To improve the convergence of the simulated fit, the "moveout" option was applied. This feature of the simulation preferentially generates moves for atoms that, from the creation of an initial random configuration, violate the hard-sphere cut-off constraint. For "unconstrained" RMC simulations fit only to the experimental $S(q)$, the hard-sphere distance between the smallest atoms was determined from the minimum before the first peak in $g(r)$. Goldschmidt radii [35] of the atoms were used to scale the cutoffs for the remaining partial-pairs of atomic elements. In this thesis, "Constrained" RMC (CRMC) simulations were fit to both the experimentally determined $S(q)$ and partial PDFs obtained from MD simulations. Hard-sphere cut-offs for constrained simulations were determined from the minima before the first peak in the respective partial PDFs. Further details of the RMC simulations are described in data analysis discussions of subsequent chapters.

2.7.2 Honeycutt-Anderson Analysis

Honeycutt-Anderson (HA) analysis [25] is a form of common neighbor analysis (CNA), which was originally proposed by Clarke and Jónsson [36]. CNA measures multi-body correlation between neighboring atoms by assigning each pair of atoms a three-number index, *jkl*. HA analysis includes a fourth index, *i*, representing pairs by *ijkl*. The index *i* refers to the bonding of the pair of atoms, or whether or not the atoms are nearest neighbors ($i = 1$ for bonded pairs and $i = 2$ for non-bonded pairs). CNA assumes $i = 1$. The index *j* counts the number of common nearest-neighbor atoms, or the number of atoms that are bonded to both atoms of the original pair. The index *k* is the number of bonds between the common nearest-neighbors. For the original CNA, *l* is the number of bonds in the longest continuous chain formed by the *k* bonds. HA uses the arbitrary index *l* to distinguish between bond geometries of pairs whose first three indices are the same.

HA analysis detects various local atomic arrangements by indexing atomic pairs using a chosen bond (or HA cut-off) distance. The cut-off is usually set to the distance corresponding to the size of the average first coordination shell, which can be determined by a variety of methods [37, 38]. In this thesis, the size of the first coordination shell was determined from the first minimum after the first peak in the total PDF. Typical HA indices identified in liquid and glass structures include 1421 & 1422, mainly representing pairs in face-centered cubic and hexagonal close packed structures, 1661, mainly representing pairs in body-centered cubic structures, 1551, representing pairs in perfect icosahedral structures, and 1431 and 1541, representing pairs in distorted icosahedral structures. It is important to note that these indices are not unique to the associated structures. For example, both the Z9 Frank-Kasper cluster (discussed in Section 2.7.3) and the perfect icosahedron contain several 1551 pairs [38]. Graphical representations of

these structures can be found elsewhere [1, 39]. Further discussion of HA analysis and the relationship between HA indices and the true first neighbor shell structure can also be found elsewhere [40].

2.7.3 Voronoi Analysis

The Voronoi analysis [41] uses the Voronoi tessellation [42] scheme, which divides the three-dimensional space containing the atomic configuration into cells centering around each atom. Planes are drawn to bisect the lines between neighboring atoms, and the cells are defined by the inner planes surrounding the atoms. Just as for Wigner-Seitz cells, the space of the Voronoi cell contains the volume closer to the central atom than to any other atom. An advantage of the Voronoi analysis over the HA analysis is that an input for the cutoff distance is not needed. The coordination number, or number of nearest neighbors around a central atom, is unambiguously determined by the Voronoi tessellation, and the nearest-neighbor atoms are identified as those sharing a Voronoi cell face. Voronoi cells can be indexed by the number and shape of its faces (i.e. <n3, n4, n5, n6, …>) [41]. In the Voronoi index, n3 represents the number of triangular (3-sided) faces, n4 the number of quadrangular (4-sided) faces, n5 the number of pentagonal (5-sided) faces, and so on.

The Voronoi polytetrahedral analysis [26-29] specifically looks at the prevalence of polyhedral structures related to polytetrahedral packing in liquids and glasses [43, 44]. Typical polytetrahedral structures identified [38, 41, 45] are the canonical Kasper polyhedra [46, 47] (Fig. 2.6), also defined as “Z clusters”. Voronoi indices corresponding to the most relevant polytetrahedrally packed clusters in metallic liquids and glasses [38], which includes the “Z clusters” as well as several distortions of the clusters, can be found in Table 2.4.

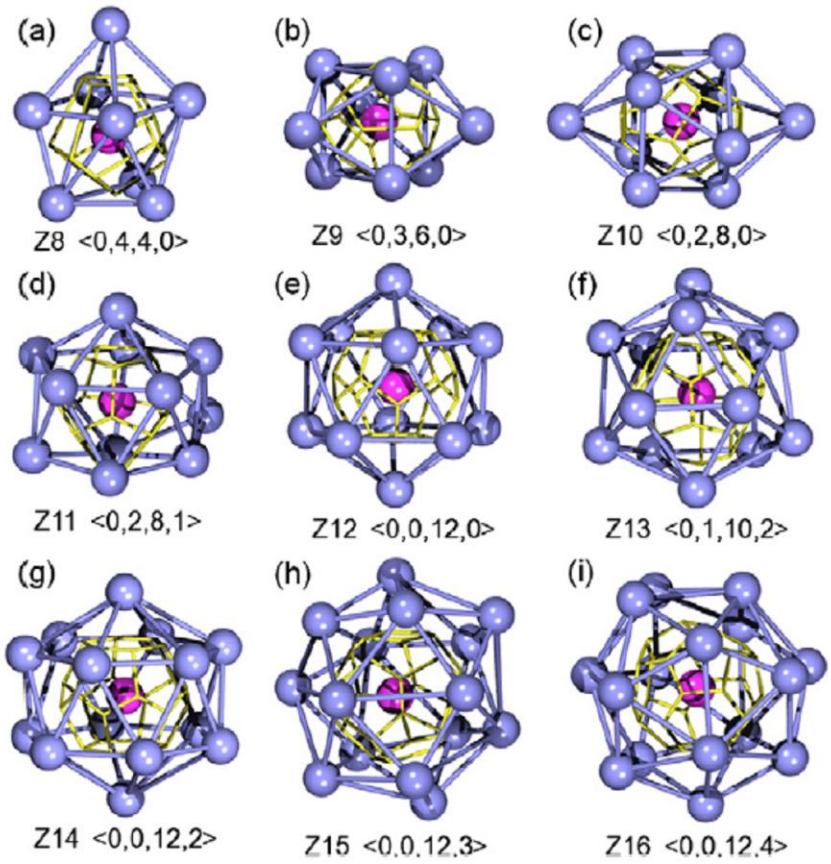

Figure 2.6: Z clusters with polytetrahedral packing and triangulated shell. For each cluster, the center atom is colored pink, and the yellow edges outline the Voronoi cell. [reprinted from Progress in Materials Science, 56, Y. Q. Cheng , E. Ma, Atomic-level structure and structure-property relationship in metallic glasses, p. 424, Copyright (2011), [38] with permission from Elsevier].

Table 2.4: Voronoi indices for polytetrahedral Z-clusters with increasing distortion (left to right)

x (CN)	Zx (Z Clusters)	Zx.1	Zx.2	Zx.3	Zx.4
8	<0, 4, 4, 0>				
9	<0, 3, 6, 0>	<0, 4, 4, 1>			
10	<0, 2, 8, 0>	<0, 3, 6, 1>	<0, 4, 4, 2>		
11	<0, 2, 8, 1>	<0, 3, 6, 2>	<0, 4, 4, 3>		
12	<0, 0, 12, 0>	<0, 2, 8, 2>	<0, 3, 6, 3>	<0, 4, 4, 4>	
13	<0, 1, 10, 2>	<0, 2, 8, 3>	<0, 3, 6, 4>	<0, 4, 4, 5>	
14	<0, 0, 12, 2>	<0, 1, 10, 3>	<0, 2, 8, 4>	<0, 3, 6, 5>	<0, 4, 4, 6>
15	<0, 0, 12, 3>	<0, 1, 10, 4>	<0, 2, 8, 5>	<0, 3, 6, 6>	<0, 4, 4, 7>
16	<0, 0, 12, 4>	<0, 1, 10, 5>	<0, 2, 8, 6>	<0, 3, 6, 7>	<0, 4, 4, 8>
17	<0, 0, 12, 5>	<0, 1, 10, 6>	<0, 2, 8, 7>	<0, 3, 6, 8>	<0, 4, 4, 9>

The Voronoi analysis performed in this thesis on RMC generated configurations was carried out using an in-house program (VoronoiReadin_8-13-2013.py) written by Z. Markow and R. Soklaski [48]. A cut-off distance representing one-tenth of the box length was used to accelerate the analysis by limiting the number of bisecting planes analyzed around a particular atom. A Voronoi tessellation calculation for a particular configuration was rejected if the volume occupied by the tessellation was less than the total configuration box-size. For the Voronoi analysis used here, bisection was not weighted by the atomic size.

2.8 References

[1] V. M. Wessels, Ph.D. Thesis, Washington University in St. Louis, 2009.
[2] N. A. Mauro, Ph.D. Thesis, Washington University in St. Louis, 2011.
[3] H. Okamoto, Journal of Phase Equilibria and Diffusion **28** (6), 583 (2007).
[4] N. Jakse, T. L. T. Nguyen and A. Pasturel, Journal of Physics: Condensed Matter **23** (40), 404205 (2011).
[5] Y. Li, Materials Transactions **42** (4), 556 (2001).
[6] J. C. Bendert, Ph.D. Thesis, Washington University in St. Louis, 2013.
[7] R. S. Davis, Metrologia **29** (1), 67 (1992).
[8] M. J. Assael, H. M. T. Avelino, N. K. Dalaouti, J. M. N. A. Fareleira and K. R. Harris, International Journal of Thermophysics **22** (3), 789 (2001).
[9] A. K. Gangopadhyay, G. W. Lee, K. F. Kelton, J. R. Rogers, A. I. Goldman, D. S. Robinson, T. J. Rathz and R. W. Hyers, Review of Scientific Instruments **76** (7) (2005).
[10] N. A. Mauro and K. F. Kelton, Review of Scientific Instruments **82** (3) (2011).
[11] T. Meister, H. Werner, G. Lohoefer, D. M. Herlach and H. Unbehauen, Control Engineering Practice **11** (2), 117 (2003).
[12] M. A. Khan, C. Allemand and T. W. Eagar, Review of Scientific Instruments **62** (2), 392 (1991).
[13] S. K. Chung, D. B. Thiessen and W. K. Rhim, Review of Scientific Instruments **67** (9), 3175 (1996).
[14] R. C. Bradshaw, D. P. Schmidt, J. R. Rogers, K. F. Kelton and R. W. Hyers, Review of Scientific Instruments **76** (12) (2005).
[15] J. H. Lee, C. C. Aydiner, J. Almer, J. Bernier, K. W. Chapman, P. J. Chupas, D. Haeffner, K. Kump, P. L. Lee, U. Lienert, A. Miceli and G. Vera, Journal of Synchrotron Radiation **15** (5), 477 (2008).
[16] J. C. Bendert, N. A. Mauro and K. F. Kelton, Journal of Applied Crystallography **46** (4), 999 (2013).
[17] N. A. Mauro, M. L. Johnson, J. C. Bendert and K. F. Kelton, Journal of Non-Crystalline Solids **362** (0), 237 (2013).

[18] T. Egami and S. J. Billinge, *Underneath the Bragg peaks: structural analysis of complex materials*. (Elsevier, 2003).
[19] J. H. Hubbell and S. M. Seltzer, Report No. PB--95-220539/XAB; NISTIR--5632; TRN: 51812148 United StatesTRN: 51812148Mon Dec 01 07:31:32 EST 2008NTISGRA; SCA: 663620; PA: GRA-95:12148; EDB-95:109083; SN: 95001416131English, 1995.
[20] J. C. Bendert, M. E. Blodgett and K. F. Kelton, Acta Crystallographica Section A **69** (2), 131 (2013).
[21] A. P. Hammersley, S. O. Svensson, M. Hanfland, A. N. Fitch and D. Hausermann, High Pressure Research **14** (4-6), 235 (1996).
[22] H. Balyuzi, Acta Crystallographica Section A **31** (5), 600 (1975).
[23] D. Waasmaier and A. Kirfel, Acta Crystallographica Section A **51** (3), 416 (1995).
[24] P. F. Peterson, E. S. Bozin, T. Proffen and S. J. L. Billinge, Journal of Applied Crystallography **36** (1), 53 (2003).
[25] J. D. Honeycutt and H. C. Andersen, The Journal of Physical Chemistry **91** (19), 4950 (1987).
[26] J. Finney, Proceedings of the Royal Society of London A **319** (1539), 479 (1970).
[27] J. L. Finney, Nature **266** (5600), 309 (1977).
[28] V. A. Borodin, Philosophical Magazine A **79** (8), 1887 (1999).
[29] V. A. Borodin, Philosophical Magazine A **81** (10), 2427 (2001).
[30] R. L. McGreevy, Journal of Physics: Condensed Matter **13** (46), R877 (2001).
[31] F. H. Stillinger and T. A. Weber, Science **225** (4666), 983 (1984).
[32] F. H. Stillinger and T. A. Weber, Physical Review A **25** (2), 978 (1982).
[33] G. Evrard and L. Pusztai, Journal of Physics: Condensed Matter **17** (5), S1 (2005).
[34] O. Gereben and L. Pusztai, Journal of Computational Chemistry **33** (29), 2285 (2012).
[35] E. A. Brandes and G. B. Brook, *Smithells Metals Reference Book*. (Butterworth-Heinemann, 1992).
[36] A. S. Clarke and H. Jónsson, Physical Review E **47** (6), 3975 (1993).
[37] Y. Waseda, *The structure of non-crystalline materials: liquids and amorphous solids*. (McGraw-Hill International Book Company New York, 1980).
[38] Y. Q. Cheng and E. Ma, Progress in Materials Science **56** (4), 379 (2011).
[39] T. H. Kim, Ph.D. Thesis, Washington University in St. Louis, 2007.
[40] L. Huang, C. Z. Wang, S. G. Hao, M. J. Kramer and K. M. Ho, Physical Review B **81** (1), 014108 (2010).
[41] H. W. Sheng, W. K. Luo, F. M. Alamgir, J. M. Bai and E. Ma, Nature **439** (7075), 419 (2006).
[42] G. Voronoi, Journal Fur Die Reine Und Angewandte Mathematik **134**, 198 (1908).
[43] D. R. Nelson and F. Spaepen, (1989), Vol. 42, pp. 1.
[44] D. R. Nelson, Physical Review B **28** (10), 5515 (1983).
[45] J. P. K. Doye and D. J. Wales, Science **271** (5248), 484 (1996).
[46] F. C. Frank and J. S. Kasper, Acta Crystallographica **11** (3), 184 (1958).
[47] F. C. Frank and J. S. Kasper, Acta Crystallographica **12** (7), 483 (1959).
[48] R. Soklaski, Z. Nussinov, Z. Markow, K. F. Kelton and L. Yang, Physical Review B **87** (18), 184203 (2013).

Chapter 3

Anomalous structural evolution and liquid fragility signatures in Cu-Zr and Cu-Hf liquids and glasses [1]

This chapter is has been published in Acta Materialia and was co-authored in collaboration with N. A. Mauro, M. L. Johnson, J. C. Bendert, Ryan Soklaski, Li Yang, and K. F. Kelton. The author's personal contribution includes participation in data collection during the BESL 2010 and APS 2011 runs, X-ray image reduction, $S(q)$ and $g(r)$ generation, density data collection and analysis for the Cu-Hf liquids, $S(q)$, $g(r)$, and PPCF peak analysis, and preparation of the first drafts of the manuscript. Glass and Cu-Zr liquid density measurements were performed by N. A. Mauro and J. C. Bendert, and Debye-Waller extrapolations were performed by M. L. Johnson. MD simulation data were provided by R. Soklaski and L. Yang.

3.1 Introduction

Recent developments in levitation techniques, and in particular in electrostatic levitation [2, 3], have provided the ability to containerlessly process and study a variety of metallic liquids at high temperatures. X-ray and neutron scattering studies of levitated liquids have demonstrated that with increased supercooling those liquids develop significant short-range and often medium-range order [4-6]. Some of these metallic liquids also have a high glass-forming ability (GFA), particularly the Zr-based alloys [7, 8]. However, both the relationship between developing structure within the liquid and the structure of the glass and the connection between liquid

structure and GFA are poorly understood. The rapidly slowing kinetics in the liquid near the glass transition temperature, T_g, plays a critical role in glass formation. As the temperature is decreased the viscosity increases with an Arrhenius behavior for some liquids (strong), but shows highly non-Arrhenius behavior in other liquids (fragile), for which the apparent activation energy increases rapidly near T_g. It has been observed that strong liquids tend to have higher GFA than fragile ones [9-11], making fragility of practical as well as fundamental interest. The evolution of order, both topological as well as chemical, can be important for glass formation [12-16]. While chemical ordering has been observed in glasses [17, 18] and glass-forming supercooled liquids [6], further study is needed to better understand its nature, significance, and universality.

Because of their relative simplicity, binary liquids and glasses are ideal for studying topological and chemical ordering. While binary transition metal (TM) liquids that form glasses typically have lower GFA values than metallic liquids with multiple elements, some binary bulk metallic glasses (BMGs) have been reported in Cu-Zr [19-23], Cu-Hf [22, 24-26], Ni-Nb [25], and Ni-Ta [27] alloys. The Cu-Zr alloys have been studied extensively, largely because they form BMGs of several specific alloy compositions [21-23, 28]. It has been observed that: (1) strong liquids tend to have higher GFA than fragile ones [9-11]; (2) metallic liquids with more components (which tend to have higher GFA) are generally stronger than those liquids with fewer components [29]. However, the relationship between GFA and fragility is particularly problematic because a single GFA parameter is not universally accepted and measures such as the critical casting thickness (CCT) and the reduced supercooled region are strongly influenced by sample impurities and contaminants. More fundamentally, though, it has been observed that in several metal and metal-metalloid BMG-forming systems the correlation between fragility and

any measure of GFA breaks down [30]. Cu-Zr liquids are consistent with being designated fragile systems, as characterized by both viscosity [31] and structural [32] measurements. Theoretical studies of Cu-Zr glasses and liquids [23, 33-43] have indicated the formation of chemically and topologically ordered clusters in the supercooled liquid that survive in the glass. A recent analysis of molecular dynamics (MD) simulations in Cu-Zr alloys [44] determined that a bimodal distribution of ordering in the liquid occurs, with the formation of an extensive backbone of connected icosahedra that grows rapidly near T_g constituting a distinguishing feature of good glass-forming compositions. Other MD simulation have also shown the formation of spatial heterogeneities that contain a large amount of icosahedral short-range order (ISRO) during the structural evolution of the supercooled liquid [15], as well as the formation of networked structures with a high degree of medium-range order arising from ordering of these clusters [45]. In addition, those studies [23, 33, 34, 44] showed a continuous increase in the number of icosahedral clusters with an acceleration of the development of icosahedral order upon cooling from the liquidus (T_L) to the glass transition temperature. Recent experimental evidence in a supercooled Cu-Zr liquid has demonstrated that chemical ordering accompanies this topological ordering [6]. Reverse Monte Carlo (RMC) and MD simulations from that work also confirmed acceleration in ordering below the liquidus temperature.

An acceleration of structural change in supercooled liquids has also been observed experimentally in Ni-Nb liquids [46], as shown by a large difference between the extrapolated height of the first peak of the total structure factor $S(q_1)$ of the liquid down to the glass transition temperature with that of the glass (extrapolated from room temperature to T_g using the Debye theory [47]). Given evidence for an acceleration of structural change in the supercooled liquid and its relation to bulk GFA and fragility [48], Mauro et al. [46] suggested that temperature-

dependent structural changes observed in $S(q)$ and in the total pair correlation functions $g(r)$ obtained from X-ray diffraction studies could be an indicator of liquid fragility [48].

Since Zr and Hf have almost identical atomic sizes and chemical properties it might be expected that the structures and properties of Cu-Hf binary liquids would be very similar to those of Cu-Zr ones. This assumption that Zr can be replaced by Hf without influencing the structure of the as-quenched glasses is well founded, having been utilized in early isomorphic substitution studies [49, 50]. Further, previous studies have demonstrated that some Cu-Hf liquids form BMGs [22, 24-26], including $Cu_{55}Hf_{45}$ [22, 26]. Because of the large difference in X-ray scattering strength from the two elements a study of Cu-Hf liquids and their glasses would complement the extensive studies of Cu-Zr liquids. To our knowledge, however, there are no existing structural studies of Cu-Hf liquids.

To better understand ordering in Cu-Zr and Cu-Hf liquids and how this might relate to glass formability and liquid fragility, the results from experimental and theoretical investigations of the local structures of the liquids and glasses are reported here. The liquid alloys were processed over a wide temperature range in a high vacuum, containerless environment using the electrostatic levitation technique [3]. The $S(q)$ values for the liquids show typical ordering behavior, with a sharpening of the peaks and an increase in their magnitude with decreasing temperature. From these structural metrics the ordering increases approximately linearly with decreasing temperature. However, the height of the first peak in $S(q)$ of the liquids extrapolated to the glass transition temperatures is less than that of the glasses in almost all cases, suggesting acceleration of ordering in the liquid at temperatures below those where measurements could be made (limited by crystallization of the liquids). Interestingly, both the liquid and glass pair correlation functions show distinct ordering at two length scales in the first coordination shell for

$Cu_{46}Zr_{54}$ (confirming previous experimental results [6]) as well as for $Cu_{54}Zr_{46}$, $Cu_{55}Hf_{45}$, and $Cu_{60.8}Hf_{39.2}$. Subtle differences in the strength of ordering with composition, as well as anomalous trends in peak growth down to the glass temperature, are analyzed and discussed.

3.2 Experimental Procedure

Master ingots of all compositions were prepared by arc melting high purity Cu (99.999%), Zr (99.97%, primary impurity Hf) and Hf (99.97%, primary impurity Zr) on a Cu hearth in a high purity (99.999%) Ar atmosphere. A Ti-Zr getter located close to the sample was melted prior to arc melting to further reduce the oxygen concentration in the chamber. Each ingot was melted three times to ensure that the compositions of the samples were homogeneous; each melt cycle lasting approximately 60 s. The mass losses during arc melting were negligible (less than 0.1%). The ingots were crushed and portions re-melted to obtain small spherical samples (~2.5 mm diameter) for in situ liquid structural studies at the Advanced Photon Source (APS) in 6-ID-D using the Washington University Beamline Electrostatic Levitator (WU-BESL) [2, 3]. As already discussed in this thesis, the WU-BESL is optimized for X-ray diffraction studies of levitated, containerlessly processed, liquids in a high vacuum environment (~10^{-7} Torr). Several of the prepared master ingots were melted by radio frequency induction heating to 1050-1100 °C (above the liquidus temperatures) in a graphite crucible under a high purity (99.998%) Ar atmosphere and rapidly quenched onto a copper wheel that was rotating at ~60 m s^{-1}, producing continuous 3-10 cm ribbons with an average cross-section of 1-2 mm x 20-30 μm. Laboratory X-ray (Rigaku, Cu K_α $\lambda = 1.54$ Å radiation) and high energy synchrotron diffraction studies confirmed that the as-quenched ribbons were fully amorphous. Synchrotron scattering

studies of the glasses were made at the APS in transmission geometry by mounting the ribbon samples on the 6-ID-D beamline goniometer.

The temperatures of the levitated liquids in the WU-BESL were measured from 160 °C to 2300 °C using two infrared pyrometers with overlapping temperature ranges. A single color Process Sensors Metis MI18 MB8, operating at 1.89 μm wavelength, was used for low temperature measurements (160-800 °C), and a Process Sensors Metis MQ22 two color pyrometer, operating at 1.40 and 1.64 μm wavelengths, was used for high temperature measurements (600-2300 °C). Ratio pyrometers provide more accurate measurements of the temperature because emissivity changes with temperature are accounted for [51]. Because of the proximity of the measured wavelengths relative changes in the emissivity at each wavelength over a narrow temperature range are expected to be small. Emissivity ratios were calibrated by matching the melt plateau in the temperature versus time curve obtained on heating in the ESL (the onset corresponding to the solidus temperature T_S) to the endothermic transition signature measured in a differential thermal analyzer (DTA) (Labsys^{TM} DTA/DSC, Setaram Instrumentation).

Samples were heated, melted and subsequently thermally processed using a fiber-coupled diode laser (980 nm, 50 W continuous maximum power output). A constant emissivity ratio was assumed for the entire temperature range over which structural data were acquired. Crystallization from the metastable liquid, marked by a sharp rise in temperature (recalescence), limited the lowest temperature of the X-ray diffraction studies to 290 °C below the liquidus temperature. Sample masses were measured before and after ESL processing to determine the mass loss during processing, which would indicate a change in composition. In all cases the mass loss was negligible.

The temperature measurements were correlated with non-contact volume measurements of the liquid samples. These were made using the shadow method [52, 53] with a Pixelink PL-B741G CMOS camera and a 455 nm collimated microscope LED, which has a total beam power of 240 mW and a beam diameter of 37 mm. The pixel dimensions were calibrated before and after each sample measurement using 2.38125 ± 0.00076 mm diameter (grade 3) tungsten carbide standards. The sample volume was determined from the shadow of the backlit levitated sample [54] and the density was then calculated by multiplying the sample mass by the inverse of the volume. The video data were taken at a frame rate of 20-25 fps. Details of the machine vision volume measurement algorithm are given elsewhere [52]. The relative precision of the density data was ~0.3% over the temperature range studied, with an absolute accuracy of ~0.5%; the measurement error is dominated by errors in the volume and mass calibrations. The densities of the amorphous ribbons at room temperature were determined using Archimedes' method, with toluene as the working fluid; the uncertainties in the values obtained were between 0.1% and 0.2% after error propagation.

Diffraction studies of the liquids and glasses were made in transmission geometry, using high energy X-rays (E = 129 keV, λ = 0.0961 Å for liquid studies; E = 100 keV, λ = 0.1243 Å for glass studies) to obtain data over a scattering range of 0.7 to 15 $Å^{-1}$. A GE Revolution 41-RT amorphous Si flat panel X-ray detector was used to measure the scattering data at a sampling rate of 1 Hz. The sample to detector distance, detector tilt, and detector center were calibrated by fitting the diffraction pattering of a levitated polycrystalline Si sample. These detector values were confirmed using a NIST Si standard in a capillary placed at the position of the levitated sample. The scattering data obtained were processed by masking bad pixels, applying a pixel efficiency gain map, averaging the images obtained during the isothermal hold, and subtracting

the appropriate dark current. Images were then corrected for oblique incidence, absorption, multiple scattering, fluorescence, polarization, sample geometry, and Compton scattering contributions using in-house analysis packages written in LabView™ [55]. A series of measurements of 10-20 s duration were made at each temperature step to obtain the total structure factor using

$$S(q) = \frac{I(q) - \sum_{i=1}^{n} c_i |f_i(q)|^2}{\left|\sum_{i=1}^{n} c_i f_i(q)\right|^2} + 1 \qquad (3.1)$$

where $I(q)$ is the measured diffraction intensity, c_i is the atomic fraction of each element, and $f_i(q)$ is the q-dependent atomic form factor for each species. The sums were made over all species and an isotropic and statistically homogeneous atomic distribution was assumed.

The positions and magnitudes of the first peaks in $S(q)$ were refined by fitting a cubic spline to the peak. Total uncertainties were estimated by considering perturbations from independent sources of errors, including statistical uncertainties, estimated following the method described by Hammersley [56] and the confidence intervals of fitted corrections (e.g. intensity normalization). Based on this the precision of the peak heights in both $S(q)$ and $g(r)$ is ~0.5-1.0% and the accuracy of the peak heigts in $g(r)$ is ~4%.

Classical MD simulations of canonical (NVT) Cu-Zr liquids were made using LAMMPS [57] and a semi-empirical potential developed by Mendelev et al., which uses the Finnis and Sinclair generalizations of the embedded atom method [58]. The potential was developed using X-ray diffraction, liquid density, and enthalpy of mixing data, and first-principles results. Each simulation consisted of 2000 atoms contained within a cubic box with periodic boundaries and a volume set to yield zero pressure at the terminal temperature of the simulation. The initial

positions of the atoms were generated randomly and were subsequently evolved for 0.25 ns in 5 fs time steps at 1327 °C. The system was then quenched at a rate of 1012 °C s^{-1} to 12 temperatures below the initial annealing step, spaced approximately 100 °C apart. At each temperature during the 1 ns of evolution 78 atomic configurations were recorded. A total of three independent simulations, with different initial atomic configurations, were made for each composition of the Cu-Zr liquid, with the partial pair correlation functions (PPCFs) obtained from each being averaged. To investigate size effects systems of $Cu_{50}Zr_{50}$ and $Cu_{64}Zr_{36}$ with 10,000 atoms and target temperatures of 300 K were also simulated. No system size effects were observed in the PPCFs nor in other structural features of the metallic alloys [44]. Additionally, an analogous NPT ($P = 0$) simulation of $Cu_{50}Zr_{50}$ was conducted. The resulting average PPCFs were indistinct from those obtained in the NVT simulations.

3.3 Results and Discussion

Figure 3.1 shows the measured total static structure factors $S(q)$ and the total pair distribution functions $g(r)$ for Cu_xZr_{100-x} (x = 46 and 54) and Cu_xHf_{100-x} (x = 55 and 60.8) liquids and glasses for the entire temperature range over which data were collected. For each composition the first peak in $S(q)$ grows in magnitude, consistent with an increasing structural ordering of the liquid, and shifts toward higher q with decreasing temperature, consistent with an overall increasing density. The high q shoulder in the second peak of $S(q)$, often taken to be indicative of icosahedral short-range ordering (ISRO) [4, 59], develops with decreasing temperature in the liquid and is most clearly defined in the glass for each composition.

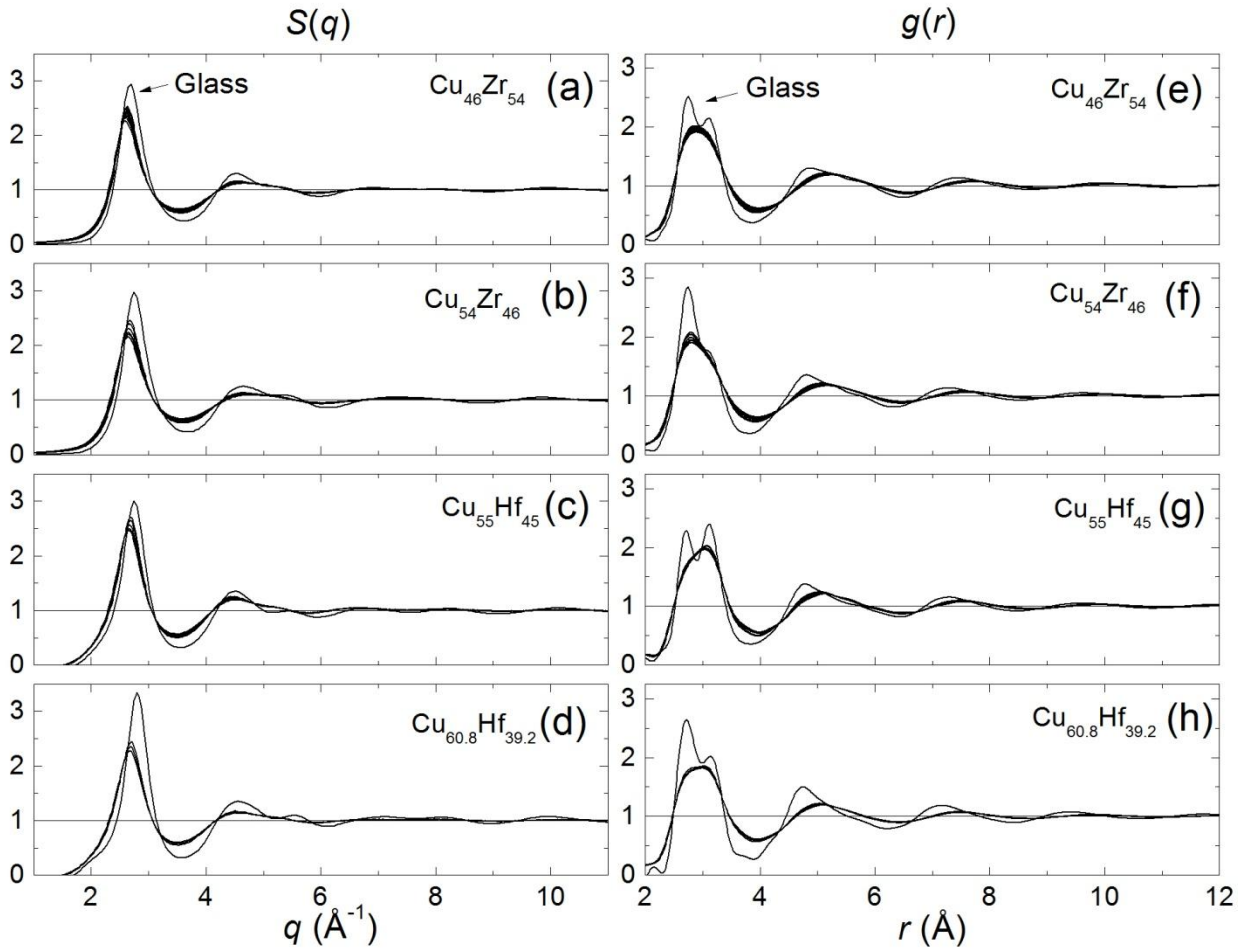

Figure 3.1: Total structure factors, $S(q)$, for (a) $Cu_{46}Zr_{54}$, (b) $Cu_{54}Zr_{46}$, (c) $Cu_{55}Hf_{45}$, and (d) $Cu_{60.8}Hf_{39.2}$ and pair correlation functions, $g(r)$, for (e) $Cu_{46}Zr_{54}$, (f) $Cu_{54}Zr_{46}$, (g) $Cu_{55}Hf_{45}$, and (h) $Cu_{60.8}Hf_{39.2}$ for liquids measured at each temperature step and glasses measured at room temperature.

The pair correlation functions $g(r)$, shown for each composition in Figure 3.1, were calculated from the experimentally determined $S(q)$ values using a Fourier transform,

$$g(r) - 1 = \frac{1}{4\pi\rho_0}\frac{2}{\pi}\int (S(q) - 1)\frac{\sin(qr)}{qr} q^2 dq \qquad (3.2)$$

where ρ_0 is the average number density. While the second and higher order peaks in $g(r)$ shift toward lower r with decreasing temperature, consistent with an increasing density, the most interesting feature shown by all of the liquids and glasses is a broad, asymmetric first

coordination peak. This is more evident in Figure 3.2, where only the first peaks in $g(r)$ are shown. The asymmetries of the first coordination shells in the glasses are more pronounced than in the liquids, showing a distinct splitting of the peaks for each of the compositions. The two peaks in the first coordination shell for the quenched glasses are at the same position as the emerging maxima in the liquids, indicating a similar short-range order in the two phases. For the $Cu_{46}Zr_{54}$ metallic glass extended X-ray absorption fine structure (EXAFS) measurements [60], neutron diffraction studies [61], and MD simulations (this work) demonstrate that the observed maxima at low r in the first coordination shell for the Cu-Zr liquids and glasses is due to contributions from Cu-Cu and Cu-Zr atom pairs, whereas the maxima at higher r contains only Zr-Zr pairs. Given the similarities in the atomic size of Zr and Hf and their similar enthalpy of mixing with Cu it is reasonable to assume that the maximum at low r in the first coordination shells for the Cu_xHf_{100-x} (x = 55 and 60.8) glasses is due to Cu-Cu and Cu-Hf pairs, while the maximum at larger r is due to Hf-Hf pairs.

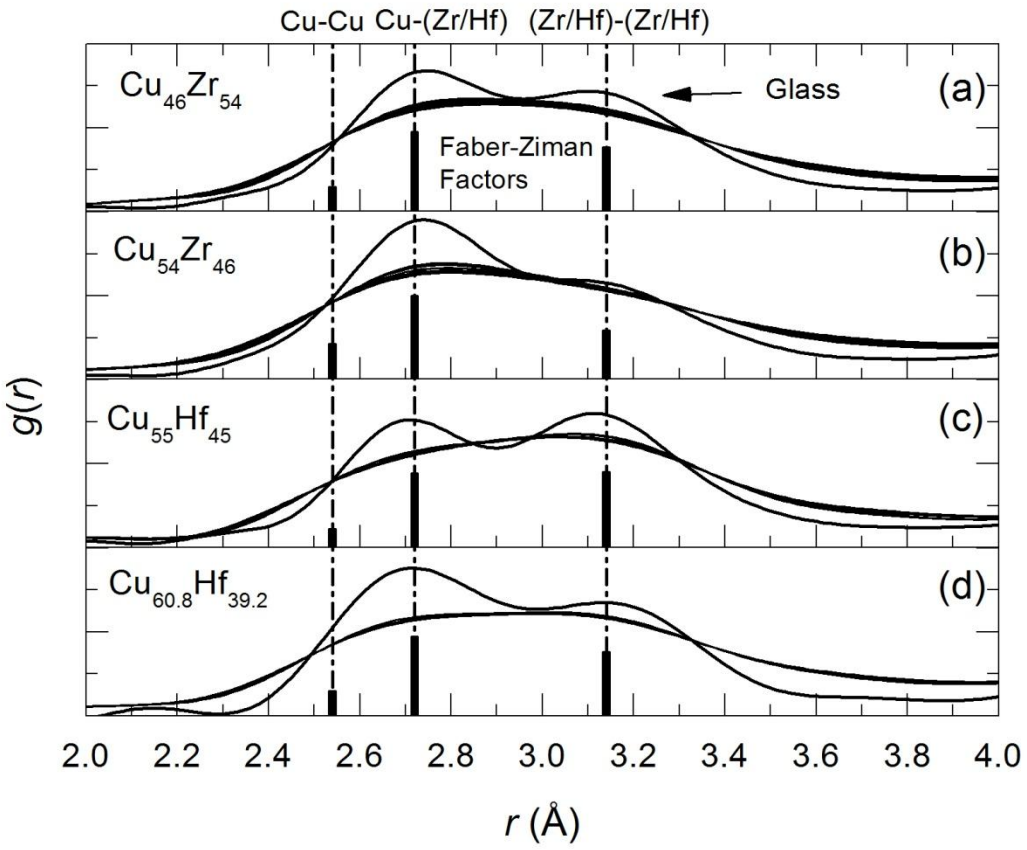

Figure 3.2: The first coordination shell (FSC) in $g(r)$ measured at each temperature in the liquid and at room temperature for the glass for each composition: (a) $Cu_{46}Zr_{54}$; (b) $Cu_{54}Zr_{46}$; (c) $Cu_{55}Hf_{45}$; (d) $Cu_{60.8}Hf_{39.2}$. Vertical dot-dash lines correspond to the average distances for the partial Cu-Cu (r = 2.54 Å), Cu-Zr (r = 2.72 Å) and Zr-Zr (r = 3.14 Å) atom pairs as determined by EXAFS measurements of $Cu_{46}Zr_{54}$ [60]. Vertical black bars under each peak illustrate the relative Faber-Ziman factor weightings, listed in Table 3.1, for each of the partial pairs, Cu-Cu, Cu-Zr (Cu-Hf), and Zr-Zr (Hf-Hf).

The evolution with temperature of the average nearest neighbor structure is represented by the behavior of the first coordination shell, shown in Figure 3.2. It is important to quantify the evolution of that local order. According to the Faber-Ziman (FZ) formalism [62] the total structure factor for a binary alloy is a weighted sum of the three chemically specific partial structure factors (PSF) $S_{ij}(q)$,

$$S(q) - 1 = \sum_i \sum_j w_{ij}(q)\big(S_{ij}(q) - 1\big) \tag{3.3}$$

$$w_{ij}(q) = c_i c_j \frac{f_i(q) f_j(q)}{\langle f(q)\rangle^2} \tag{3.4}$$

where c_i is the concentration of the ith atom species and $f_i(q)$ is its corresponding atomic scattering factor. For X-ray diffraction measurements the scattering factors are momentum transfer dependent, making the weighting factors $w_{ij}(q)$ also q dependent. The partial structure factors are related to the PPCFs by a Fourier transform,

$$g_{ij}(r) - 1 = \frac{1}{4\pi\rho_0}\frac{2}{\pi}\int \big(S_{ij}(q) - 1\big)\frac{\sin(qr)}{qr} q^2 dq \tag{3.5}$$

Substituting Eqs. 3.3 and 3.4 into Eq. 3.2 gives an expression for the total pair correlation function in terms of the partial structure factors and weighting factors,

$$g(r) - 1 = \frac{1}{4\pi\rho_0}\frac{2}{\pi}\int \sum\nolimits_i \sum\nolimits_j w_{ij}(q)\big(S_{ij}(q) - 1\big)\frac{\sin(qr)}{qr} q^2 dq \tag{3.6}$$

$$g(r) - 1 = \sum_{ij} \frac{1}{4\pi\rho_0}\frac{2}{\pi}\int c_i c_j \frac{f_i(q) f_j(q)}{\langle f(q)\rangle^2}\big(S_{ij}(q) - 1\big)\frac{\sin(qr)}{qr} q^2 dq \tag{3.7}$$

We see in Eq. 3.7 that because the scattering factors are q dependent the pair correlation function cannot be directly constructed from the PPCFs. However, the weighting factors $w_{ij}(q)$

vary slowly with q compared with $S_{ij}(q)$, allowing the weighting functions to be replaced by their lowest order approximation

$$w_{ij}(0) = c_i c_j \frac{Z_i Z_j}{\langle Z \rangle^2} \tag{3.8}$$

where Z_i is the atomic number of the ith element. This approximation has been shown to be valid for amorphous metallic alloys [18, 63, 64]. By substituting Eqs. 3.5 and 3.8 into Eq. 3.7 the total pair correlation function can be related to the chemically specific PPCFs:

$$g(r) \cong \sum_i \sum_j c_i c_j \frac{Z_i Z_j}{\langle Z \rangle^2} g_{ij}(r) = \sum_i \sum_j w_{ij}(0) g_{ij}(r) \tag{3.9}$$

Using PPCFs obtained from MD simulations of liquid $Cu_{46}Zr_{54}$ the lowest order approximation reproduces the first coordination shell to within ~2%, which validates the approach.

Using the relation in Eq. 3.9 the evolution of the order can be tracked for the two dominant atomic pair distances observed in Figure 3.2. Two important observations about the asymmetry of the first coordination shells motivate this analysis. First, as already noted, the two dominant features in the first coordination shell correspond closely to the Cu-(Zr/Hf) and (Zr/Hf)-(Zr/Hf) average atomic distances. These are well separated from each other and are well separated from the Cu-Cu distance. Second, the relative heights of the two features in each pair correlation function are well correlated with the FZ weighting factors (shown in Fig 3.2 and calculated in Table 3.1) for the Cu-(Zr/Hf) and (Zr/Hf)-(Zr/Hf) PPCFs for all compositions.

Table 3.1: FZ weighting factors, $w_{ij}(0)$, calculated according to Eq. 3.8 and scaled as $w_{ij}(0)/w_{\text{Cu-(Zr/Hf)}}(0)$ to show the relative magnitude with respect to the cross-partial.

Composition	$w_{\text{Cu-Cu}}(0)$	$w_{\text{Cu-(Zr/Hf)}}(0)$	$w_{\text{(Zr/Hf)-(Zr/Hf)}}(0)$	$w_{\text{Cu-Cu}}(0)$ scaled	$w_{\text{Cu-(Zr/Hf)}}(0)$ scaled	$w_{\text{(Zr/Hf)-(Zr/Hf)}}(0)$ scaled
$Cu_{46}Zr_{54}$	0.146	0.472	0.382	0.309	1.000	0.810
$Cu_{54}Zr_{46}$	0.211	0.497	0.292	0.426	1.000	0.587
$Cu_{55}Hf_{45}$	0.109	0.442	0.449	0.246	1.000	1.016
$Cu_{60.8}Hf_{39.2}$	0.148	0.473	0.379	0.312	1.000	0.800

By measuring the difference in g(r) at each temperature with respect to that at the highest temperature (T_0) the evolution of $g(r)$ with respect to cooling is clearly observed. Figure 3.3 shows difference curves, $\Delta g(r) = g_T(r) - g_{T_0}(r)$, for $Cu_{46}Zr_{54}$ (T_0 = 1120 °C), $Cu_{54}Zr_{46}$ (T_0 = 1140 °C), $Cu_{55}Hf_{45}$ (T_0 = 1110 °C), and $Cu_{60.8}Hf_{39.2}$ (T_0 = 1210 °C).

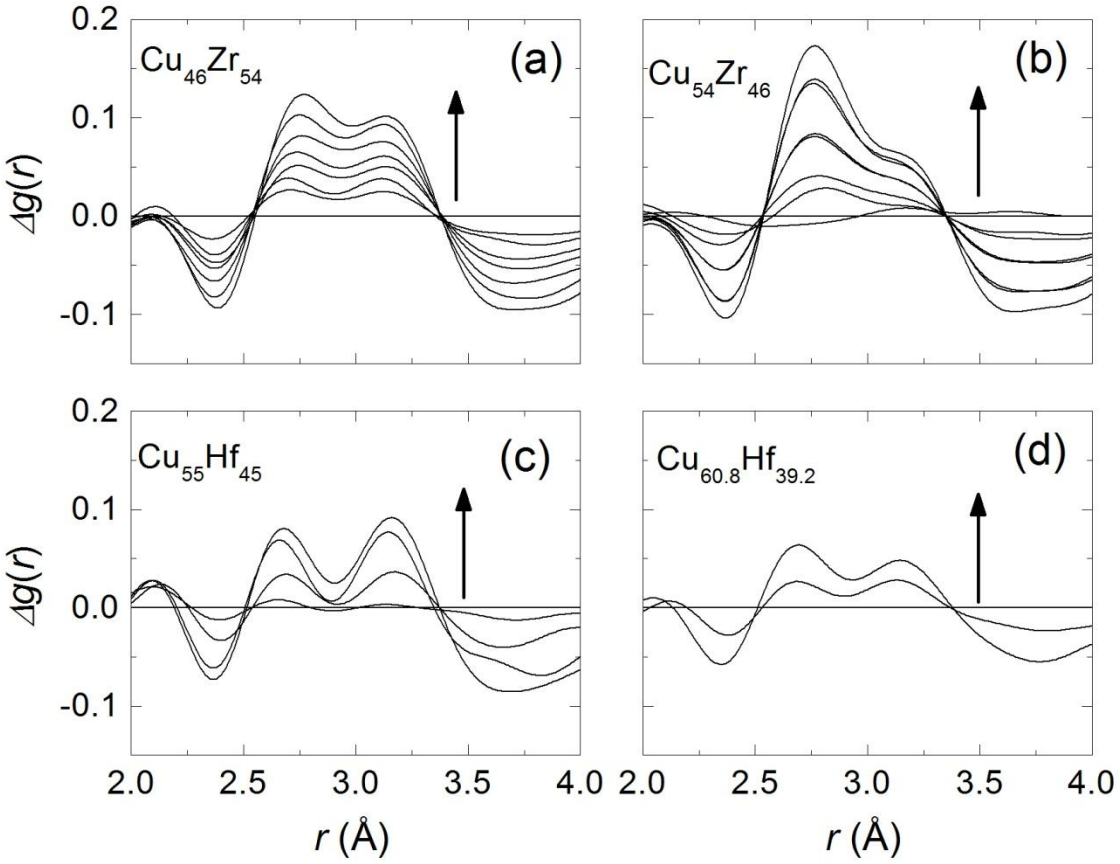

Figure 3.3: Difference curves for the liquid first coordination shells for each composition: (a) $Cu_{46}Zr_{54}$; (b) $Cu_{54}Zr_{46}$; (c) $Cu_{55}Hf_{45}$; (d) $Cu_{60.8}Hf_{39.2}$. Arrows indicate the direction of change in $g(r)$ with decreasing temperature, with curves evolving upward from the baseline $\Delta g(r,T_0) = 0$.

Two distinct maxima of nearly equal intensity develop with decreasing temperature in the difference curves for $Cu_{46}Zr_{54}$, $Cu_{55}Hf_{45}$, and $Cu_{60.8}Hf_{39.2}$, while a clear shoulder develops for $Cu_{54}Zr_{46}$. As reported previously [6] for $Cu_{46}Zr_{54}$, the maximum at lower r increases more rapidly with decreasing temperature than does that at high r. This difference is attributed to chemical ordering, or an increase in the number of Cu-Zr atomic pairs with decreasing temperature. The larger contribution of Cu-Zr pairs over the contribution of Zr-Zr pairs is clearly observed in the quenched glass (Fig. 3.2). For $Cu_{54}Zr_{46}$ the weighting factor for Zr-Zr relative to that for Cu-Zr is smaller than in $Cu_{46}Zr_{54}$, which decreases the contribution to the

large *r* maximum, eliminating peak splitting in the difference curves. It may be that the actual chemical ordering in the $Cu_{54}Zr_{46}$ liquid is similar to that in $Cu_{46}Zr_{54}$, but the difference in FZ weighting factors makes it difficult to discern. Like $Cu_{46}Zr_{54}$, the $Cu_{55}Hf_{45}$ liquid shows the development of local maxima in the difference curves. In this case, however, it is the peak at large *r* that increases faster with decreasing temperature, consistent with the more intense peak at large *r* in the glass (Fig. 3.2). Although this might be taken to indicate that the number of Hf-Hf pairs is increasing more rapidly than the number of Cu-Hf pairs, it is important to note that in this case the FZ factors for the two atomic pairs are very similar, unlike the case for Cu-Zr. Maxima due to Cu-Hf and Hf-Hf pairs are observed in $\Delta g(r)$ for the $Cu_{60.8}Hf_{39.2}$ liquid; these are similar to the Cu-Zr and Zr-Zr peaks observed for the $Cu_{46}Zr_{54}$ liquid and glass. Comparable peaks are observed because the FZ factors for $Cu_{46}Zr_{54}$ and $Cu_{60.8}Hf_{39.2}$ are quite similar (see Table 3.1).

The growth rates of the dominant length scales were quantified by examining the curves produced in Figure 3.3 and extending the analysis into the glass. Since it was not possible to supercool the liquid to T_g the data from the glasses, measured at room temperature, were extrapolated to T_g for comparison with the behavior of the liquid when extrapolated from high temperature. Since the structure of the glass is approximately constant below T_g changes in $S(q)$ with temperature will be due to atomic vibrations, which can be calculated from the Debye theory [47] according to

$$\frac{S_{T_2}(q)-1}{S_{T_1}(q)-1} = \exp\{-2[W_{T_2}(q)-W_{T_1}(q)]\}$$
$$W_T(q) = \frac{3}{2}\frac{\hbar^2 q^2}{Mk_B}\frac{T^2}{\theta_D^3}\int_0^{\theta_D/T}\left[\frac{1}{2}+(e^z-1)\right]zdz \qquad (3.10)$$

where $W_T(q)$ is the Debye-Waller factor at temperature T, θ_D is the Debye temperature, M is the atomic mass, k_B is Boltzmann's constant, T_1 is the temperature at which the static structure factor $S_{T_1}(q)$ was measured, and T_2 is the temperature at which the structure factor $S_{T_2}(q)$ is calculated. The Debye temperatures were estimated from a weighted average of the Debye temperatures of the alloy elements [65], giving 277.6, 282.4, 266.35, and 271.976 K for $Cu_{46}Zr_{54}$, $Cu_{54}Zr_{46}$, $Cu_{55}Hf_{45}$, and $Cu_{60.8}Hf_{39.2}$, respectively. Using Eq. 3.10 $S(q)$ was estimated near the glass transition temperature for each sample, using the $S(q)$ value measured at room temperature. Using Eq. 3.2 the corresponding $g(r)$ values were also estimated at T_g by taking a Fourier transform of the extrapolated $S(q)$.

Figure 3.4 shows the changes in the peak heights as a function of temperature for each composition. The data are normalized to the highest temperature. Each composition shows strikingly similar behavior. The Cu-(Zr/Hf) peak in the first coordination shell grows linearly with decreasing temperature in the liquid, and when it is projected to T_g a mismatch is observed between the extrapolation from the liquid and the Debye extrapolation in the glass. On the other hand, the (Zr/Hf)-(Zr/Hf) extrapolated liquid peak values show almost perfect agreement with that extrapolated from the room temperature glass, with no mismatch observed.

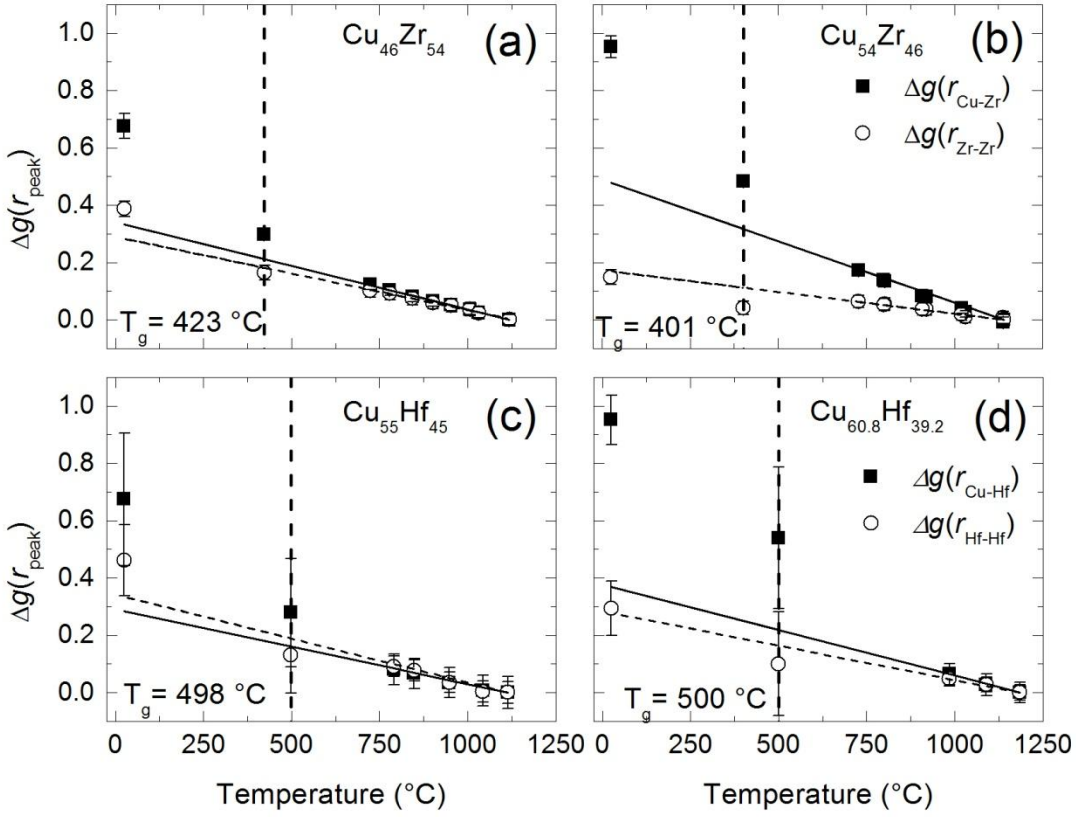

Figure 3.4: Temperature-dependent changes in $g(r)$ at the r positions of the PPCF peaks. The solid black squares are the changes at the Cu-Zr (r = 2.75 Å) and Cu-Hf (r = 2.69 Å) distances, while the open circles are the changes at the Zr-Zr and Hf-Hf (r = 3.15 Å) distances. The solid and dashed lines indicate the respective linear extrapolations of the measured changes in the liquids at the Cu-(Zr/Hf) and (Zr/Hf)-(Zr/Hf) distances. Vertical dashed lines indicate the glass transition temperatures as measured for (a) $Cu_{46}Zr_{54}$ [23], (b) $Cu_{54}Zr_{46}$ [61], and (c) $Cu_{55}Hf_{45}$ [22], and estimated for (d) $Cu_{60.8}Hf_{39.2}$ as extrapolated from measurements for $Cu_{60}Hf_{40}$ [22].

The trends observed in Figure 3.4 must take into account two effects to accurately reflect the growth of the PPCFs. First, the peaks observed in Figure 3.3 are weighted by their respective FZ factors. Even if the ordering at the two distances were to grow at the same rate with temperature, their differing scattering factors would cause one to appear to grow faster. Secondly, note that the changes observed in Figure 3.3 are (from Eq. 3.9)

$$\frac{\Delta g(r)}{\Delta T} = \sum_i \sum_j w_{ij} \frac{\Delta g_{ij}(r)}{\Delta T} \tag{3.11}$$

showing that the rate of increase in the magnitude of $g(r)$ at a particular position is determined by the weighted growth rates of the individual PPCFs. If the increase at a value of r were completely dominated by growth in one particular PPCF the rate of increase in that PPCF peak could be extracted by scaling the increase in $g(r)$ at the positions of the Cu-(Zr/Hf) and (Zr/Hf)-(Zr/Hf) atomic lengths by their respective FZ factors. Simply scaling the rate of increase by the respective FZ factors, however, does not account for contributions from changes in the non-dominant PPCFs. As an illustration, Figure 3.5 shows the PPCFs for $Cu_{46}Zr_{54}$ determined from MD simulations of the liquid and glass. In this case each PPCF is weighted according to its FZ factor. The peaks are well separated and sharpen with decreasing temperature. Most also move in position, although the Zr-Zr distance remains essentially unchanged upon cooling from the high temperature liquid to the glass. The peak movements and alterations in shape change their relative contribution to the total $g(r)$. At 25 °C the tail at high r for the Cu-Zr PPCF accounts for nearly 25% of the intensity in the total pair correlation function at the Zr-Zr peak position, while at 1123 °C it accounts for more than 40%.

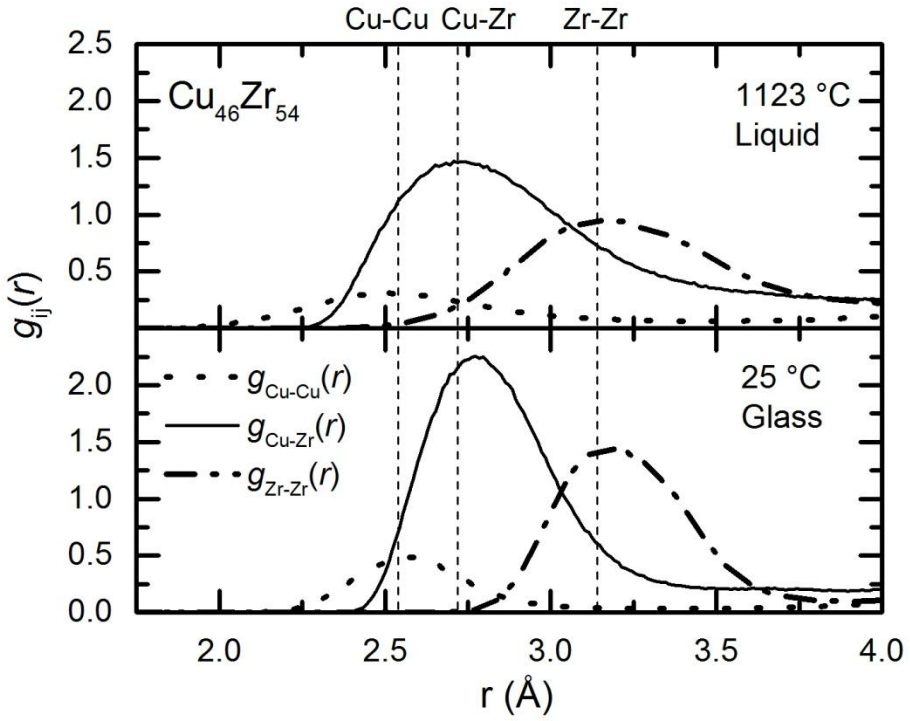

Figure 3.5: PPCF values calculated from MD simulations of $Cu_{46}Zr_{54}$ in the liquid (1123 °C) and glass (25 °C) states, weighted according to the FZ X-ray scattering factors. Although the peak positions are well separated the peaks move slightly relative to one another and the peak widths sharpen as the temperature is decreased.

In the absence of experimental data for the PPCFs the MD data were used to isolate the peak growth rates for a particular PPCF from the contributions of the other PPCFs. The MD results for liquid $Cu_{46}Zr_{54}$ show that at each of the positions corresponding to the first coordination shell peaks for the Cu-Zr and Zr-Zr PPCFs the proportional contributions from each of the three PPCFs, Cu-Cu, Cu-Zr, and Zr-Zr, scale linearly with temperature. The temperature dependence of the percentage contributions of the PPCF of interest to the total $g(r)$ at the PPCF's peak position is used in combination with the experimental data to estimate the experimental PPCF peak height. Because of the similarity between the Cu-Zr and the Cu-Hf alloys, and because it has been demonstrated that the PPCFs change very slowly as a function of

composition [63] (if at all), the same $Cu_{46}Zr_{54}$ MD PPCFs were used for the estimates in both alloys.

Figure 3.6 shows the corrected PPCF peak height trends with temperature, accounting for both the FZ weighting factors and the effect of overlapping PPCFs. Solid lines and dashed lines represent the respective linear extrapolations of the changes in the measured liquid Cu-(Zr/Hf) and (Zr/Hf)-(Zr/Hf) pair distances. In all cases the Cu-(Zr/Hf) PPCF peaks grow more rapidly than do the (Zr/Hf)-(Zr/Hf) peaks.

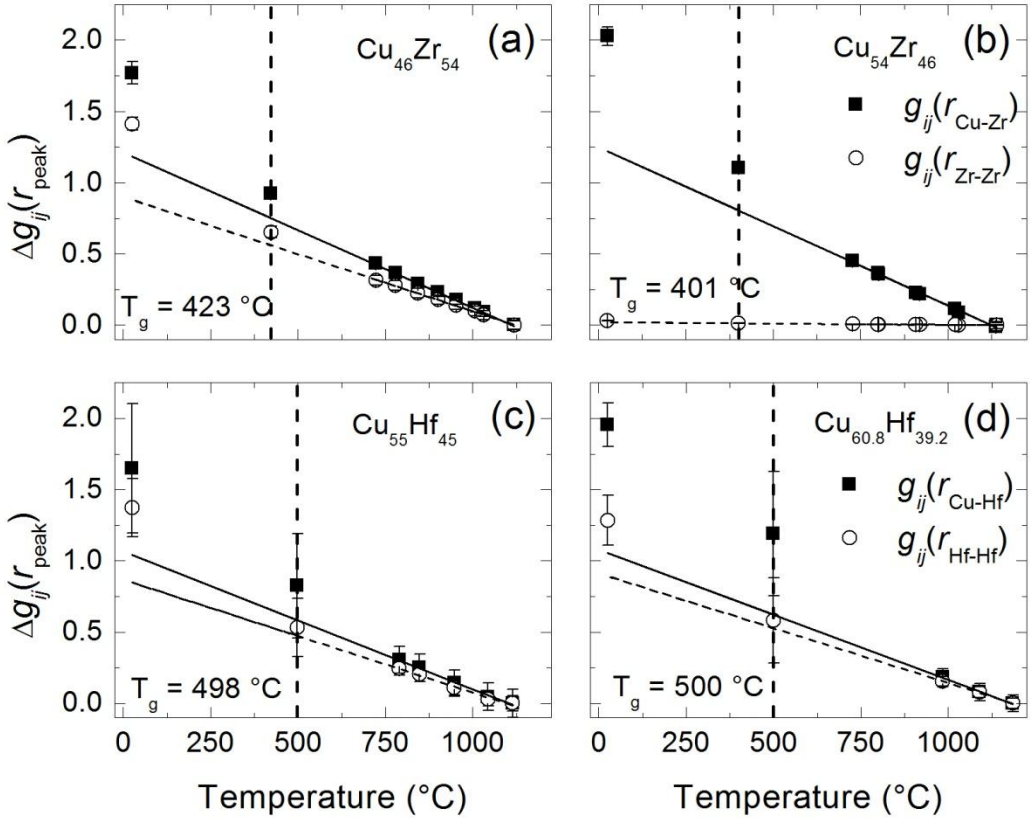

Figure 3.6: Pair correlation function peaks heights with respect to temperature accounting for both the FZ weighting factors and the effect of overlapping PPCF values for (a) $Cu_{46}Zr_{54}$, (b) $Cu_{54}Zr_{46}$, (c) $Cu_{55}Hf_{45}$, and (d) $Cu_{60.8}Hf_{39.2}$. Solid lines and dashed lines represent the respective linear extrapolations of the changes in the measured liquid Cu-(Zr/Hf) and (Zr/Hf)-(Zr/Hf) pair distances.

For all compositions the trend of the PPCF peak heights for (Zr/Hf)-(Zr/Hf) do not show evidence of accelerated ordering in the supercooled liquid near the glass transition temperature. However, the Cu-(Zr/Hf) PPCF peak trends do show evidence for this. Recent MD simulations identified two distinct types of liquid structures in Cu-Zr liquids, one region that was rich in Cu and another rich in Zr; it is likely that similar regions occur in Cu-Hf liquids. The different behavior observed in the (Zr/Hf)-(Zr/Hf) and Cu-(Zr/Hf) PPCF peak trends suggest that the rates of ordering in these two regions are different. It is also interesting to compare the rates of change of each PPCF in the liquids and glasses. The liquid structure evolves very slowly, as shown by the small values of the slopes of the peak heights as a function of temperature, shown in Figure 3.6(a) and (b). For each PPCF, regardless of chemical specificity, the evolution of the peak heights in the glasses, estimated from the Debye extrapolation, changes much more rapidly with temperature. The small rate of change of the liquid structure with temperature, as well as the observed discontinuities in the Cu-(Zr/Hf) PPCFs, are qualitatively different from the behavior observed for the supercooled liquids for the high GFA Zr- and Pd-based BMG forming compositions [5, 66, 67], where no sudden change in the structure is observed near T_g. If, in fact, structural evolution of the liquid with respect to temperature is an indicator of fragility, as suggested by Mauro et al. [46] and schematically illustrated in Figure 3.7, then the acceleration of peak height growth near the glass transition temperature indicates that these are fragile liquids.

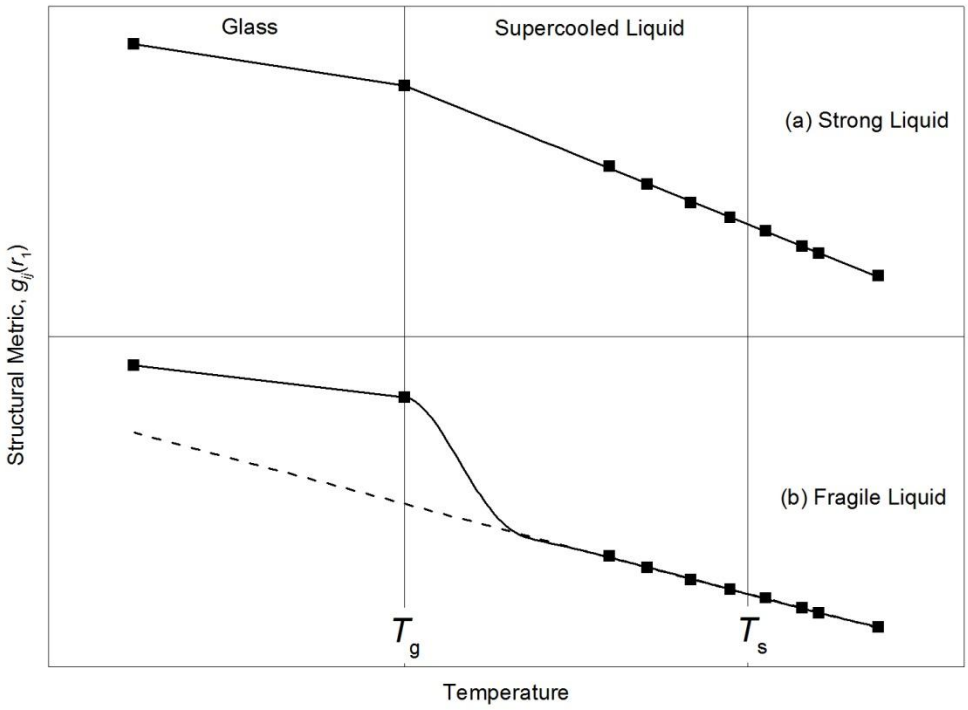

Figure 3.7: Schematic illustration of the different behaviors of the liquid structural metrics for (a) strong and (b) fragile liquids. The dashed line indicates linear extrapolation of the evolving liquid data down to room temperature. Because the glass structure is approximately constant up to the glass transition temperature the evolution of its structural metric (peak height) with temperature is dominated by effects due to atomic vibrations, as described by Debye theory [47]. Thus the underestimate at T_g of the linear extrapolation for fragile liquid (b) points to a necessary acceleration in the structural ordering near T_g.

The data in Figure 3.6 provide a measure of the evolution of the nearest neighbor order. Information on ordering at larger length scales is obtained from the temperature dependence of the height of the first peak in the structure factor $S(q_1)$, which contains information from all of the coordination shells in the total pair correlation function. This is shown in Figure 3.8 for the liquid and the glass. A linear fit to the liquid data, extrapolated to the glass transition temperature, is shown, as are the 1 σ confidence intervals for the fit (dashed lines). As for the pair correlation functions, a discontinuity between the extrapolated liquid data to T_g and that calculated from room temperature glass using a Debye extrapolation is observed for all compositions except for $Cu_{55}Hf_{45}$ (Fig. 3.8(c)). It is important to note that the diffraction

measurements were made on as-quenched amorphous ribbons containing a large population of high energy local atomic configurations that depress $S(q_1)$. When these glasses are annealed near T_g structural relaxation causes the distribution of local structures to decrease and increases the height of $S(q_1)$ by several percent. Zr- and Pd-based BMGs used in previous studies, which showed no evidence of an acceleration of ordering near the glass transition temperature, were pre-annealed to relax the structure. If the glasses studied here were annealed then discontinuities shown in Figure 3.8 would increase, and $S(q_1)$ for $Cu_{55}Hf_{45}$ would show a behavior similar to the other Cu-Zr and Cu-Hf alloys.

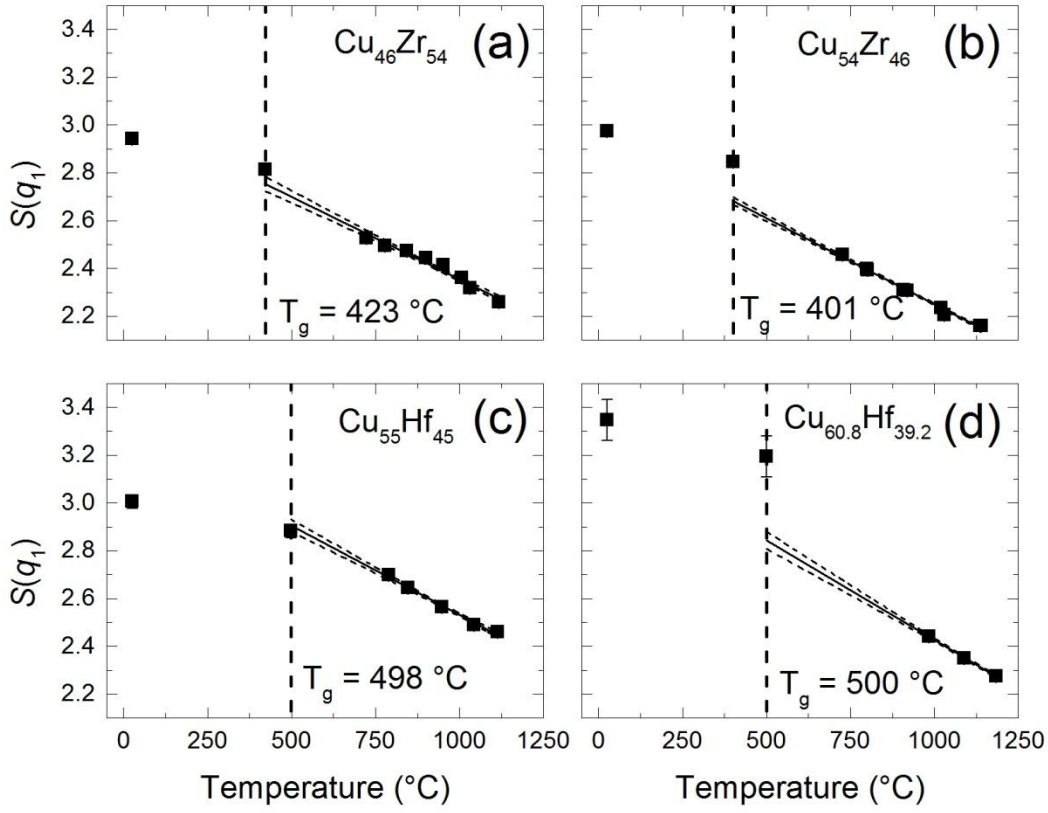

Figure 3.8: Height of the first peak in the static structure factor $S(q_1)$ as a function of temperature for (a) $Cu_{46}Zr_{54}$, (b) $Cu_{54}Zr_{46}$, (c) $Cu_{55}Hf_{45}$, and (d) $Cu_{60.8}Hf_{39.2}$. The linear fits to the liquid data and extrapolations to T_g are shown in each plot, as are the 1 σ confidence intervals (dashed lines).

It is interesting to consider the differences in magnitudes of the discontinuities of the extrapolated liquid and glass $S(q_1)$ values for $Cu_{55}Hf_{45}$ and $Cu_{60.8}Hf_{39.2}$. Since these two alloys have very similar compositions and similar glass-forming abilities [22] such differences are surprising. They suggest a difference in the fragility of these two liquids. A similar difference in structural evolution is observed between $Cu_{46}Zr_{54}$ and $Cu_{54}Zr_{46}$ (Fig. 8(a) and (b)) albeit smaller than in the Cu-Hf comparison, again suggesting that the liquids have different fragilities.

3.4 Conclusions

In summary, high energy X-ray diffraction studies of $Cu_{100-x}Zr_x$ (x = 46 and 54) and Cu_xHf_{100-x} (x = 55 and 60.8) liquids were made without a container using the BESL. Complementary X-ray data were obtained from rapidly quenched amorphous ribbons of these liquids using traditional methods. The growth of the asymmetry in the second peak of $S(q)$ suggests icosahedral ordering with decreasing temperature in all liquids and in the glasses. The total pair correlations show that chemical ordering accompanies this topological ordering. All alloys show similar development in the first coordination shell, including distinct peak splitting, linear growth in the correlations in the liquid, and acceleration in ordering near the glass transition. Subtle differences observed in the evolution of the total structure factor with temperature suggest a structural signature of fragility, manifest as an accelerated ordering in the liquid near the glass transition temperature, required to match the extrapolated values for $S(q_1)$ in the liquid with those of the glass. Differences between the extrapolated liquid and glass $S(q_1)$ values for different alloys suggest that the structural data are sensitive to differences in fragility. The complicated behavior of the partial structure factors with temperature and the inability to

strictly deconvolute the contributions from each requires that the partial structure factors are measured, either experimentally or from simulations.

It is possible that the observed chemical ordering in the liquids, i.e. splitting of the first coordination shell, may be universal in binary glass-forming systems, but detection is limited by the inability to resolve the two (or more) distinct features. For the Cu-Zr and Cu-Hf systems studied here the favorable FZ weighting, as well as the well separated Cu-(Zr/Hf) and (Zr/Hf)-(Zr/Hf) lengths, allow these to be resolved. However, measurements of the experimental chemically specific PPCFs are required to confirm the presence of chemical ordering. Simulations in Zr-TM binaries [68] suggest that the observed chemical ordering is a common feature in these alloys, which are characterized by a high heat of mixing between elements. The quantitative differences between the structural evolution in the Cu-(Zr/Hf) systems and these in lower GFA Zr-TM binaries may provide important insights about why BMG formation is possible in the former and not in the later.

3.5 References

[1] N. A. Mauro, A. J. Vogt, M. L. Johnson, J. C. Bendert, R. Soklaski, L. Yang and K. F. Kelton, Acta Materialia **61** (19), 7411 (2013).

[2] A. K. Gangopadhyay, G. W. Lee, K. F. Kelton, J. R. Rogers, A. I. Goldman, D. S. Robinson, T. J. Rathz and R. W. Hyers, Review of Scientific Instruments **76** (7) (2005).

[3] N. A. Mauro and K. F. Kelton, Review of Scientific Instruments **82** (3) (2011).

[4] K. F. Kelton, G. W. Lee, A. K. Gangopadhyay, R. W. Hyers, T. J. Rathz, J. R. Rogers, M. B. Robinson and D. S. Robinson, Physical Review Letters **90** (19), 195504 (2003).

[5] Y. T. Shen, T. H. Kim, A. K. Gangopadhyay and K. F. Kelton, Physical Review Letters **102** (5), 057801 (2009).

[6] V. Wessels, A. K. Gangopadhyay, K. K. Sahu, R. W. Hyers, S. M. Canepari, J. R. Rogers, M. J. Kramer, A. I. Goldman, D. Robinson, J. W. Lee, J. R. Morris and K. F. Kelton, Physical Review B **83** (9), 094116 (2011).

[7] T. Zhang, A. Inoue and T. Masumoto, Materials Transactions **32** (11), 1005 (1991).

[8] A. Peker and W. L. Johnson, Applied Physics Letters **63** (17), 2342 (1993).

[9] E. S. Park, J. H. Na and D. H. Kim, Applied Physics Letters **91** (3) (2007).

[10] H. Tanaka, Journal of Non-Crystalline Solids **351** (8–9), 678 (2005).

[11] A. Meyer, R. Busch and H. Schober, Physical Review Letters **83** (24), 5027 (1999).
[12] P. J. Desré, E. Cini and B. Vinet, Journal of Non-Crystalline Solids **288** (1–3), 210 (2001).
[13] P. H. Gaskell, Nature **276** (5687), 484 (1978).
[14] D. B. Miracle, Nature Materials **3** (10), 697 (2004).
[15] H. W. Sheng, W. K. Luo, F. M. Alamgir, J. M. Bai and E. Ma, Nature **439** (7075), 419 (2006).
[16] J. Hafner, Physical Review B **21** (2), 406 (1980).
[17] G. S. Cargill III and F. Spaepen, Journal of Non-Crystalline Solids **43** (1), 91 (1981).
[18] C. N. J. Wagner, Journal of Non-Crystalline Solids **76** (1), 29 (1985).
[19] D. Wang, Y. Li, B. B. Sun, M. L. Sui, K. Lu and E. Ma, Applied Physics Letters **84** (20), 4029 (2004).
[20] D. Xu, G. Duan and W. L. Johnson, Physical Review Letters **92** (24), 245504 (2004).
[21] Y. Li, Q. Guo, J. A. Kalb and C. V. Thompson, Science **322** (5909), 1816 (2008).
[22] A. Inoue and W. Zhang, Materials Transactions **45** (2), 584 (2004).
[23] G. Duan, D. Xu, Q. Zhang, G. Zhang, T. Cagin, W. L. Johnson and W. A. Goddard, Physical Review B **71** (22), 224208 (2005).
[24] G. Duan, D. Xu and W. L. Johnson, Metallurgical and Materials Transactions A **36 A** (2), 455 (2005).
[25] L. Xia, D. Ding, S. T. Shan and Y. D. Dong, Journal of Physics: Condensed Matter **18** (15), 3543 (2006).
[26] P. Jia and J. Xu, Journal of Materials Research **24** (1), 96 (2009).
[27] Y. Wang, Q. Wang, J. Zhao and C. Dong, Scripta Materialia **63** (2), 178 (2010).
[28] D. Xu, B. Lohwongwatana, G. Duan, W. L. Johnson and C. Garland, Acta Materialia **52** (9), 2621 (2004).
[29] L. Shadowspeaker and R. Busch, Applied Physics Letters **85** (13), 2508 (2004).
[30] I. Gallino, J. Schroers and R. Busch, Journal of Applied Physics **108** (6) (2010).
[31] J. C. Bendert and K. F. Kelton, Journal of Non-Crystalline Solids **376** (0), 205 (2013).
[32] N. A. Mauro, A. J. Vogt, M. L. Johnson, J. C. Bendert and K. F. Kelton, Applied Physics Letters **103** (2) (2013).
[33] Y. Q. Cheng, H. W. Sheng and E. Ma, Physical Review B **78** (1), 014207 (2008).
[34] M. I. Mendelev, M. J. Kramer, R. T. Ott, D. J. Sordelet, M. F. Besser, A. Kreyssig, A. I. Goldman, V. Wessels, K. K. Sahu, K. F. Kelton, R. W. Hyers, S. Canepari and J. R. Rogers, Philosophical Magazine **90** (29), 3795 (2010).
[35] G. A. Almyras, C. E. Lekka, N. Mattern and G. A. Evangelakis, Scripta Materialia **62** (1), 33 (2010).
[36] N. Jakse and A. Pasturel, Physical Review B **78** (21), 214204 (2008).
[37] H. L. Peng, M. Z. Li, W. H. Wang, C.-Z. Wang and K. M. Ho, Applied Physics Letters **96** (2) (2010).
[38] Y. L. Sun and J. Shen, Journal of Non-Crystalline Solids **355** (31–33), 1557 (2009).
[39] L. Yang, J. H. Xia, Q. Wang, C. Dong, L. Y. Chen, X. Ou, J. F. Liu, J. Z. Jiang, K. Klementiev, K. Saksl, H. Franz, J. R. Schneider and L. Gerward, Applied Physics Letters **88** (24) (2006).
[40] C. E. Lekka, A. Ibenskas, A. R. Yavari and G. A. Evangelakis, Applied Physics Letters **91** (21) (2007).

[41] S.-C. Lee, C.-M. Lee, J.-C. Lee, H.-J. Kim, Y. Shibutani, E. Fleury and M. L. Falk, Applied Physics Letters **92** (15) (2008).
[42] K.-W. Park, J.-i. Jang, M. Wakeda, Y. Shibutani and J.-C. Lee, Scripta Materialia **57** (9), 805 (2007).
[43] X. D. Wang, S. Yin, Q. P. Cao, J. Z. Jiang, H. Franz and Z. H. Jin, Applied Physics Letters **92** (1) (2008).
[44] R. Soklaski, Z. Nussinov, Z. Markow, K. F. Kelton and L. Yang, Physical Review B **87** (18), 184203 (2013).
[45] M. Li, C. Z. Wang, S. G. Hao, M. J. Kramer and K. M. Ho, Physical Review B **80** (18), 184201 (2009).
[46] N. A. Mauro, M. L. Johnson, J. C. Bendert and K. F. Kelton, Journal of Non-Crystalline Solids **362** (0), 237 (2013).
[47] S. Sinha, P. L. Srivastava and R. N. Singh, Journal of Physics: Condensed Matter **1** (9), 1695 (1989).
[48] C. A. Angell, Journal of Physics and Chemistry of Solids **49** (8), 863 (1988).
[49] D. Chipman, L. Jennings and B. Giessen, Bulletin of the American Physical Society **23** (3), 467 (1978).
[50] G. H. Bezerra, L. Q. Amaral, A. F. Craievich and D. Raoux, Journal of Non-Crystalline Solids **126** (3), 239 (1990).
[51] M. A. Khan, C. Allemand and T. W. Eagar, Review of Scientific Instruments **62** (2), 392 (1991).
[52] R. C. Bradshaw, D. P. Schmidt, J. R. Rogers, K. F. Kelton and R. W. Hyers, Review of Scientific Instruments **76** (12) (2005).
[53] S. K. Chung, D. B. Thiessen and W. K. Rhim, Review of Scientific Instruments **67** (9), 3175 (1996).
[54] T. Ishikawa, P.-F. Paradis and S. Yoda, Review of Scientific Instruments **72** (5), 2490 (2001).
[55] N. A. Mauro, V. Wessels, J. C. Bendert, S. Klein, A. K. Gangopadhyay, M. J. Kramer, S. G. Hao, G. E. Rustan, A. Kreyssig, A. I. Goldman and K. F. Kelton, Physical Review B **83** (18), 184109 (2011).
[56] A. P. Hammersley, S. O. Svensson, M. Hanfland, A. N. Fitch and D. Hausermann, High Pressure Research **14** (4-6), 235 (1996).
[57] S. Plimpton, Journal of Computational Physics **117** (1), 1 (1995).
[58] M. I. Mendelev, M. J. Kramer, R. T. Ott, D. J. Sordelet, D. Yagodin and P. Popel, Philosophical Magazine **89** (11), 967 (2009).
[59] S. Sachdev and D. R. Nelson, Physical Review Letters **53** (20), 1947 (1984).
[60] A. Sadoc, Y. Calvayrac, A. Quivy, M. Harmelin and A. M. Flank, Journal of Non-Crystalline Solids **65** (1), 109 (1984).
[61] D. Ma, A. D. Stoica, X. L. Wang, Z. P. Lu, M. Xu and M. Kramer, Physical Review B **80** (1), 014202 (2009).
[62] T. E. Faber and J. M. Ziman, Philosophical Magazine **11** (109), 153 (1965).
[63] N. Mattern, A. Schöps, U. Kühn, J. Acker, O. Khvostikova and J. Eckert, Journal of Non-Crystalline Solids **354** (10–11), 1054 (2008).
[64] N. Mattern, P. Jóvári, I. Kaban, S. Gruner, A. Elsner, V. Kokotin, H. Franz, B. Beuneu and J. Eckert, Journal of Alloys and Compounds **485** (1–2), 163 (2009).

[65] C. Y. Ho, R. W. Powell and P. E. Liley, Journal of Physical and Chemical Reference Data **1** (2), 279 (1972).
[66] N. Mattern, H. Hermann, S. Roth, J. Sakowski, M.-P. Macht, P. Jovari and J. Jiang, Applied Physics Letters **82** (16), 2589 (2003).
[67] N. Mattern, J. Sakowski, U. Kühn, H. Vinzelberg and J. Eckert, Journal of Non-Crystalline Solids **345–346** (0), 758 (2004).
[68] L. Huang, C. Z. Wang, S. G. Hao, M. J. Kramer and K. M. Ho, Physical Review B **81** (1), 014108 (2010).

Chapter 4

Experimental Measurements of the Structural Evolution in Liquid $Pd_{82}Si_{18}$

This chapter includes both DSC measurements of the melt temperature for this alloy provided by C. Pueblo and liquid density and expansivity measurements provided by M. E. Blodgett (Washington University in St. Louis, St. Louis, MO). Result from MD simulations, for use in constrained reverse Monte Carlo simulations, presented in this chapter were provided by J. Ding and E. Ma (Johns Hopkins University, Baltimore, MD). Results of their MD work are published elsewhere [1]. Voronoi analysis of the constrained reverse Monte Carlo (CMRC)-produced configurations was performed using software developed by Z. Markow (Washington University in St. Louis, St. Louis, MO).

4.1 Introduction

The ability to form bulk metallic glasses (BMGs) from the supercooled liquid is very much related to the behavior of the liquid as it evolves from the equilibrium liquid to the metastable solid state. As already mentioned, the glass-forming ability (GFA) of a liquid is correlated with its dynamical and thermophysical properties, such as fragility [2-4], density [5],

expansivity [6], kinetic strength [7], and specific heat (C_p) evolution with temperature [8]. These liquid thermodynamic and kinetic properties are inherently related to the structure of the liquid [9], and structural ordering in the liquid can be important for glass formation [10-14]. Because of the difficulty in accessing the supercooled liquid and measuring its structure, many recent attempts to relate structural ordering in the supercooled liquid with its thermophysical properties, and ultimately its GFA, rely on molecular dynamics (MD) simulation data [1, 15-18]. Simulation data ultimately requires both verification and refinement from experimental measurements. Recent developments in the beamline electrostatic levitation (BESL) technique provide a way to do this by making *in situ* experimental measurements of the bulk supercooled liquid structure of a variety of metallic alloys [19].

The $Pd_{82}Si_{18}$ alloy is a very well-studied binary metallic glass-forming system, but its bulk-formability [20, 21] and unique structural and liquid property characteristics have only recently been probed. Most BMGs are formed from multicomponent alloys liquids with complex structures [22], making quantitative structural studies difficult. However, simpler binary alloy BMG-forming liquids have been discovered [5, 18, 23-30], making them ideal for studies of topological and chemical ordering. The metal-metalloid glasses in particular exhibit unique structural and dynamical properties that are distinct from transition metal (TM) based metal-metal alloys [10, 14]. Further, the Pd-Si phase diagram contains a deep eutectic near the $Pd_{82}Si_{18}$ composition [31], indicating a stability of the equilibrium liquid down to low temperatures. This thermodynamic stability of the equilibrium liquid aids in the glass formability by providing a smaller supercooled liquid region [32, 33]. The structure of the equilibrium (and supercooled) liquid must play an important role in the formation of the deep eutectic and the relative stability of the liquid compared to the competing crystalline phases [34,

35]. However, Pd-Si exhibits BMG formability over a very limited composition range in the region of the eutectic [33] in contrast with the TM binary systems, like Cu-Zr, which show GFA over a wide composition range [5, 18, 24, 25].

Recent MD studies by Ding et al. [1] of the $Pd_{82}Si_{18}$ binary alloy contrast the temperature evolution of C_p with that of the widely-studied $Cu_{64}Zr_{36}$ binary Zr-based metal-metal BMG alloy [16, 17, 24, 36, 37]. In their study, upon entering the supercooled liquid regime a weaker temperature dependence of the C_p for $Pd_{82}Si_{18}$ is correlated with a more gradual development of the topological and chemical short-range order (CSRO) of the system. MD simulations show that in metal-metalloid systems, including Pd-Si, the local order tends to consist of metalloid-centered clusters of 8-10 coordinated Kasper polytetrahedra [14]. According to Ding et al., the slower structural change and C_p evolution is responsible for the weaker temperature dependence of the dynamics, ultimately resulting in a stronger, less fragile behavior of the liquid. This is in contrast to the rapid acceleration of CSRO, icosahedral short-range order (ISRO), and excess specific heat in the Cu-Zr binary alloy, seen both experimentally and in MD simulations [38, 39]. The continuous increase in the number of 12-coordinated iscosahedral clusters with a rapid acceleration of ISRO in the Cu-Zr binary system, observed in several MD studies [16-18, 40], is believed to be important to its GFA [17]. In general, results from MD simulations connect the evolution of the structure in the liquid with the kinetic behavior of the liquid, but using structural change as a measure of the differences in dynamical behavior between systems has only recently been investigated in experimental studies via high-energy X-ray diffraction (XRD) [39, 41, 42].

Here the results for *in situ* high-energy XRD studies of the $Pd_{82}Si_{18}$ liquid alloy in a containerless environment are presented. The studies were performed using the BESL technique, correlating temperature and density measurements with structural information for the bulk liquid

in both the equilibrium and supercooled liquid states, obtained from the XRD data. We report the evolution of the structural metrics from both the static structure factor, $S(q)$, and the pair distribution function, PDF or $g(r)$, as well as discuss the measures from the aspect of the weighted elemental form factors from XRD. Further structural analysis resulting from Reverse Monte Carlo (RMC) simulations, constrained by the results of MD simulations, of the experimental data are also be presented.

4.2 Experimental Procedure

Samples prepared for study in the WU-BESL were first fluxed in B_2O_3 to improve processibility and supercooling [43]. For temperature measurement in the WU-BESL, emissivity calibration for the pyrometers was made by matching the melt plateau on heating of the temperature-time curve in the ESL with measurements of the melt temperature using a Labsys Setaram DTA/DSC [44]. Liquid density and expansivity data were obtained in the WU-BESL prior to XRD data acquisition, and pixel dimensions for the density video were calibrated before and after the sample measurement using a tungsten carbide standard (radius $r = 0.46875 \pm 0.00015$ in.). Diffraction studies were carried out during the BESL 2013 run at Station 6-ID-D at the Advanced Photon Source, Argonne National Laboratory. Data for the liquid sample were obtained during 10-20 s isothermal holds as well as during radiative free cool cycles. Crystallization from the metastable liquid limited the lowest temperature of the X-ray diffraction studies to about 700 °C. No mass loss due to evaporation of the molten sample was found. Additional details for sample preparation, thermophysical property measurement, WU-BESL

design and operation, and XRD experiments during the BESL 2013 run can be found in Chapter 2.

The total structure factor was obtained by,

$$S(q) = \frac{I(q) - \sum_{i=1}^{n} c_i [f_i(q)]^2}{[\sum_{i=1}^{n} c_i f_i(q)]^2} - 1 \quad (4.1)$$

where $I(q)$ is the measured diffraction intensity, c_i is the atomic fraction and $f_i(q)$ is the q-dependent atomic form factor of each element. The sums were made over both Pd and Si, and a statistically homogeneous atomic distribution was assumed. The PDF was then obtained by

$$g(r) - 1 = \frac{1}{4\pi\rho}\frac{2}{\pi}\int (S(q) - 1)\frac{\sin(qr)}{qr} q^2 dq \quad (4.2)$$

Where ρ is the average density and q is integrated over the entire data range with q from 0 to q_{min} extrapolated to 0. Positions and magnitudes of the various peaks in both $S(q)$ and $g(r)$ were refined by fitting a cubic spline to the peak. Uncertainties were estimated considering perturbations from independent sources of error, including statistical uncertainties estimated following the method described by Hammersley [45], uncertainties in the density measurement (for PDF peaks), and confidence intervals of fitting parameters such as normalization and fluorescence. Additional details regarding XRD analysis can be found in Chapter 2.

Atomic configurations were obtained by Reverse Monte Carlo [46-48] simulation fits to the $S(q)$ measurements in order to determine the average atomic structure as a function of temperature. Fits were constrained using partial pair correlation functions (PPCFs) obtained from MD simulations using embedded atom method (EAM) interatomic potentials fitted to the Pd-Si system [1]. For the RMC simulations, configurations of 10000 atoms (Pd 8200, Si1800) were prepared in a cube with dimensions determined from the experimental density (e.g. L = 52.6286 Å at 805 °C). In order to accelerate convergence to the PPCF constraints, minimum distances were set to 2.2, 2.0, and 2.75 Å for the Pd-Pd, Pd-Si, and Si-Si partial pairs, respectively. For each temperature, five sets of simulations, each with a different random starting configuration, were performed in order to determine statistical errors related to the simulation's convergence behavior. Local atomic configurations generated from the CRMC simulations were analyzed in terms of their Voronoi Polytetrahedral (VI) distributions. A Voronoi tessellation [49-51] of the atomic configurations was performed using an in-house program written in Python [17]. Of the polyhedra generated from the analysis, only distributions of polytetrahedral structures related to Frank-Kasper structures, or Z-clusters, and their distortions [52-54] common to amorphous metallic structures [55] were analyzed. Additional details regarding RMC analysis can be found in Chapter 2.

4.3 Results and Discussion

X-ray diffraction data were obtained at 8 different temperatures (719, 744, 773, 805, 843, 887, 942, and 975 °C) both above and below the solidus temperature (T_S = 808 °C , as measured in-house and consistent with previously published data [31]). The static structure factors, shown

in Figure 4.1, show clear oscillations about unity out to 15 $Å^{-1}$ indicating the high quality of the experimental data. As the temperature decreases, the first peak increases in height, decreases in width, and shifts toward high-*q*, all consistent with structural ordering and an increasing density of the liquid. The first peak height (Fig. 4.1(b)) increases linearly with decreasing temperature from high temperature into the supercooled liquid regime. The second peak (Fig. 4.1(c)) features a developing shoulder, often correlated with increasing ISRO or icosahedral-like order [56, 57], with the lower-*q* peak increasing with decreasing temperature. It should be noted, however, that ISRO is not typically associated with the structure of metal-metalloid systems. The behavior of the pair correlation function, $g(r)$, in Figure 4.1(d) is discussed later in this chapter.

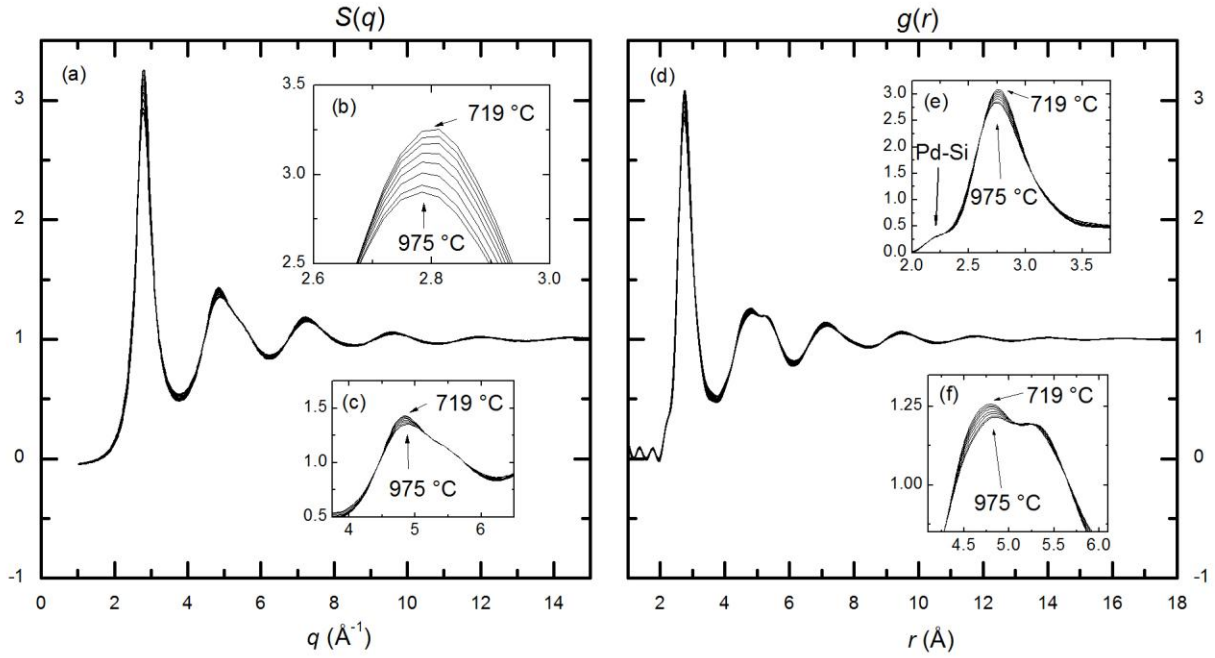

Figure 4.1: (a) Total structure factor and (d) total PDF for $Pd_{82}Si_{18}$ at temperatures both above and below T_S, the solidus temperature. (b) The first peak height, $S(q_1)$, of the total structure factor increases and shifts to higher q with decreasing temperature, while the second peak (c) exhibits a developing shoulder. The low-q peak height of the second peak, $S(q_2)$ increases with decreasing temperature. (e) The first peak, $g(r_1)$, of the total PDF increases with decreasing temperature, while the position shifts to higher r. (f) The second coordination shell in the PDF exhibits a split peak, with the lower-r sub-peak increasing with decreasing temperature.

Figure 4.2 shows the peak height growth as the sample temperature decreases and enters the supercooled liquid regime. The height of the first peak, $S(q_1)$, (Fig. 4.2(a)) increases linearly with decreasing temperature, showing no apparent inflection or slope change in the supercooled liquid regime. This suggests that if there is any rapid structural ordering in the supercooled liquid, it must take place between ~700 °C and the glass transition temperature, T_g = 350 °C [58]. The rate of growth in the peak ($dS(q_1)/dT$ = -14.10 ± 0.25 x 10^{-4} K^{-1}) is approximately double that of the $Cu_{50}Zr_{50}$ liquid [42]. A higher rate of structural ordering (i.e. a larger growth rate for $S(q_1)$) near the melt temperature may be a signature of a stronger, i.e. a more Arrhenius-type temperature dependence of the structural ordering, compared to the presumed fragile behavior of

the $Cu_{50}Zr_{50}$ liquid. It is important to note, however, that the growth rate of $S(q_1)$ will be influenced by the growth rates and relative peak positions, q_1, of the individual chemical partial structure factors (PSFs), and that while $S(q_1)$ is representative of the overall structure, certain scattering and chemical effects may influence the perceived signal in the peak height growth. As discussed in Chapter 3 and to be discussed further in Section 4.4, due to X-ray scattering factors, the total $S(q)$ for $Pd_{82}Si_{18}$ is dominated by the contribution from the Pd-Pd PSF, and therefore the growth rate in $S(q_1)$ will most strongly reflect the growth rate of $S_{Pd\text{-}Pd}(q_1)$. On the other hand, for $Cu_{50}Zr_{50}$, separation in q_1 of the first peaks of the PSFs (i.e. the Cu-Zr and Zr-Zr PSFs) will depress to the total $S(q_1)$ height as well as its apparent growth rate. Therefore X-ray scattering factors may influence the perceived relative growth rates. In relation to the $S(q_1)$ growth rate or $Pd_{82}Si_{18}$, Fig. 2(b) shows similar qualitative behavior in the development of the second peak, $S(q_2)$, with larger relative error bars due to the smaller absolute values and rate of growth ($dS(q_2)/dT = -3.034 \pm 0.078 \times 10^{-4}\ K^{-1}$)

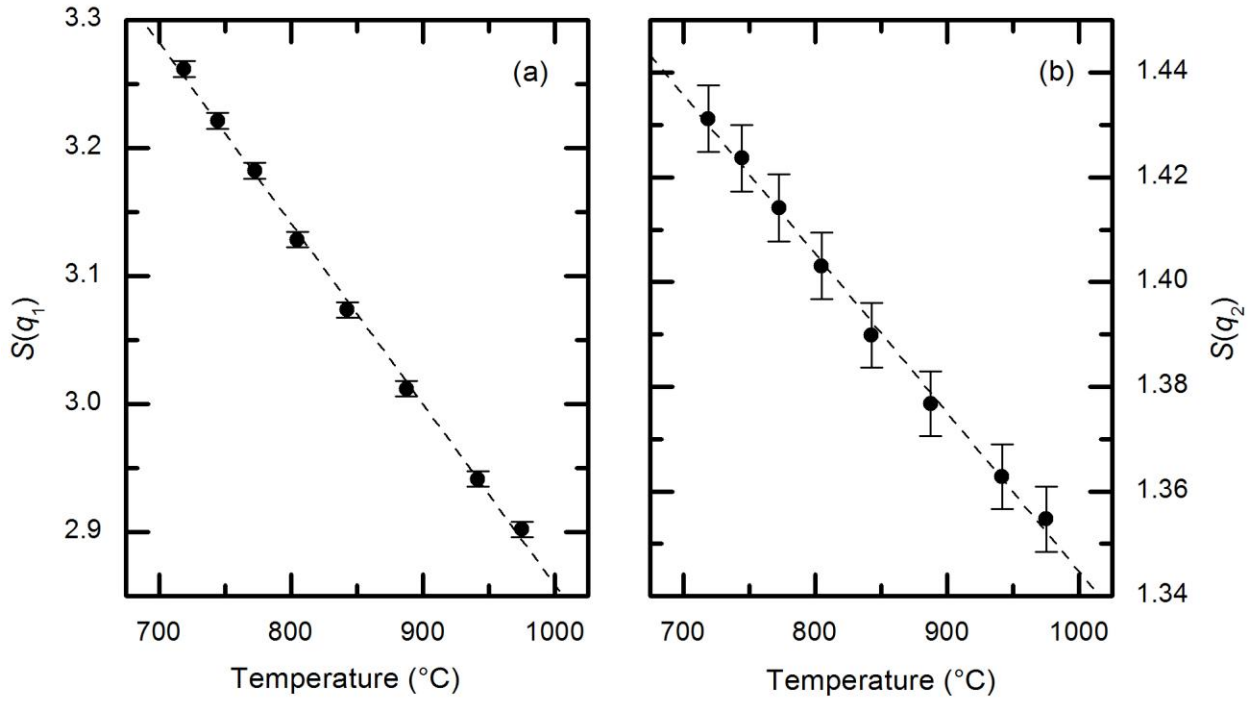

Figure 4.2: (a) The amplitude of the first peak and (b) the second peak height in the total $S(q)$ as a function of temperature. Both heights increase linearly with decreasing temperature from the high temperature liquid to below the melting solidus temperature (T_S = 808 °C).

The total PDFs, $g(r)$, determined from the Fourier transform of the $S(q)$s in Figure 4.1(a), and using the measured density and change with respect to temperature ($\rho(T = 0\ °C) = 10.75 \pm 0.04$ gcm^{-3}, $d\rho/dT = -7.52 \pm 0.04 \times 10^{-4}$ gcm^{-3}K^{-1}) obtained from non-contact experimental measurements, are presented in Figure 4.1(d). Oscillations about unity in the PDF show significant structure in the first few coordination shells, but the oscillations damp out quickly on approaching 20 Å. The amplitude of the first peak in $g(r)$ increases with decreasing temperature, as shown in Figure 1(e), indicating atomic ordering within the nearest neighbor shell. The peak position of the first coordination shell shifts toward lower-r with increasing temperature, indicating an "anomalous contraction with increasing temperature"; this is consistent with previously published results [59, 60]. A small shoulder in the first peak at low-r (~2.25 Å) is due to the contribution from the first peak in the Pd-Si PPCF [61, 62]. Figure 4.1(f) shows a

developing shoulder, or split peak, in the second coordination shell, with the low-r peak increasing in height with decreasing temperature. The splitting of the second peak appears to be a characteristic feature of many non-crystalline metallic alloys, and it is correctly predicted by dense random packing of hard sphere (DRPHS) models [50, 51, 63]. Although the feature has been commonly found in metallic glasses [63], there is some evidence from MD simulation that the feature may be present in liquid PPCFs [18]. In particular, this split peak has been observed in previous studies of metal-metalloid binary metallic glasses [14, 61, 64-66], but its absence in the liquid structure for Pd-Si binary alloys has been noted. This study provides the first evidence of the presence of a split peak of the second coordination shell in the Pd-Si liquid. Figure 4.3 shows the temperature dependence of the heights and positions of the peaks in the PDF. Similar to the $S(q)$ peak growth behavior (Fig. 4.2), both the first peak height, $g(r_1)$, and the first peak position, r_1, (Fig. 4.3(a)) as well as the second peak height, $g(r_2)$, (Fig. 4.3(b)) increase linearly with decreasing temperature well into the supercooled liquid regime. On the other hand, the second peak position, r_2, decreases with decreasing temperature, consistent with previous results [60], indicating the expected thermal contraction in the higher coordination shells. A similar thermal contraction is observed for the third and fourth coordination shells (Fig. 1(b)). The existence of the split second peak in the PDF of the high temperature liquid, similar to that of the glass [61, 66]), suggests that the liquid and glass structures share very similar second nearest neighbor correlations and quite possibly similar local structure as well. Without corresponding measurements of the evolution of the glass structure upon heating, though, a strong conclusion cannot be made about the existence of an accelerated ordering in the deeply supercooled liquid state.

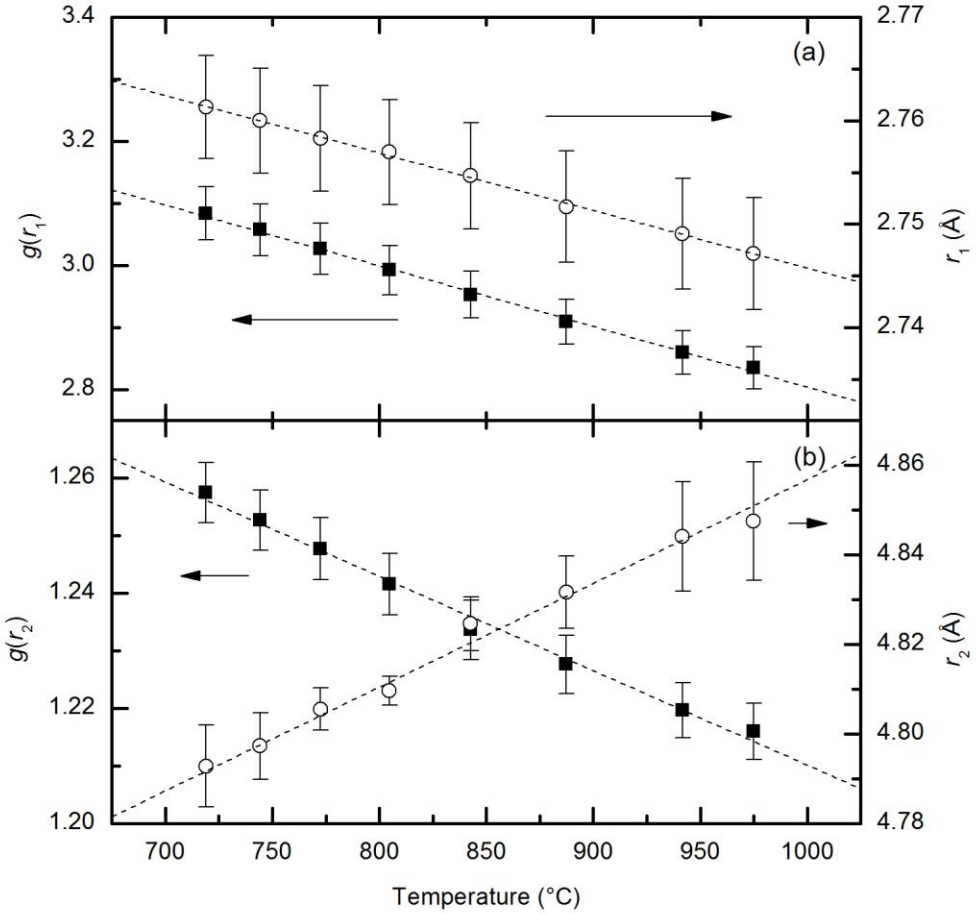

Figure 4.3: Peak heights and positions as a function of temperature for (a) the first coordination shell, $g(r_1)$, and (b) the low-r sub-peak in the second coordination shell, $g(r_2)$. Peak heights are represented by closed squares and correspond to the left vertical axes. Peak positions are represented by open circles and correspond to the right vertical axes.

4.4 Reverse Monte Carlo Analysis and Structure Determination

Three-dimensional atomic structures of the liquids studied were determined by constrained RMC (CRMC) fits to the experimental $S(q)$s in Fig. 1. Because X-ray diffraction measurements capture the many configurations in the dynamically changing liquid structure, RMC approaches are reasonable for obtaining plausible average local atomic structures. Without proper constraints on the RMC simulation, though, non-physical PPCFs can be produced. MD simulations provide information about the local chemical environment, and are expected to be

accurate for simulations of highly mobile and high temperature liquids, since ordering beyond the first few coordination shells is minimal [51]. Constraints from MD PPCFs have been successfully used to study Zr-based binary liquids and glasses [67-69].

The contributions from the individual PPCFs to the total X-ray PDF can be understood through the Faber-Ziman formalism [70, 71]. In this formalism, the total static structure factor is constructed from the sum of the partial structure factors (PSFs), $S_{ij}(q)$, weighted by the individual atomic scattering factors

$$S(q) - 1 = \sum_{ij} w_{ij} \left(S_{ij}(q) - 1\right), \tag{4.3}$$

where the Faber-Ziman weighting factor, $w_{ij}(q)$, is

$$w_{ij}(q) = \frac{c_i c_j f_i(q) f_j(q)}{\langle f(q) \rangle}. \tag{4.4}$$

Since the atomic form factor of the i^{th} element scales like the atomic number, Z_i [72], and since the weighting factors varying slowly with q compared to the $S_{ij}(q)$, a lowest order approximation can be used,

$$w_{ij}(0) = \frac{c_i c_j Z_i Z_j}{\langle Z \rangle}. \tag{4.5}$$

This approximation gives a weighting, $w_{ij}(0)$, of 0.8787, 0.1174, and 0.0039 for the Pd-Pd, Pd-Si, and Si-Si atomic pairs, respectively. From this we see that the X-ray weighted total $S(q)$ for $Pd_{82}Si_{18}$ is dominated by the Pd-Pd PSF. Similarly, the contributions from the Pd-Si and Si-Si PSFs are difficult to determine due to the relative lack of strength in the construction of the total $S(q)$. The MD constraints are, therefore, particularly important for analyzing the X-ray scattering data obtained for this liquid. While unconstrained RMC fits to the total $S(q)$ provide reasonable Pd-Pd PPCFs, non-physical Pd-Si and Si-Si PPCFs are generated from a lack of signal from which to fit the simulation.

Similar to Eq. 4.3, the PPCFs are related to the PSFs by a Fourier transform,

$$g_{ij}(r) - 1 = \frac{1}{4\pi\rho}\frac{2}{\pi}\int \big(S_{ij}(q) - 1\big)\frac{\sin(qr)}{qr}q^2 dq. \tag{4.6}$$

By substituting the result of Eq. 4.3 into Eq. 4.2, using the lowest order approximation in Eq. 4.5, and substituting the result of Eq. 4.6, the total PDF can be approximated from the PPCFs by

$$g(r) \cong \sum_{ij} w_{ij}(0) g_{ij}(r) = \sum_{ij} \frac{c_i c_j Z_i Z_j}{\langle Z \rangle} g_{ij}(r). \tag{4.7}$$

This approximation has been shown to be valid for amorphous metallic alloys [39, 73]. Here again we see that the total PDF is dominated by the Pd-Pd PPCF. This implies that many of the

major features exhibited in the total PDF are most likely the dominant features exhibited by the Pd-Pd PPCF.

For the CRMC fits, the configurations were constrained to only the Pd-Si and Si-Si MD PPCFs. A constraint to the Pd-Pd PPCF was made only up to a portion of the first coordination shell (0 – 2.5 Å) in order to generate physical behavior in the low-*r*, closest approach region. The strongest constraint was made to the fit of the $S(q)$ in order to bias the influence in the simulation towards the experimentally determined data. Figure 4.4 shows a representative RMC fit, comparing the experimentally determined total PDF to the RMC generated PPCFs, weighted by their respective $w_{ij}(0)$s. It can be seen that the contribution from the Si-Si PPCF produces very little contribution to the total PDF, and that the Pd-Pd PPCF closely resembles the total PDF. As mentioned earlier, the largest contribution of the Pd-Si PPCF is to the low-*r* shoulder in the first peak in the PDF, corresponding to the first coordination shell. This is expected given the strong chemical affinity between Si and the noble metal [11, 14, 74, 75]. The RMC generated PPCFs are qualitatively similar to those generated for a $Pd_{82}Si_{18}$ glass [61], suggesting that they can be used to probe more deeply into the structure.

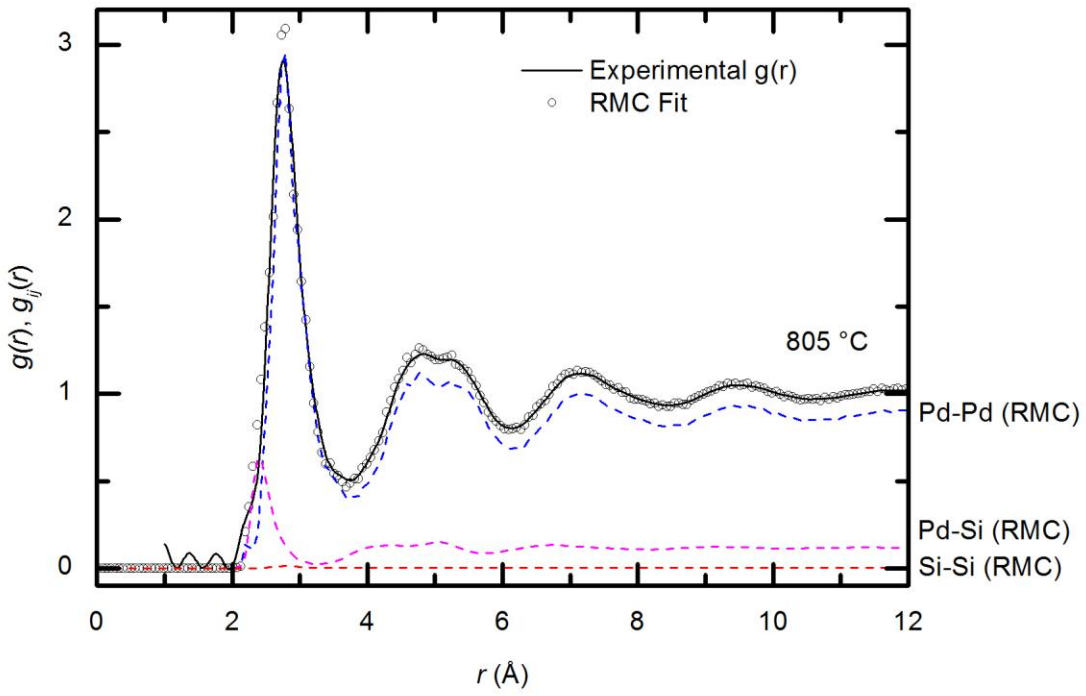

Figure 4.4: A representative RMC simulation result. The dashed lines represent the Pd-Pd (blue), Pd-Si (purple), and Si-Si (red) PPCFs (weighted by their respective $w_{ij}(0)$s) determined from a single CRMC simulation. Open circles represent the total $g(r)$ calculated from the PPCFs using Eq. 4.7. The solid black line represents the experimentally determined total $g(r)$ corresponding the $S(q)$ fit by the simulation.

The Pd-Pd PPCF in Figure 4.4 also shows the split peak in the second coordination shell, indicating that it is this correlation that is the origin of these two length scales. As mentioned previously, the split second peak is a feature predicted from DRPHS model [50], where the length scales can be taken as corresponding to the distance between the apices to the of common base (where the apex refers to the vertex opposite the common base) or coplanar tetrahedra (where the apex refers to the vertex in the same plane as and opposite the edge shared by the coplanar bases) or to the existence three-membered collineations. Figure 4.5 illustrates the various distances for the 2nd nearest neighbor separations scaled to the average Pd-Pd distance as determined from MD simulations. The low-*r* peak in the second coordination shell is located near the second nearest neighbor distance for atoms at the apices of tetrahedral with coplanar bases. The high-*r* peak is located at a value less than the distance for three collinear atoms,

suggesting a slight departure from the ideal collineation angle for 2nd nearest neighbors in the average atomic environment. The presence of interstitial Si atoms in the liquid structure might also result in deviations from these idealized 2nd nearest neighbor distances. Ultimately, the split peak in the second coordination shell suggests there could be large regions of the liquid exhibiting a dense random packing structure, as previously proposed for this composition's amorphous solid structure [61].

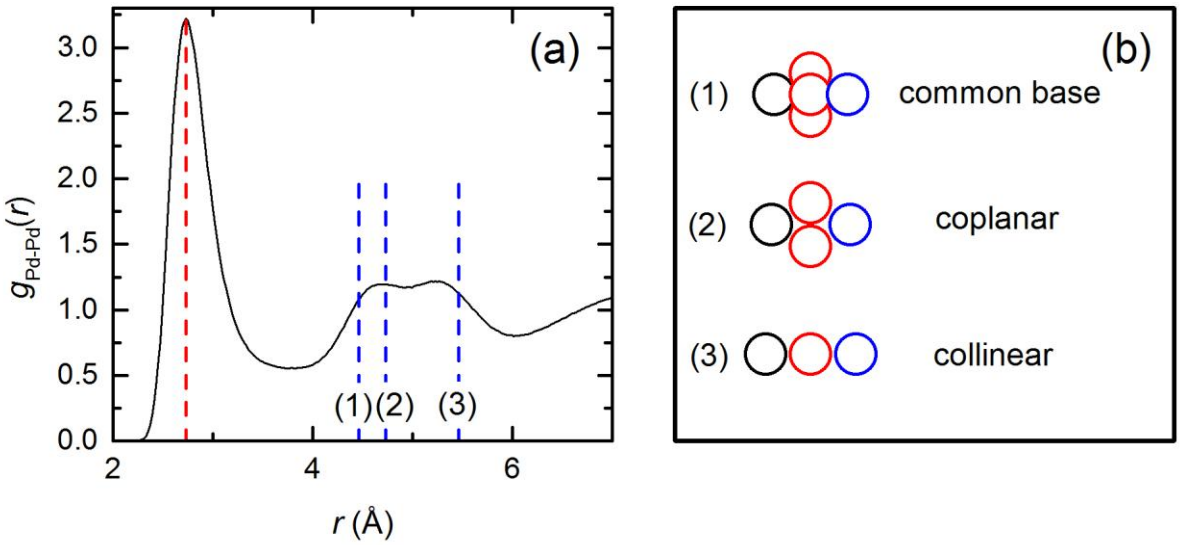

Figure 4.5: (a) Pd-Pd partial PDF (as determined from MD simulations) with the vertical lines indicating the average nearest-neighbor distance (red, low-*r*) and idealized 2nd nearest neighbor distances for (1) tetrahedra sharing a common base, (2) tetrahedra with coplanar bases, and (3) three-membered collineations. (b) Illustrations of the three 2nd nearest neighbor spacings indicated from left-to-right as the central atom (black), the nearest neighbors (red), and the 2nd nearest neighbors (blue).

Representative fits to the experimental $S(q)$ and to the Pd-Si and Si-Si MD PPCFs are shown in Figure 4.6. For the $S(q)$ (Fig 4.6(a)), the RMC simulations fit the experimental data quite well, particularly to the first $S(q)$ peak. The Pd-Si MD PPCF is also fit well by the RMC simulation across the entire fit range of 0 to 12 Å; again the first peak is fit particularly well. While the RMC fit to the Si-Si MD PPCF is good beyond the first peak, there are small

discrepancies in the fit to the split first peak. The largest deviation is in the fit to the low-*r* (closest approach) region, prior to the midpoint of the first coordination shell. Setting the simulation minimum distance for the Si-Si pair to 2.75 Å improves convergence in the 0 – 2.75 Å region, but the unphysical number of atoms located at a distance just above 2.75 Å indicates a difficulty of the RMC to fit easily fit all three sets of data. Increasing or decreasing the minimum distance only redistributes the atoms over the *r* region leading up to the first coordination shell, and increasing the minimum distance decreases the quality of fit to the peaks in the first coordination shell.

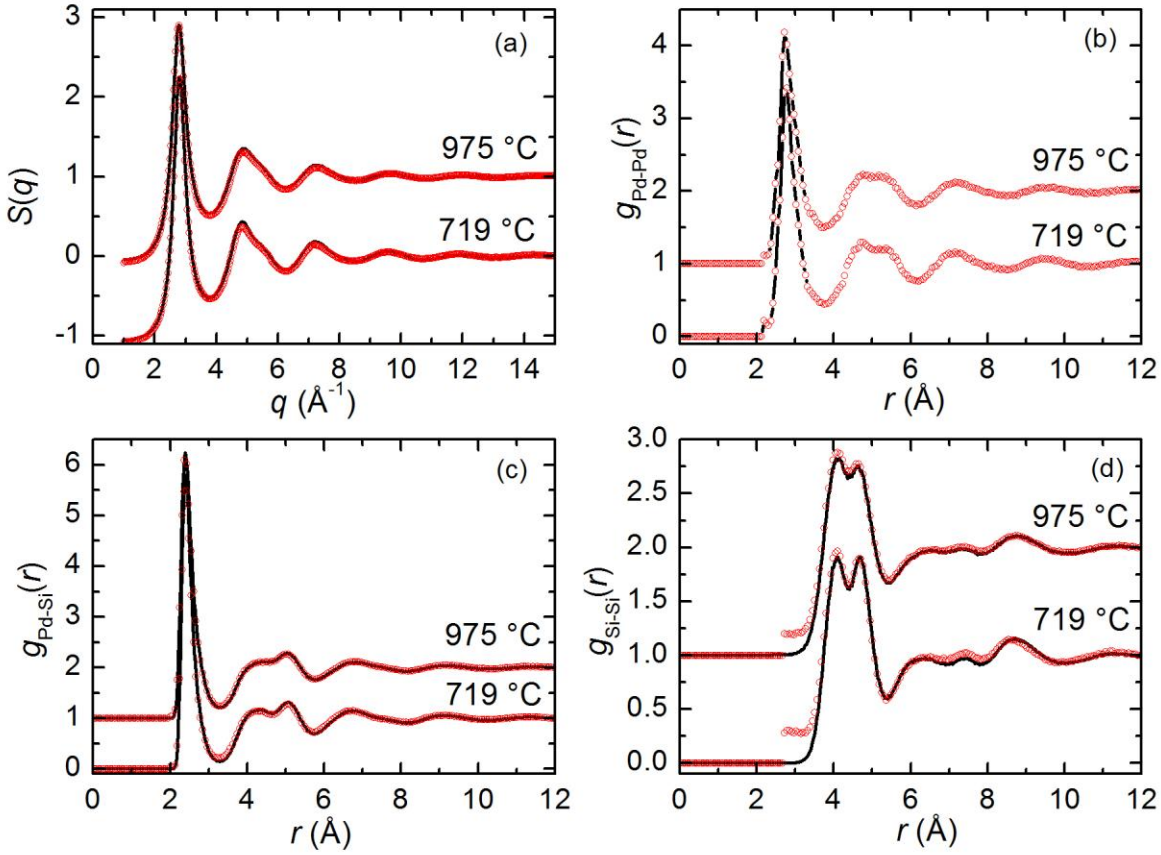

Figure 4.6: Representative RMC fits to (a) the experimental S(q) as well as to the constraints of the (b) Pd-Pd, (c) Pd-Si, and (d) Si-Si MD PPCFs. Solid black lines represent the input data and open red circles represent the RMC fits. Data shown are for two distinct RMC simulations, each fit to data corresponding to the highest (975 °C) and the lowest (719 °C) temperatures. Pd-Pd RMC fits (b) are constrained to MD data only in the range 0 to 2.5 Å.

Discrepancies in the RMC fit and the constraining data are likely due to differences in experimental data and the PPCFs generated from MD, which may point to issues with the MD potentials. Figure 4.7 shows the difference between the MD $g(r)$, constructed from the individual PPCFs weighted by $w_{ij}(0)$, and the experimental $g(r)$. The first peak in the MD-generated $g(r)$ is smaller and shifted to slightly lower-r, and lacks the definitive low-r shoulder from the Pd-Si PPCF contribution (Fig. 4.1(b)). If the Pd-Pd average atomic spacing, or the first

peak position in the Pd-Pd PPCF, $r_{Pd\text{-}Pd}$, is not well separated from the Pd-Si average atomic spacing, $r_{Pd\text{-}Si}$, then the individual contributions of the PPCF peaks to the total $g(r)$ first peak cannot be resolved. This implies an inaccuracy in the MD determined positions for $r_{Pd\text{-}Pd}$ and $r_{Pd\text{-}Si}$. The second coordination shell in the MD-determined $g(r)$ shows a split peak, but with relative heights of the lower-r and higher-r peak that are opposite to that of the split second peak in the experimental $g(r)$. The qualitative feature of second nearest-neighbor Pd-Pd correlations are captured by the MD simulation, but quantitative differences raise questions about the accuracy of each of the MD partials in capturing the true liquid structure.

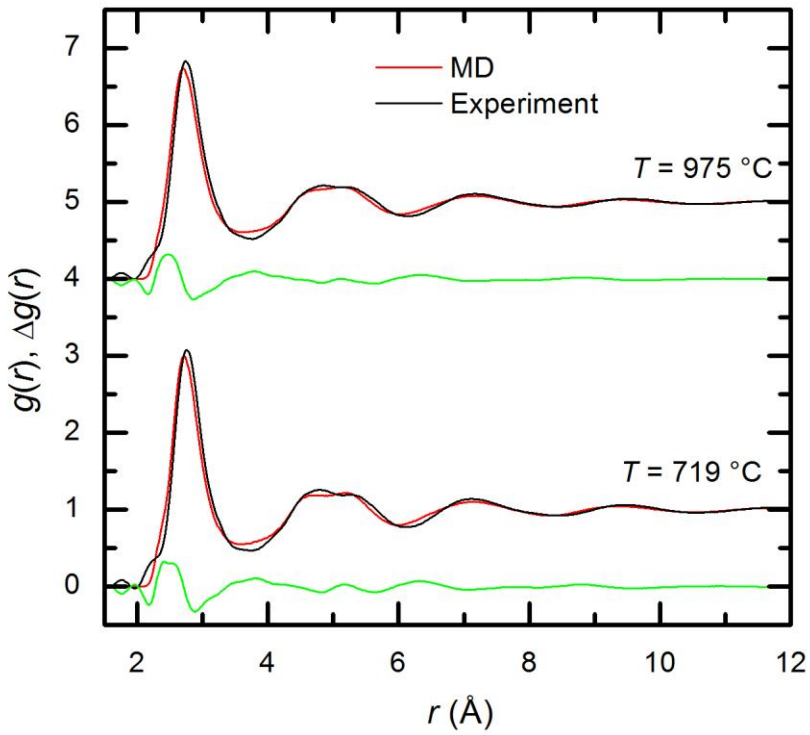

Figure 4.7: Comparisons of the experimentally determined total $g(r)$ (black) to the total $g(r)$ constructed from the MD PPCFs (red) for the highest and lowest temperatures. Green lines represent the differences between the two data sets, where $\Delta g(r) = g_{MD}(r) - g_{Experiment}(r)$.

Figure 4.8(b) shows the number of occurrence of a variety of Si-centered clusters at each temperature, averaged over each configuration. The error bars represent the standard deviation

from the results acquired for several RMC simulations. The Voronoi indices presented represent the most prevalent clusters found in the RMC configurations as well as the most prevalent clusters found in the original MD configurations [1]. The distributions are sorted first by increasing coordination number and then by increasing distortion of the ideal Z-cluster [55] for each particular coordination number. The first feature to note is the overall low abundances of each of the Z-clusters relative to the number of Si-centered polyhedral in the configuration. This is most likely due to both the inability to extract 'inherent structures'[76, 77] from the RMC configurations (as is done during MD structural analysis [1, 14-16]) as well as not applying a face-exclusion criterion for small polyhedral faces from the Voronoi tessellation [14]. The second feature of note is the weak temperature dependence of the atomic fractions of most indices, especially to within the standard deviation. This agrees with the small temperature dependence observed in the other structural features (Figs. 4.1-4.3) and the small temperature dependence of the structural/thermodynamic properties determined from MD by Ding et al. [1]. The relative abundances of <0 2 8 0> and <0 3 6 1> are consistent with the MD data from Ding et al., but are inconsistent when compared to the abundances of <0 4 4 0> and <0 3 6 0>. The particularly small abundance of < 0 4 4 0> polyhedra and the relatively high abundance of 11 and 12 coordinated Z-clusters are consistent with the large number of atoms found in the low-*r* region below the MD Si-Si PPCF first coordination shell (Fig. 4.6(d)).

Figure 4.8(a) shows the distribution of the ten most prevalent Pd-centered polytetrahedral clusters. The majority of Pd-centered Z-clusters are 13 to 15-coordinated structures, which is higher than the coordination numbers obtained from the MD PPCFs. This may be an artifact arising from small faces on the Voronoi polyhedra relative to the total surface area. The <0 3 6 4> index, a second degree distortion of the Z13 cluster, and the <0 2 8 4> index, a first degree

distortion of the Z14 cluster, represent the most prevalent Pd-Centered polytetrahedra. The <0 3 6 4> index, found to be prevalent in several constrained and unconstrained RMC simulations of binary metallic liquids [78], increases slightly with decreasing temperature. Other indices show either a very small increase with decreasing temperature, or no significant temperature dependence at all, consistent with a lack of significant or accelerated structural ordering in the supercooled liquid regime.

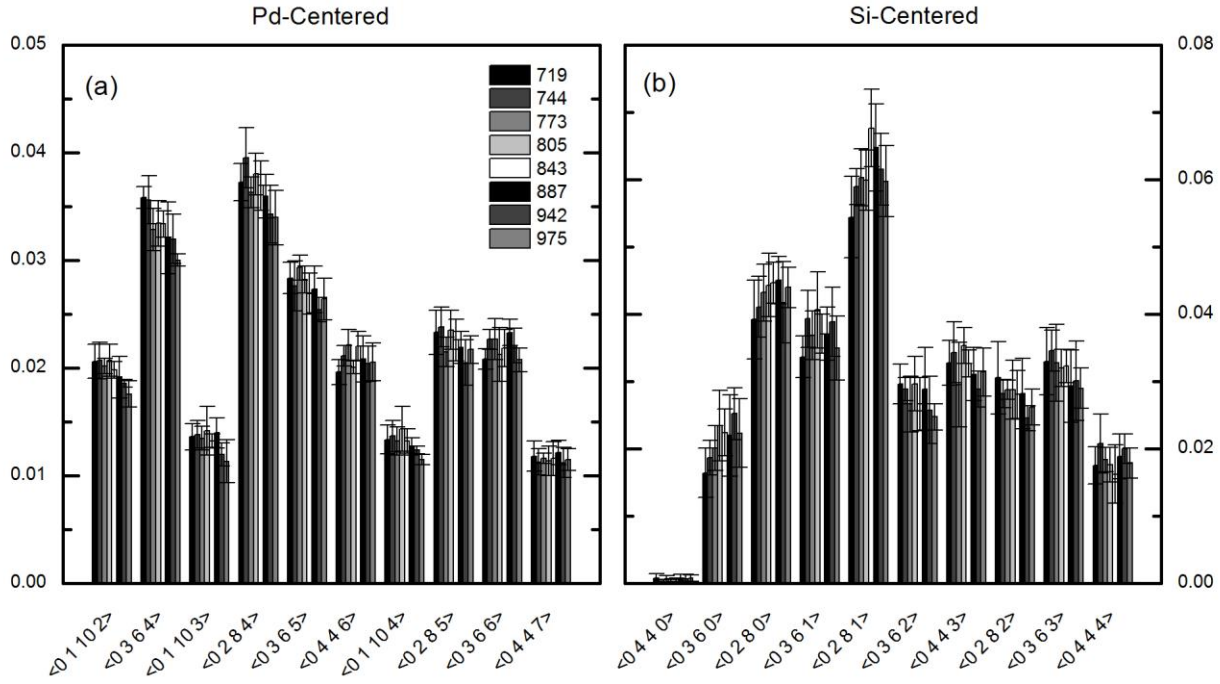

Figure 4.8: Fractions of the (a) Pd-centered and (b) Si-Centered clusters as a function of temperature for most prevalent Voronoi indices as well as Si-centered indices of interest [1].

4.5 Conclusions

High energy X-ray diffraction measurements of $Pd_{82}Si_{18}$ liquid in a containerless environment were made using the WU-BESL. An analysis of features in the peaks in the liquid $S(q)$ and $g(r)$ shows structural ordering that increases linearly with temperature as the liquid is cooled from high temperature into the supercooled liquid regime. The first peak in the total structure factor, which contains information from all of the coordination shells in the total pair correlation function, grows at a faster rate near the melting temperature in the $Pd_{82}Si_{18}$ liquid than does the binary Cu-Zr liquid, suggesting that the $Pd_{82}Si_{18}$ is a stronger liquid, in agreement with arguments from MD simulations. The developing shoulder in the second peak of $S(q)$ suggests that the Pd-Si liquid has developing ISRO. Given the large contribution of the Pd-Pd PSF to the total $S(q)$ and the expectation of 9-coordinated Si-centered cluster structures (from theoretical results), Pd-Pd clusters are likely responsible for the observed ISRO signature, which is common in TM-TM binary liquids and glasses. The presence of Pd-centered distorted icosahedral (<0 2 8 2> and <0 3 6 3>) Z-clusters in the MD-simulated glass structure has been shown [79], but their presence or development in the supercooled liquid has not been investigated. "Anomalous contraction" of the first coordination shell with increasing temperature, universally found among pure and binary metallic systems, is observed in the $g(r)$ of the $Pd_{82}Si_{18}$ liquid. The contribution from the Pd-Si partial can be seen in the low-r shoulder in the first coordination shell, confirming the shortened Pd-Si average atomic bond distance expected from the strong chemical affinity of the elements. Splitting of the second peak, typically found in metal-metalloid glasses but not liquids, is observed in the liquid at all temperatures, and develops with decreasing temperature. Because of the large contribution of

the Pd-Pd PPCF to the total $g(r)$, the split second coordination shell suggests the development of two distinct length scales for the second nearest Pd-Pd neighbor distance.

Results from a RMC analysis constrained to the PPCFs generated from MD simulations reveal a weak temperature dependence for changes in the local topological structures, characterized by their Voronoi indices, consistent with total structural information from both $S(q)$ and $g(r)$. The weak temperature dependence of structural change is again consistent with the fact that the Pd-Si liquid is strong. While the prevalence in Si-centered Z9 and Z10 Kasper structures in the RMC generated configurations are expected, their lower abundance relative to higher-coordinated clusters and the poor fit to the low-r region of the Si-Si PPCF point to the difficulty constraining to both experimental and MD simulated data. The poor fit of the RMC simulation to the Si-Si PPCF is likely due to the difficulty fitting the large Si-Si average atomic nearest-neighbor distance (indicative of the solute-solute avoidance in the MD-simulated liquid). Discrepancies between the MD-simulated structures and the experimental data also impact the RMC fit. A more accurate description of the average liquid atomic configurations requires experimental measurements of the PSFs, which are difficult to obtain given the relative FZ weightings of the more abundant, strongly scattering Pd atoms and the dilute, weakly scattering Si atoms. Neutron scattering studies of the supercooled liquid would provide the complimentary experimental data needed.

4.6 References

[1] J. Ding, Y.-Q. Cheng, H. Sheng and E. Ma, Physical Review B **85** (6), 060201 (2012).
[2] E. S. Park, J. H. Na and D. H. Kim, Applied Physics Letters **91** (3) (2007).
[3] H. Tanaka, Journal of Non-Crystalline Solids **351** (8–9), 678 (2005).
[4] A. Meyer, R. Busch and H. Schober, Physical Review Letters **83** (24), 5027 (1999).

[5] Y. Li, Q. Guo, J. A. Kalb and C. V. Thompson, Science **322** (5909), 1816 (2008).
[6] J. C. Bendert, A. K. Gangopadhyay, N. A. Mauro and K. F. Kelton, Physical Review Letters **109** (18), 185901 (2012).
[7] J. C. Bendert and K. F. Kelton, Journal of Non-Crystalline Solids **376** (0), 205 (2013).
[8] R. Busch, J. Schroers and W. H. Wang, MRS Bulletin **32** (08), 620 (2007).
[9] P. G. Debenedetti and F. H. Stillinger, Nature **410** (6825), 259 (2001).
[10] P. H. Gaskell, Nature **276** (5687), 484 (1978).
[11] J. Hafner, Physical Review B **21** (2), 406 (1980).
[12] P. J. Desré, E. Cini and B. Vinet, Journal of Non-Crystalline Solids **288** (1–3), 210 (2001).
[13] D. B. Miracle, Nature Materials **3** (10), 697 (2004).
[14] H. W. Sheng, W. K. Luo, F. M. Alamgir, J. M. Bai and E. Ma, Nature **439** (7075), 419 (2006).
[15] N. Jakse and A. Pasturel, Physical Review B **78** (21), 214204 (2008).
[16] Y. Q. Cheng, H. W. Sheng and E. Ma, Physical Review B **78** (1), 014207 (2008).
[17] R. Soklaski, Z. Nussinov, Z. Markow, K. F. Kelton and L. Yang, Physical Review B **87** (18), 184203 (2013).
[18] G. Duan, D. Xu, Q. Zhang, G. Zhang, T. Cagin, W. L. Johnson and W. A. Goddard, Physical Review B **71** (22), 224208 (2005).
[19] A. K. Gangopadhyay, G. W. Lee, K. F. Kelton, J. R. Rogers, A. I. Goldman, D. S. Robinson, T. J. Rathz and R. W. Hyers, Review of Scientific Instruments **76** (7) (2005).
[20] Y. Ke-Fu and R. Fang, Chinese Physics Letters **22** (6), 1481 (2005).
[21] K. Yao and N. Chen, Science in China Series G **51** (4), 414 (2008).
[22] Y. Li, S. J. Poon, G. J. Shiflet, J. Xu, D. H. Kim and J. F. Löffler, MRS Bulletin **32** (08), 624 (2007).
[23] D. Wang, Y. Li, B. B. Sun, M. L. Sui, K. Lu and E. Ma, Applied Physics Letters **84** (20), 4029 (2004).
[24] D. Xu, B. Lohwongwatana, G. Duan, W. L. Johnson and C. Garland, Acta Materialia **52** (9), 2621 (2004).
[25] A. Inoue and W. Zhang, Materials Transactions **45** (2), 584 (2004).
[26] G. Duan, D. Xu and W. L. Johnson, Metallurgical and Materials Transactions A **36 A** (2), 455 (2005).
[27] L. Xia, D. Ding, S. T. Shan and Y. D. Dong, Journal of Physics: Condensed Matter **18** (15), 3543 (2006).
[28] P. Jia and J. Xu, Journal of Materials Research **24** (1), 96 (2009).
[29] L. Xia, W. H. Li, S. S. Fang, B. C. Wei and Y. D. Dong, Journal of Applied Physics **99** (2) (2006).
[30] Y. Wang, Q. Wang, J. Zhao and C. Dong, Scripta Materialia **63** (2), 178 (2010).
[31] H. Okamoto, Journal of Phase Equilibria **14** (4), 536 (1993).
[32] D. Turnbull, Contemporary Physics **10** (5), 473 (1969).
[33] S. Y. Hong, W. H. Guo and H. W. Kui, Journal of Materials Research **14** (09), 3668 (1999).
[34] H. S. Chen, Acta Metallurgica **22** (12), 1505 (1974).
[35] H. S. Chen, J. T. Krause, K. Shirakawa and T. Masumoto, Journal of Non-Crystalline Solids **41** (1), 79 (1980).
[36] Y. Q. Cheng, E. Ma and H. W. Sheng, Physical Review Letters **102** (24), 245501 (2009).

[37] M. I. Mendelev, D. J. Sordelet and M. J. Kramer, Journal of Applied Physics **102** (4) (2007).
[38] V. Wessels, A. K. Gangopadhyay, K. K. Sahu, R. W. Hyers, S. M. Canepari, J. R. Rogers, M. J. Kramer, A. I. Goldman, D. Robinson, J. W. Lee, J. R. Morris and K. F. Kelton, Physical Review B **83** (9), 094116 (2011).
[39] N. A. Mauro, A. J. Vogt, M. L. Johnson, J. C. Bendert, R. Soklaski, L. Yang and K. F. Kelton, Acta Materialia **61** (19), 7411 (2013).
[40] M. I. Mendelev, M. J. Kramer, R. T. Ott, D. J. Sordelet, M. F. Besser, A. Kreyssig, A. I. Goldman, V. Wessels, K. K. Sahu, K. F. Kelton, R. W. Hyers, S. Canepari and J. R. Rogers, Philosophical Magazine **90** (29), 3795 (2010).
[41] N. A. Mauro, M. L. Johnson, J. C. Bendert and K. F. Kelton, Journal of Non-Crystalline Solids **362** (0), 237 (2013).
[42] N. A. Mauro, A. J. Vogt, M. L. Johnson, J. C. Bendert and K. F. Kelton, Applied Physics Letters **103** (2) (2013).
[43] H. W. Kui, A. L. Greer and D. Turnbull, Applied Physics Letters **45** (6), 615 (1984).
[44] J. C. Bendert, Ph.D. Thesis, Washington University in St. Louis, 2013.
[45] A. P. Hammersley, S. O. Svensson, M. Hanfland, A. N. Fitch and D. Hausermann, High Pressure Research **14** (4-6), 235 (1996).
[46] R. L. McGreevy, Journal of Physics: Condensed Matter **13** (46), R877 (2001).
[47] G. Evrard and L. Pusztai, Journal of Physics: Condensed Matter **17** (5), S1 (2005).
[48] O. Gereben and L. Pusztai, Journal of Computational Chemistry **33** (29), 2285 (2012).
[49] G. Voronoi, Journal Fur Die Reine Und Angewandte Mathematik **134**, 198 (1908).
[50] J. Finney, Proceedings of the Royal Society of London A **319** (1539), 479 (1970).
[51] J. L. Finney, Nature **266** (5600), 309 (1977).
[52] F. C. Frank and J. S. Kasper, Acta Crystallographica **11** (3), 184 (1958).
[53] V. A. Borodin, Philosophical Magazine A **79** (8), 1887 (1999).
[54] V. A. Borodin, Philosophical Magazine A **81** (10), 2427 (2001).
[55] Y. Q. Cheng and E. Ma, Progress in Materials Science **56** (4), 379 (2011).
[56] S. Sachdev and D. R. Nelson, Physical Review Letters **53** (20), 1947 (1984).
[57] K. F. Kelton, G. W. Lee, A. K. Gangopadhyay, R. W. Hyers, T. J. Rathz, J. R. Rogers, M. B. Robinson and D. S. Robinson, Physical Review Letters **90** (19), 195504 (2003).
[58] N. Chen, Y. Li and K.-F. Yao, Journal of Alloys and Compounds **504, Supplement 1** (0), S211 (2010).
[59] H. Lou, X. Wang, Q. Cao, D. Zhang, J. Zhang, T. Hu, H.-k. Mao and J.-Z. Jiang, Proceedings of the National Academy of Sciences **110** (25), 10068 (2013).
[60] A. K. Gangopadhyay, M. E. Blodgett, M. L. Johnson, J. McKnight, V. Wessels, A. J. Vogt, N. A. Mauro, J. C. Bendert, R. Soklaski, L. Yang and K. F. Kelton, The Journal of Chemical Physics **140** (4) (2014).
[61] T. Ohkubo and Y. Hirotsu, Physical Review B **67** (9), 094201 (2003).
[62] K. Suzuki, T. Fukunaga, M. Misawa and T. Masumoto, Materials Science and Engineering **23** (2–3), 215 (1976).
[63] G. S. Cargill, Journal of Applied Physics **41** (5), 2248 (1970).
[64] D. E. Polk, Acta Metallurgica **20** (4), 485 (1972).
[65] D. S. Boudreaux and J. M. Gregor, Journal of Applied Physics **48** (1), 152 (1977).
[66] T. Fukunaga and K. Suzuki, Science Reports of the Research Institutes, Tohoku University, Series A **29** (2), 153 (1981).

[67] S. Y. Wang, C. Z. Wang, M. Z. Li, L. Huang, R. T. Ott, M. J. Kramer, D. J. Sordelet and K. M. Ho, Physical Review B **78** (18), 184204 (2008).
[68] N. A. Mauro, V. Wessels, J. C. Bendert, S. Klein, A. K. Gangopadhyay, M. J. Kramer, S. G. Hao, G. E. Rustan, A. Kreyssig, A. I. Goldman and K. F. Kelton, Physical Review B **83** (18), 184109 (2011).
[69] N. A. Mauro, W. Fu, J. C. Bendert, Y. Q. Cheng, E. Ma and K. F. Kelton, The Journal of Chemical Physics **137** (4) (2012).
[70] T. E. Faber and J. M. Ziman, Philosophical Magazine **11** (109), 153 (1965).
[71] Y. Waseda, *The structure of non-crystalline materials: liquids and amorphous solids*. (McGraw-Hill International Book Company New York, 1980).
[72] D. Waasmaier and A. Kirfel, Acta Crystallographica Section A **51** (3), 416 (1995).
[73] C. N. J. Wagner, Journal of Non-Crystalline Solids **76** (1), 29 (1985).
[74] K. Tanaka, T. Saito, K. Suzuki and R. Hasegawa, Physical Review B **32** (10), 6853 (1985).
[75] A. Takeuchi and A. Inoue, Materials Transactions **41** (11), 1372 (2000).
[76] F. H. Stillinger and T. A. Weber, Science **225** (4666), 983 (1984).
[77] F. H. Stillinger and T. A. Weber, Physical Review A **25** (2), 978 (1982).
[78] Z. Markow, (Private Communication).
[79] Y. Q. Cheng, J. Ding and E. Ma, Materials Research Letters **1** (1), 3 (2012).

Chapter 5

Experimental Measurement of the Structural Evolution in (Au, Pd, Ni)-(Cu)-Si Liquids and Glasses

This chapter includes both DSC measurements of the solidus and liquidus temperatures for the alloys provided by C. Pueblo and liquid density and expansivity measurements provided by M. E. Blodgett (Washington University in St. Louis, St. Louis, MO).

5.1 Introduction

Metallic glass formation from transition metal (TM) - metalloid based alloy liquids has been studied since the discovery of metallic glasses in 1960 [1]. The first metallic alloy liquid, $Au_{75}Si_{25}$, to be quenched into a metallic glass required a cooling rate on the order of 10^6 K/s in order to bypass crystallization. Since then, new alloys with progressively improved glass-forming ability (GFA) have been discovered, from millimeter diameter rods of Pd-Cu-Si, formed at cooling rates near 10^3 K/s [2], to ~1 cm ingots of a fluxed Pd-Ni-P alloy formed at cooling rates near 10^2 K/s [3], and finally to 5 cm bulk-metallic glass (BMG) forming [4] $Pd_{40}Cu_{30}Ni_{10}P_{20}$ alloys with a critical cooling rates around 0.1 to 1 K/s [5]. In recent years, there has been a large body of work dedicated to understanding the connections between GFA and structure, thermophysical properties, and kinetic behavior of metallic liquids [6-9]; investigations of metal-metalloid alloys compliment those of the widely-studied Zr-based alloys.

The rapidly slowing kinetics of the liquid as it is supercooled are known to play a critical role in glass formation. The concept of fragility [10] describes the temperature dependence of the viscosity of the liquid as it cooled to the glass transition temperature, T_g. Strong liquids have a more Arrhenius temperature dependence for the viscosity, while fragile liquids exhibit a highly non-Arrhenius temperature dependence. The relationship between thermodynamic and kinetic properties of the liquid has been established theoretically and experimentally [11-13], and the relationship to excess entropy and specific heat points to a structural signature of the kinetic behavior. This structural signature of fragility has been suggested by molecular dynamics (MD) simulations [14-17], and had been demonstrated experimentally in TM-TM liquids [18-21].

More recently, the connection between structure and fragility has been studied in metal-metalloid systems as well. Embedded Atom Model (EAM) MD simulations of the $Au_{81}Si_{19}$ eutectic liquid show a rapid increase in the icosahedral short range order (ISRO) below the melting temperature, which decreases the atomic mobility and is ultimately responsible for the non-Arrhenius slowing of the dynamics [22, 23]. Similar EAM MD simulations also show that Si-alloying in Ni-Si liquids lowers the local symmetry in $Ni_{80}Si_{20}$ and $Ni_{75}Si_{25}$ compared to liquids with less Si, resulting in GFA [24, 25]. The weaker local ordering from increased Si-concentration results in a sharp decrease in the diffusion rates at low temperatures and an increase in the non-Arrhenius behavior of the liquid viscosity. Alternatively, Si-alloying in Pd-Si liquids, studied via EAM MD simulations, shows a weaker temperature dependence of the structure, excess specific heat, and viscosity, compared to that of the more fragile $Cu_{64}Zr_{36}$ binary liquid [26]. The weaker temperature dependence in the excess specific heat, and ultimately stronger kinetic behavior, is similar to the experimental results obtained for the $Pd_{40}Cu_{30}Ni_{10}P_{20}$ metal-metalloid-based BMG-forming liquid [27].

Metal-metalloid alloys, such as the Au-Si [28], Pd-Si [29], and Ni-Si [30] binary alloys, have a eutectic that occurs over a very small composition range in the Si-lean portion of their respective phase diagrams. While Au-Si and Pd-Si show deeper eutectics near the compositions $Au_{81}Si_{19}$ and $Pd_{82}Si_{18}$ respectively, the Ni-Si system has a shallower eutectic near $Ni_{80}Si_{20}$. As mentioned previously, the existence of a deep eutectic is associated with improved GFA, since the liquid can be held in equilibrium at temperatures much lower and closer to the glass transition temperature, compared to alloys far from the eutectic composition [31]. The structure of the liquid, influenced by the chemical affinity between TM and Si in all three binary systems[32], plays an important role in the formation of the deep eutectic by stabilizing the metal-metalloid liquid structure and destabilizing the competing crystalline structures that would nucleate in the supercooled liquid [2, 24, 33-36]. This chemical affinity also results in strong chemical short range order (CSRO) and the specific local topologies found in MD simulations of $Au_{81}Si_{19}$ [22, 23], $Pd_{82}Si_{18}$ [26], and $Ni_{75}Si_{25}$ [24, 25]. Although both $Au_{81}Si_{19}$ and $Pd_{82}Si_{18}$ exhibit strong CSRO, which serves to stabilize the respective liquid structures, its influence on the liquids kinetic fragility, as suggested from MD, seems to show opposing effects, making $Au_{81}Si_{19}$ a more fragile liquid and $Pd_{82}Si_{18}$ a stronger liquid. Ultimately, though, while the $Au_{81}Si_{19}$ liquid has marginal GFA and the $Ni_{75}Si_{25}$ liquid only has GFA that is suggested from molecular dynamics (MD) simulation [24, 25], the $Pd_{82}Si_{18}$ liquid is the only one of the three for which bulk-forming ability has been demonstrated [37, 38]. Adding additional alloying elements to Pd-Si, such as Cu to form Pd-Cu-Si ternaries, has been found to significantly improve GFA [39].

As for the liquids discussed in previous chapters, experimental observations in the deeply supercooled states, as well as at high temperatures, have only recently been made possible by

containerless processing techniques. Developments in levitation techniques, particularly electrostatic levitation [40, 41], extend previous X-ray studies by allowing scattering studies of the bulk supercooled liquid in a containerless, high-vacuum, environment, while simultaneously allowing the acquisition of thermophysical property data, such as temperature, density, and viscosity, through non-contact optical measurements. Many of these structure/property probing levitation studies have focused on the TM-TM based liquids, particularly Zr-based ones [19, 20, 42-47]; the ability to study metal-metalloid based liquids has only recently been realized.

Here we present the results for X-ray scattering studies of levitated liquid $Au_{81}Si_{19}$, $Pd_{82}Si_{18}$, $Pd_{77}Cu_6Si_{17}$, and $Ni_{75}Si_{25}$ alloys. Structure factors, $S(q)$, and pair distribution functions, $g(r)$, were determined from the liquid samples and were correlated with non-contact temperature and density measurements. In Section 5.3 the unique features and temperature dependence of the primary and secondary peaks of both the $S(q)$ and $g(r)$ are analyzed and compared. In Section 5.4, information about the average atomic bond lengths is determined from an analysis of the first coordination shells for the liquid $g(r)$s. The evolution with respect to temperature of the dominant correlation lengths and average atomic distances are measured and compared. Finally, a measure of the "structural fragility index" [21] is determined using the liquid $Pd_{77}Cu_6Si_{17}$ data in combination with temperature dependent measurements of the bulk amorphous alloy. The measure is then used to make a prediction regarding the structural fragility of the closely related $Pd_{82}Si_{18}$ liquid.

5.2 Experimental Procedure

Samples were prepared and, unless otherwise noted, liquidus and solidus temperatures were measured in-house, using the procedures outlined in Chapter 2. A notable difference is that

the $Pd_{82}Si_{18}$ sample was fluxed in B_2O_3 prior to processing in the BESL. Liquid data for $Au_{81}Si_{19}$, $Pd_{82}Si_{18}$, $Pd_{77}Cu_6Si_{17}$, and $Ni_{75}Si_{25}$ were acquired utilizing the BESL technique [41]. Density data for all compositions were acquired both at Washington University in St. Louis and at the APS at Argonne National Laboratory. X-ray scattering data for $Au_{81}Si_{19}$ were acquired during the "BESL 2010" experimental run in August of that year, and scattering data for the other three compositions were acquired during the "BESL 2013" experimental run. Glass data for $Pd_{77}Cu_6Si_{17}$ were acquired for a sample that was dropped from levitation while in the liquid state and rapidly quenched upon contact with the copper bottom electrode. The amorphous structure of the sample obtained was confirmed through the acquisition of high-energy X-ray diffraction data in the "BESL 2013" configuration. The near-spherical amorphous sample was then subsequently levitated, heated to near and above the glass transition, and studied using the same technique as for liquid samples in the BESL. X-ray diffraction data acquisition and analysis was performed using the procedure outlined in Chapter 2.

5.3 Results

Total structure factors, $S(q)$, and total pair distribution functions (PDFs), $g(r)$, for $Au_{81}Si_{19}$, $Pd_{82}Si_{18}$, $Pd_{77}Cu_6Si_{17}$, and $Ni_{75}Si_{25}$ are shown in Figure 5.1. Structural data were obtained in both the equilibrium and supercooled liquid regions for both $Au_{81}Si_{19}$ (300 °C to 550 °C, T_S = 360 °C) and $Pd_{82}Si_{18}$ (720 °C to 975 °C, T_S = 808 °C). Because the sample readily crystallized at temperatures below the liquidus temperature, T_L, structural data for $Pd_{77}Cu_6Si_{17}$ were only obtained in the high temperature equilibrium and supercooled liquid phases above the solidus temperature T_S (780 to 990 °C, T_S = 740 °C, T_L = 855 °C [5]). Similarly, structural data for $Ni_{75}Si_{25}$ were only obtained in the high temperature equilibrium liquid region above T_L (1200

to 1480 °C, T_S = 1150 °C, T_L = 1200 °C). Surface crystallization may be responsible for the lack of supercooling in this liquid [25]. For all compositions, the first peak in $S(q)$ shifts toward higher q with decreasing temperature, indicative of an increase in the overall density in the system. The peak also grows and sharpens indicating structural ordering as the liquid is cooled. Oscillations in the $Ni_{75}Si_{25}$ decay more strongly with increasing q, which may be a reflection of the higher temperature of the liquid compared to the other alloys or indicate a tendency against extended ordering in the liquid. As shown in capillary diffraction studies of pure Au and Au-Si [48], for lower temperatures the $S(q)$ for the $Au_{81}Si_{19}$ liquid shows clear oscillations out to high-q and maintains the general features of the pure Au liquid structure. The $S(q)$s and $g(r)$s for $Pd_{82}Si_{18}$ and $Pd_{77}Cu_6Si_{17}$ are nearly indistinguishable reflecting the similarity in their composition, X-ray scattering strength, and structure.

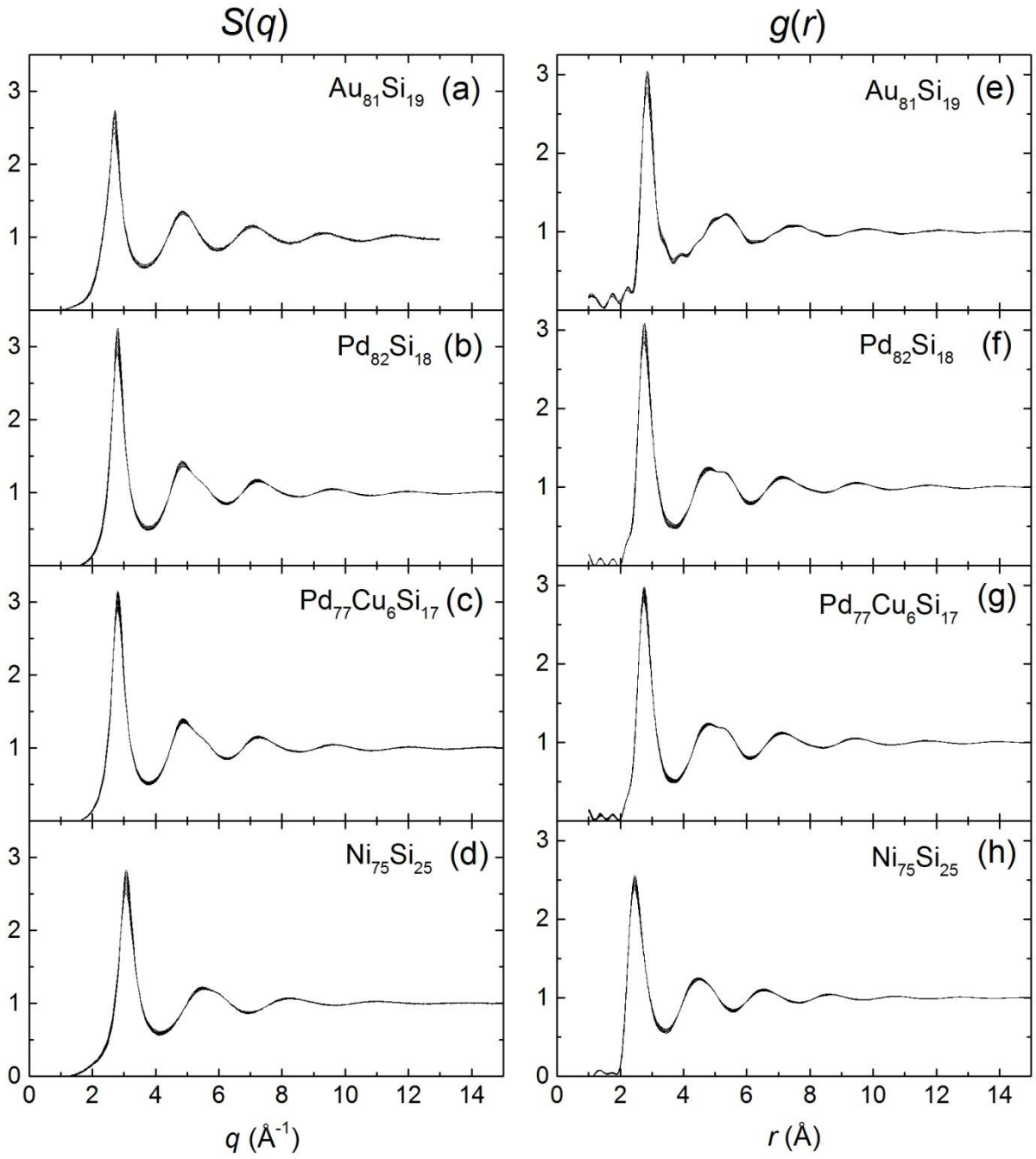

Figure 5.1: Total structure factors (a-d), $S(q)$, and total pair distribution function (e-h), $g(r)$, for $Au_{81}Si_{19}$, $Pd_{82}Si_{18}$, $Pd_{77}Cu_6Si_{17}$, and $Ni_{75}Si_{25}$ liquids at all temperatures.

In Figure 5.2, a closer inspection of the first two peaks in $S(q)$ for the binary liquids is presented. For each composition, the structure factors are shown for the highest, intermediate, and lowest liquid temperatures. Qualitatively, the growth and shift behavior of the first peak is

similar in all three compositions. The first feature to note, though, is the differences in the positions of the first peaks, $q_{1,}$ for each of the liquids. The $Au_{81}Si_{19}$ liquid exhibits the lowest average q_1, while $Ni_{75}Si_{25}$ shows the highest average q_1. The $Pd_{82}Si_{18}$ liquid shows an intermediate average q_1, with values closer to that of $Au_{81}Si_{19}$. The differences reflect the average atomic separations and ultimately the atomic size differences of the TM atoms in each of the liquids.

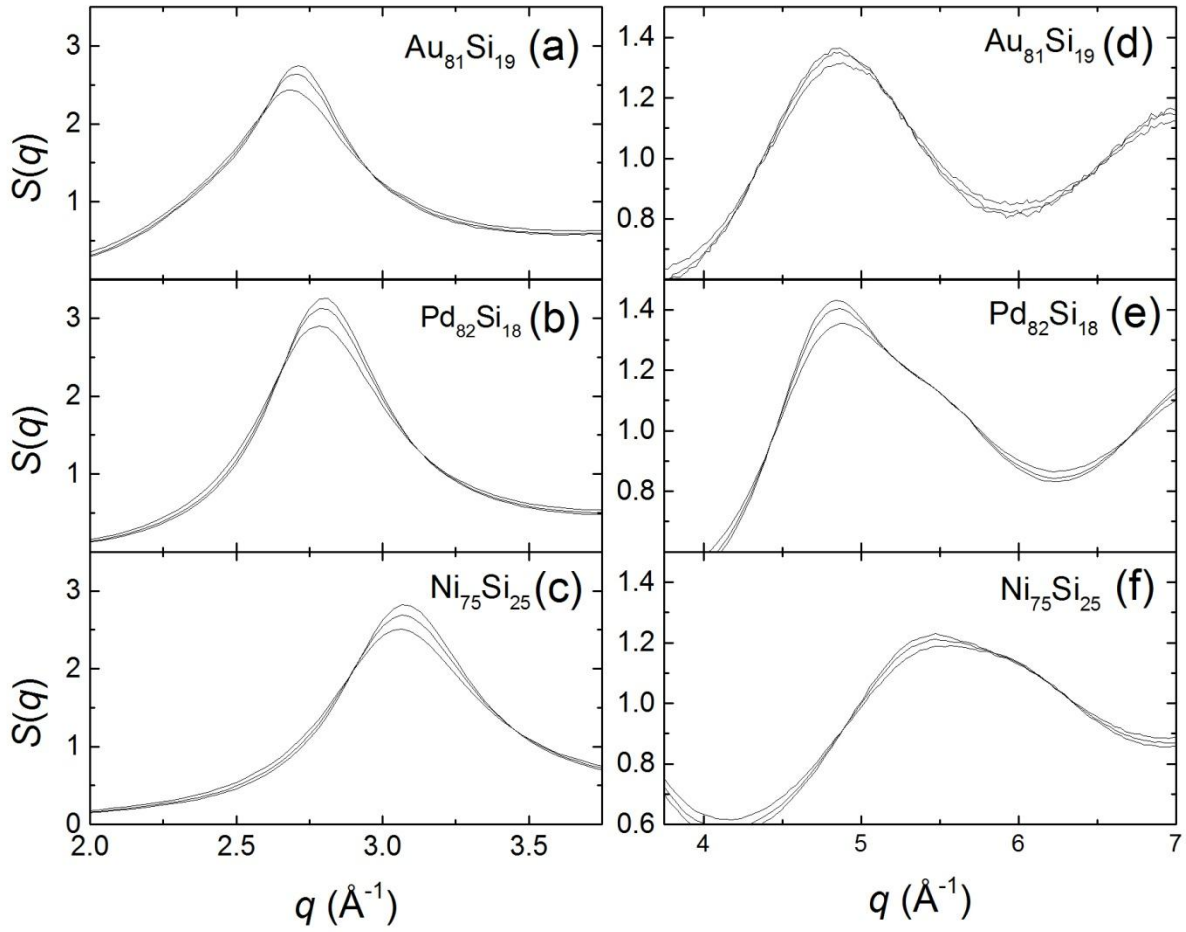

Figure 5.2: $S(q)$ first peaks for (a) $Au_{81}Si_{19}$, (b) $Pd_{82}Si_{18}$, and (c) $Ni_{75}Si_{25}$ and second peaks for (d) $Au_{81}Si_{19}$, (e)$Pd_{82}Si_{18}$, and (f) $Ni_{75}Si_{25}$ showing the differences in the heights, shapes, and shifts with temperature. Shown are the structure factors for the highest temperature (lowest amplitude), an intermediate temperature, and lowest temperature (highest amplitude) of the data for each composition.

The evolution of the second peak in $S(q)$ (Fig. 5.2) is also characteristic of enhanced local ordering, with a developing high-q shoulder with decreasing temperature that is often associated with ISRO [42, 45, 49]. The $Pd_{82}Si_{18}$ and $Ni_{75}Si_{25}$ liquids both show a developing shoulder, with an increase in the low-q shoulder on the second peak with decreasing temperature. While the shoulder in the second peak for the $Pd_{82}Si_{18}$ liquid is not quite as pronounced, it has a very similar character to shoulders found in other TM-TM liquids [42, 44, 45]. As mentioned in Chapter 4, the shoulder may originate from ISRO in the Pd-Pd partial pair correlations. The $Ni_{75}Si_{25}$ second peak shows a broader character similar to that of pure liquid Ni, which does contain a significant amount of ISRO [50, 51]. The uniformity and symmetry of the second $S(q)$ peak for $Au_{81}Si_{19}$ is in stark contrast to what is observed in most metallic liquid alloys. While the lack of shoulder might suggest a lack of ISRO in this system, MD studies have shown evidence for iscosahedral-like order in the $Au_{81}Si_{19}$ liquid [22, 23]. This suggests that those MD results might be incorrect or that there may be subtle effects in either the particular local ordering in these liquids or in X-ray scattering effects to the construction of the total $S(q)$.

To further highlight the differences between the binary liquids, figure 5.3 shows the first and second peaks in the total $g(r)$ as calculated from the Fourier transform of the total $S(q)$ using

$$g(r) - 1 = \frac{1}{4\pi\rho_0}\frac{2}{\pi}\int (S(q) - 1)\frac{\sin(qr)}{qr}q^2 dq, \qquad (5.1)$$

where ρ_0 is the average density. With regards to the first peaks, or first coordination shells, we see a qualitatively similar temperature evolution, with a growing, sharpening peak and a shift towards higher r with decreasing temperature. Although a shift of the peak towards lower r with increasing temperature suggests thermal contraction, the observed "anomalous contraction" of

the first coordination shells is common among pure metallic [52] and metallic alloy liquids [43]. Just as in the first peak of $S(q)$ (Fig. 5.2), the differences in the average atomic nearest-neighbor spacing, r_1, between the liquid alloys trend inversely with their respective average q_1 (again as expected from atomic size differences in the TM elements). $Au_{81}Si_{19}$ exhibits the largest average r_1, while $Ni_{75}Si_{25}$ has the shortest. The average nearest neighbor distance for $Pd_{82}Si_{18}$ is at an intermediate value, closer to that of $Au_{81}Si_{19}$. It is also important to note the low-r sub-peak and shoulder for the $Au_{81}Si_{19}$ and $Pd_{82}Si_{18}$ liquids respectively. As previously suggested [53, 54], these features could be due to the first peaks of the Au-Si and Pd-Si PPCFs respectively. The contributions of the PPCFs to the total $g(r)$ will be discussed in further detail in the next section.

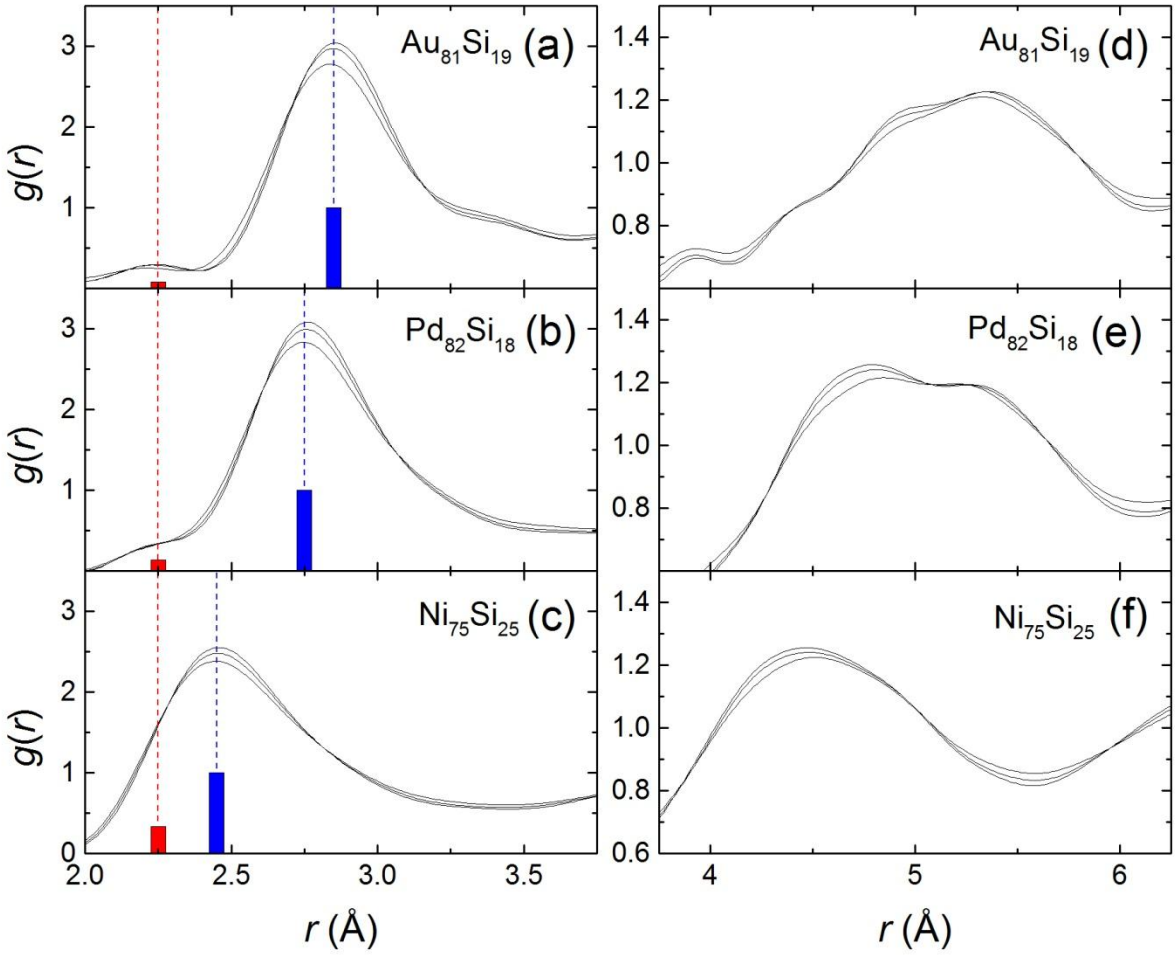

Figure 5.3: PDF first peaks for (a) $Au_{81}Si_{19}$, (b) $Pd_{82}Si_{18}$, and (c) $Ni_{75}Si_{25}$ and second peaks for (d) $Au_{81}Si_{19}$, (e) $Pd_{82}Si_{18}$, and (f) $Ni_{75}Si_{25}$. Shown are the highest temperature (lowest amplitude), intermediate temperature, and lowest temperature (highest amplitude) PDFs corresponding to the $S(q)$s in Fig. 5.2 for each composition. For Figs. (a-c), shown are the estimated average atomic distances for the TM-Si atomic pairs (red) and TM-TM pairs (blue). Vertical bars illustrate the relative strengths of the X-ray FZ weightings for the TM-Si (red) and TM-Pd (blue) PPCFs.

The character of the second coordination shell in $g(r)$ is can also be examined in Figure 5.3. The second peaks for both $Au_{81}Si_{19}$ and $Pd_{82}Si_{18}$ show distinct asymmetries, with a developing shoulder or splitting of the peak. The peak splitting in $Au_{81}Si_{19}$ has been observed previously [48], exhibiting a growing lower-*r* shoulder, with a dominant higher-*r* peak. The second coordination shell for $Pd_{82}Si_{18}$ exhibits a developing lower-*r* peak and a higher-*r*

shoulder, with the relative sub-peak heights opposite to those for $Au_{81}Si_{19}$. As mentioned in Chapter 4, this splitting of the second peak is clearly observed in Pd-Si binary glasses [54, 55], but had not been observed in the liquid. The splitting of the second coordination shell is a feature common to both simulations [56] and experimental measurements [57] of metal-metalloid amorphous alloys, and it is also observed in dense random packing of hard-sphere (DRPHS) and soft-sphere (DRPSS) models [58]. For $Ni_{75}Si_{25}$, however, the second coordination shell does not exhibit a split peak, but rather a slight asymmetric character typical for TM-TM based liquids [45, 59]. Ultimately, given the differences in atomic radii of the TM elements, as well as the similar stoichiometry of each of the three binary liquids, the qualitative differences in the first two peaks of both the static structure factors and the pair distribution functions point to some possible combination of structural, chemical, and X-ray scattering effect differences in these alloy liquids and glasses.

5.4 Analysis and Discussion

5.4.1 Structural, Chemical, and Scattering Effects

As discussed in Chapter 3 of this thesis, the asymmetric or unique features in the shape of the first coordination shell (FCS) in the $g(r)$ result from the contributions of nearest neighbor correlations from each chemically specific pair of elements in the alloy. The features of note, mentioned in Section 5.3 and visualized in Figure 5.3, are the differences in the positions of the first maxima for each binary liquid and the existence of a low-r sub-peak and shoulder in the $Au_{81}Si_{19}$ and $Pd_{82}Si_{18}$ binary liquids respectively. Given the smaller atomic size of Si compared with the sizes of Au and Pd, and given the chemical affinity between Si and both Au and Pd, the average atomic spacing for the TM-Si PPCF is likely much smaller than the Au-Au or Pd-Pd

average atomic spacing, giving a large separation in the respective first peak heights and, therefore, allowing their respective contributions to the first coordination shell to be resolved. On the other hand, no clear shoulder is observed for the $Ni_{75}Si_{25}$ liquid, suggesting that the average atomic Ni-Ni and Ni-Si distances are too similar for the individual PPCF peaks to be resolved in the total FCS.

In order to further understand the contributions from each of the PPCFs to the total $g(r)$ in the FCS, we must account for the atomic sizes of the constituent elements, chemical affinity between constituents, and the X-ray scattering factors for each constituent. Table 5.1 shows the average atomic distances, r, metallic and covalent atomic diameters, $r_{TM\text{-}TM}$ and $r_{TM\text{-}Si}$, and Faber-Ziman (FZ) weighting factors, $w_{ij}(0)$, for each composition. Estimates for the average atomic distances were made by assuming the first peak position in $g(r)$ corresponds to the peak position of the TM-TM PPCF (shown by the higher-r, blue dashed lines in Fig. 5.3(a-c)). This estimate is justified since the total $g(r)$ is dominated by the contribution from the TM-TM PPCF in all three binary liquids, as illustrated by the relative TM-TM FZ weighting (higher-r, blue bars) to those of the TM-Si weighting (lower-r, red bars). The TM-Si peak position was estimated from the positions of the low-r shoulders in both the $Au_{81}Si_{19}$ and $Pd_{82}Si_{18}$ PDFs (shown by the lower-r, red dashed lines in Fig. 5.3(a-c)). Because there is no shoulder in the $Ni_{75}Si_{25}$ FCS, the Ni-Si average atomic distances were estimated from shoulders in the other binary liquids. While the Ni-Si average atomic distance is unlikely the same as those TM-Si distances in the other liquids, the estimation serves to illustrate the difficulty in distinguishing contributions from the PPCFs in the $Ni_{75}Si_{25}$ liquid, due to a lack of separation of their average atomic distances. Included in Table 5.1 are the average atomic distances taken from both experimental measurements [53-55, 60] and MD simulations [23-26] for comparison with the

given estimations from the liquid data. Metallic diameters for the TM elements were calculated for 12-coordination [61], and covalent atomic diameters for both the TM element and Si are calculated from covalent radii determined from a database of crystal structures [62]. The calculated metallic diameter for Si comes from the average atomic spacing found in PDF measurements of liquid Si [63, 64]. These atomic sizes serve as basic estimations for the range of average TM-TM and TM-Si distances that might be expected. For comparison, the metallic diameter for Si is 2.44-2.48 Å and the covalent diameter is 2.22 Å. Enthalpies of mixing between the TM element and Si were calculated based on Miedema's microscopic model [32]. The FZ factors, determining the relative weighting for each PPCF, are calculated using

$$w_{ij}(0) = \frac{c_i c_j Z_i Z_j}{\langle Z \rangle} \tag{5.2}$$

for the lowest order approximation to the X-ray atomic form factors.

Table 5.1: Average partial-pair atomic distances (in Angstroms), r_{ij}, enthalpies of mixing, ΔH^{mix}, and Faber-Ziman X-ray weighting factors, $w_{ij}(0)$, for each binary liquid.

	$Au_{81}Si_{19}$		$Pd_{82}Si_{18}$		$Ni_{75}Si_{25}$	
	$r_{Au\text{-}Au}$	$r_{Au\text{-}Si}$	$r_{Pd\text{-}Pd}$	$r_{Pd\text{-}Si}$	$r_{Ni\text{-}Ni}$	$r_{Ni\text{-}Si}$
Distance (This Work)	2.85	2.25	2.75	2.25	2.45	[2.25]*
Distance[1] (MD)	2.76	2.48	2.73	2.54	2.49	2.48
Distance[2] (Experiment)	2.82-2.83	2.40-2.42	2.73, 2.8	2.54, 2.42	2.59	2.37
Metallic spacing[3] ($r_i + r_j$)	2.88	2.66-2.68	2.74	2.59-2.61	2.5	2.47-2.49
Covalent spacing[4] ($r_i + r_j$)	2.72	2.47	2.78	2.5	2.48	2.35
ΔH^{mix} (TM-Si)[5] ($kJ \cdot mol^{-1}$)	-30		-55		-40	
$w_{TM\text{-}TM}(0)$	0.9218		0.8787		0.7347	
$w_{TM\text{-}Si}(0)$	0.0766		0.1174		0.2449	
$w_{Si\text{-}Si}(0)$	0.0016		0.0039		0.0204	

*Estimate from Au-Si and Pd-Si FCS
[1]Distances reported from MD simulations for $Au_{81}Si_{19}$ [23], $Pd_{82}Si_{18}$ [26], and $Ni_{75}Si_{25}$[24, 25].
[2]Distances estimated from previous X-ray and neutron scattering measurements of $Au_{81}Si_{19}$ [53], $Pd_{82.5}Si_{17.5}$ [54], $Pd_{80}Si_{20}$ [55], and $Ni_{50}Si_{50}$ [60] liquids and glasses.
[3]Metallic radii for TM atoms calculated for 12-coordination [61] and for Si from experimental measurements of liquid Si average nearest neighbor distances [63, 64]
[4]Covalent spacings calculated from covalent radii determined from a database of crystal structures [62].
[5]Enthalpies of mixing calculated based on Miedema's microscopic model [32].

As shown in Table 5.1, the estimates for the Pd-Pd and Ni-Ni average atomic distances using the peak positions of the FCS are consistent with both previously published results and estimates based on the metallic diameters measured for the elements. The slightly lower value for the Ni-Ni distance compared to the MD and metallic radius estimates is most likely due to the shift of the overall shape of FCS towards lower *r* due to stronger contributions from the Ni-Si PPCF in the first coordination shell. This is also consistent with the expectation that the Ni-Si average atomic distance is smaller than the Ni-Ni distance, assuming either chemical affinity between Ni and Si or possible covalent-like bonding between the elements, adding weight to the low-*r* portion of the total FCS peak. On the other hand, the estimate of the Au-Au average atomic distance is slightly larger than, but close to, the value from previous experimental

measurements, and both are larger than the simulated Au-Au pair distance calculated from MD. A possible explanation for the slightly smaller value in the total average atomic separation compared to the metallic radius of Au is that the total PDF average distance is decreased due to smaller "interstitial" solute Si atoms and small contributions from the Au-Si partial to the total FCS. This explanation, however, is inconsistent with the data for $Pd_{82}Si_{18}$ and, therefore, may require a more in-depth analysis of the specific local topologies in the liquid that is beyond the scope of this thesis.

In the $Au_{81}Si_{19}$ liquid, the estimate for the Au-Si distance is smaller than the value 2.40-2.42 Å reported in Si-rich Au-Si alloys [53], the value 2.48 Å calculated from MD simulation [23, 65], and the value 2.66-2.68 Å calculating by combining their respective metallic radii [62]. This implies that either the shoulder is the result of spurious ripples due to truncation error during PDF determination [66], or that the published data underestimate the chemical affinity between the two elements (and therefore overestimate the partial pair average atomic distance). It is interesting that the sub-peaks for $Au_{81}Si_{19}$ and $Pd_{82}Si_{18}$ are at a similar distance even though the atomic radius for Au is larger and its enthalpy of mixing with Si is estimated to be smaller. It is also interesting to the note that the low-*r* shoulder observed in neutron scattering experiments in much more similar in character to the shoulder for the $Pd_{82}Si_{18}$ liquid. This again suggests that the separated low-*r* sub-peak arises from an unphysical ripple due to truncation error and that the Au-Si peak cannot be resolved in the total FCS using X-ray diffraction.

A similar analysis of the peak and shoulder positions for Pd-Si alloys was performed. X-ray diffraction measurements of $Pd_{82.5}Si_{17.5}$ found the Pd-Pd and Pd-Si distances to be 2.73Å and 2.54 Å respectively [54], while neutron measurements of $Pd_{80}Si_{20}$ found the distances to be 2.8 and 2.42 Å respectively [55]. The range given by these measured values encompasses the

distances determined from both MD simulations and estimated from the covalent radii, but all three values given for the Pd-Si average atomic distance overestimate the distance determined in this work. MD simulations of the $Pd_{82}Si_{18}$ liquid simply do not show the low-*r* shoulder (see Ch. 4) and therefore may incorrectly model the Pd-Si average atomic distance. On the other hand, one possible explanation for the overestimate from previous experimental measurements is that the measurements were made from glassy samples, and given the observed anomalous contraction of the first peaks in the PPCFs for many systems, the average Pd-Si atomic distances will be larger in the amorphous solid state than in the liquid state. Similarly, sharpening of the PPCF peak with decreasing temperature will narrow the spread of the Pd-Si PPCF and may result in a perceived higher-*r* shoulder position. Finally, the similar character of the shoulder compared to the one found for the $Au_{81}Si_{19}$ via neutron diffraction measurements also indicates that it likely results from the Pd-Si PPCF peak.

RMC simulations constrained by structure factors determined from neutron scattering using the isotopic substitution technique gave Ni-Ni and Ni-Si average pair distances for $Ni_{50}Si_{50}$ of 2.59 Å and 2.37 Å respectively [60], producing values deviating from those from MD simulations by ±0.11 Å for each partial pair. The MD simulation results closely resemble the estimates given for the respective metallic radii. The expected average Ni-Si bond distance, however, should be smaller than the sum of the respective metallic radii, either because of the estimate for the large enthalpy of mixing between Ni and Si or the possibility for covalent like bonding in the liquid. The measured FCS peak position for the $Ni_{75}Si_{25}$ liquid is close to the value of expected by assuming an ideal mixing for a Ni-centered, 12-coordinated cluster using the atomic distances calculated from the covalent radii (assuming that the Si-Si contribution to the X-ray signal from Si-centered clusters is small due to the low relative FZ weighting). This

suggests that there is either some covalent-like bonding in this system, or that the chemical affinity between Ni and Si is large enough to reduce the average atomic distance in the liquid from estimates based on metallic radii. In fact, MD studies suggest that covalent bonding is not prevalent in low-Si content Ni-Si alloy liquids, enhancing arguments suggesting stronger chemical affinity [24].

Diffraction measurements from the liquid Si [63, 64, 67], liquid $Ni_{50}Si_{50}$ and $NiSi_2$ [60], and crystalline structures of (Yb, Ca, Ce)-Au-Si alloys [68-70] have suggested that the Si-Si average atomic distance are anywhere in the range of 2.19 – 2.77 Å. Because of the small Si-Si FZ factors relative to the other partials, contributions from the Si-Si PPCF, and ultimately the average atomic distance, are impossible to resolve from the total $g(r)$. Only the Si-Si distances determined from MD simulations of $Pd_{82}Si_{18}$ [26] lie outside of this experimentally suggested range, likely due to a tendency toward extreme solute-solute avoidance in the simulations. The experimental evidence for small TM-Si bonding distances ultimately suggests a need for improved measurements and refined MD potentials in order to understand the true bonding character in these TM-Si binary liquids.

5.4.2 Structural Evolution

As mentioned in Sect. 5.3, the total structure factor $S(q)$, and the total pair distribution function, $g(r)$, exhibit sharpening and growth in the various peaks with decreasing temperature. Similar to discussions in Chapters 3 and 4, as well as from previous experimental results [18-21], quantitative measures of the first peak in the structure factor, $S(q_1)$, allow distinctions to be made about the temperature evolution of the average liquid structure. The rate of change of ordering in the system, as measured by changes in the peak height and the acceleration of ordering, provide

insight into the relationship between the structural evolution and the kinetic behavior of the system. While $S(q_1)$ reflects the average structure of the system, changes in $g(r_1)$, or changes in the correlation strength for nearest neighbor atoms, can also be used to qualitatively distinguish the temperature evolution of the average local structure [18].

Figure 5.4 shows the temperature dependence of both $S(q_1)$ and $g(r_1)$ for each of the three binary liquids, $Au_{81}Si_{19}$, $Pd_{82}Si_{18}$, and $Ni_{75}Si_{25}$. The first peak heights in $S(q)$ (Fig. 5.4(a-c)) show linear behavior as the liquid evolves from the equilibrium high temperature liquid down to the liquidus or eutectic temperatures (represented by vertical dashed lines), and, in the case of $Au_{81}Si_{19}$ and $Pd_{82}Si_{18}$, into the supercooled liquid regime. The changes in the peak heights normalized to the heights at the solidus temperatures, $\frac{1}{[S(q)]}\frac{dS(q)}{dT}$ at T_S, are -4.7440 x 10^{-4}, -4.5025 x 10^{-4}, and -3.9944 x 10^{-4} for $Au_{81}Si_{19}$, $Pd_{82}Si_{18}$, and $Ni_{75}Si_{25}$ respectively. This suggests a larger relative structural change with decreasing temperature for $Au_{81}Si_{19}$ than for $Pd_{82}Si_{18}$, with $Ni_{75}Si_{25}$ having the smallest relative peak growth. For $Au_{81}Si_{19}$ (Fig. 5.4(a)), based on the relatively large peak height measured at the highest temperature (T = 550 °C) compared to the linear average, there does appear to be a slight upward inflection in the $S(q_1)$ evolution. The inflection is small, though, and its existence would need to be confirmed by measurements of the liquid structure down to lower temperatures, possibly by the use of neutron diffraction since high-energy X-rays have been found overcharge Au-Si samples, destabilizing levitation at the equilibrium and supercooled temperatures.

As mentioned in Chapter 4, it is important to note that the peak heights and relative peak growth rates are influenced by the scattering strength from and relative peak positions of each of the partial structure factors (PSFs). Of these three binary alloy liquids, we might expect $Pd_{82}Si_{18}$, the kinetically strongest of the three, to have the largest peak growth rate at the melt temperature.

However, a separation of the first peak positions, q_1, between the Pd-Pd and Pd-Si PSFs, will depress both the total $S(q_1)$ peak height and the growth rate. The scattering strength of the TM-TM partial (see Table 5.1) will determine how strongly the peak growth rate of the TM-TM PSF influences the total $S(q_1)$ growth rate (as discussed for PPCFs in Chapter 3). Therefore, the larger relative weighting of the Au-Au partial might result in a larger growth rate due to the smaller influence from the other partials, explaining why the peak growths trend with TM-TM FZ weighting. It might not be possible to discern a structural signature of the kinetic strength from the growth rate at the melting temperature without further knowledge of the chemically specific PSFs.

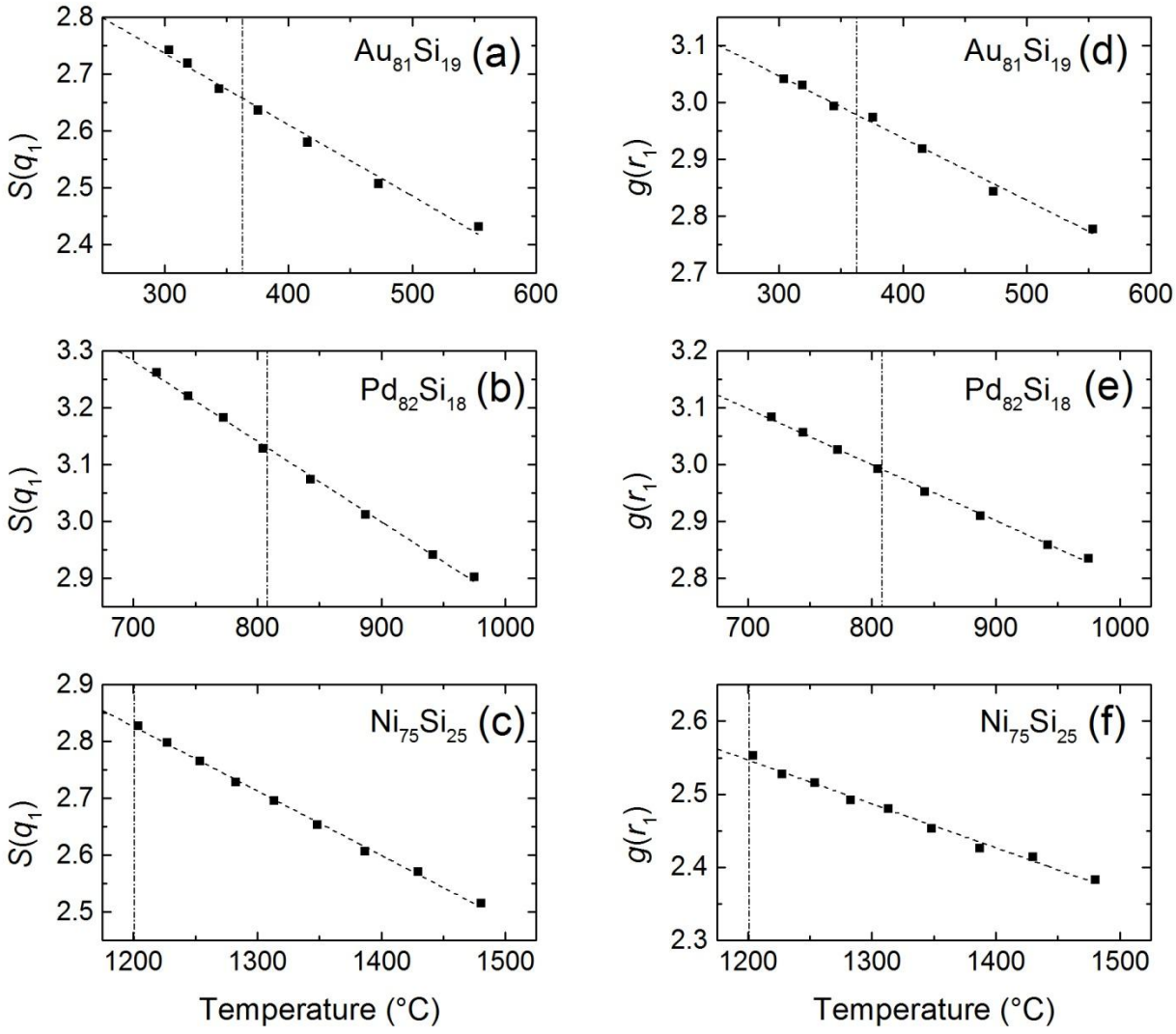

Figure 5.4: First peak heights, $S(q_1)$, of the total structure factor for (a) $Au_{81}Si_{19}$, (b) $Pd_{82}Si_{18}$, and (c) $Ni_{75}Si_{25}$, and first peak heights, $g(r_1)$, of the total pair distribution function for (d) $Au_{81}Si_{19}$, (e) $Pd_{82}Si_{18}$, and (f) $Ni_{75}Si_{25}$. Diagonal dashed lines represent the best linear fit to the peak height growth with decreasing temperature. Vertical dash-dot lines signify the solidus temperature, T_S, for each $Au_{81}Si_{19}$ (T_S = 360 °C), $Pd_{82}Si_{18}$ (T_S = 808 °C), and $Ni_{75}Si_{25}$ (T_L = 1200 °C).

A similar discussion can be made for the first peak heights in $g(r)$ (Fig. 5.4(d-f)). Again, each increases linearly with decreasing temperature. The growth in $g(r)$ with decreasing temperature, relative to the peak height at the solidus temperature, $\frac{1}{[g(r)]}\frac{dg(r)}{dT}$ at T_S, is 3.6954 x 10^{-4}, -3.2876 x 10^{-4}, and -2.3601 x 10^{-4} for $Au_{81}Si_{19}$, $Pd_{82}Si_{18}$, and $Ni_{75}Si_{25}$ respectively. The

average nearest neighbor correlation again grows most strongly with decreasing temperature for $Au_{81}Si_{19}$, with slower relative growth for $Pd_{82}Si_{18}$ and $Ni_{75}Si_{25}$. Because of the finite q-range of the experimental data and truncation effects when transforming $S(q)$, measures of $g(r)$ are less reliable as quantitative measures of the structural evolution. Relative uncertainties in $g(r_1)$, as determined from uncertainties in intensity (determined by the method described by Hammersly [71]), fluorescence and scaling corrections, and measurements of the density, are on the order of 1.25-2.5%. Therefore, fluctuations in the peak height above and below the linear average shown in Figure 5.4(d-f) are well within the estimated uncertainty for the peak heights.

5.4.3 Structural Fragility

As discussed in Chapter 3 and mentioned in previous experimental results [18, 19, 21], the rate of structural ordering in the supercooled liquid regime seems to correlate with the kinetic fragility of the liquid. The structural basis for the kinetic fragility can be measured by comparing the structural ordering in the high temperature and supercooled liquid to the structure of the corresponding glass. In this experiment, measurements of the temperature evolution of the glass structure were obtained only for the ternary bulk-glass former, $Pd_{77}Cu_6Si_{17}$. Because of the qualitative and quantitative similarities in the structures of the $Pd_{77}Cu_6Si_{17}$ and $Pd_{82}Si_{18}$, liquids, measurements of the structural fragility in one system can provide insight into the structural behavior of the other.

Figure 5.5 shows the total structure factors, $S(q)$, and the reduced pair distribution function, $G(r)$, for both the bulk glass and bulk liquid samples for $Pd_{77}Cu_6Si_{17}$. $G(r)$ is related to $g(r)$ since it is the straightforward Fourier transform of $S(q)$, given by

$$G(r) = 4\pi r\rho_0(g(r) - 1) = \frac{2}{\pi}\int q(S(q) - 1)\sin(qr)\,dq. \qquad (5.3)$$

While very similar in character to the PDF, $G(r)$ allows us to qualitatively understand the temperature evolution of the real space correlations, even without a direct measurement of the average atomic density, which is difficult to obtain for samples without perfectly smooth, spherical surfaces [72, 73]. The glass structure shows sharpening and growth of the peaks with decreasing temperature. Since slow kinetics will not allow the structure to change significantly below T_g, the observed changes must be due to atomic vibrations, which can be described within the Debye Theory [74]. The inset in Figure 5.5(a) shows the dramatic growth and shift toward high-q of the first peak in $S(q)$ for the glass. A well-defined shoulder in the second peak is also observed, typical of many metallic glasses. Similarly, the reduced PDF for the glass data show a sharpening and growth of each of the coordination shells, with a shift toward higher r of the first coordination shell from the liquid to the glass (as shown in the inset for Fig. 5.5(b)). The splitting of the second coordination shell is more pronounced in the glass, exhibiting two distinct peaks similar to those found in previously reported structural data for Pd-Si glasses [54, 55] (see Chapter 4).

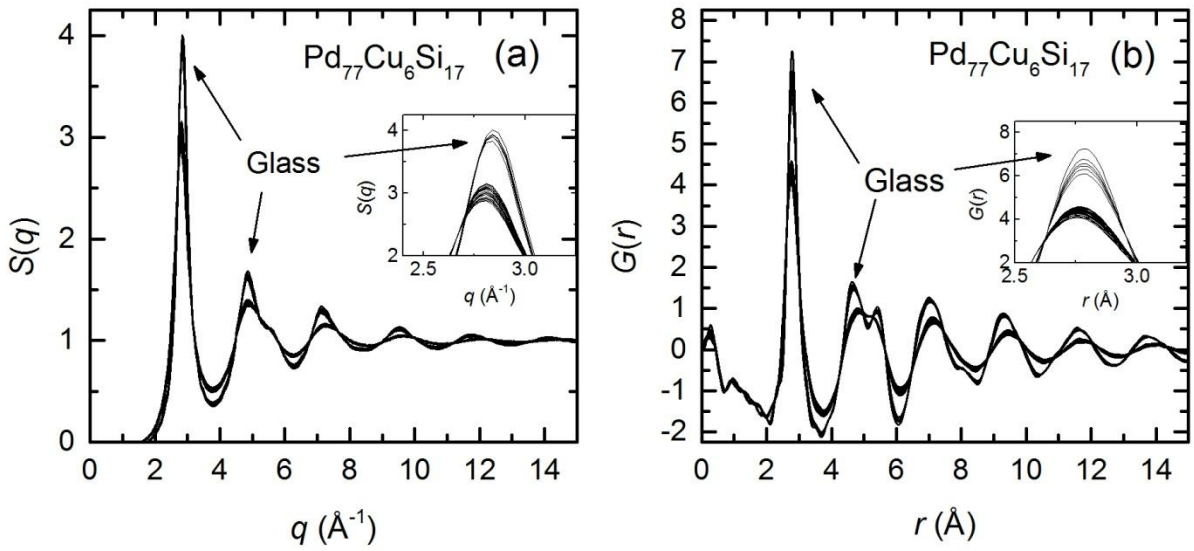

Figure 5.5: (a) Total structure factor, $S(q)$, and (b) reduced pair distribution functions, $G(r)$, for $Pd_{77}Cu_6Si_{17}$ for both the liquid and glass measurements at all temperatures. Insets in both (a) and (b) show the development of the first peak. Glass data exhibit sharper peaks and include a splitting of the second peak in $G(r)$.

As seen in Figure 5.1, the total $S(q)$ and $g(r)$ for both the $Pd_{82}Si_{18}$ and $Pd_{77}Cu_6Si_{17}$ liquids are quite similar and evolve similarly with decreasing temperature. This similarity in the reduced PDFs is clearly seen in Figure 5.6. Here the highest and lowest temperatures for both liquids are shown in combination with the bulk glass data taken for $Pd_{77}Cu_6Si_{17}$. Given the similarities in the S(q)s and G(r)s for the two liquids, and the similar peak character and positions in both the liquid and glass for $Pd_{77}Cu_6Si_{17}$, it is reasonable to assume that their respective glass structures of the two alloys may also exhibit similar character. Both the liquids and the glass data show a shoulder in the low-r region of the first coordination shell, which is attributed to the first peak Pd-Si PPCF. The evolution of the shoulder from liquid $Pd_{77}Cu_6Si_{17}$ suggests an increase in the average atomic Pd-Si spacing upon cooling from the high temperature liquid down to the glass. This shift fits with our explanation in Section 5.4.1 of the differences in the estimated Pd-Si average atomic distance in the liquid with previous experimental measurements of the amorphous solid. The sharpness of the shoulder is most likely the result of improved resolution

due to the sharpening of the individual PPCF first coordination peaks. The shift of the shoulder to higher *r* from the liquid to the glass, though, suggests an increase in the Pd-Si average atomic distance, quite possibly due to "anomalous contraction" effects [43] from increased Pd-Si coordination.

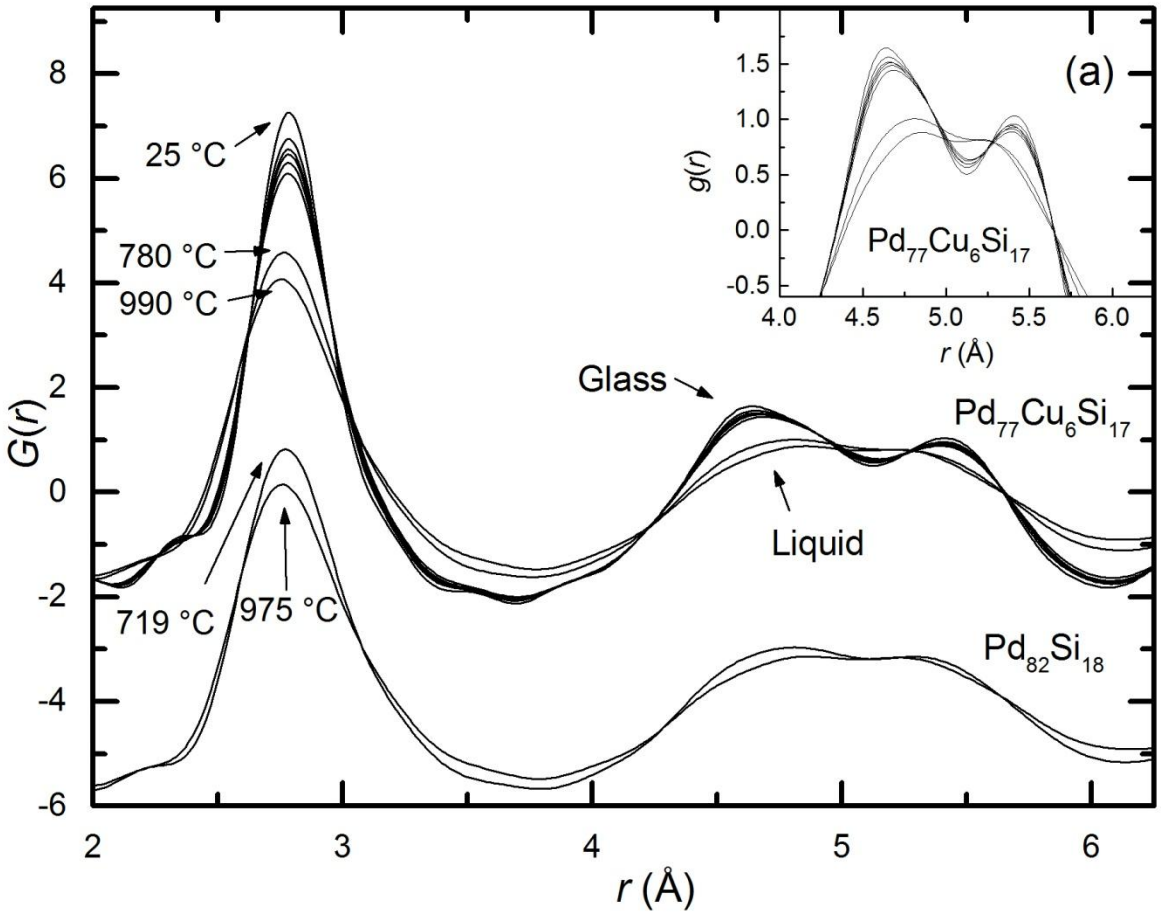

Figure 5.6: Total reduced pair distribution functions, $G(r)$, for the highest (smaller amplitude) and lowest (larger amplitude) $Pd_{82}Si_{18}$ liquid data (bottom) as well as the highest and lowest temperature liquid data for $Pd_{77}Cu_6Si_{17}$ (top). Liquid data for both compositions are incredibly similar in shape, position, and amplitude. Also included are the glass $G(r)$ for $Pd_{77}Cu_6Si_{17}$ for every temperature measured. The (a) inset shows the development of the split second peak from liquid to glass.

Using measurements of the strength of the average correlation length, $S(q_1)$, for both liquid and glass data, a measure of the "structural fragility index" [21], γ, given by

$$\gamma = 100 * \frac{\left(S(q_1)_{glass} - S(q_1)_{liquid\ extrapolation}\right)}{S(q_1)_{glass}} \text{ at } T_g, \tag{5.4}$$

can be calculated. Figure 5.7 shows the difference in $S(q_1)$ between the glass and the extrapolation of the liquid data at the glass transition temperature (T_g = 380 °C for $Pd_{77.5}Cu_6Si_{16.5}$ [75]). The structural fragility index can be related to the kinetic strength of the liquid by fitting measurements of the viscosity to the Vogel-Fulcher-Tammen equation, given by

$$\eta = \eta_0 \exp\left(\frac{D^* T_0}{T - T_0}\right), \tag{5.5}$$

where D^* is the kinetic strength parameter, η_0 is the viscosity in the infinite temperature limit and T_0 is the temperature at which the viscosity becomes infinite. Using previously measured viscosity data compiled by Komatsu [75], the kinetic strength parameter for $Pd_{77.5}Si_6Si_{16.5}$, D^*, is 6.9. Assuming the kinetic strength does not shift dramatically with the 0.5% substitution of Si for Pd, the measured index for $Pd_{77}Cu_6Si_{17}$ (γ = 4.03) fits well with the correlation empirically measured by Mauro et al. [21] for a range of metallic alloys, given by

$$\gamma = -3.30308 * D^* + 26.64598, \tag{5.6}$$

which predicts a value of γ = 3.85 for a D^* of 6.9.

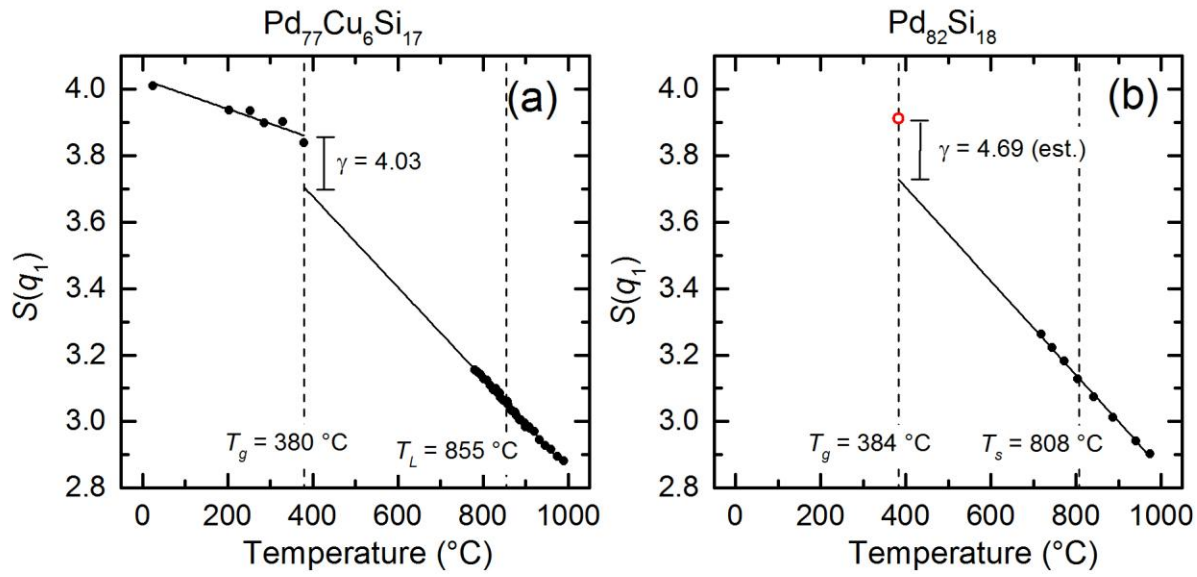

Figure 5.7: The evolution in the total structure factor first peak height, $S(q_1)$, for both (a) $Pd_{77}Cu_6Si_{17}$ and (b) $Pd_{82}Si_{18}$. Solids represent the linear extrapolations of the liquid $S(q_1)$ data down to the respective T_g's of each composition as well as the extrapolation of the glass data up to T_g. Vertical dashed lines represent T_g and the solidus temperature T_S for each composition. (a) The calculated structural fragility index is shown from the measure of the discrepancies in the liquid and glass extrapolations to T_g. (b) The $S(q_1)$ height at T_g (red open circle) is predicted from the estimated structural fragility index using previously published viscosity data [75] and the fit to the experimentally determined correlation [21] between the structural fragility index and the fragility strength parameter D^*.

Because of the similarities in the liquid structures for $Pd_{82}Si_{18}$ and $Pd_{77}Cu_6Si_{17}$, the structural fragility indices for the two systems are likely similar and proportional to their respective kinetic behaviors. From this assumption, the proportionality ($d\gamma/dD^* = -3.30308$) from the empirical correlation in Eq. 5.6 can be used in combination with the measured kinetic strength of $Pd_{82}Si_{18}$ ($D^* = 6.7$ [75]) to estimate its structural fragility index. Using the estimated index, $\gamma = 4.69$, a prediction for the peak height in the glass at T_g can be made. Fig. 5.7(b) shows the estimated jump from the liquid extrapolation to the estimated glass peak height at T_g, $S(q_1) = 3.911$. The fragility index measured for $Pd_{77}Cu_6Si_{17}$ and estimated for $Pd_{82}Si_{18}$ is smaller than for some of the binary TM-TM liquids ($\gamma \sim 7$ to 13) [18, 19, 21], particular the Cu-Zr binary ($Cu_{50}Zr_{50}$, $\gamma \sim 10$) [19]. The stronger kinetic behavior, as estimated from the structural fragility

index and the viscosity evolution, for $Pd_{82}Si_{18}$ is consistent with previously published MD results [26].

It is important to note, though, that Komatsu's compiled viscosity data originate from two distinct sources; the primary source taken from viscosity data measured near T_L [76], and the secondary source taken from data measured near T_g [77]. While the secondary source contains data for $Pd_{77}Cu_6Si_{17}$, among other compositions, its parameters for the fitting the viscosity data vary considerably from those in the primary source. The D^* measured for $Pd_{77}Cu_6Si_{17}$ from the secondary source predicts a fragility index of $\gamma = 5.84$ which is considerably larger than the jump measured in our data. Also, the empirical correlation measured by Mauro et al., from which Eq. 5.6 is obtained, measures the kinetic strength parameter at a temperature near T_L, and therefore would be more consistent with data provided by Komatsu's primary source. Finally, the secondary source does not contain a measurement for $Pd_{82}Si_{18}$, and therefore any inconsistencies between experimental measurement techniques of the two sources will become apparent when trying to compare between the binary and ternary liquids. Ultimately, it will be important to measure the viscosities of both $Pd_{77}Cu_6Si_{17}$ and $Pd_{82}Si_{18}$ in the WU-BESL as well as make similar glass ribbon measurements for both compositions to verify these results and predictions.

5.5 Conclusions

The results presented show the first liquid structural data collected for four metal-metalloid based alloys utilizing a containerless processing technique. In all cases, liquid data were obtained above and below T_L, and below the eutectic temperatures in the cases of $Au_{81}Si_{19}$ and $Pd_{82}Si_{18}$. Differences in the average correlation length between the three binary liquids were observed, while shapes of the $Pd_{82}Si_{18}$ and $Ni_{75}Si_{25}$ second peaks indicated the possibility of

ISRO in these systems. The $Au_{81}Si_{19}$ liquid, however, exhibits a more uniform second peak, much like that of the pure Au liquid. Structural metrics, such as the first peak heights in the total structure factor, $S(q_1)$, and total pair distribution function, $g(r_1)$, show linear growth with decreasing temperature as the system cools from the high temperature equilibrium liquid into the supercooled liquid regime, suggesting that no abrupt structural shift or rapid structural change occurs at temperatures above those for which data was collected.

"Anomolous contraction" of the first coordination shell in $g(r)$ and the reduced pair distribution function, $G(r)$, was observed for all four liquids in agreement with results from many pure metallic and metallic alloy liquids. Because of the overwhelming scattering strength from the TM component of the alloy, information about the TM-Si and Si-Si correlations are difficult to discern or extract from the total scattering data. However, in the $Pd_{82}Si_{18}$ and $Pd_{77}Cu_6Si_{17}$ liquids, as well as in the $Pd_{77}Cu_6Si_{17}$ glass structures, a small contribution from the TM-Si first peak was evidenced as a shoulder to the total first coordination shell, confirming previous experimental results. The lack of shoulder and low total average atomic distance in the $Ni_{75}Si_{25}$ liquid suggests a closeness in the Ni-Ni and Ni-Si average atomic distances. Although slightly overestimated in the case of $Au_{81}Si_{19}$, the main peak position of the first coordination shell provides an accurate estimate for the TM-TM average atomic distance in the binary $Au_{81}Si_{19}$ and $Pd_{82}Si_{18}$ liquids. Estimates for the TM-Si average atomic distance underestimate previous experimental and theoretical results and may require data from other scattering techniques, such as neutron scattering, for a more accurate measurement.

The second coordination shells for $Au_{81}Si_{19}$, $Pd_{82}Si_{18}$, and $Pd_{77}Cu_6Si_{17}$ all exhibit a split peak common to TM-metalloid glasses, but not previously observed for the $Pd_{82}Si_{18}$ liquid. The distances corresponding to the split, which develops into two distinct peaks in the case of the

$Pd_{77}Cu_6Si_{17}$ glass, are similar to those found in early DRPHS models as well as in early experimental data and MD simulation data. Similar to previous experimental results for $Au_{81}Si_{19}$, the relative heights of the low-*r* and high-*r* subpeaks in the second coordination shell qualitatively match that of theoretical studies. On the other hand, the general shape of the second coordination shell for $Pd_{82}Si_{18}$ and $Pd_{77}Cu_6Si_{17}$ more closely resembles experimental data for TM-metalloid amorphous alloys.

Finally, a measure of the structural fragility was obtained for the $Pd_{77}Cu_6Si_{17}$ corroborating previous experimental results and indicating a relatively strong liquid compared to that of other TM-TM binary liquids. A measurement of the structural fragility index for $Pd_{77}Cu_6Si_{17}$, combined with experimentally determined viscosity data, gives a prediction for the structural fragility index of $Pd_{82}Si_{18}$. Measurements of the liquid viscosity via electrostatic levitation and structural measurements of the glass in both systems are necessary, though, to confirm the results and predictions of the structural fragility.

5.6 References

[1] W. Klement, R. H. Willens and P. O. L. Duwez, Nature **187** (4740), 869 (1960).
[2] H. S. Chen, Acta Metallurgica **22** (12), 1505 (1974).
[3] A. J. Drehman, A. L. Greer and D. Turnbull, Applied Physics Letters **41** (8), 716 (1982).
[4] N. Mattern, H. Hermann, S. Roth, J. Sakowski, M.-P. Macht, P. Jovari and J. Jiang, Applied Physics Letters **82** (16), 2589 (2003).
[5] Y. Li, Materials Transactions **42** (4), 556 (2001).
[6] R. Busch, J. Schroers and W. H. Wang, MRS Bulletin **32** (08), 620 (2007).
[7] Y. Q. Cheng and E. Ma, Progress in Materials Science **56** (4), 379 (2011).
[8] C. A. Angell, MRS Bulletin **33** (05), 544 (2008).
[9] J. C. Bendert and K. F. Kelton, Journal of Non-Crystalline Solids **376** (0), 205 (2013).
[10] C. A. Angell, Journal of Physics and Chemistry of Solids **49** (8), 863 (1988).
[11] K. Ito, C. T. Moynihan and C. A. Angell, Nature **398** (6727), 492 (1999).
[12] L. M. Martinez and C. A. Angell, Nature **410** (6829), 663 (2001).
[13] S. Sastry, P. G. Debenedetti and F. H. Stillinger, Nature **393** (6685), 554 (1998).
[14] G. Duan, D. Xu, Q. Zhang, G. Zhang, T. Cagin, W. L. Johnson and W. A. Goddard, Physical Review B **71** (22), 224208 (2005).

[15] Y. Q. Cheng, H. W. Sheng and E. Ma, Physical Review B **78** (1), 014207 (2008).
[16] N. Jakse and A. Pasturel, Physical Review B **78** (21), 214204 (2008).
[17] R. Soklaski, Z. Nussinov, Z. Markow, K. F. Kelton and L. Yang, Physical Review B **87** (18), 184203 (2013).
[18] N. A. Mauro, M. L. Johnson, J. C. Bendert and K. F. Kelton, Journal of Non-Crystalline Solids **362** (0), 237 (2013).
[19] N. A. Mauro, A. J. Vogt, M. L. Johnson, J. C. Bendert and K. F. Kelton, Applied Physics Letters **103** (2) (2013).
[20] N. A. Mauro, A. J. Vogt, M. L. Johnson, J. C. Bendert, R. Soklaski, L. Yang and K. F. Kelton, Acta Materialia **61** (19), 7411 (2013).
[21] N. A. Mauro, M. Blodgett, M. L. Johnson, A. J. Vogt and K. F. Kelton, Nature Materials, (In Review) (2014).
[22] A. Pasturel, E. S. Tasci, M. H. F. Sluiter and N. Jakse, Physical Review B **81** (14), 140202 (2010).
[23] N. Jakse, T. L. T. Nguyen and A. Pasturel, Journal of Physics: Condensed Matter **23** (40), 404205 (2011).
[24] Y. J. Lü and P. Entel, Physical Review B **84** (10), 104203 (2011).
[25] Y. Lü and M. Chen, Acta Materialia **60** (11), 4636 (2012).
[26] J. Ding, Y.-Q. Cheng, H. Sheng and E. Ma, Physical Review B **85** (6), 060201 (2012).
[27] I. R. Lu, G. Wilde, G. P. Görler and R. Willnecker, Journal of Non-Crystalline Solids **250–252, Part 2** (0), 577 (1999).
[28] H. Okamoto and T. B. Massalski, Bulletin of Alloy Phase Diagrams **4** (2), 190 (1983).
[29] H. Okamoto, Journal of Phase Equilibria **14** (4), 536 (1993).
[30] P. Nash and A. Nash, Bulletin of Alloy Phase Diagrams **8** (1), 6 (1987).
[31] D. Turnbull, Contemporary Physics **10** (5), 473 (1969).
[32] A. Takeuchi and A. Inoue, Materials Transactions **41** (11), 1372 (2000).
[33] H. S. Chen and D. Turnbull, Journal of Applied Physics **38** (9), 3646 (1967).
[34] R. M. Waghorne, V. G. Rivlin and G. I. Williams, Journal of Physics F: Metal Physics **6** (2), 147 (1976).
[35] H. S. Chen, J. T. Krause, K. Shirakawa and T. Masumoto, Journal of Non-Crystalline Solids **41** (1), 79 (1980).
[36] S. Y. Hong, W. H. Guo and H. W. Kui, Journal of Materials Research **14** (09), 3668 (1999).
[37] Y. Ke-Fu and R. Fang, Chinese Physics Letters **22** (6), 1481 (2005).
[38] K. Yao and N. Chen, Science in China Series G **51** (4), 414 (2008).
[39] D. Hong-Yu, L. Yang and Y. Ke-Fu, Chinese Physics Letters **27** (12), 126101 (2010).
[40] A. K. Gangopadhyay, G. W. Lee, K. F. Kelton, J. R. Rogers, A. I. Goldman, D. S. Robinson, T. J. Rathz and R. W. Hyers, Review of Scientific Instruments **76** (7) (2005).
[41] N. A. Mauro and K. F. Kelton, Review of Scientific Instruments **82** (3) (2011).
[42] K. F. Kelton, G. W. Lee, A. K. Gangopadhyay, R. W. Hyers, T. J. Rathz, J. R. Rogers, M. B. Robinson and D. S. Robinson, Physical Review Letters **90** (19), 195504 (2003).
[43] A. K. Gangopadhyay, M. E. Blodgett, M. L. Johnson, J. McKnight, V. Wessels, A. J. Vogt, N. A. Mauro, J. C. Bendert, R. Soklaski, L. Yang and K. F. Kelton, The Journal of Chemical Physics **140** (4) (2014).
[44] N. A. Mauro and K. F. Kelton, Journal of Non-Crystalline Solids **358** (23), 3057 (2012).

[45] G. W. Lee, A. K. Gangopadhyay, R. W. Hyers, T. J. Rathz, J. R. Rogers, D. S. Robinson, A. I. Goldman and K. F. Kelton, Physical Review B **77** (18), 184102 (2008).
[46] M. I. Mendelev, M. J. Kramer, R. T. Ott, D. J. Sordelet, M. F. Besser, A. Kreyssig, A. I. Goldman, V. Wessels, K. K. Sahu, K. F. Kelton, R. W. Hyers, S. Canepari and J. R. Rogers, Philosophical Magazine **90** (29), 3795 (2010).
[47] V. Wessels, A. K. Gangopadhyay, K. K. Sahu, R. W. Hyers, S. M. Canepari, J. R. Rogers, M. J. Kramer, A. I. Goldman, D. Robinson, J. W. Lee, J. R. Morris and K. F. Kelton, Physical Review B **83** (9), 094116 (2011).
[48] S. Takeda, H. Fujii, Y. Kawakita, S. Tahara, S.Nakashima, S. Kohara and M. Itou, Journal of Alloys and Compounds **452** (1), 149 (2008).
[49] S. Sachdev and D. R. Nelson, Physical Review Letters **53** (20), 1947 (1984).
[50] T. Schenk, D. Holland-Moritz, V. Simonet, R. Bellissent and D. M. Herlach, Physical Review Letters **89** (7), 075507 (2002).
[51] G. W. Lee, A. K. Gangopadhyay, K. F. Kelton, R. W. Hyers, T. J. Rathz, J. R. Rogers and D. S. Robinson, Physical Review Letters **93** (3), 037802 (2004).
[52] H. Lou, X. Wang, Q. Cao, D. Zhang, J. Zhang, T. Hu, H.-k. Mao and J.-Z. Jiang, Proceedings of the National Academy of Sciences **110** (25), 10068 (2013).
[53] P. Chirawatkul, A. Zeidler, P. S. Salmon, S. i. Takeda, Y. Kawakita, T. Usuki and H. E. Fischer, Physical Review B **83** (1), 014203 (2011).
[54] P. Andonov, Journal of Non-Crystalline Solids **22** (1), 145 (1976).
[55] T. Fukunaga and K. Suzuki, Science Reports of the Research Institutes, Tohoku University, Series A **29** (2), 153 (1981).
[56] H. W. Sheng, W. K. Luo, F. M. Alamgir, J. M. Bai and E. Ma, Nature **439** (7075), 419 (2006).
[57] G. S. Cargill, Journal of Applied Physics **41** (5), 2248 (1970).
[58] J. L. Finney, Nature **266** (5600), 309 (1977).
[59] N. A. Mauro, W. Fu, J. C. Bendert, Y. Q. Cheng, E. Ma and K. F. Kelton, The Journal of Chemical Physics **137** (4) (2012).
[60] S. Gruner, J. Marczinke, L. Hennet, W. Hoyer and G. J. Cuello, Journal of Physics: Condensed Matter **21** (38), 385403 (2009).
[61] A. F. Wells, *Structural Inorganic Chemistry*, 5th ed. (Claredon Press, Oxford, 1984).
[62] B. Cordero, V. Gomez, A. E. Platero-Prats, M. Reves, J. Echeverria, E. Cremades, F. Barragan and S. Alvarez, Dalton Transactions (21), 2832 (2008).
[63] H. Kimura, M. Watanabe, K. Izumi, T. Hibiya, D. Holland-Moritz, T. Schenk, K. R. Bauchspieß, S. Schneider, I. Egry, K. Funakoshi and M. Hanfland, Applied Physics Letters **78** (5), 604 (2001).
[64] M. Watanabe, K. Higuchi, A. Mizuno, K. Nagashio, K. Kuribayashi and Y. Katayama, Journal of Crystal Growth **294** (1), 16 (2006).
[65] S.-H. Lee and G. S. Hwang, The Journal of Chemical Physics **127** (22) (2007).
[66] T. Egami and S. J. Billinge, *Underneath the Bragg peaks: structural analysis of complex materials*. (Elsevier, 2003).
[67] T. H. Kim, A. I. Goldman and K. F. Kelton, Philosophical Magazine **88** (2), 171 (2008).
[68] M. Pani, F. Merlo and M. L. Fornasini, Zeitschrift für Kristallographie **214** (2) (1999).
[69] H. Nakashima, A. Thamizhavel, T. D. Matsuda, Y. Haga, T. Takeuchi, K. Sugiyama, R. Settai and Y. Ōnuki, Journal of Alloys and Compounds **424** (1–2), 7 (2006).

[70] A. S. Sefat, A. M. Palasyuk, S. L. Bud'ko, J. D. Corbett and P. C. Canfield, Journal of Solid State Chemistry **181** (2), 282 (2008).
[71] A. P. Hammersley, S. O. Svensson, M. Hanfland, A. N. Fitch and D. Hausermann, High Pressure Research **14** (4-6), 235 (1996).
[72] N. A. Mauro, Ph.D. Thesis, Washington University in St. Louis, 2011.
[73] J. C. Bendert, Ph.D. Thesis, Washington University in St. Louis, 2013.
[74] S. Sinha, P. L. Srivastava and R. N. Singh, Journal of Physics: Condensed Matter **1** (9), 1695 (1989).
[75] T. Komatsu, Journal of Non-Crystalline Solids **185** (1–2), 199 (1995).
[76] H. Davies, in *Rapidly quenched metals III*, edited by B. Cantor (The Metals Society, London, 1978), Vol. 1, pp. 1.
[77] H. S. Chen, Science Reports of the Research Institutes, Tohoku University, Series A **27** (2), 97 (1979).

Chapter 6

Development, Operation, and Commissioning of an Electrostatic Levitator Optimized for Neutron Diffraction Studies of Metallic Liquids

The results reported in this chapter were obtained in collaboration with N. A. Mauro, K. S. Derendorf, M. L. Johnson, C. Pueblo, and K. F. Kelton (Washington University in St. Louis), G. E. Rustan, D. G. Quirinale, and A. I. Goldman (Iowa State University), and K. Lokshin and T. Egami (University of Tennessee). The author's personal contribution includes aid in construction and component testing, design and construction of optical components, development of operation and operating procedures, capacity testing of system operation, and participation and direction in commissioning experiments.

6.1 Introduction

As discussed in Chapter 1, the study of supercooled liquids is highly dependent on the ability to maintain samples in this metastable state long enough to acquire structural and thermophysical property measurements. This requires the reduction or elimination of heterogeneous nucleation in the supercooled liquid, which is best achieved through containerless processing. Further, studies of metallic liquids also require inert sample environments since the liquids typically have high melting temperatures and are highly reactive with the crucible

container or surrounding atmosphere. Containers can also dominate scattering signals in diffraction studies of weakly scattering samples. The electrostatic levitation (ESL) technique [1], which utilizes electrostatic force from a high voltage (HV) electric field to balance the gravitation pull on a charged sample, has been successfully used for studies of metallic liquids. While other levitation techniques exist (see Ch. 1), ESL enables the simultaneous levitation of a sample in a high-vacuum environment, while controlling sample temperature and making a variety of thermophysical property measurements. Recent developments in electrostatic levitation also allow for high-energy X-ray scattering measurements of the levitated bulk liquid. This reduces scattering from sources other than the sample, while combining thermophysical property and structural information [2]. Optimizing the Beamline Electrostatic Levitation (BESL) technique for *in situ* liquid studies at the Advanced Photon Source, Argonne National Lab has resulted in the creation of the WU-BESL [3] (see Ch. 2), utilized for the majority of the work in this thesis.

While X-ray scattering studies have provided a great deal of insight into both the liquid structure and its connection to glass formation, the technique is not without limitations. Coherent X-ray scattering studies provide only total structural information, and more complicated X-ray Absorption Spectroscopy (XAS) is required to extract chemically specific information about local environment structures. Due to scattering from the electron cloud by X-rays, the atomic form factor, and ultimately the total coherent scattering intensity, decays with scattering angle and, therefore, information is lost at high scattering angles. In addition, atomic form factors scale with an element's atomic number, *Z*, and, therefore, high *Z* elements can dominate the X-ray scattering signals from the sample. From a practical standpoint for

electrostatic levitation, the high X-ray energies required to probe atomic length scales can have a charging effect on the sample which can interfere with levitation control.

Neutron scattering studies of levitated liquids can provide complimentary structural information. Neutrons interact with atomic nuclei, rather than the electron cloud, allowing chemical and larger high-angle diffraction signal from both coherent and incoherent scattering studies. The coherent scattering lengths, *b*, for the individual elements are not only constant with respect to momentum transfer, *q*, but they also do not necessarily scale linearly with *Z*. Without the need to invoke atomic form factors (which decay rapidly with increasing momentum transfer, *q*) for the electron cloud distributions, signal at higher-*q* can be more readily acquired. Also, some elements that scatter weakly in X-ray diffraction experiments have much larger relative signal in coherent neutron total scattering data, such as the light elements like oxygen. Similarly, through the use of isotopic substitution, signal contrast is available for different element isotopes without affecting the chemistry of the liquid alloy. This allows for the extraction of chemically specific partial pair structure information from coherent scattering experiments. In addition, because of the lower neutron energies required to probe atomic length scales, inelastic neutron scattering studies can be implemented to provide dynamic information in combination with structural measurements. Further information on the details of neutron scattering techniques can be found elsewhere [4, 5].

Previous ESL chambers [6], including those designed for beamline experiments at synchrotron X-ray source facilities like the earlier described WU-BESL (Ch. 2), are not suited for neutron scattering studies. Electrostatic levitators have been designed for neutron diffraction studies by National Space Development Agency of Japan (NASDA) [7, 8] and the German Aerospace Institute (DLR) [9], and have successfully published results [9-12] utilizing isotopic

substitution and inelastic scattering techniques at the respective Japanese JRR-3M reactor and German FRM II neutron reactor facilities. However, the Spallation Neutron Source (SNS), located at Oak Ridge National Laboratory (ORNL) and designated the most intense pulsed spallation neutron source in the world, offers neutron flux nearly forty times greater than at the FRM II neutron reactor source [13]. Because the previous ESLs are not fit for integration into beamlines at the SNS, the creation of the Neutron ElectroStatic Levitatior (NESL), optimized for use at the SNS, brings the promise of novel experimental capabilities.

Expanding the ESL technique to use at neutron source facilities offers access to the experimental advantages of neutron over X-ray scattering, but several technical challenges must be overcome. In this chapter, the design and operation of the NESL will first be outlined. This is followed by results of the development of the levitation and processing capabilities. Results from commission experiments at the SNS will also be highlighted, and a summary of future work will follow. This chapter will serve to highlight the details regarding the development of its operational capabilities both covering work from January of 2012 to September of 2013 and complimenting previously published results (Kevin Derendorf, Ph. D. Thesis [5]).

6.2 NESL Design and Function

In order to modify the design of the WU-BESL for use at the SNS, several major modifications were required. Given that the majority of the beamlines at the SNS utilize recessed wells into which the sample environments are inserted, the lateral footprint (relative to the vertical direction of the electrostatic field) of the ESL had to be reduced from an area of ~40” x 45.5” to a circular diameter smaller than 16.5”. The design of a modular vacuum chamber fitting these specifications is elaborated upon in Section 6.2.1. Because of the smaller neutron

scattering cross section compared to high-energy X-rays, samples for neutron diffraction measurements need to be much larger in size to provide sufficient scattering signal. Levitating larger samples requires a stronger electric field and therefore higher voltage amplifiers, increasing the complexity of the levitation environment. Modifications to the electrode design, along with the supporting mechanical components, will be discussed in Section 6.2.2. The reduction in the lateral footprint of the ESL, in combination with opening the scattering path to access larger scattering angles, requires modification to the design of the levitation, processing, and non-contact measurement optics. The novel optical design will be discussed further in Section 6.2.3. For neutron scattering, optics for beam collimation present yet another challenge compared to traditional X-ray scattering techniques. Depending on the incident neutron energy, different collimation, shielding, and beam stop designs are employed. The details of the optics design and beamline integration will be discussed in Section 6.2.4. Finally, this section provides only an overview of the NESL design and function; more detail about the design and its various iterations can be found elsewhere [5].

6.2.1 Vacuum Chamber Design

As shown in Figure 5.1 the original WU-BESL vacuum chamber design includes a 14" diameter cylindrical chamber mounted to a 30" by 30" optical table. The "lid" features a 14" CF flange with an Osaka Vacuum TG420MCWB turbo pump, mechanical feedthrough, and HV electrical feedthrough (for the vertical electrode HV connection) mounted on top. Eighteen ports for the various levitation, non-contact thermophysical property measurement, and diffraction optics are located in or near the "horizontal plane", or the plane orthogonal to the vertical electrostatic levitation field. Mounting optical equipment in this plane allows for direct line of

slight of the sample without obstructing the small scattering angle, 2θ, desired for sufficient momentum transfer range (q_{max} = 23 Å^{-1}) for high energy X-ray (E = 75- 130 keV, λ = 0.095 - 0.165 Å) diffraction experiments. The optical table size, and ultimately the lateral footprint, set by this design are compatible for beamline integration at the APS.

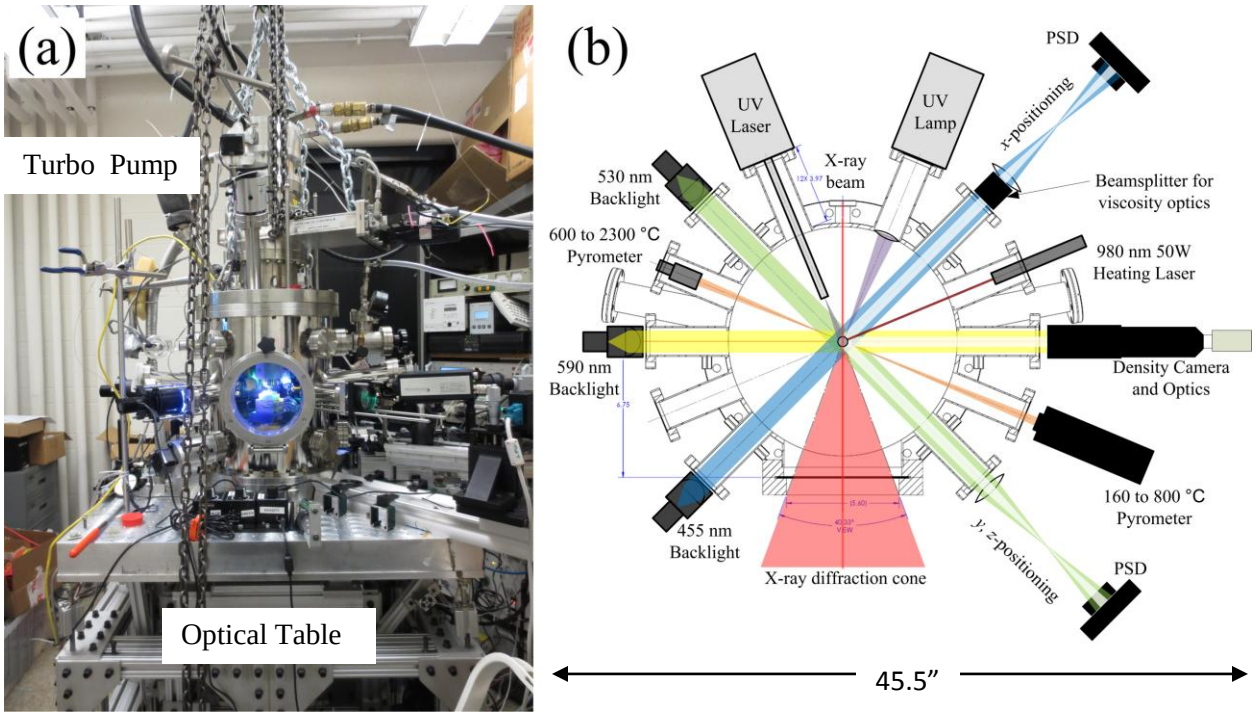

Figure 6.1: The WU-BESL (adapted from [14] with permission), both (a) in its current operational configuration, and (b) a schematic diagram (from Fig. 2.1) of the optical ports and equipment in the horizontal plane. The optical table is identified for reference to the lateral footprint of the apparatus, which is approximately 45.5” from density backlight to density camera.

This WU-BESL design and horizontal footprint, however, is not compatible with the space constraints at the SNS. Therefore a vertical, modular design, shown in Figure 6.2, was chosen. The NESL chamber design features four key components, the electrode assembly, the keystone, the headpiece, and the tailpiece. The headpiece (Fig 6.2(a)) serves as an adapter connecting the NESL to the 37” diameter well configuration of the SNS beamlines of interest. For some of the beamlines (discussed in Sect. 6.2.4), the well is part of a vacuum chamber

containing the beamline detectors. As an adapter, the 37" flange on the headpiece secures the vacuum seal for the well and the detector chamber. This detector chamber vacuum is external to and lower than the vacuum environment inside the NESL chamber. The tailpiece is sealed to the headpiece, and it contains the sample environment and the internal neutron optics. The keystone, which contains the electrode assembly, seals the internal vacuum by a flange inside the headpiece. Once sealed, the internal vacuum is contained to within the keystone (containing the electrode assembly) and the tailpiece. The keystone, together with the electrode assembly, can be lifted out of the tailpiece and headpiece for manipulation of the internal components of the NESL. As will be discussed in Section 2.6.3, the majority of the visualization, levitation, processing, and non-contact measurement optics are mounted to viewports located on the keystone. Similarly, the mirror platform is mounted internally to the bottom of the keystone, and can be accessed by lifting the keystone out of the tailpiece and headpiece. Finally, the electrode platform is a long cylindrically-shaped piece the can be inserted into and extracted from the keystone chamber, sealing the vacuum near the top of the keystone. The turbo pump and several electrical and mechanical feedthroughs are mounted to the top of the electrode assembly. As suggested by its name, the electrodes, providing the levitation field, are mounted to the electrode assembly. The electrodes and several other internal components (discussed in Sect. 6.3.2) can be accessed either by lifting the electrode assembly alone or the keystone and electrode assembly together.

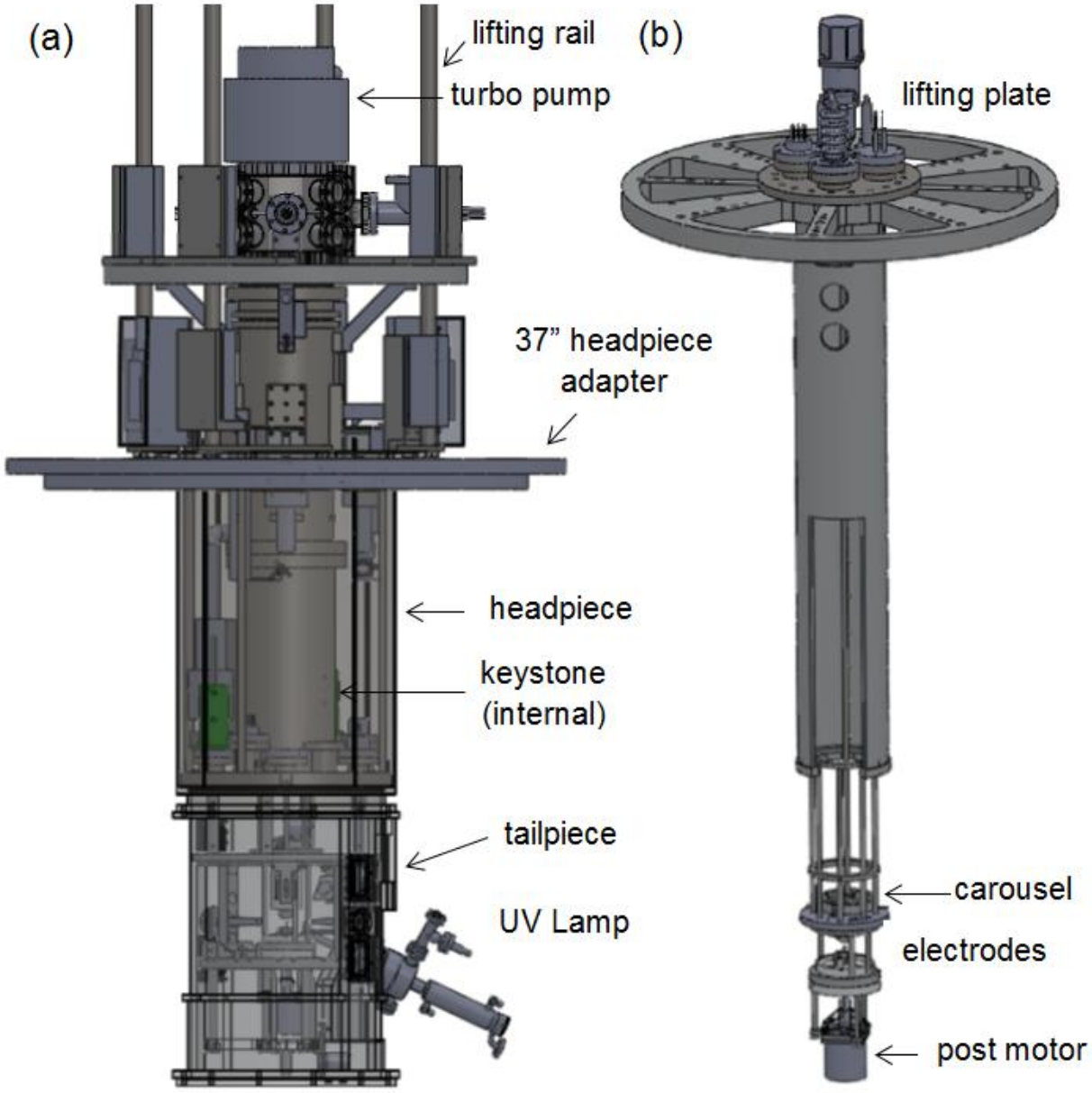

Figure 6.2: Model diagrams of (a) the full NESL in its current configuration and (b) the electrode assembly contained within the keystone, headpiece, and tailpiece assemblies (adapted from [5] with permission). Note that below the 37" headpiece adapter and external to both the headpiece and tailpiece is the detector chamber rough vacuum of the beamline. Within the tailpiece and keystone is the internal NESL vacuum, and the area within the headpiece but external to the keystone is at atmospheric pressure. All components above the 37" headpiece adapter and external to the keystone and electrode assembly are also at atmospheric pressure.

The NESL features a wide variety of feedthroughs, viewports, and other flanges that allow mechanical, electrical, and optical access to the internal vacuum chamber. While most are

not designed to be opened and resealed, the keystone and electrode assembly feature quick disconnect vacuum seals for regular access during experimental runs. The various internal electrical and mechanical components can be accessed by either lifting the electrode assembly out of the keystone assembly or by raising the keystone and electrode assembly together as once piece. Ultimately, the system can be evacuated reaching pressures of 10^{-7} torr after 2-3 hours and as low as $9 \cdot 10^{-8}$ torr during a prolonged pumping cycle. This modular design, in combination with various sealed ports, allows the operator to manipulate, modify, or troubleshoot the various optical, mechanical, and electrical components internal to the main NESL chamber.

6.2.2 Levitation Environment

Figure 6.3(a) shows a levitated sample within the electrode configuration, while Figure 6.3(b) shows the current electrode design for the levitation environment and surrounding parts. To produce the main electrostatic field for levitation, the semi-spherical top electrode (Fig 6.3) is biased to high-voltage and dynamically controlled by a gain-scheduled levitation control algorithm [15] (discussed in Sect. 6.3.1.1). The top electrode is connected to a 0 to -30 kV Trek P0621N-L high-voltage amplifier through a high-voltage feedthrough at the top of the electrode assembly and by insulating, Kapton-coated wire that runs the length of the electrode assembly. The top electrode is isolated from ground by three steatite spacers (Fig, 6.3(b)). Orthogonal side electrodes modify the electrostatic field in order to maintain the lateral sample position and keep the sample in the center of the electrode assembly. Two of the side electrodes, one from each orthogonal pair, are similarly biased to ± 5 kV each by Matsusada AMS-5B6 high-voltage amplifiers. The amplifiers are connected to the electrodes through a secondary high-voltage

feedthrough and by similar Kapton-coated wires. The other two electrodes are grounded with the chamber. The bottom electrode is grounded to the rest of the chamber, and features a central hole through which the sample and sample post can be raised and lowered. The sample post serves two primary functions, (i) to hold the sample in the requisite launch position for launching the sample into its levitation position, and (ii) to retrieve samples that have fallen and allow them to be returned to the launch position.

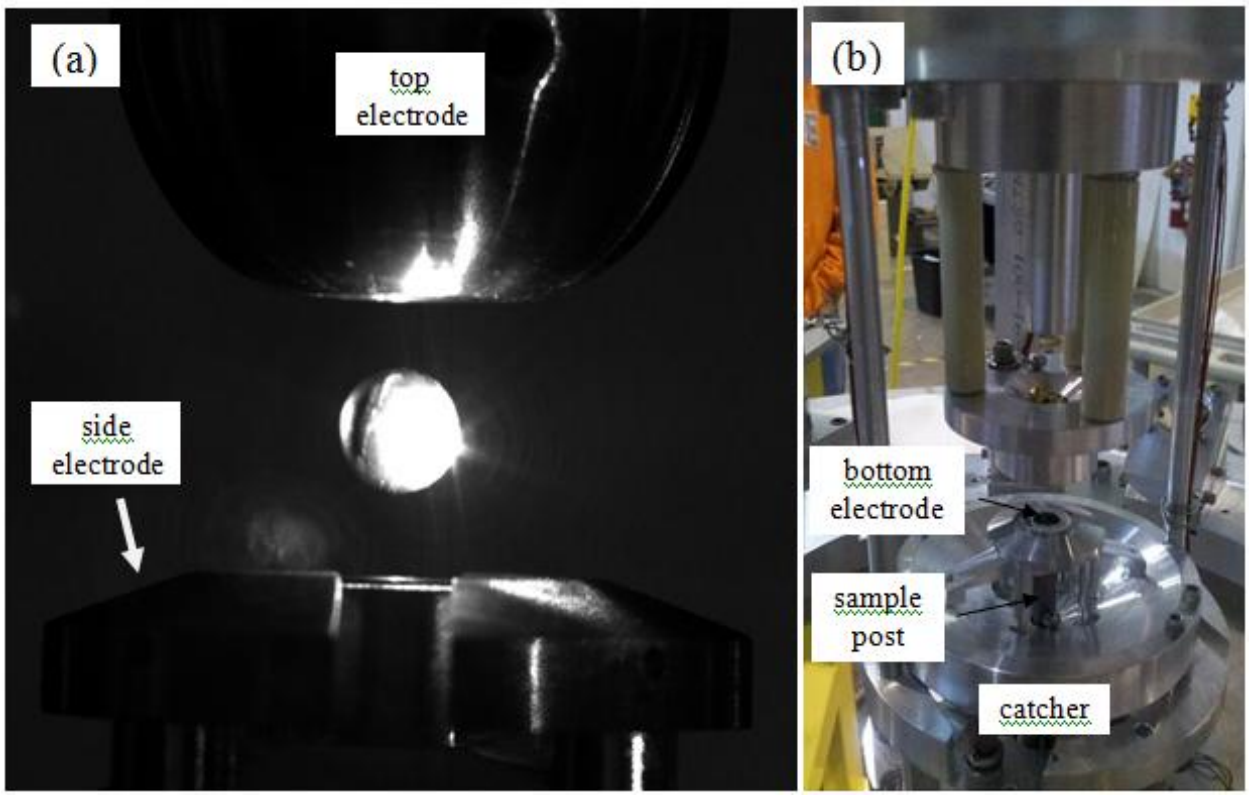

Figure 6.3: (a) Electrode environment (with a levitated sample), and (b) the lower portion of the electrode assembly, including the sample catcher, sample post, steatite insulating standoffs, and sample funnel (adapted from [5] with permission). Below the sample catcher is the lateral high-voltage connections and the post motor. Above the standoffs is the platform on which the sample carousel is mounted.

Because of the frequency with which samples drop out of levitation and to the limited number of samples that can placed in the chamber at a time, a conical sample catcher is located beneath the electrodes to retrieve fallen samples. A vacuum-rated stepper motor, with insulated

electrical connections leading to a feedthrough near the top of the electrode assembly, is attached below the sample catcher and controls the vertical position of the sample post. The post can be raised to a position near the top electrode to retrieve the next sample, or lowered below the conical sample catcher in order to let dropped samples fall into the chamber below. When data acquisition for a particular sample is complete, the post can be lowered to a position below the conical sample catcher. Then by stopping the levitation control program, the sample will fall below the catcher and down into the bottom of the chamber for retrieval.

Samples are loaded onto the post via a carousel located above the top electrode. This carousel, containing locations for 36 samples, is rotated with respect to the electrode assembly, dropping samples through a hole in the center of the top electrode. Newly loaded samples first fall through this hole, travel through the central hole in the top electrode, and finally land atop the raised sample post. The carousel is rotated via a mechanical arm connected to a rotating mechanical feedthrough near the top of the electrode assembly. Attached to the atmosphere side of the feedthrough is a stepper motor that controls the position and rotation of the carousel.

6.2.3 Optical Equipment and Mirror Platform Assembly

In order to maintain levitation, control temperature, make non-contact measurements, and visualize the sample, a host of optical devices are mounted to the keystone and tailpiece utilizing a system of mirrors to provide line-of-sight to the sample. The optical devices that are mounted externally to the keystone are located above 2 ¾" CF flange window ports. Optical devices include

1. two Pixelink PL-B741E cameras for visualization of the sample as well as the full electrode, post, and sample catcher assembly;

2. two beam expanders, for laser positioning, connected to a pair of Melles Griot 25-LHP-925-249 Helium-Neon (HeNe) laser via fiber optic cables;
3. two Position Sensing Detectors (PSDs), which measure the sample position relative to the electrodes from the shadow cast by the sample from the expanded, orthogonal laser beams from the HeNe lasers;
4. a Process Sensors Metis MQ22 two-color pyrometer with an operational range of 500-1800 °C for measurements of the sample surface temperature;
5. two fiber-coupled diode lasers (980 nm, 110 W continuous maximum power output) lasers for sample processing and temperature control, and
6. a Thorlabs high-powered mounted LED backlight for illuminating the chamber for internal visualization.

To acquire data at large scattering angles, and to meet the space requirements for the beam line sample environment wells, optical equipment must be kept out of the horizontal plane relative to the vertical levitation of the sample. To accomplish this, a system of mirrors, located above and below the sample, are used to provide line-of-sight for the optical equipment. The mirrors are attached to the mirror platform, which is itself connected to the keystone. The mirror platform, along with the electrode assembly, can be raised together by lifting the keystone out of the tailpiece and headpiece. As shown in Figure 6.4, the positioning lasers are reflected from a lower mirror, through the space between the electrodes where the sample is levitated, and back to the top of the chamber from an upper mirror to the PSD. Other optical equipment is similarly reflected by mirrors located on the top or bottom portions of the mirror platform. The mirrors are designed with adjustable mounts so that various optical alignments can be performed.

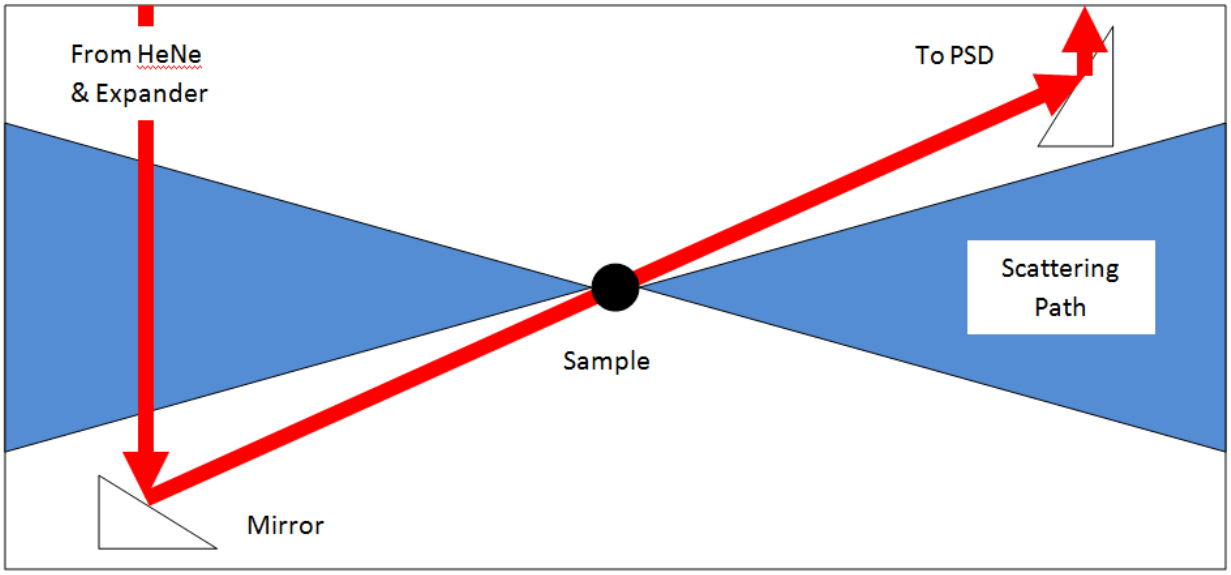

Figure 6.4: A schematic diagram of the mirror platform design for removing optical equipment from the horizontal plane. Optics are reflected from mirrors attached to the platform and aimed at the sample. This design allows access to larger 2θ scattering angle from the neutron beam.

Finally, an Omicron HIS 13 high intensity UV source is mounted to the tailpiece and is aimed at an upwards angle toward the bottom hemisphere of the sample. As discussed in Chapter 2, the UV lamp helps to maintain the surface charge of the sample during processing via the photoelectric effect. The capillary end of the UV lamp, located near the sample, is protected from contamination by sample deposition through the use of a shutter. The opening and closing of the shutter are controlled with a vacuum-rated stepper motor mounted to the mirror platform.

6.2.4 Beamline Integration

Integration of the NESL into the various beamlines of interest requires compatibility with the physical space and detector vacuum constraints of the particular beamline. Another requirement is the installation of appropriate beam collimation, shielding, and diffraction window components for the neutron energies and detector geometries specific to the beamline. The NESL is currently designed for use at the Wide Angular-Range Chopper Spectrometer

(ARCS), Nanoscale-Ordered Materials Diffractometer (NOMAD), and Cold Neutron Chopper Spectrometer (CNCS) beamlines. The NOMAD beamline is designed for high-flux, high-energy neutron diffraction utilizing a large detector coverage area for high-*q* elastic diffraction and PDF determination. The ARCS beamline is optimized for high neutron flux measurements over a large neutron energy spectrum for inelastic scattering studies. Similar to ARCS, CNCS is designed for inelastic scattering studies with a high-energy resolution and low-incident energy neutrons.

For the ARCS and NOMAD beamlines, the sample environments are located in recessed wells into vacuum environments for the detectors. For compatibility with these wells, the headpiece is designed with a 37" flange adapter to seal the detector vacuum environment. Because the UV lamp is mounted externally to the tailpiece, but internally relative to 37" flange and detector vacuum, several vacuum tight connections are made that lead from the 37" adapter to the UV lamp. These connections include a gas line for introducing the high purity helium for UV emission, the HV connection for ionizing the helium gas, water lines bringing in cooling water from the chiller, and vacuum pump lines connected to the UV's turbo for maintaining the specified pressure inside of the UV lamp. When the 37" flange is appropriately aligned with the detector well environment, the beam entrance and exit windows, as well as the sample, are in alignment with the neutron beam for the diffraction experiments.

For the passage of the incident and scattered neutron beams through the NESL apparatus, special windows are used. The entrance and exit windows for the neutron beam are machined from pure vanadium, which has a very small (near zero) coherent scattering cross section. Using vanadium eliminates the possibility of coherent scatter of the incident beam by objects other than the sample. Internal components of the system are largely made of aluminum, which is largely

"neutron-transparent" given its small neutron scattering and absorption cross sections. Finally, the scattering windows, made of 1/16" thick aluminum, comprise the cylindrical walls of the majority of the tailpiece allowing for a 2θ scattering range of ~155 °. The windows also allow ~35 ° scattering with respect to the horizontal plane; scattering in this azimuthal direction is ultimately limited by the mirror platform and electrode design.

For collimation of the neutron beam and shielding of internal components to eliminate secondary scattering effects, materials are chosen based on neutron energy. For the high neutron energies of the NOMAD beamline, boron is the absorption material of choice. A hollowed cylinder of boron nitride is placed in front of the entrance window to collimate the beam, and a hollowed cylinder of boron carbide, used in the NESL internal vacuum to further collimate the beam, is placed on the downstream side of the vanadium entrance window. Similar boron-carbide shields are used for collimation of the beam's exit path, which includes a beam-stop containing Boron-10 powder held in place by a cylindrical boron-nitride plug. In configurations for use at the CNCS and ARCS beam lines with lower neutron energies, thin gadolinium plating is used to collimate the beam and shield internal components of NESL. Special gadolinium electrodes are also used to reduce or eliminate secondary scattering from the internal components nearest to the sample.

6.3 Results (Operation Development, Performance Testing, and Commissioning Experiments)

As part of the design and construction of the NESL at Washington University in St. Louis (WUSTL), collaborators at Iowa State University (ISU) performed initial testing of the levitation equipment (i.e. high-voltage amplifiers, control computer, and signal conversion equipment) as well as developed the initial control algorithms for levitation of the large NESL-sized samples. Once the initial construction was completed, the equipment was delivered to WUSTL. This section covers the subsequent body of research (January 2012 – January 2013) and development required to make the NESL operational, and it includes initial results following two commissioning experiments; one in February of 2013 at the Engineering Materials Diffractometer (VULCAN) beamline and the other at the NOMAD beamline in September of 2013. Included in this section are the details of the operational development, performance testing of the system, and experimental results from the commissioning experiments. Table 6.1 contains a calendar of milestones for the development of the NESL since the beginning of 2012.

Table 6.1: Calendar of milestones for the development and operation of the NESL

Date	Milestone
Jan. 13, 2012	First successful levitation
Feb. 2, 2012	Largest sample levitated (Ti standard)
Feb. 17, 2012	First successful levitation of Cu-Zr sample
Mar. 13, 2012	First attempt to heat sample
May 9, 2012	New UV beam mirror installed close to sample
May 11, 2012	First preprocessing routine implemented
July 31, 2012	New UV mounting position in horizontal plane
Aug. 6, 2012	First successful melt (Cu-Zr sample)
Sept. 4, 2012	Second heating laser installed
Sept. 11-13, 2012	Photocurrent tests of UV flux
Sept. 14, 2012	First successful full processing routine (30 min melt time for Cu-Zr sample)
Oct. 5, 2012	First NESL performance test, first $Zr_{64}Ni_{36}$ processing
Oct. 22, 2012	Longest NESL single-sample operation cycle (5 hr 16 min)
Oct. 23, 2012	First holds at supercooled temperature
Nov. 12, 2012	First tests with improved purity $Zr_{64}Ni_{36}$ samples
Nov. 27, 2012	First remote operation of NESL
Nov. 30, 2012	Longest hold at supercooled temperature (1 hr 47 min)
Jan. 3, 2013	Delivery of NESL to SNS
Jan. 16, 2013	First levitation at SNS
Jan. 25, 2013	First sample melt and processing at SNS
Feb. 4-11, 2013	VULCAN commissioning experiment
Aug. 5, 2013	NOMAD Dry-fit experiment
Sept. 9-16, 2013	NOMAD commissioning experiment

6.3.1 Operation Development

6.3.1.1 Levitation

Levitation experiments began after the start of the year in 2012 and the first levitation was achieved January 13, 2012. Initial alignment of the positioning lasers and PSDs to the electrode assembly was accomplished using the experience gained from operation of the WU-BESL. A levitation control algorithm, using the method developed by Meister et al. [15], was

created for a spherical brass standard of radius r = 2.38 mm and mass m = 476.1 mg. Standard parameters were used (modified from the initial recommendation by Meister et al. through experience in operating the WU-BESL) for calculation of the gain-schedule for the control algorithm. After exhaustive trial and error of initial PSD and sample launch positions (as controlled by the position of the sample post), along with slight adjustments in the lateral amplifier saturation limits and the gain multipliers for the later position signals, successful levitation was achieved.

Experience from the WU-BESL suggested that a single algorithm, designed for a sample of moderate-to-high mass and density (relative to the operational sample size limits of the WU-BESL design), could be used to successfully levitate most samples, regardless of mass or density. An algorithm design for larger NESL samples, on the other hand, was found to be more complex. Successful levitation of lighter (r = 2.38 mm, m = 252.3 mg) and heavier (r = 3.18, m = 597 mg, the largest and most massive ever levitated in the NESL) spherical Ti standards required the use of algorithms designed for their respective sizes and masses. On the other hand, a brass sample (m = 476.1 mg) was successfully levitated using parameters designed for larger sample (m = 749 mg), though the use of this algorithm was not explored further.

Cu-Zr alloy samples, prepared for testing heating and processing operation in the NESL, were first levitated on February 16, 2012. Using a new algorithm designed for a sample of mass m = 300.3 mg (r = 2.12 mm), successful levitation tests were performed on a series of samples ranging in mass from 285 to 315 mg. This particular Cu-Zr algorithm was used extensively for the NESL development, even through the second commissioning run in September of 2013. Similar success was found for levitating a $Ti_{39.5}Zr_{39.5}Ni_{21}$ sample (m = 210.4 mg, r = 2.02 mm),

the lightest ever levitated in the NESL) using an algorithm designed for a sample of radius r = 2.0 mm and mass m = 200 mg.

Stability of the sample during levitation has varied over the course of the NESL's development, and though it is not fully understood at the time of the writing of this thesis, it is believed that the largest improvements in stability come from modifications in and the use of the appropriate levitation algorithm. Using the control computer's interpretation of the sample position, vertical stability ranges in fluctuations from ± 20 to ± 500 μm (for scale, note that a typical sample radius is r = 2.25 mm and the gap spacing between electrodes is 12 mm). Noise contributions from mechanical vibration have largely been ruled out through several tests. First, by damping vibrations from the rough pump hose, small contributions resulting in 50-60 Hz vibrations were eliminated. Samples have also been found to maintain levitation even when vibrations are intentionally introduced into the system. Figure 6.5 is a plot of the interpreted sample vertical position with respect to time both before and after damping mechanisms for the chamber lifting rails were removed. Although most sources of electrical and mechanical noise have been investigated, a 10 Hz oscillation, as interpreted by the computer, still persists with and without sample levitation (as seen in Fig. 6.5). This instability is amplified when the levitated sample is particularly unstable, such as when the wrong algorithm is used for levitation. Figure 6.6 shows the difference in vertical stability when an ~ 425 mg $Zr_{64}Ni_{36}$ liquid sample is levitated using (a) an algorithm designed for a r = 2.12 mm and m = 300.3 mg Cu-Zr sample and (b) an algorithm designed for a r = 2.42 mm and m = 432.6 mg $Zr_{64}Ni_{36}$ sample. While in-flight levitation stability is improved by the appropriate choice of algorithm, the ability to launch a sample into levitation is more inconsistent.

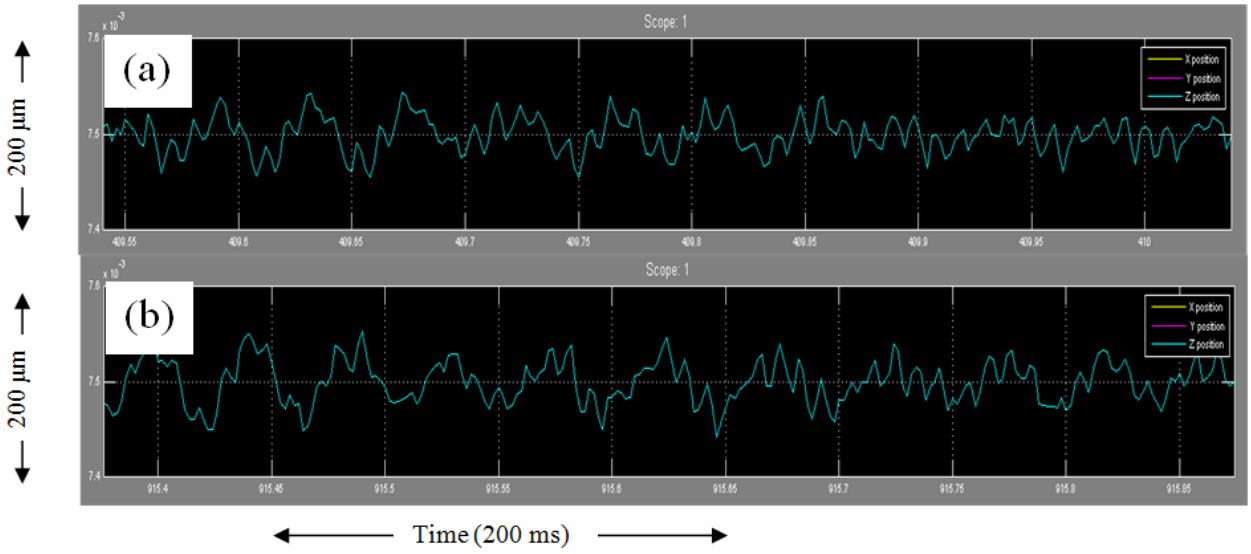

Figure 6.5: Vertical position (as interpreted by the control computer) with respect to time for a levitated brass standard (a) before the removal of the lifting rail damping mechanism and (b) after the removal. The sample stability was essentially the same in both cases, suggesting that mechanical noise does not play a major role in sample instability. Another important feature to note is the persistent ~10 Hz oscillation (from an unidentified source) found both during levitation and without a sample in the positioning laser profile.

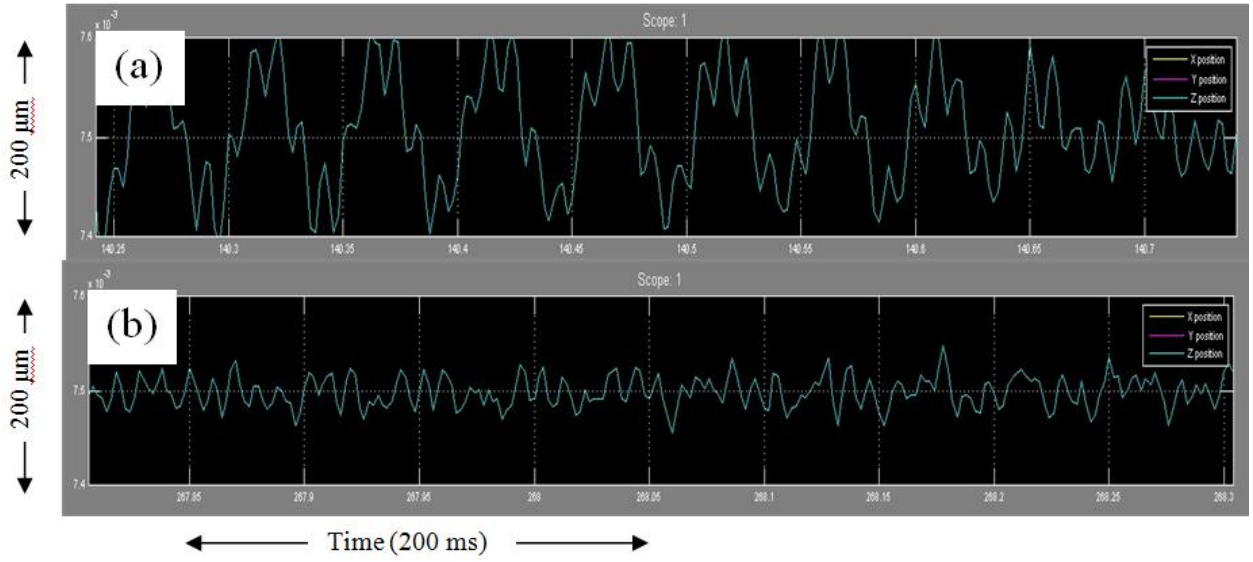

Figure 6.6: Vertical position with respect to time for liquid $Zr_{64}Ni_{36}$ (m = 425 mg) sample using both the (a) Cu-Zr (r = 2.12 mm, m = 300.3 mg) algorithm and (b) Zr-Ni (r = 2.42, m = 432.6 mg) algorithm. Position measurements are as interpreted by the control computer. The stability in (b) is on the level of the inherent noise (without a sample in the positioning laser path) in the interpreted position signal.

For the NESL launching a sample into levitation has been found to be incredibly sensitive to positioning laser and PSD alignment, sample launch position as controlled by the sample post, and levitation algorithm parameters. Early levitation trials found that several attempts were typically needed in order to launch a particular sample. Samples would typically drift laterally out of the positioning laser profile before the lateral voltages could be adjusted to respond. Only by iterative adjustments to PSD and launch positions, along with a little bit of luck, could a sample finally be levitated. Even with the necessary adjustments, it was found that in some cases the sample made an initial "jump" before landing back on to the post. While the sample was sitting on the post, the algorithm would slowly "ramp" the individual lateral (*x* and *y*) and vertical, *z*, voltages until the second launch occurred. This "slow ramping" would allow the *x* and *y* voltages to start at a high enough values to counter the lateral drift of the sample upon launch. Consistent, successful launches were finally achieved by (a) upgrading the lateral amplifiers from outputs of ± 3 kV to ± 5 kV, and (b) modifying the Cu-Zr levitation algorithm to reduce the lateral voltage-change response time. A slight change in the initial algorithm construction parameters produced a gain-schedule with half of the original characteristic response time to changes in surface charge, as shown in Figure 6.7. While this allowed smaller (250 to 350 mg) samples to be launched without an initial "jump", the algorithm would only perform optimally for samples within a narrow range of mass. As mentioned before and shown in Figure 6.6, the algorithm provided insufficient stability for larger $Zr_{64}Ni_{36}$ samples. Construction of a similarly modified algorithm for the larger Zr-Ni samples was unsuccessful due to the gain-scheduling program's inability to converge to the appropriate performance factors. A more in-depth investigation of the control algorithm design may be necessary in order to idealize launch and levitation of samples.

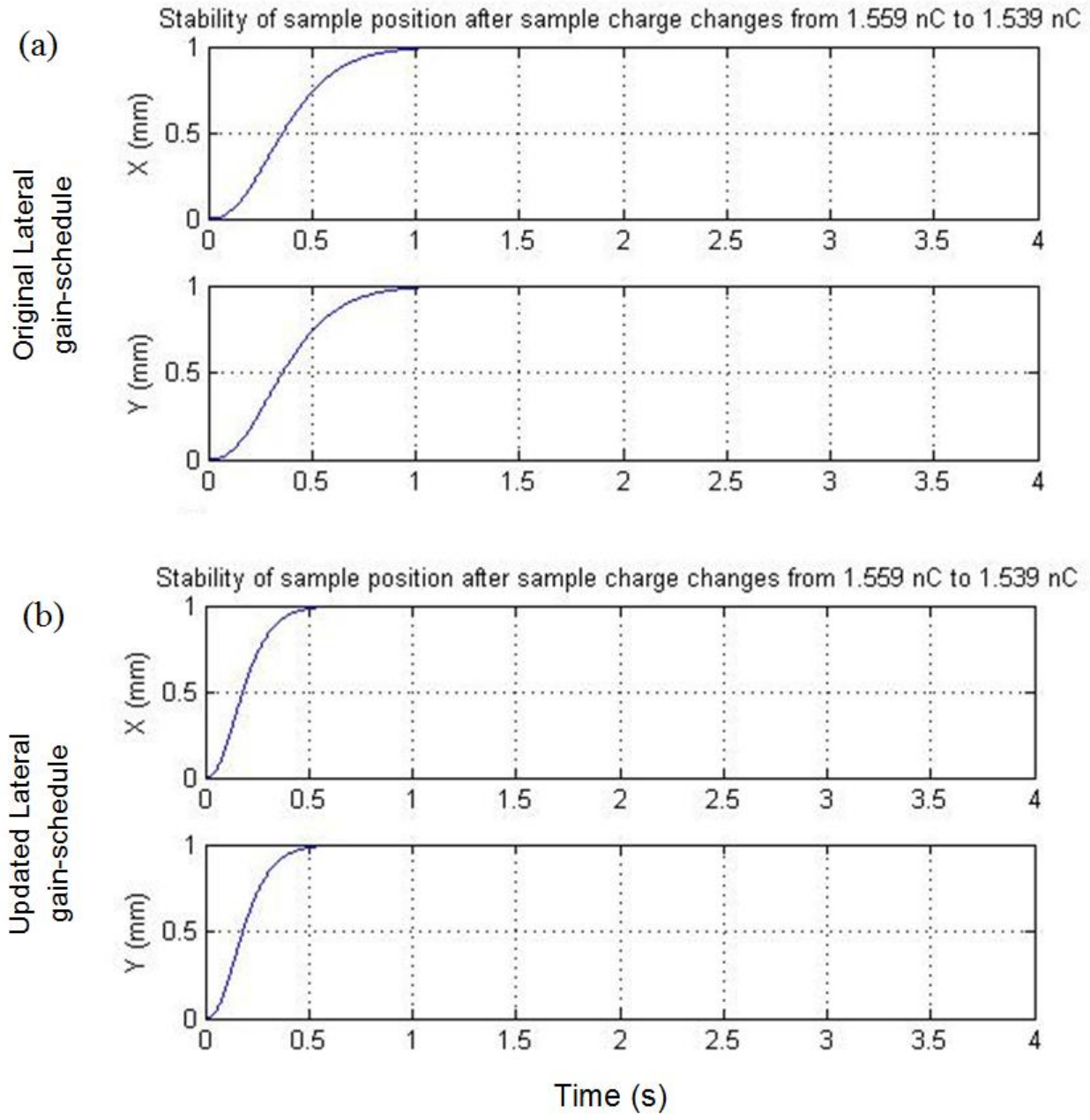

Figure 6.7: Outputs of the simulated sample position change in response to drop in surface charge for (a) the original algorithm developed for the Cu-Zr samples and (b) the modified algorithm with the faster response to changes in lateral position.

Launch and levitation issues have been further complicated by various electrical issues related to the system. Several iterations of the electrode assembly, HV wiring, and external cabling management were made from January, 2012 to September, 2013 in order address these issues. The first is that of arcing from the HV connections to the grounded chamber walls and

internal components of the NESL. Arcing is most prevalent when larger absolute voltages are used to bias the top electrode, as well as during large fluctuations in voltage during levitation. Spontaneous "dropping" of sample from levitation can occur during an arcing event. Similarly, electrical interference between the HV cabling and other electronic components, such as those for the control computer, pyrometer, visualization cameras, and analog-to-digital conversion connections, interfere with successful launching and monitoring of the system. While these electrical issues can be quite complex, improved internal HV insulation and physical and electrical isolation of external equipment has helped mitigate these problems, allowing for successful experiments from the fall of 2012 through the first commissioning experiment in February, 2013. That being said, electrical issues and spontaneous dropping of samples returned as a problem for the September, 2013 commissioning experiment, and are still in the process of being resolved.

The final issue influencing consistent launching and levitation of samples is that of drift in the HeNe positioning laser polarization and intensity. The root cause of this issue is still yet to be determined, but PSD measures of the integrated laser intensity are found to be inconsistent from day-to-day or, as the case has been found since the NESL was delivered to ORNL, even over the course of several hours. Several possible culprits have been identified, including laser source temperature, fiber-optic cable vibrations and movements, and fluctuations in the fiber-optic coupler connections. Given improvements in control algorithm design since the NOMAD commissioning experiment in September, 2013, drift in the PSD readings from the fluctuations in the positioning laser intensity has been identified as one of the likeliest causes for problems regarding levitation and spontaneous dropping of samples.

6.3.1.2 Initial Processing Attempts and UV Issues

In its initial configuration, the UV lamp was mounted vertically to one of the several keystone ports, similar to that of the heating and positioning laser optics. The lamp included a torroidal mirror to focus the UV beam onto the sample from above. Initial testing showed that there was some increased surface charge on the sample due to the UV source, as measured by the change in the required vertical voltage necessary to maintain levitation. The voltage change, however, was small, and attempts to heat the sample to its melting temperature proved unsuccessful. The first attempt to heat and process a levitated sample occurred on March 3 using a single infrared heating laser. Heating of both Cu-Zr and Ti-Zr-Ni alloy samples proved unsuccessful over the course of the next two months, as the required voltage to maintain levitation increased monotonically with sample surface temperature. Once the absolute voltage required for levitation increased to 80-90% of the amplifier's capacity, sudden drops of the sample were extremely likely. The behavior is typical when heating samples without the use of a UV lamp to maintain surface charge, since surface charge is carried away with outgassed material and evaporation of surface contaminates. Under the assumption that valence electrons could be more effectively and permanently discharged from the sample (via the photoelectric effect) when removed for the surface nearest to the positively biased (grounded) electrode, a reflective mirror was placed in a position near the sample to reflect the UV beam onto the bottom hemisphere of the sample. This attempt at improving the UV performance, using both silver and gold coated mirrors, proved unsuccessful, and it was reasoned that the loss of UV beam intensity, due to reflection from two separate mirrors, was too large.

By July 31, the NESL chamber was redesigned in order to mount the UV lamp in the horizontal plane, as is the case for the WU-BESL and the ESL at ISU. This dramatically

increased the surface charging of the levitated sample, as evidenced by the larger drop in the absolute voltage required to levitate the sample. After many attempts to heat the sample and several realignments of the UV source, on August 6, a Cu-Zr sample was successfully melted and heated to ~ 100 °C above its melting temperature. Testing proceeded with limited repeatable success until (a) the second heating laser was installed on September 4, allowing simultaneous heating of opposite sides of the sample, and (b) the UV lamp flux was optimized after measuring the photocurrent using an experimental setup designed by Nicholas Mauro. For the photocurrent measurements, both the original UV lamp and a newly purchased lamp for use on the WU-BESL were tested by adjusting parameters of inlet He gas pressure and high-voltage ionization current. Figure 6.8 shows the results for the two UV lamps, where the optimum pressure and current were determined to be in the ranges of 1.1–1.2 x 10^{-1} mBar and 130-160 mA respectively. It is important to note that the newly purchase UV lamp showed measurably improved performance over the original lamp, although the reasons for thus discrepancy were never fully investigated.

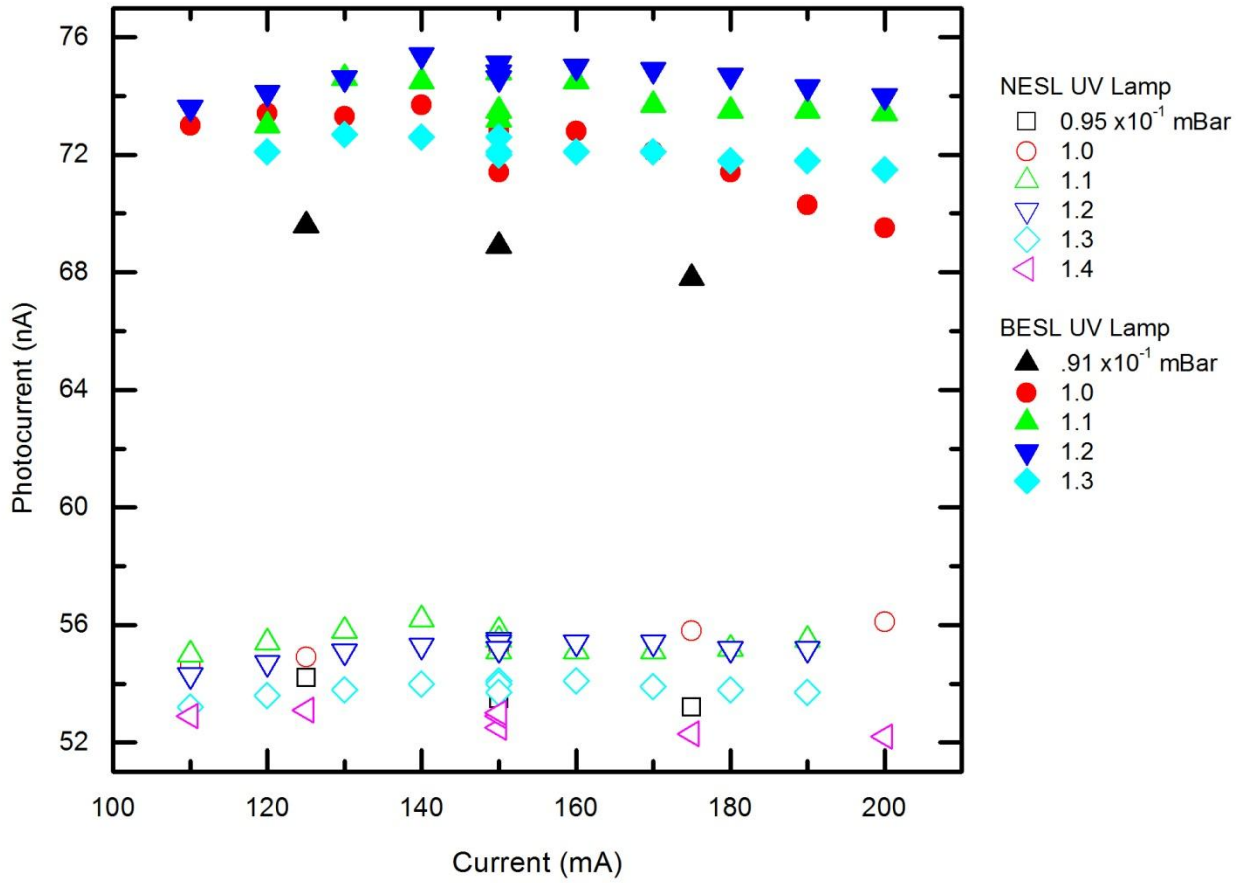

Figure 6.8: Results from the UV flux test for various inlet He gas pressures measuring photocurrent versus ionization current set for the UV lamps. Shown are both the results from the original NESL UV lamp (open symbols) and the results from the newer BESL UV lamp (closed symbols) of the same model.

6.3.1.3 Processing

As mentioned previously, the first successful melt of a Cu-Zr sample occurred on August 6, 2012. After optimization of the UV lamp flux and the installation of a second heating laser, progress over the next several months showed continued improvement of the NESLs performance and ability to heat, melt, and process samples. Progress was made through flight algorithm development (as discussed in Section 6.3.1.1), optimization of UV alignment, development of a "preprocessing" routine for samples, and improvements in sample preparation.

As alluded to in Section 6.3.1.2, the processing ability of a sample (the ability to heat, melt, and hold samples at high temperature) is highly sensitive to UV alignment and flux for maintaining charge on the sample's surface. Although the UV flux was optimized, both by adjusting ionization current and gas pressure parameters and by relocating the UV source to a position perpendicular to the direction of levitation, beam alignment to the sample was found to play a major role in its effectiveness. Figure 6.9 shows both the eclipse of the UV beam by the sample, as seen by one of the visualization cameras located opposite the UV source, and the profile of the beam on the sample as seen by the visible spectrum portion of the source reflected by the sample and the sample post. It is found that by aiming the beam, with a slight offset, to the portion of the sample below its equator, the UV lamp becomes more effective in maintaining surface charge. Similar results have been seen in both the WU-BESL and the ESL at Iowa State University. With the changes in tailpiece design for the VULCAN and NOMAD commissioning experiments, the UV is now mounted at an angle with respect to the horizontal plane. Because the eclipse in the beam from the sample can no longer be visualized, optimization of UV alignment has not been well characterized for the new tailpiece configurations. Because this might be a potential issue for processing samples, particularly in the most recent iteration of the NESL design, more work is needed to optimize UV alignment.

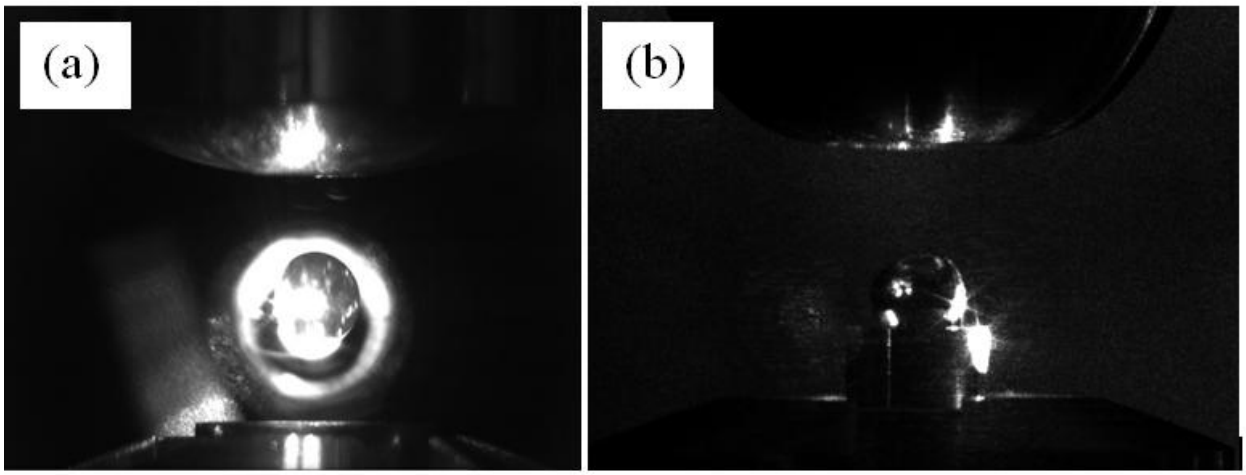

Figure 6.9: Views of the UV beam alignment on the sample from directions (a) opposite of the UV source and (b) orthogonal to the source. The eclipse of the UV beam, the bright spot within the ring, can clearly be seen below the sample in (a). The circular UV beam profile can be seen on the *in situ* sample and the sample post in (b), showing alignment of the beam to the lower hemisphere of the sample.

"Preprocessing" routines were initially developed for improving the processing ability of samples in the WU-BESL. Such a routine involves heating and melting the sample many times, melting *in situ* on the sample post before heating during levitation. Preprocessing serves to eliminate surface contaminants and remove sample impurities that may result in charge loss during levitated processing. On September 14, it was demonstrated that by preprocessing a Cu-Zr sample through two melts while on the sample post, the sample could be successfully melted in a matter of 30 min from the initial start of heating. This is a three-to-four fold improvement over previous attempts. Similarly, after several trials using $Zr_{64}Ni_{36}$ alloy samples, a preprocessing routine of two consecutive melts on the post was found to be the minimum requirement for successful melting of a levitated sample. While preprocessing typically improves processing ability, other confounding factors, such as sample purity and other issues already mentioned, make it difficult to measure the true effectiveness of preprocessing routines.

Early difficulties in processing Cu-Zr samples were also attributed to the poor mixing of the constituent materials during sample preparation. For some samples, clear regions of pure Cu

and pure Zr were visible on the sample surface. While the effect of poor sample mixing has not been well characterized, it has not proven possible to process samples with similar levels of chemical heterogeneity in either the WU-BESL or the NESL. Processing difficulties have also been attributed to impurities and gasses trapped in grain boundaries of the arc-melted samples. This reasoning can partially explain (a) why preprocessing is so effective in improving processing ability during levitation and (b) why the larger NESL-sized samples tend to exhibit more outgassing, charge loss, and other processing issues than smaller samples. These processing issues related to larger sample sizes are evidenced by sudden sample drops, intermittent levitation instabilities correlated with spikes in the chamber pressure, and long recharging times, measured by the time required for the levitation voltage to return to reasonable levels after increasing the heating laser current.

The O_2 content in the starting materials, as well as O_2 absorption during sample processing, also affect the ability to melt, process and undercool a sample. For studies of $Zr_{64}Ni_{36}$, beginning on October 4, 2012, and continuing through November 12, 2012, experiments showed that the maximum achievable undercooling was ~ 170 °C, with a reduced undercooling value, T_r, of 13% ($T_r = (T_L\text{-}T_{min})/T_L$ in K). This reduced undercooling value is low compared to the greater than 18 % achieved in similar studies of Zr-based liquids. Processing cycles to high liquid temperatures ($T_{eutectic}$ = 1010 °C) revealed an inflection in the temperature-time plot near 1160 °C. This inflection correlated with the elimination of reflection spots on the chamber walls (much like that of a disco ball) in the visualization of the sample as well as a reduction in the noise of the pyrometer signal. Temperature hold measurements at values below 1160 °C, but above $T_{eutectic}$, showed that, with time, there was a gradual increase in pyrometer signal noise and the introduction of reflection spots as seen in the visualization camera.

Measurements in the WU-BESL of samples made from the same source material confirmed these features, suggesting that a low temperature oxide (possibly a surface oxide), which dissolved at temperatures above 1160 °C, contributed to poor undercooling. Samples made later from low O_2-containing Zr source material showed improved undercooling and cleaner pyrometer signal at temperatures above $T_{eutectic}$. However, it was discovered that after multiple melts and long processing cycles, samples began to develop the oxide features seen in the lower purity samples. This suggests that even in the high-vacuum environment, O_2 absorption by the levitated liquid can become problematic over long processing periods.

6.3.2 Performance Testing

Prior to commissioning at the SNS, several tests were performed in order to characterize the possible limitations of the NESL. Included were performance tests measuring processing time required to melt a sample, length of run times for a single sample, temperature measurements of various internal components during processing cycles, sample mass loss during processing, levitation stability in the liquid state, temperature stability during holds, maximum undercooling of a liquid sample, and maximum hold duration at supercooled temperatures. The $Zr_{64}Ni_{36}$ alloy composition was chosen both because of its ease of processing in previous ESL experiments and to verify previous experimental measurements obtained by the neutron ESL measurements made by German colleagues [9].

As mentioned in Section 6.3.1.3, it was found that for the $Zr_{64}Ni_{36}$ alloy samples, a minimum of two preprocessing cycles, involving a full *in situ* melt of the sample on the sample post, were required in order successfully melt a levitated sample. After the preprocessing cycles, the average time required to heat a levitated sample from room temperature through the melt

plateau was approximately 40 min. Later results confirmed that if a sample required longer melting times, it was unlikely to be successfully melted and might require further preprocessing. Once melted, samples were continuously heated, cooled, and held at specific temperatures for various periods of time, similar to the processing cycles utilized during WU-BESL experiments (Ch. 2).

The longest total run time, *i.e.* maintaining levitation and processing a single sample, occurred on Oct. 24, 2012. Two full preprocessing melts were performed, and the sample was melted 22 min after initial levitation. The sample was cycled to maximize undercooling, and held at various high temperatures, the longest being 135 min at 150 °C above $T_{eutectic}$. Over the course of whole experiment, the sample was levitated for a total of 5 hours and 16 minutes, demonstrating the NESL's ability to perform long experimental runs for a single sample.

To measure the NESL's capacity for processing high temperature samples for long periods of time, a J-type thermocouple was installed and placed in various locations inside of the chamber. The most critical measurements were at locations nearest to the levitated sample, including the bottom, side, and top electrodes. The biggest concern for system failure is overheating of the top electrode, since it is thermally isolated from the rest of the chamber (due to the high vacuum environment and the use of steatite insulating standoffs). *In situ* measurements of the top electrode temperature made using the thermocouple could not be performed due to the HV environment, but temperature measurements were made immediately following long time experiments. From these experiments, it was discovered that the side electrodes reached a maximum temperature of 66 °C after a 2 hour 40 minute hold of the sample at 1300 °C, the chamber wall (far from the sample) reached a maximum temperature of 31 °C after 3.75 hours holding the sample at 1200 °C, and the mirrors on the mirror platform showed

an increase of about 1 °C after 2 hours of sample processing. To measure the temperature of the top electrode, the chamber was brought up to atmospheric pressure (taking ~10 min) after holding a sample at 1450 °C from 46 min and the thermocouple was inserted in to the hole at the center of the electrode. A temperature of 99 °C was measured for the top electrode, well below temperatures of concern for the various internal parts. A more informative test, however, of the heating of the top electrode could be performed by using a second pyrometer for non-contact temperature measurement of the electrode's surface, but the use of a second pyrometer was not available during that time. External temperature measurements of the thin aluminum scattering windows showed no discernible temperature increase during processing runs, confirming the NESL's ability to handle the heat loads from the high temperature liquid samples. More detailed information on heat load testing can be found elsewhere [5].

In addition to chamber temperature measurements, measurements of the sample levitation and temperature stability were monitored during the high temperature holds. An automated temperature-hold feedback program, designed by Nicholas Mauro, was used to adjust the heating laser current to maintain the sample temperature for long time holds. It was found that over the course of a 2 hour 40 minute hold at 1300 °C, fluctuations in the vertical position increased from ± 50 μm to ± 200 μm (as determined from the levitation control computer). Temperature stability was in the range of ± 3°C to ± 10 °C. The decreased stability near the end of the hold was associated with O_2 absorption over time by the liquid sample. Similar tests of high purity $Zr_{64}Ni_{36}$ samples held in supercooled states showed fluctuations of < 1°C and ± 20 μm in the vertical position. It is important to note, too, that all of the $Zr_{64}Ni_{36}$ samples processed during long periods showed no discernible mass loss (within experimental error of the mass balance described in Ch. 2).

To test the NESL's capabilities for measurement of supercooled liquids, tests were performed not only to measure the maximum undercooling of a sample, but to measure the maximum time for which a sample could be held in the supercooled state. As mentioned in Section 6.3.1.3, the maximum undercooling achieved for the low purity $Zr_{64}Ni_{36}$ samples was 170 °C, resulting in a T_r = 13.0 %. The longest undercooled hold lasted 16 minutes and 10 seconds at 35 °C below $T_{eutectic}$. Using higher purity source material, ~ 425 mg $Zr_{64}Ni_{36}$ samples were undercooled to a maximum of 240 °C (T_r = 18.7%), typically achieved by a free cool following a 20 second hold at 290 °C above $T_{eutectic}$. The temperature of the samples could also be held anywhere from 1 to 10 minutes in the supercooled state. On November 30, 2012, the last day of testing before packing of the NESL for shipment to ORNL, a $Zr_{64}Ni_{36}$ sample was held at 125 °C below the $T_{eutectic}$ (T_r = 9.7%) for an extraordinary 107 minutes and 55 seconds. During the hold, the temperature fluctuations were less than 1 °C and the vertical stability was measured to be ± 20 μm. Though sample composition dependent, these tests demonstrated the NESL's ability to hold at supercooled temperatures for long enough periods for sufficient neutron data acquisition.

6.3.3 Commissioning Experiments

6.3.3.1 VULCAN

Upon delivery to the SNS in January, 2013, final modifications to the NESL were made before the first commissioning experiment at the VULCAN beamline. A new tailpiece was installed, which included the new UV mount angled with respect to the horizontal plane. The NESL and its host of ancillary equipment were reassembled on the Spallation Target floor, and

operational performance was re-tested prior to the experimental run. After last minute levitation and chamber temperature tests, the NESL was moved to the VULCAN beamline.

Figure 6.10 shows the NESL as installed at VULCAN during the experimental run in Feburary, 2013. Because the beamline does not contain the recessed well environment typical of the NOMAD, ARCS, and CNCS beamlines, access to the full apparatus was available throughout the experiment. A stand, shown in Fig. 6.10, was constructed in order to mount the NESL in the beamline configuration. For the experimental run, Gd enclosed the V entrance and exit windows, Gd electrodes, and Gd shielding were installed in the chamber in order to collimate the neutron beam and reduce, or eliminate, primary and secondary coherent scattering from sources other than the sample. Further details on the experimental setup at VULCAN can be found elsewhere [5].

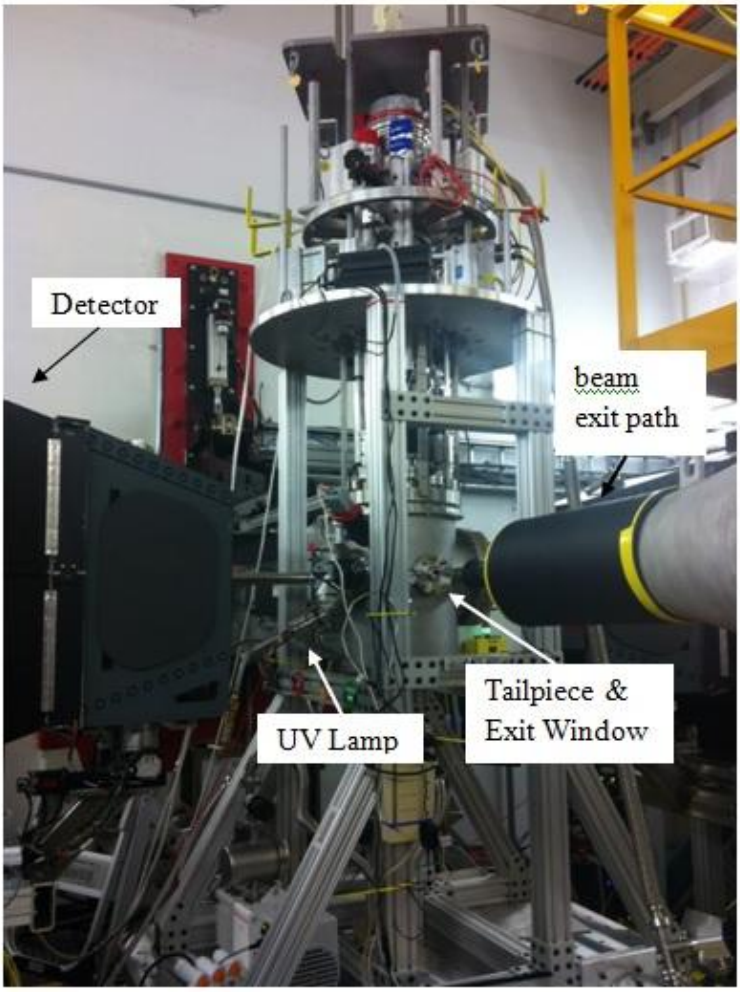

Figure 6.10: The NESL and its stand installed at the VULCAN beamline (as viewed from the downstream perspective relative to the neutron beam path) for the first commissioning experiment. The original disc-shaped headpiece flange is mounted to the top of the stand. Two detectors are placed in positions orthogonal to the beam path.

During the run, data were acquired for $V_{95.7}Nb_{4.3}$, $Ni_{64}Zr_{36}$, $Ti_{37.5}Zr_{37.5}Ni_{21}$, and $Cu_{46}Zr_{54}$ samples. Because of the near-ideal mixing of V and Nb, and the small, negative scattering length of V, the alloying of $V_{95.7}Nb_{4.3}$ gives a total coherent cross section that is nearly zero. The composition can then be used as a standard for subtracting the incoherent portion of the scattering signal. Figure 6.11 shows the scattered intensity from a levitated spherical V-Nb standard, combining a total of 6 hours-worth of collection time to compile the data set. It is important to note that most neutron scattering experiments used pure V as their standard, and

although its coherent scattering length is larger than that of $V_{95.7}Nb_{4.3}$, the V-Nb does show a small signal at low-q from the short range chemical structure of the alloy (due to a slight chemical affinity between the elements). Ultimately, the smoothness of the data, and the lack of observable crystalline peaks, points to the effectiveness of the neutron optics and shielding and eliminated scattering from sources other than the sample.

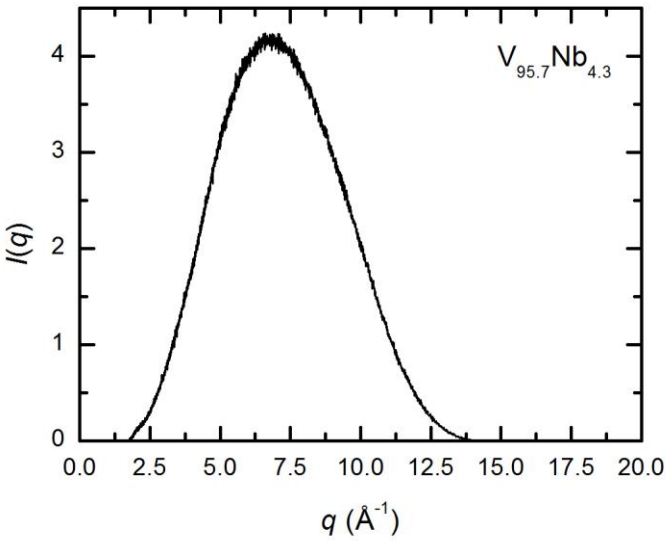

Figure 6.11: $I(q)$ for the $V_{95.7}Nb_{4.3}$ standard acquired over a 6 hour scan [16]. Because of the near-zero coherent scattering length of the composition, no significant coherent structure is observed in the intensity profile. This demonstrates that there are no significant primary or secondary scattering contributions in the signal from sources other than the V-Nb standard.

Scattering data from $Ti_{37.5}Zr_{37.5}Ni_{21}$ also exhibits the expected character of a metallic alloy liquid, but due to low signal from a small total coherent scattering cross section (the scattering length of Ti is negative), poor statistics prevented a more detailed analysis of the data. Scattering from a room temperature crystalline $Cu_{46}Zr_{54}$ sample was also measured for the purpose of measuring activation in samples with exposure to the primary beam.

Figure 6.12 shows $S(q)$ data obtained for $Zr_{64}Ni_{36}$ in both the high temperature and supercooled liquid state. Because of the difficulty in maintaining the sample in the supercooled

liquid state, several isothermal holds were necessary to obtain sufficient signal. The high temperature data, however, were collected for holds lasting multiple hours. The difference in the hold times can be clearly observed by the noise level in the acquired $S(q)$s, especially from the scatter in the data in the low-signal high-q range. As expected, the amount of scatter in the data is directly correlated with the number of counts (proportional to the acquisition time) acquired from scattered neutrons. The major feature of the static structure factor is that they clearly exhibit the character of a liquid metallic alloys and in particular that of previously obtained results from both neutron [9, 17] and X-ray [16] scattering studies. A more in-depth analysis of the data will be performed for future publication.

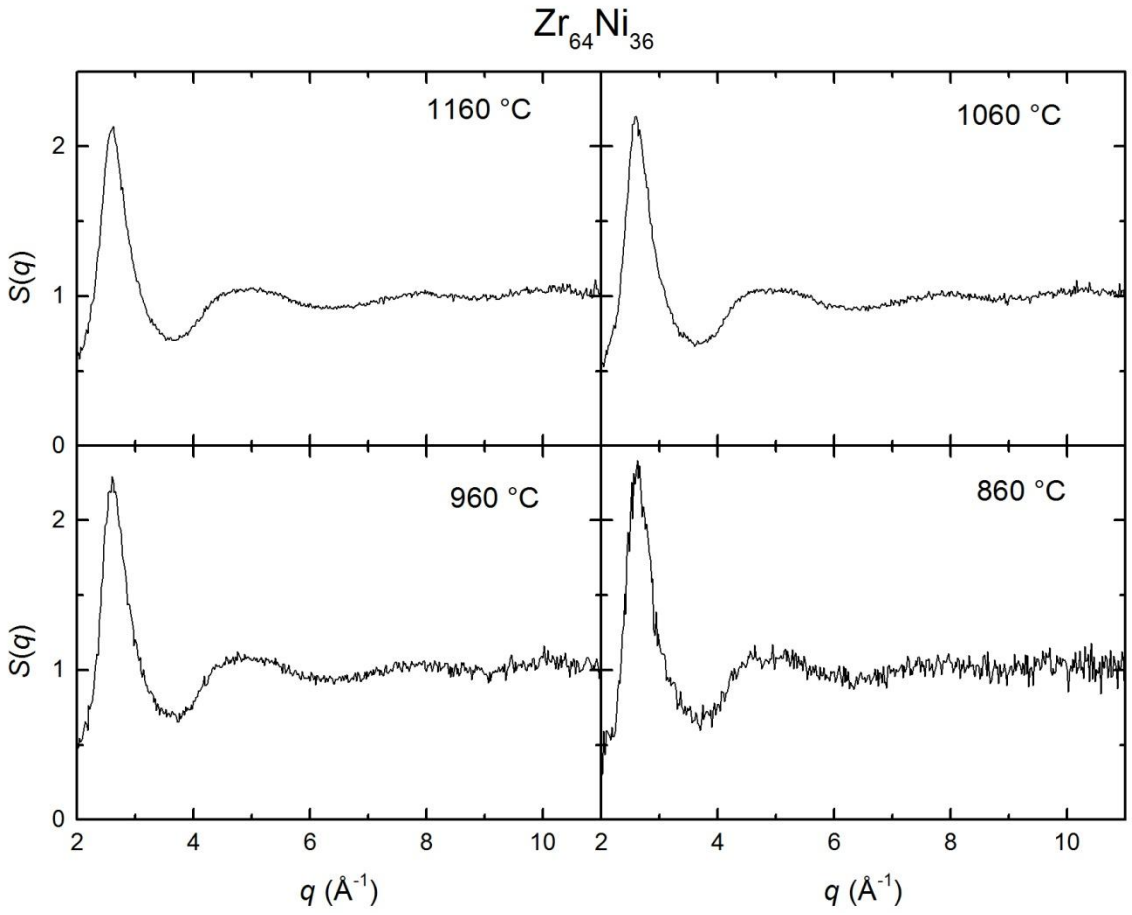

Figure 6.12: $S(q)$ data acquired during the VULCAN commissioning run for $Zr_{64}Ni_{36}$ in the equilibrium high temperature (1060 & 1160 °C) and supercooled (860 & 960 °C) liquid states [16]. The general structural features resemble those from previous neutron [9, 17] and X-ray [16] scattering studies.

6.3.3.2 NOMAD

From February to the end of July 2013, several modifications were made to the NESL in order to make it compatible for installation at the NOMAD beamline. The height of the overall chamber was reduced in order for the system to be lifted over the beamline wall and in to the recessed detector well. A new tailpiece was also designed and manufactured to increase the available scattering angle for diffraction measurements. A redesign of the UV mount placement and capillary length was also implemented to reduce the horizontal footprint of the NESL. Finally, a new headpiece with a 37" adapter flange was installed in order to connect the NESL to

adapt and seal the beamline well. The details of the final NESL design can be found elsewhere [5].

To test the new 37" adapter and the external vacuum connections for the UV lamp, as described in Section 6.2.4, a dry-fit at the NOMAD beamline was carried out in early August of 2013. The dry-fit successfully demonstrated (a) the ability to integrate the system into the detector vacuum chamber design of the NOMAD beamline (and maintain vacuum in the NOMAD detector chamber) and (b) the ability to operate and cool the UV lamp after insertion into the vacuum of the detector chamber on NOMAD.

Finally, in September, 2013, the NESL was installed at the NOMAD beamline for the second commissioning experiment. Diffraction data for room temperature Ni and high temperature crystalline phases of $Zr_{64}Ni_{36}$, $Cu_{46}Zr_{54}$, $Ni_{62}Nb_{38}$, and $Zr_{77}Rh_{23}$ were acquired. Due to time constraints related to the modifications to the NESL chamber, proper UV optimization and alignment could not be accomplished. In addition, several technical issues arose, such as electrical arcing inside the chamber, external HV cable damage, and exacerbated positioning laser intensity drift, all of which prevented samples from being fully processed. Samples, upon heating, would spontaneously drop, particularly during the melting of the sample. Various preprocessing routines failed to produce results. While tests of the neutron optical design, background reduction, and beamline integration were successful, liquid diffraction data could not be obtained.

6.4 Conclusions and Future Work

In conclusion, tests, both at WUSTL in the Fall of 2012 as well as during the two commissioning experiments at the SNS in 2013, successfully demonstrated the capabilities of the

NESL. With modifications to the original WU-BESL design, the NESL can be integrated in to multiple beamlines at the SNS for neutron diffraction experiments. Its ability to levitate, melt, process, and probe the structure of liquid metallic alloys have also been demonstrated.

At WUSTL, the NESL successfully levitated samples ranging in mass from 200 – 600 mg, and was capable of maintaining continuous levitation of samples for up to 5 hours. Both Cu-Zr and Zr-Ni metallic alloys were successfully levitated, melted, processed, and supercooled. Tests processing the $Zr_{64}Ni_{36}$ alloy successfully demonstrated the NESL's ability to undercool samples up to 230 °C and to hold them in the supercooled state for extended (1 – 100 min) periods of time, necessary for elastic neutron scattering measurements and isotopic substitution studies. Alloys can also be held at a single high temperature state for several hours without system failure, a necessity for inelastic neutron scattering measurements.

Successful liquid data acquisition during the VULCAN commissioning experiment provided the essential proof of concept for the NESL. Liquid structures obtained for $Zr_{64}Ni_{36}$ and $Ti_{39.5}Zr_{39.5}Ni_{21}$ in both high temperature and supercooled liquid state demonstrated the NESL's ability to acquire neutron scattering data for the levitated metallic liquid samples. Structural data acquired at VULCAN were artifact free, demonstrating the success of the design of the chamber and neutron optics. Although the signal obtained for scattering measurements at VULCAN were less than ideal, the NESL was not conceptualized for use at this particular beamline, but rather for the NOMAD, ARCS, and CNCS beamlines.

The NESL was also successfully integrated into the NOMAD beamline, demonstrating the ability to (a) to maintain the internal vacuum in the NESL and the vacuum environment for the NOMAD detector chamber, (b) operate the UV lamp in the rough vacuum of the detector chamber, (c) levitate and heat samples in the NESL, and (d) acquire high temperature crystalline

diffraction data without significant background contributions. In spite of these successes, the inability to melt and process samples at the NOMAD beamline raised questions that will require a third commissioning experiment to resolve. This is currently planned for late summer, 2014. Before the final commissioning can occur, the NESL must be re-tested and optimized in its current configuration for heating, melting, and processing of metallic alloy samples, as was achieved prior to the VULCAN commissioning experiment. Several issues have been identified, and plans are being carried out in order to improve the NESL's performance.

Finally, pending a successful third commissioning step, future work with NESL will include isotopic substitution and elastic scattering measurements at the NOMAD beamline, as well as integration and inelastic scattering studies at the ARCS and CNCS beamlines. The first isotopic substitutions studies will include partial structure factor determination in both Cu-Zr and Ni-Nb alloys to use in combination with X-ray diffraction data for experimental validation of previous studies of these systems and to provide new information on chemical ordering in the liquid. Inelastic scattering measurements will also be performed to correlate structural and atomic diffusion measurements with studies of the bulk liquid viscosity already carried out on a variety of metallic alloys. As the full capabilities of the NESL are realized, magnetic scattering studies connecting magnetic and structural correlations in the liquid will be performed.

6.5 References

[1] W. K. Rhim, M. Collender, M. T. Hyson, W. T. Simms and D. D. Elleman, Review of Scientific Instruments **56** (2), 307 (1985).

[2] A. K. Gangopadhyay, G. W. Lee, K. F. Kelton, J. R. Rogers, A. I. Goldman, D. S. Robinson, T. J. Rathz and R. W. Hyers, Review of Scientific Instruments **76** (7) (2005).

[3] N. A. Mauro and K. F. Kelton, Review of Scientific Instruments **82** (3) (2011).

[4] T. Egami and S. J. Billinge, *Underneath the Bragg peaks: structural analysis of complex materials*. (Elsevier, 2003).

[5] K. Derendorf, Ph.D. Thesis, Washington University in St. Louis, 2013.

[6] P.-F. Paradis, T. Ishikawa, G.-W. Lee, D. Holland-Moritz, J. Brillo, W.-K. Rhim and J. T. Okada, Materials Science and Engineering R: Reports **76** (0), 1 (2014).
[7] H. Aoki, P.-F. Paradis, T. Ishikawa, T. Aoyama, T. Masaki, S. Yoda, Y. Ishii and T. Itami, Review of Scientific Instruments **74** (2), 1147 (2003).
[8] P.-F. Paradis, T. Ishikawa and S. Yoda, Journal of Non-Crystalline Solids **312–314** (0), 309 (2002).
[9] T. Kordel, D. Holland-Moritz, F. Yang, J. Peters, T. Unruh, T. Hansen and A. Meyer, Physical Review B **83** (10), 104205 (2011).
[10] J. Brillo, A. I. Pommrich and A. Meyer, Physical Review Letters **107** (16), 165902 (2011).
[11] F. Yang, T. Kordel, D. Holland-Moritz, T. Unruh and A. Meyer, Journal of Physics: Condensed Matter **23** (25), 254207 (2011).
[12] D. Holland-Moritz, F. Yang, T. Kordel, S. Klein, F. Kargl, J. Gegner, T. Hansen, J. Bednarcik, I. Kaban, O. Shuleshova, N. Mattern and A. Meyer, Europhysics Letters **100** (5), 56002 (2012).
[13] A. Taylor, M. Dunne, S. Bennington, S. Ansell, I. Gardner, P. Norreys, T. Broome, D. Findlay and R. Nelmes, Science **315** (5815), 1092 (2007).
[14] J. C. Bendert, Ph.D. Thesis, Washington University in St. Louis, 2013.
[15] T. Meister, H. Werner, G. Lohoefer, D. M. Herlach and H. Unbehauen, Control Engineering Practice **11** (2), 117 (2003).
[16] M. L. Johnson, (Private Communication).
[17] D. Holland-Moritz, S. Stüber, H. Hartmann, T. Unruh, T. Hansen and A. Meyer, Physical Review B **79** (6), 064204 (2009).

Chapter 7

Summary and Conclusions

This thesis has discussed work that is part of a larger effort in the experimental determination of liquid structure and its relationship to liquid dynamics, thermophysical properties, and ultimately glass forming ability (GFA). More specifically, the work has investigated questions regarding the relationship between GFA, structural and chemical ordering, and kinetic behavior of metallic alloy liquids. Through high-energy X-ray diffraction measurements, this work characterized the structural evolution in metallic liquids as they are cooled from the high temperature, equilibrium state, to the metastable, supercooled liquid state. This was achieved through using WU-BESL, an electrostatic levitation facility that is optimized for *in situ* synchrotron X-ray diffraction studies of levitated, high-temperature metallic liquids. From these measurements, information on both the local and average atomic structures was combined with topological atomic information obtained from Reverse Monte Carlo (RMC) simulations, as well as with theoretical and experimental studies of liquid viscosity, thermophysical properties, and GFA. Through this combination, the connection between structural ordering and kinetics, the universality of chemical ordering, and the development of various local structures is inferred. Further, these studies motivate the need for a new experimental facility to address questions uncovered in this work.

In Chapter 3, diffraction studies of the structure of Cu-Zr and Cu-Hf liquids and glasses were described. X-ray data from both quenched amorphous ribbons and equilibrium and supercooled levitated liquids were used to describe the evolution of structural and chemical

ordering in four binary alloys from these systems. Measurements of the total structure factor, $S(q)$, for each of the liquids suggest developing icosahedral short-range order (ISRO) and accelerated ordering in the region between the lowest supercooled temperature measurement and T_g. Total pair distribution functions (PDFs) also show that chemical ordering accompanies this topological ordering. Asymmetries and peak splitting in the first coordination shells for the liquids were analyzed using the results of Molecular Dynamics (MD) simulation studies and arguments concerning atomic size, scattering strength, and chemical behavior of the constituent elements. This analysis suggests a connection between chemical ordering and a signature of kinetic fragility in the liquid from the inferred acceleration of ordering. It is also suggests that the chemical ordering observed in these liquids may be universal to binary glass-forming alloys. Studies of similar transition metal binary liquids with lower GFA and experimental measurements of the chemically specific partial pair correlation functions (PPCFs) are required to confirm these results.

In Chapter 4, the first containerless X-ray diffraction studies of the $Pd_{82}Si_{18}$ binary bulk metallic glass (BMG)-forming liquid were used to verify the results from recent MD simulations. Measurements of the total structure factors show evidence of ISRO, which is suggested to result from the Pd-based clusters in the liquid. Dominant peaks in S(q) grow linearly with temperature as the liquid evolves from high-temperature equilibrium to the supercooled state, suggesting a lack of accelerated ordering over the observed temperature region. Measurements of the dominant correlation lengths in the pair distribution function, in combination with analysis of the local topological order as determined from constrained RMC simulations, confirm a lack of accelerated or increase in chemical ordering upon entering the supercooled liquid regime, as contrasted with the behavior of the widely studied Cu-Zr binary BMG-forming liquids. Finally,

discrepancies between experimental and MD data, along with difficulties in obtaining proper RMC fits to the data set combination, suggest a need for refinement in the MD model potentials.

In Chapter 5, novel high-temperature and supercooled liquid structural measurements were analyzed for Si-containing binary and ternary metallic liquids. Measurements of the local order and structural evolution in the $Au_{81}Si_{19}$, $Pd_{82}Si_{18}$, and $Ni_{75}Si_{25}$ binary liquids show a lack of accelerated ordering, anomalous thermal contraction of the first coordination shells, and a variety of shapes and positions of the dominant correlations in the total structure factors and pair distribution functions. Differentiation in the local ordering in the binary liquids are reflected in the shapes of the second peak in $S(q)$, indicating a variation in amount and type of ISRO, and in the average nearest-neighbor atomic spacing, reflecting differences in atomic size and chemical bonding of the constituent elements. Measurements of levitated liquid and quenched BMG structures of the $Pd_{77}Cu_6Si_{17}$ ternary alloy support previous studies relating liquid kinetic strength to structural differences in the glass and liquid $S(q_1)$ peak heights. Finally, similarities in the measured structure factors of the Pd-Si binary and the Pd-Cu-Si ternary lead to a prediction in the jump from the Pd-Si liquid to its glass peak height at T_g.

Finally, in Chapter 6, the design, operational development, commissioning and results from a new levitation facility optimized for neutron scattering measurements at the Spallation Neutron Source in Oak Ridge, TN were discussed. With the NESL, neutron measurements can be combined with previous X-ray diffraction studies to extract both chemically specific partial structure factors and kinetic information from metallic liquids. However, in order to obtain diffraction measurements from weakly scattering neutrons within the constraints of the beamlines at the SNS, several design and operational challenges had to be overcome. After several design changes and operational studies, tests of the NESL demonstrated its ability to

levitate, melt, and process larger samples (eight times more massive than those used in WU-BESL studies), to hold at both high temperature and in the supercooled state for long durations in order to obtain sufficient scattering signal, and to obtain artifact-free structural measurements for metallic alloys in the crystalline solid and amorphous liquid state. Although a proof-of-concept for the experiment was successfully demonstrated during the first commissioning run at the VULCAN beamline, a variety of mechanical and electrical failures during the second commissioning at the NOMAD beamline run prevented the acquisition of the desired scientific measurements. A plan-of-action is in place in order to troubleshoot and recalibrate the NESL for a third commissioning run in order to demonstrate its experimental capabilities. Future work with the NESL will provide the necessary partial structure and kinetic information needed to address the questions posed from the results in this thesis.

Through the use of the WU-BESL for *in situ* high-energy X-ray diffraction measurements, information on structural evolution, chemical ordering, and the relationship between structure, kinetics, and thermophysical properties was obtained. Novel measurements of metallic alloys in both the high-temperature and supercooled liquid states provide experimental validation of theoretical investigations. Because of the limitations of X-ray diffraction, the development of the NESL for neutron diffraction studies will allow deeper investigations into the chemical structure and kinetic behavior of metallic liquids. Future measurements of complimentary alloy systems, partial structure factor determination for binary BMG-forming liquids, and direct structural and kinetic measurements will further our understanding of the relationships between liquid structure, kinetics, thermophysical properties, and GFA.